Title

ALPHA PARTICLE BOMBARDMENT OF Si AND GaAs DIODES; ENERGY CONVERSION AND RADIATION DAMAGE

Author

Posey, Lawrence.

Publication Date

1965-06-01

UCRL-11958

c. 2

University of California

Ernest O. Lawrence Radiation Laboratory

ALPHA PARTICLE BOMBARDMENT OF Si AND GaAs DIODES; ENERGY CONVERSION AND RADIATION DAMAGE

Berkeley, California

DISCLAIMER

Research and Development

UCRL-11958

UNIVERSITY OF CALIFORNIA

Lawrence Radiation Laboratory
Berkeley, California

AEC Contract No. W-7405-eng-48

ALPHA PARTICLE BOMBARDMENT OF Si AND GaAs DIODES; ENERGY CONVERSION AND RADIATION DAMAGE

Lawrence D. Posey
(Ph.D. Thesis)

June 1965

ALPHA PARTICLE BOMBARDMENT OF Si AND GaAs DIODES;
ENERGY CONVERSION AND RADIATION DAMAGE

Contents

Abstract vii

I. Introduction 1

II. The Particle-Voltaic Effect 6

III. Alpha-Voltaic Energy Conversion 18

A. Performance of a Particle-Voltaic Device. 18

B. Spatial Distributions for the Production of Electron-Hole Pairs and Lattice Displacements 23

1. Electron-Hole Pair Production 24

2. Lattice Displacement Production 25

C. Operating Performance of an Alpha-Voltaic Device . . 30

1. Alpha Generated Current 32

2. Dark I-V Characteristic 34

3. Irradiated I-V Characteristic 37

4. Bombardment Induced Changes in Device Performance 43

IV. Dark Current-Voltage Characteristics for Silicon and Gallium Arsenide Solar Cells 47

A. Theory 47

B. Experimental Method 54

C. Results and Discussion 65

1. P-on-N Si Cells 70

2. N-on-P Si Cells 88

3. P-on-N GaAs Cells 93

4. Series Resistance 101

D. Conclusions 103

V. Alpha Particle Bombardment of Silicon and Gallium Arsenide Solar Cells 110

A. Theory 110

B. Experimental Method 118

C. Results and Discussion 128

1. Alpha Source Angular Distribution and Energy Spectrum 129

2. Initial Energy Conversion Properties 133

3. Bombardment Induced Changes in Device Performance 139

4. Diffusion Length Degradation Constant 156

5. Initial Diffusion Length Estimates 177

6. Bombardment Induced Changes in the Dark I-V Characteristics 181

D. Conclusions 191

VI. Summary 194

Nomenclature 197

Acknowledgments 202

Appendices 203

A. Semiconductor Diode Dark I-V Characteristics . . . 203

B. Charged Particle Energy Loss in Semiconductors . . 218

1. Atomic Electron Excitation and Ionization . . . 218

2. Valence Band to Conduction Band Electron Excitation 237

3. Atomic Collision Stopping Power and the Production of Lattice Displacements 246

4. Spatial Variation of the Electronic Stopping Power and the Lattice Displacement Production Rate 266

C. Current-Voltage Characteristic of a Semiconductor Diode Under Charged Particle Bombardment 272

D. Performance of a Particle-Voltaic Device 284

E. Error Analysis Technique 292

References 297

ALPHA PARTICLE BOMBARDMENT OF Si AND GaAs DIODES; ENERGY CONVERSION AND RADIATION DAMAGE

Lawrence D. Posey

Inorganic Materials Research Division, Lawrence Radiation Laboratory, and Department of Nuclear Engineering, College of Engineering, University of California, Berkeley, California

June 1965

ABSTRACT

The α-voltaic effect, associated with α-particle stopping in a semiconductor diode, was investigated in p-on-n and n-on-p Si solar cells and p-on-n GaAs solar cells at operating temperatures of 200°K and 275°K. An initial maximum conversion efficiency of approximately 4%, well below theoretical predictions, was realized for all three cell types at 200°K, and in all cases at 275°K the efficiency was less than 1%. The discrepancy between theory and experiment was attributed to the substantial non-ideal contribution to the dark I-V characteristic present in all the cells employed.

The dark I-V characteristics of p-on-n and n-on-p Si solar cells and p-on-n GaAs solar cells were measured for temperatures between 90°K and 360°K. The ideal diffusion term was isolated for all the cells, but sheet resistance effects in the surface region were not discernible. The non-ideal current term was found to be more consistent with a junction tunneling current than with a junction recombination-generation current.

The GaAs solar cells were found to be the most resistant to radiation damage from a device standpoint while the n-on-p and p-on-n Si cells exhibited decreasing radiation resistance in that order. The diffusion length degradation constants were also determined for both materials at

200°K and 275°K. These values in order of decreasing radiation resistance are, for the p-type Si, $K_p(Si) \approx 3X10^{-5} cm^{-2}\alpha^{-1}$ at 275°K and $5X10^{-5} cm^{-2}\alpha^{-1}$ at 200°K, for the n-type Si, $K_n(Si) \approx 7X10^{-5} cm^{-2}\alpha^{-1}$ at both temperatures, and for the n-type GaAs, $K_n(GaAs) \approx 4X10^{-4} cm^{-2}\alpha^{-1}$.

The dark I-V characteristics of the cells underwent substantial changes during exposure. The changes in the ideal current were consistent with a bombardment induced decrease in minority carrier lifetime. The changes in the non-ideal current term for all the cell types tested were not consistent with a junction recombination-generation current and in fact indicate that a substantial current contribution must be controlled by the surface state of the cells.

I. INTRODUCTION

The diverse ways in which an energetic particle (α, β, γ, etc.) interacts with a semiconductor material or device have proven to be of considerable value in many areas of research as well as in a number of practical applications. The mechanism of charge carrier production by energetic particles makes possible the use of semiconductor diodes as energy converters and charged particle detectors and is the basis for numerous photo-sensitive devices. The mechanism of lattice displacement production in a solid under energetic particle bombardment has been used as a tool in studying the basic properties of a solid. This is particularly true for semiconductors whose electrical properties are quite sensitive to the defect centers resulting from the production of lattice displacements during bombardment.

The ability of a semiconductor diode to convert the energy of an incident particle directly into useful electrical energy depends upon the phenomenon termed the particle-voltaic effect; that is, the mechanism whereby the current arising from the bombardment produced charge carriers flows in a suitably chosen load under the influence of a voltage induced at the diode p-n junction. This phenomenon and its application have been studied in a number of semiconducting materials using various particle types.

The greatest amount of effort has been devoted to the study of the photo-voltaic effect[14,45] and associated solar energy conversion[36,40,51,61,67] owing to the potential importance of the sun as an energy source.

The particle-voltaic effect using energetic particles other than photons has received attention in only a few scattered instances; namely, the beta-voltaic effect[47,50] and the fission-fragment-voltaic effect.[29]

The limited interest in charged particle energy conversion using semiconductor diodes resulted from the fact that a degradation in the device performance was found to accompany the energy conversion process.[47,50] This was attributed to changes in the material properties resulting from the presence of bombardment produced lattice displacements.

Neglecting the effect of radiation damage, the initial maximum energy conversion efficiency for a semiconductor diode under energetic particle bombardment is given by

$$\eta_{max,o} = \frac{P_{out}}{P_{in}} \approx (qV_{mp})(Q/\epsilon) \qquad (I\text{-}1)$$

where ϵ is the energy per electron-hole pair for the semiconducting material, Q is the charge collection efficiency, and V_{mp} is output voltage at maximum power. V_{mp} is obtained from

$$(1+\lambda V_{mp}/A)\exp(\lambda V_{mp}/A) = I_G/I_{ol} \qquad (I\text{-}2)$$

where I_G, the particle generated current, results from the electron-hole pairs produced by the incident energetic particles. A and I_{ol}, the non-ideal exponential factor and the effective reverse saturation current respectively, define the dark I-V characteristic of the diode in the current interval $0.1I_G \lesssim I \lesssim 10I_G$. We see from Eqs. (I-1) and (I-2) that the energy conversion efficiency of a particle-voltaic device is strongly dependent upon the dark I-V characteristic of the device (the dark characteristic is, in part, determined by the material purity) which is indeed found to be the case for solar cells.[35,49] From these equations it is evident that the energy conversion efficiency is also dependent upon the material purity through the charge collection efficiency.[16,37,59] In contrast to these factors the energy per electron-hole pair is relatively independent of purity for a given material.[43]

Our primary concern in this report is the α-voltaic effect associated with α-particle stopping in Si and GaAs diodes. In light of the existing energy sources associated with naturally occurring and artificially produced α-particle emitters, an investigation of the α-voltaic effect is of practical interest.

In the particular case of a moderately pure Si α-voltaic device (corresponding to a $Q \approx 0.8$) subject to α-particle bombardment from a 0.5 mC source, we expect, from Eqs. (I-1) and (I-2), that V_{mp} is to be found from

$$(1+42.5V_{mp}/2)\exp(42.5V_{mp}/2) \approx 10^{-6}/10^{-9}$$

and then

$$\eta_{max} \approx (0.24)(0.8/3.55) \approx 5.5\%$$

at T = 275°K where the values of A and I_{ol} employed are typical of diffused Si diodes.[53,63]

The scope of the present work includes an analytical study of the energy conversion performance expected of various purity Si α-voltaic devices and an experimental investigation of Si and GaAs solar cells under α-particle bombardment which includes the determination of both the initial performance and the bombardment induced changes in Q and the dark I-V characteristics.

The charge collection efficiency of photo-voltaic and electron-voltaic devices has been found to decrease with increasing exposure through a decrease in the minority carrier lifetime resulting from the introduction of defect recombination centers during bombardment. A substantial amount of work has been performed for electron and proton bombardment of Si solar cells.[1,17,38,52] This sensitivity of the charge collection efficiency and therefore the short circuit current to

radiation damage has been used as a means of studying the nature of the lattice defects produced by high energy electron bombardment of Si diodes.[25,26,39]

Si and GaAs solar cells were employed in this work owing to the fact that of all the commercially available semiconductor junction devices they come the closest to possessing the optimum α-voltaic device geometry. Si was chosen for its high purity and associated superior charge collection efficiency, while GaAs was chosen for its larger forbidden energy gap and correspondingly greater device output voltage.

When the results of this work are used in conjunction with Eq. (I-2), the V_{mp} typical of a p-on-n Si solar cell under α-particle bombardment is found from

$$(1+42.5V_{mp}/2.5)\exp(42.5V_{mp}/2.5) \approx 10^{-6}/10^{-7}$$

so that

$$\eta_{max,o} \approx (.04)(0.9/3.55) \approx 1\%$$

at 275°K and

$$(1+58V_{mp}/3.4)\exp(58V_{mp}/3.4) \approx 10^{-6}/10^{-8}$$

so that

$$\eta_{max,o} \approx (.18)(0.9/3.55) \approx 4.5\%$$

at 200°K. An alpha source activity of approximately 0.5mC was used in obtaining these estimates. It is evident from these results that the inferior performance of the p-on-n Si solar cells under α-particle bombardment, as compared to that of the moderately pure diffused Si diode mentioned above, is primarily due to the "soft" dark I-V characteristics of the solar cells (compare the values of I_{o1} and A for the two devices). A Si diode designed specifically for operation as an

α-voltaic device should not be as severely hampered by charge carrier generation and current flow in surface inversion layers as a Si solar cell owing to the greater junction depth and higher material purity required for the α-voltaic device.

The dark I-V characteristics of all types of Si diodes are found to deviate markedly from the ideal junction I-V characteristic for currents less than or on the order of 10^{-4} to 10^{-5}A. The non-ideal current contributions have been investigated for a number of Si devices such as power rectifiers, tunnel diodes, etc.,[13,15,20,53,63] and theory is generally found to be in good agreement with experiment. Investigations of the dark I-V characteristics of solar cells,[49,66] however, have thus far proven to be less profitable, and their soft nature is as yet not completely understood. In the present work we attempt to improve this situation by studying the dark I-V characteristics prior to, during, and subsequent to bombardment.

II. THE PARTICLE-VOLTAIC EFFECT

As an energetic particle passes through a semiconducting material, it gives up energy to the solid by way of electron excitation (in the terminology of semiconductor theory, this process is referred to as electron-hole pair production) and by atomic collisions with the constituent atoms of the lattice. These latter collisions lead to both lattice heating and the production of lattice defects. For the specific case of a semiconductor diode a fraction of the charge carriers created in the base regions of the diode by an incident energetic particle diffuse to the junction (see Fig. II.3), and the remaining charge carriers are lost through surface and volume recombination. Assuming negligible recombination in the junction, the charge carriers reaching the junction are swept into the other base region under the influence of the junction electric field. This gives rise to a current flow in the external circuit. If an external load is present, the diode furnishes the voltage required to maintain the current flow through the load. This is the phenomenon commonly referred to as the particle-voltaic effect. The remainder of this section deals with this effect in greater detail.

First, let us consider the equilibrium state of semiconducting material not subject to illumination. Figure II.1 presents the electron potential energy diagram for both n- and p-type materials. In this figure the density of states function, $Z(E)$, at the top of the valence band and the bottom of the conduction band is assumed to be proportional to $E^{1/2}$. In the figures of this section the electron distribution functions are highly exaggerated for purposes of illustration. The Fermi-Dirac distribution function is

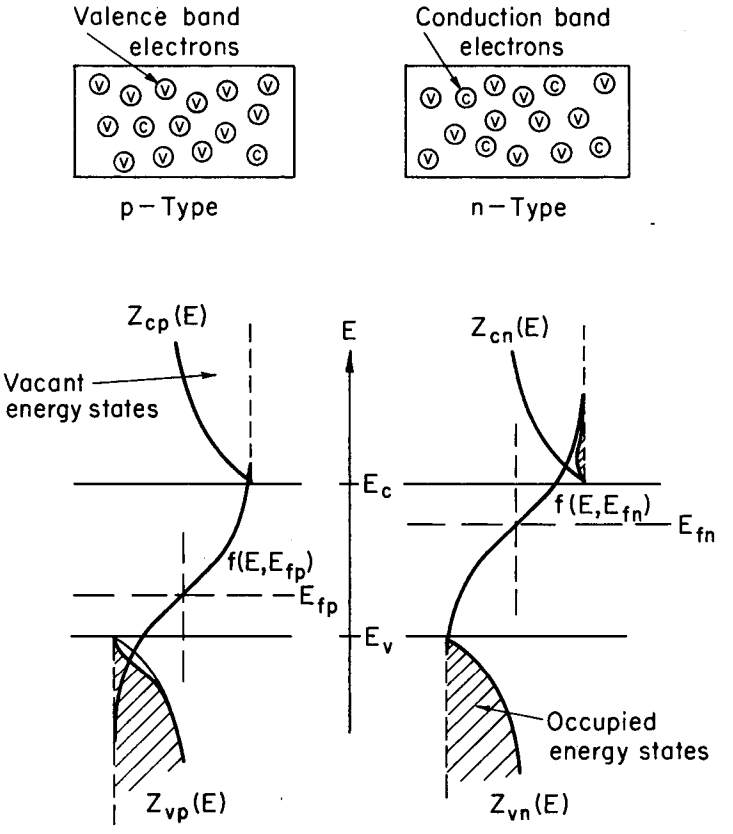

Fig. II.1. Energy diagram for electrons in isolated n- and p-type material.

$$f(E,E_f) = \frac{1}{1 + \exp\left(\frac{E-E_f}{kT}\right)} \qquad \text{(II-1)}$$

where E is the electron energy and E_f is the Fermi energy.

When the two material types are brought into contact as is the situation for a semiconductor diode, we can see from Fig. II.1 that electrons will flow from the n- to the p-type material until the potential produced by the net charges developed in the contact region will hinder a further flow of electrons. This space charge results from a redistribution of the electrons with respect to the immobile ionized donor and acceptor atoms in such a way that the condition of charge neutrality is no longer satisfied in the transition region. The resulting potential energy diagram for a p-n junction in the non-illuminated (henceforth to be referred to as dark) equilibrium state is shown in Fig. II.2. The electric field existing in the space charge region is required in order to maintain a zero net electron current from one base region of the diode into the other. Therefore, the equilibrium condition corresponds to a balance between the field limited diffusion current from the n-type region and the diffusion-drift current from the p-type region.

In order to solve for the electron distribution function and therefore the dark current-voltage characteristic of a semiconductor diode, it is in general necessary to simultaneously solve the current equation, the continuity equation, and Poisson's equation applying appropriate boundary conditions. At open circuit the net current is zero, and for an applied bias the electrostatic potential drop across the junction is equal to the sum of the applied bias and the equilibrium contact potential. The current density, $j(x,E)$ is

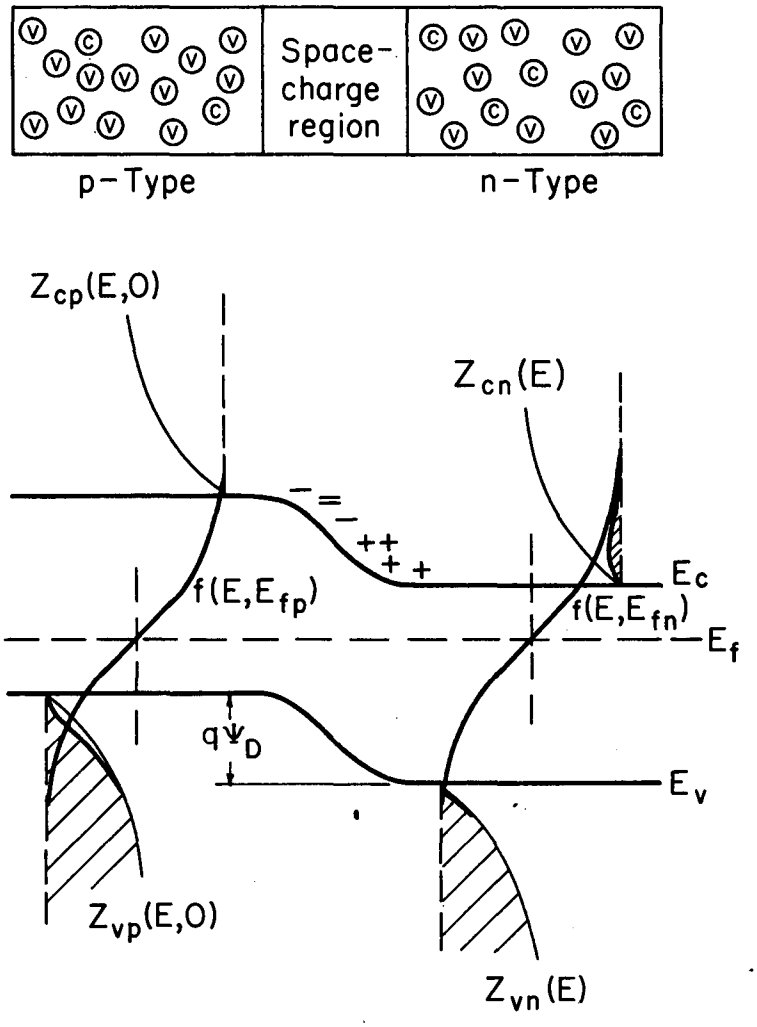

Fig. II.2. Equilibrium energy diagram for electrons in a p-n junction diode.

$$j(x,E)dE = q\mu_e(x,E)n(x,E)\text{grad}V(x)dE + qD_n(x,E)\text{grad}n(x,E)dE, \quad \text{(II-2)}$$

where q is the magnitude of the electron charge, $\mu_e(x,E)$ is the electron mobility, V(x) is the potential the electron experiences, $D_n(x,E)$ is the electron diffusion coefficient, and n(x,E), the electron distribution function, is

$$n(x,E) = Z(x,E)f(E,E_f(x)). \quad \text{(II-3)}$$

The relative importance of the two terms in Eq. (II-2) is, in general, different in the base regions than in the transition region.

The total current density passing through the junction is

$$J(x) = \int j(x,E)dE, \quad \text{(II-4)}$$

and is equal to zero at equilibrium. Equation (II-2) must be solved simultaneously with the continuity equation

$$\frac{\partial n(x,E)}{\partial t} = -\text{ div } j(x,E) + g(x,E) - Cn(x,E) \quad \text{(II-5)}$$

and Poisson's equation

$$\text{div } \mathcal{E}(x) = \nabla^2 V(x) = \frac{\rho(x)}{K_\epsilon \epsilon_o} \quad \text{(II-6)}$$

where K_ϵ is the dielectric constant, ϵ_o is the permitivity of free space, -Cn(x,E) is the loss rate for electrons, g(x,E) is the production rate, and $\rho(x)$ is the net charge density. The generation rate being composed of a thermal generation term and a term representing the contribution from external stimuli is

$$g(x,E) = g_{th}(x,E) + g_{ex}(x,E). \quad \text{(II-7)}$$

The net charge density is given by

$$\rho(x) = N_D^+(x) + [N - \int_o^{E_V} n(x,E)dE] - N_A^-(x) - \int_{E_c}^{\infty} n(x,E)dx, \quad \text{(II-8)}$$

where the number of electrons associated with the lattice atoms is

$$N = \int_o^{E_v} Z(x,E)dE.$$

This procedure is in general quite involved, and two schemes are commonly employed to describe the principle of operation of a semiconductor diode. On the one hand, the concept of a hole is introduced and the behavior of the diode treated on the basis of a minority carrier diffusion process in each of the base regions. This approach is used in Appendices A and C.

The alternate method of analysis, similar to that introduced by Hemenway, Henry, and Caulton,[31] to be used in the remainder of this section is limited to the case of negligible electron loss in the space charge region and also of negligible energy exchange during transit through the space charge region. Under these limiting conditions the net current can be written[34]

$$I = \int_o^\infty i(E)dE = \int_o^\infty [i_{n,p}(E) - i_{p,n}(E)]\, dE, \qquad \text{(II-9)}$$

where $i_{n,p}(E)dE$ is the current passing from the n- to the p-type region and $i_{p,n}(E)$ is the current passing in the opposite direction. These currents are dependent upon the electron distribution function existing in the material to either side of the transition region and the probability for an electron traversing the transition region. The current passing from the n- to the p-type region is

$$i_{n,p}(E)dE = T_{n,p}(E)Z_n(E)f(E,E_{fn})[1-f(E,E_{fp})]Z_p(E,V)dE, \qquad \text{(II-10)}$$

where $Z_n(E)f(E,E_{fn})$ is the electron distribution function in the n-type material, $[1-f(E,E_{fp})]Z_p(E,V)$ is the distribution function for the available states in the p-type material, and $T_{n,p}(E)$ is the probability for an electron transition from the n-type to the p-type material. The current passing in the opposite direction is

$$i_{p,n}(E)dE = T_{p,n}(E)Z_p(E,V)f(E,E_{fp})\ [1-f(E,E_{fn})]\ Z_n(E)dE, \qquad \text{(II-11)}$$

where the terms are to be interpreted in the same manner as for Eq. (II-10). The net current, obtained upon substituting Eqs. (II-10) and (II-11) into Eq. (II-9), is

$$I = \int_o^\infty Z_n(E)Z_p(E,V)\left\{T_{n,p}(E)f(E,E_{fn})[1-f(E,E_{fp})]\right.$$
$$\left. - T_{p,n}(E)f(E,E_{fp})[1-f(E,E_{fn})]\right\} dE. \qquad \text{(II-12)}$$

The density of states function for either base region is composed of localized energy levels and energy bands available for electron population. The integral in Eq. (II-12) need only be carried out over the partially filled bands, since the low-lying filled bands and the empty bands will not contribute to the net current. It is possible for tunneling of electrons between localized energy levels in the forbidden energy gap and available energy states in the partially filled bands to contribute to the current (see Appendix A), but this process will be neglected in the present analysis. In most practical situations encountered for semiconductors, consideration is therefore limited to the two bands bracketing the Fermi level which will in general lie in the forbidden energy gap. The net current can then be broken up into the terms arising from these two bands. Then

$$I = \int_o^{E_v} Z_{vp}(E,V)Z_{vn}(E)T(E)[f(E,E_{fn}) - f(E,E_{fp})]dE$$
$$+ \int_{E_c}^\infty Z_{cn}(E)Z_{cp}(E,V)T(E)[f(E,E_{fn}) - f(E,E_{fp})]dE, \qquad \text{(II-13)}$$

where E_v and E_c designate the top of the valence band and the bottom of the conduction band respectively. The limits of integration can be left as zero and infinity, since each density of states function exists only in the energy interval of the band under consideration. In arriving at Eq. (II-13), it has also been assumed that $T_{n,p}(E) = T_{p,n}(E) = T(E)$.

It is now possible to consider the equilibrium state of a diode. This corresponds to the situation of zero net current flow. Equation (II-13) shows that this can only be satisfied if $[f(E,E_{fn}) - f(E,E_{fp})] = 0$, which implies a constant Fermi level throughout the material. Therefore, the equilibrium condition (see Fig. II.2) is

$$E_{fo} = E_{fn} = E_{fp} + q\psi_D \tag{II-14}$$

and therefore the contact potential is

$$q\psi_D = E_{fn} - E_{fp}. \tag{II-15}$$

Upon the application of an external bias to the diode, a current will flow, and a non-equilibrium situation will exist whereby the Fermi level is no longer the same in both of the base regions. Under these conditions the current flow can be obtained from Eq.(II-13).

$$I = \int_o^{E_{vn}} Z_{nv}(E)Z_{pv}(E,V)T(E)[f(E,E_{fn}) - f(E,E_{fp})]dE$$

$$+ \int_{E_{cp}}^{\infty} Z_{nc}(E)Z_{pc}(E,V)T(E)[f(E,E_{fn}) - f(E,E_{fp})]dE. \tag{II-16}$$

In the conduction band it is possible to approximate the Fermi-Dirac distribution function by a Boltzmann factor (when $E_c - E_{fn} > kT$) so that the contribution to the current from the conduction band becomes

$$\int_{E_{cp}}^{\infty} Z_{nc}(E)Z_{pc}(E,V)T(E)\left\{\exp-\left(\frac{E-E_{fn}}{kT}\right) - \exp-\left(\frac{E-E_{fp}}{kT}\right)\right\}dE$$

$$= \left[\exp\left(\frac{E_{fn}-E_{fp}}{kT}\right)-1\right]\int_{E_{cp}}^{\infty} Z_{cn}(E)Z_{cp}(E,V)T(E)\exp-\left(\frac{E-E_{fp}}{kT}\right)dE. \tag{II-17}$$

One can derive an analogous relation for the contribution to the current from the valence band. The net current, therefore, becomes

$$I = \left[\exp\left(\frac{E_{fn}-E_{fp}}{kT}\right) -1\right]\left\{\int_o^{E_{vn}} Z_{vn}(E)Z_{vp}(E,V)T(E)\exp\left(\frac{E-E_{fn}}{kT}\right)\ dE\right.$$

$$+ \int_{E_{cp}}^{\infty} Z_{cp}(E) Z_{cn}(E,V) T(E) \exp - \left(\frac{E-E_{fp}}{kT}\right) \Big\} dE \quad . \qquad \text{(II-18)}$$

The difference in the Fermi levels is equal to the applied bias (existing across the junction alone) so that Eq. (II-18) can be written as

$$I = I_o(e^{\lambda V_j} - 1), \qquad \text{(II-19)}$$

where $\lambda = q/kT$

and $$I_o = \int_o^{E_{vn}} Z_{vn}(E) Z_{vp}(E,V) T(E) \exp \left(\frac{E-E_{fn}}{kT}\right) dE$$

$$+ \int_{E_{cp}}^{\infty} Z_{cn}(E) Z_{cp}(E,V) T(E) \exp - \left(\frac{E-E_{fp}}{kT}\right) dE \qquad \text{(II-20)}$$

is referred to as the reverse saturation current. This is the ideal current-voltage characteristic for a semiconductor diode without external charge carrier generation and is the result obtained by Hemenway et al.

The analysis will now be extended to the non-equilibrium case with external charge carrier generation present. The electrons no longer obey an equilibrium Fermi-Dirac distribution function, and the true situation is generally approximated by introducing separate distribution functions for the two bands under consideration. Each distribution function is characterized by a quasi-Fermi level and is of the form of Eq. (II-3). The short circuit current (net current flow for zero induced bias across the junction) for this illuminated condition (see Fig. II.3) is

$$I_{sc} = \int_o^{\infty} [i_{n,p}(E) - i_{p,n}(E)] dE$$

$$= \int_o^{E_{vn}} Z_{vn}(E) Z_{vp}(E,0) T(E) [f(E,\bar{E}_{fvn}) - f(E,\bar{E}_{fvp})] dE$$

$$+ \int_{E_{cp}}^{\infty} Z_{cn}(E) Z_{cp}(E,0) T(E) [f(E,\bar{E}_{fcn}) - f(E,\bar{E}_{fcp})] dE, \qquad \text{(II-21)}$$

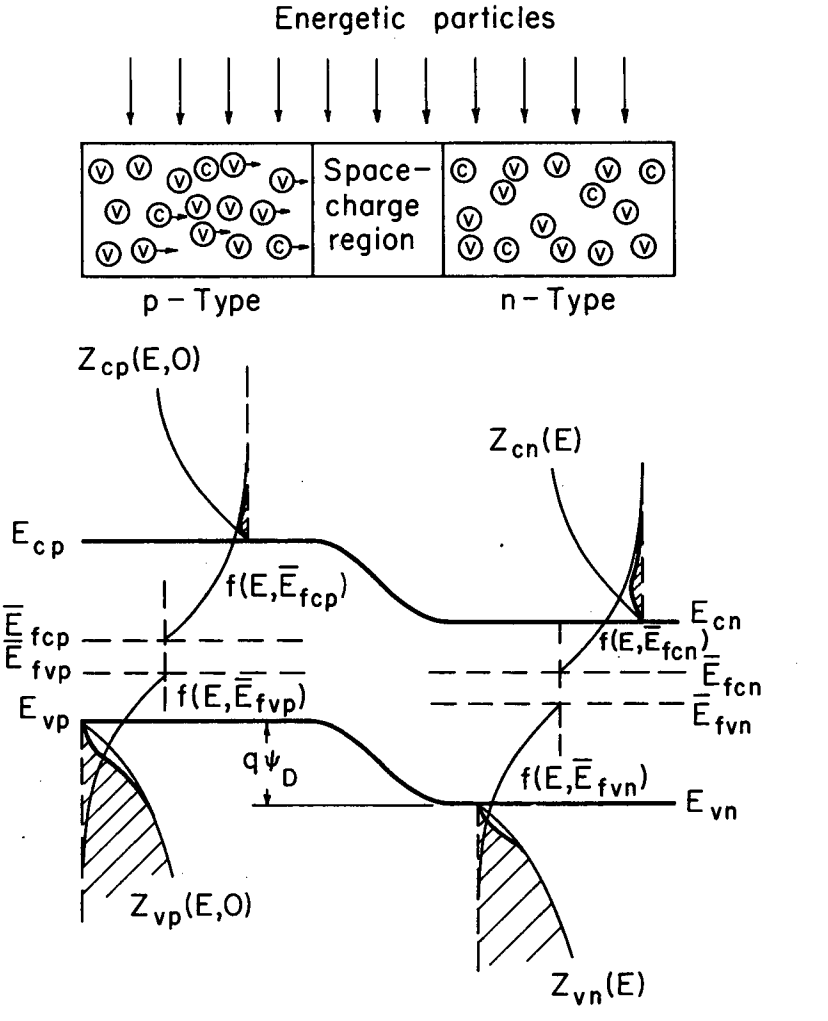

Fig. II.3. Short-circuit condition energy diagram for electrons in a p-n junction diode under irradiation.

where $\overline{E}_{fvn}$ and $\overline{E}_{fvp}$ are the quasi-Fermi levels for the valence band electrons in the n- and p-type materials respectively and $\overline{E}_{fcn}$ and $\overline{E}_{fcp}$ are analogous quantities for the conduction band electrons.

The induced bias, which is developed across the junction in order to drive current through an applied load, produces a change in the relative positions of the quasi-Fermi levels on either side of the space charge region. The current flow corresponding to an output voltage V is

$$I = \int_o^{E_{vn}} Z_{vn}(E)Z_{vp}(E,V)T(E)[f(E,\overline{E}_{fvn}) - f(E,\overline{E}_{fvp} - qV)]dE$$

$$+ \int_{E_{cp}}^{\infty} Z_{cn}(E)Z_{cp}(E,V)T(E)[f(E,\overline{E}_{fcn}) - f(E,\overline{E}_{fcp} - qV)]dE, \qquad \text{(II-22)}$$

where $Z_{vp}(E,V)$ and $Z_{cp}(E,V)$ indicate the effect of the induced bias upon the position of the energy bands and therefore the density of states functions.

The open circuit condition is realized when the net current is equal to zero. In general it would therefore be necessary to solve for the open circuit voltage, V_{oc}, using Eq. (II-22). Figure II.4 shows the special case of equal differences between the quasi-Fermi levels in both of the base regions. The open circuit voltage for this case is then

$$V_{oc} = (\overline{E}_{fcp} - \overline{E}_{fcn}) = (\overline{E}_{fvp} - \overline{E}_{fvn}). \qquad \text{(II-23)}$$

The purpose of the discussions of this section was to point out the basic processes responsible for the particle-voltaic effect. The general form of the I-V characteristic we obtained (namely, Eq. (II-22)) is of little use in the succeeding analytical work. Therefore the form of the illuminated I-V characteristic which is an explicit function of ascertainable material properties (see Appendix C) is employed throughout the remainer of this report.

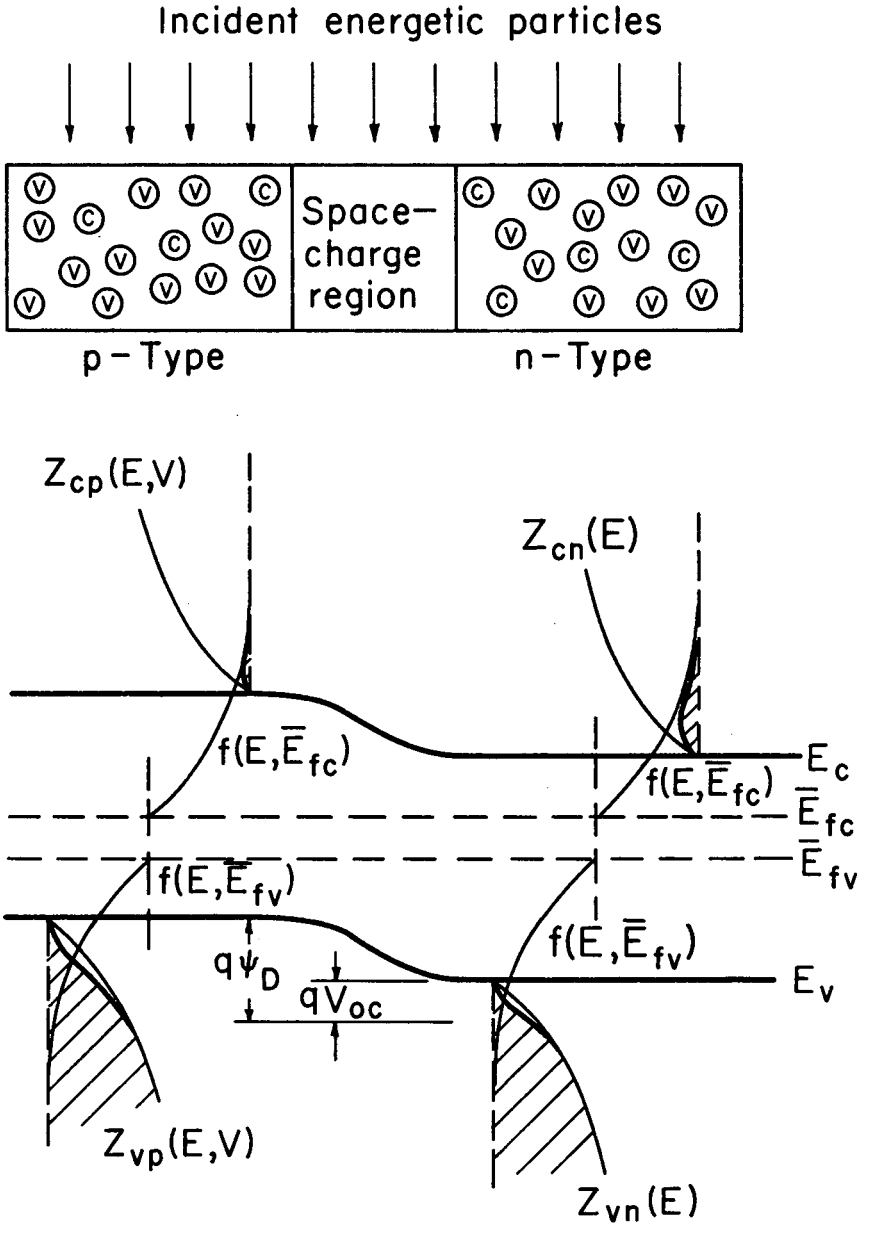

Fig. II.4. Open-circuit condition energy diagram for electrons in a p-n junction diode under irradiation.

III. ALPHA-VOLTAIC ENERGY CONVERSION

A. Performance of a Particle-Voltaic Device

It was shown in Section II that upon bombardment of a semiconductor diode with energetic particles (x-rays, electrons, protons, etc.), a voltage is developed at the p-n junction of the diode which retards the current flow arising from the collection of those electron-hole pairs produced in the bulk semiconducting material as the incident particle loses energy. At the short circuit condition all the charge carriers collected by the junction contribute to the current providing there is negligible series resistance. At open circuit the voltage developed at the p-n junction produces a current equal in magnitude and opposite in sign to that of the collected charge carriers.

Over a limited voltage range the irradiated current-voltage characteristic for any type of a semiconductor diode (point contact diode, broad area junction diode, etc.) can be adequately represented by (see Section IV and Appendix C for more detail)

$$I = \frac{(V-R_s I)}{R_{SH}} + I_{ol}\left(\exp\left[\frac{\lambda}{A}(V-R_s I)\right] - 1\right) - I_G \qquad \text{(III-1)}$$

where the first term is the shunt conductance current, the second term is just the junction I-V characteristic of the diode with no radiation field present (in the remainder of this section these two terms or modifications of them will be referred to as the dark I-V characteristic), and the third term represents the current arising from the collection of the electron-hole pairs produced by the radiation field (see Appendix C).

Making use of Eq. (III-1), the short circuit current is found to be

$$I_{sc} = -\frac{R_s I_{sc}}{R_{SH}} + I_{ol}\left(\exp\left[-\frac{\lambda R_s I_{sc}}{A}\right] - 1\right) - I_G \qquad \text{(III-2a)}$$

and for negligible series resistance this becomes

$$I_{sc} = -I_G \qquad \text{(III-2b)}$$

as mentioned above. The open circuit voltage as obtained from Eq. (III-1) upon setting I = 0 is

$$\frac{V_{oc}}{R_{SH} I_{ol}} + \exp\left[\frac{\lambda V_{oc}}{A}\right] = \left(\frac{I_G}{I_{ol}} + 1\right). \qquad \text{(III-3)}$$

For an ideal diode $I_{ol} = I_o$, the low injection level reverse saturation current, and A is equal to unity.[56]

High Output Voltage. The shunt conductance can in general be neglected for operating conditions where the output voltage is large. Then the maximum power output (see Appendix D) is

$$P_{max} = R_s I_{mp}^2 + \frac{A}{\lambda}\,\frac{I_{mp}^2}{(I_{mp}+I_G+I_{ol})} \qquad \text{(III-4)}$$

where the current at maximum power is found from

$$0 = 2R_s I_{mp} + \frac{A}{\lambda}\ln\left(\frac{I_{mp}+I_G+I_{ol}}{I_{ol}}\right) + \frac{A}{\lambda}\,\frac{I_{mp}}{(I_{mp}+I_G+I_{ol})}\,. \qquad \text{(III-5)}$$

The power input to the device (i.e. the energy flux of the incident particles) is

$$P_{in} = \int_o^\infty \dot{N}(E)E\,dE = \dot{N}\bar{E}\,. \qquad \text{(III-6)}$$

The maximum efficiency is therefore given by

$$\eta_{max} = \frac{1}{\dot{N}\bar{E}}\left[R_s I_{mp}^2 + \frac{A}{\lambda}\,\frac{I_{mp}^2}{(I_{mp}+I_G+I_{ol})}\right]. \qquad \text{(III-7)}$$

Low Output Voltage. In the region of operation where the output voltage is small, the maximum power output (see Appendix D) is

$$P_{max} = \frac{V_{mp}^2}{R_{SH}} + \left(\frac{\lambda I_{ol}}{A}\right) V_{mp}^2 \exp\left[\frac{\lambda V_{mp}}{A}\right] . \qquad \text{(III-8)}$$

Since the series resistance is unimportant for low output voltages, the voltage at maximum power is obtained from

$$\frac{2V_{mp}}{I_{ol} R_{SH}} + \left(1 + \frac{\lambda V_{mp}}{A}\right) e^{\frac{\lambda V_{mp}}{A}} = \left(\frac{I_G}{I_{ol}} + 1\right). \qquad \text{(III-9)}$$

The maximum efficiency is obtained from Eqs. (III-6) and (III-8),

$$\eta_{max} = \frac{1}{\dot{N}\bar{E}} \left(\frac{V_{mp}^2}{R_{SH}} + \left(\frac{\lambda I_{ol}}{A}\right) V_{mp}^2 \exp\left[\frac{\lambda V_{mp}}{A}\right] \right) . \qquad \text{(III-10)}$$

Intermediate Voltage Region. For suitably prepared diodes (small series resistance and high shunt resistance) in a region of operation yielding intermediate output voltages, the maximum power is

$$P_{max} = \frac{A}{\lambda} \frac{I_{mp}^2}{(I_{mp} + I_G + I_{ol})} = \left(\frac{\lambda I_{ol}}{A}\right) V_{mp}^2 \exp\left[\frac{\lambda V_{mp}}{A}\right] \qquad \text{(III-11)}$$

where the voltage at maximum power is found from

$$\left(\frac{I_G}{I_{ol}} + 1\right) = \left(1 + \frac{\lambda V_{mp}}{A}\right) \exp\left[\frac{\lambda V_{mp}}{A}\right] = \exp\left[\frac{\lambda V_{oc}}{A}\right] \qquad \text{(III-12)}$$

Use of Eqs. (III-6) and (III-11) leads to a maximum efficiency of

$$\eta_{max} = \frac{\left(\frac{\lambda I_{ol}}{A}\right)}{\dot{N}\bar{E}} V_{mp}^2 \exp\left[\frac{\lambda V_{mp}}{A}\right] . \qquad \text{(III-13)}$$

The effective reverse saturation current, I_{ol}, is not in practice given by the ideal diffusion theory prediction[56] but in this and a number of other specific cases (i.e., the junction recombination-generation current or surface current) it can be well represented by a relationship to the form

$$I_{ol} = C \exp\left[-\frac{E_g}{\beta k T}\right] . \qquad \text{(III-14)}$$

In most situations of practical interest the particle generated current is large compared to the effective reverse saturation current so that

$$\left(\frac{I_G}{I_{ol}} + 1\right) \approx \frac{I_G}{I_{ol}} \qquad \text{(III-15)}$$

and therefore

$$\left(1 + \frac{\lambda V_{mp}}{A}\right) \exp\left[\frac{\lambda V_{mp}}{A}\right] \approx \left(\frac{\lambda V_{mp}}{A}\right) \exp\left[\frac{\lambda V_{mp}}{A}\right] . \qquad \text{(III-16)}$$

The errors introduced by the approximation of Eq. (III-16) are presented in Table III.I.

Table III.I. Errors in V_{mp} introduced using the approximations represented in Eqs.(III-16) and (III-17) instead of Eq. (III-12).

I_G/I_{ol}	10	10^2	10^3	10^4	10^5	10^6
Eq. (III-16)	23%	6.3%	2.6%	1.5%	1.1%	1.1%
Eq. (III-17)	62%	45%	35%	29%	25%	22%

To simplify the analysis, it is necessary to neglect $\lambda V_{mp}/A$ as compared to 1 which gives

$$\frac{I_G}{I_{ol}} \approx \exp\left[\frac{\lambda V_{mp}}{A}\right] \qquad \text{(III-17)}$$

The errors associated with the use of this approximation are also presented in Table III.I. These approximations overestimate the value of V_{mp}.

For particle generated currents encountered in solar cells under normal illumination, the ratio, I_G/I_{ol}, is in the range of 10^3 to 10^5. If we now make use of the approximations represented by Eqs.(III-16) and (III-17), Eq. (III-13) becomes

$$\eta_{max} = \frac{qV_{mp}}{\epsilon} Q \qquad \text{(III-18)}$$

where the charge collection efficiency, Q, is defined by

$$Q = \frac{\epsilon I_G}{q\dot{N}\bar{E}} \qquad \text{(III-19)}$$

and ϵ is the average energy required to produce an electron-hole pair. Using Eq.(III-14) in Eq. (III-17) yields

$$eV_{mp} = AkT\ln\left(\frac{I_G}{C}\right) + \left(\frac{AE_g}{\beta}\right) \qquad \text{(III-20)}$$

so that the maximum efficiency becomes

$$\eta_{max} = \frac{AQE_g}{\beta\epsilon} - \frac{AQkT}{\epsilon}\ln\left(\frac{C\epsilon}{q\dot{N}\bar{E}Q}\right). \qquad \text{(III-21)}$$

At first glance it appears that the efficiency of a device should increase with decreasing temperature. The realization of this behavior is however influenced by the temperature dependence of A, Q, E_g, and ϵ. Therefore, it is necessary to consider the temperature dependence of these properties in more detail prior to making predictions relative to device performance. The temperature dependence of I_{ol} and A for broad area Si and GaAs p-n junction diodes was studied and the results are presented in Section IV. The temperature dependence of ϵ was investigated and the results will be presented in a separate UCRL report. E_g has been measured as a function of temperature by Macfarlane et al.[41] and the variation of Q with temperature was determined from the temperature dependence of the minority carrier mobilities and lifetimes. We shall see later in Section V that the efficiency does indeed increase with decreasing temperature.

From Eq. (III-21) it is also expected that higher efficiencies are achieved for materials with larger energy gaps. Again this expected behavior is influenced by the fact that ϵ is dependent upon the energy

gap. The variation of ϵ with E_g and temperature has been studied by McKay.[43] The results of Section V for Si and GaAs solar cells, however, show that the maximum efficiency increases as E_g increases.

Another important factor which must be considered is the effect of radiation damage upon Q, A, and I_{ol}. The effect of temperature upon the bombardment induced changes in the performance of solar cells under α-particle bombardment was investigated, and the results are presented in Section V. Alpha-particle bombardment is seen to reduce the charge collection efficiency, Q, and, in general, modify A and I_{ol} in such a way that the energy conversion efficiency is reduced.

B. Spatial Distributions for the Production of Electron-Hole Pairs and Lattice Displacements.

Prior to the calculation of the α-particle generated current, $I_{G\alpha}$, it is necessary to determine the spatial distribution function for the production of electron-hole pairs in a Si diode by an α-particle. An α particle passing through Si loses the major portion of its energy via electron excitation and ionization. The intermediate energy electrons produced in this manner suffer subsequent collisions with other atomic electrons, and this results in further electron excitation and ionization. After a sufficient period of time (which is generally much less than the lifetime of the excess carriers), further excitation is energetically impossible and a finite number of excess electron-hole pairs exist in the solid. In theory the number of electron-hole pairs produced in an increment of the α-particle track could be calculated using Monte Carlo calculational techniques. This is, however, a very lengthy process; and, therefore, in this section the α-particle stopping power is used directly to obtain the electron-hole pair production rate.

This is accomplished by assuming the energy required to produce an electron-hole pair to be constant over the entire α-particle track.

The procedure used to calculate the stopping power curve for α-particle stopping in Si is described in detail in Appendix B. The electronic stopping power was calculated from Gryzinsky's classical stopping power equation[28] for all electron ionization and excitation processes excepting the valence band to conduction band transitions. The energy loss corresponding to these transitions was calculated using a relation developed by Seitz and Koehler.*[55] The calculation of the atomic collision stopping power was based upon classical Rutherford scattering at high α-particle energy ($E_\alpha > 24$keV) and classical hard sphere scattering at low α-particle energy ($E_\alpha < 240$eV) as suggested by Seitz and Koehler.[55] The atomic collision stopping power determines the extent of the radiation damage produced by the α particles. The number of lattice displacements produced by an α particle was calculated using the lattice displacement model of Kinchen and Pease.[34] The details of this calculation can also be found in Appendix B.

1. Electron-Hole Pair Production. The energy of an α-particle with $\bar{E}_{\alpha o} = 5$ MeV as a function of track length was determined from the numerical integration of the total stopping power curve (see Fig.B.18, Appendix B), and the result is shown in Fig. B.21. Using Fig. B.21 in conjunction with Fig. B.10 it is possible to obtain the spatial variation of the electronic stopping power, $[dE_\alpha(x)/dx]_{el}$. The calculated electronic stopping power

---

* Sietz and Koehler considered only neutral particle induced transitions. It was necessary to extend the analysis so as to consider charged particles in which case a coulomb form was assumed for the interaction potential.

is represented by the solid curve in Fig. III.1. In order to facilitate calculation of the alpha generated current, $I_{G\alpha}$, and to obtain an analytical expression for the I-V characteristic of a Si diode under α-particle bombardment, the electronic stopping power curve was fit with a polynomial using the method of least squares. Employing a polynomial of the form

$$[dE_\alpha/dx]_{el} = A + Bx + Cx^2 + Dx^3 + Fx^4, \qquad \text{(III-22)}$$

the fit represented by the dashed curve in Fig. III.1 was obtained. Assuming that the energy required to produce an electron-hole pair is constant along the α-particle track and equal to 3.55 eV for Si,[3] the electron-hole pair production rate per incident α particle obtained from Eq.(III-22) is

$$g_\alpha(x) = \frac{1}{\epsilon}[dE_\alpha/dx]_{el} = a + bx + cx^2 + dx^3 + fx^4. \qquad \text{(III-23)}$$

The constants obtained from the least square fit are listed in Table III.II.

2. Lattice Displacement Production. The lattice displacement production rate as calculated in the manner described above was found to be (c.f. Eq.B-87, Appendix B)

$$\delta\dot{N}_D(x) = \dot{N}_\alpha n_D(x)\ \delta x \qquad \text{(III-24)}$$

where $n_D(x)$ as plotted in Fig. III.2 was obtained from Fig. B.21 (that is, E_α as a function of x) and Fig. B.16 which presents the calculated number of lattice displacements produced by an α particle of energy E_α per unit track length. The total number of displacements produced by an α particle with $\bar{E}_{\alpha o} = 5$ MeV is found to be

$$n_D = \int_o^{R_\alpha} n_D(x)dx \approx 10^3. \qquad \text{(III-25)}$$

The spatial dependence of the displacement production rate is seen to be peaked at the end of the α-particle track. As previously mentioned,

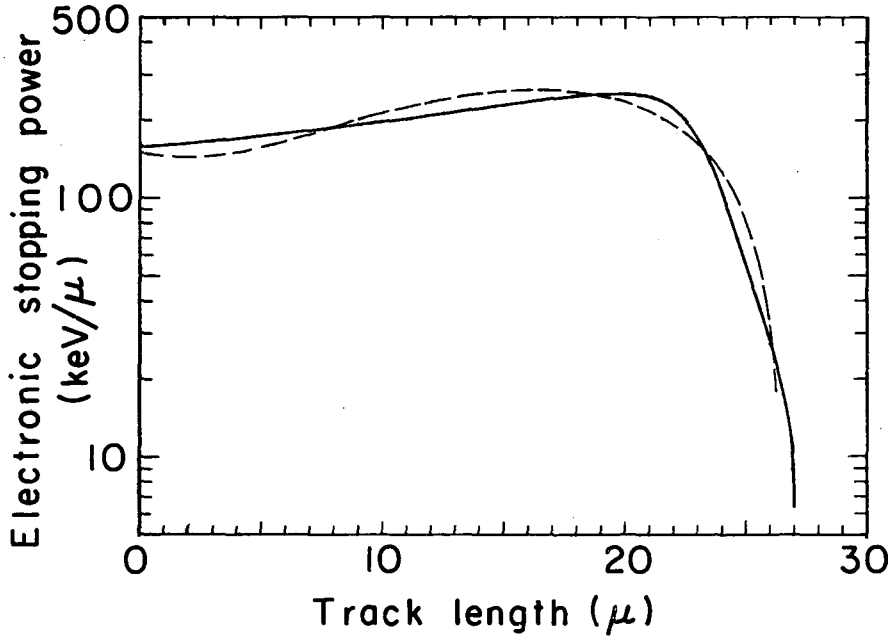

Fig. III.1. Electronic stopping power for 5-Mev α-particle stopping in Si (the dashed curve represents the polynomial fit).

Table III.II. Constants obtained from least-squares fit for $[dE/dx]_{el}$ and $g_a(x)$.

$\bar{E}_{ao}$	4 MeV	5 MeV
a, eh/μa	5.33×10^{4}	4.22×10^{4}
b, eh/μ^2a	-1.25×10^{3}	-2.04×10^{3}
c, eh/μ^3a	3.52×10^{2}	5.97×10^{2}
d, eh/μ^4a	2.93	-2.18×10
f, eh/μ^5a	-1.17	-2.96×10^{-3}
A, keV/μa	1.89×10^{2}	1.50×10^{2}
B, keV/μ^2a	-4.44	-7.23
C, keV/μ^3a	1.25	2.12
D, keV/μ^4a	1.04×10^{-2}	-7.75×10^{-2}
F, keV/μ^5a	-4.15×10^{-3}	-1.05×10^{-5}
R, μ	20.3	26.5

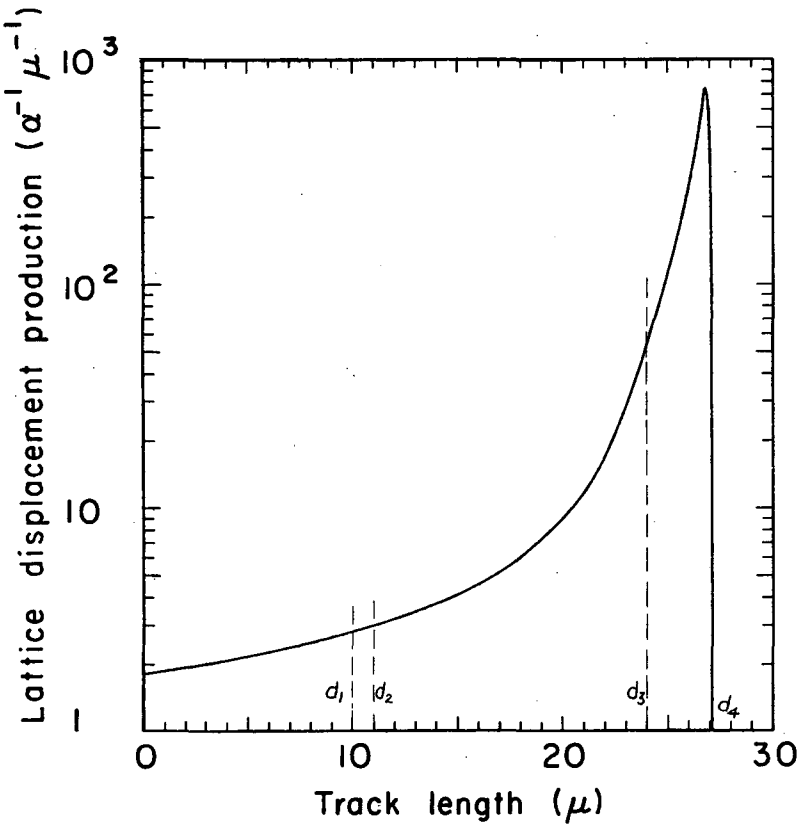

Fig. III.2. Lattice displacement production, $n_D(x)$, for 5-Mev α-particle stopping in Si.

the lattice displacements produce changes in the minority carrier lifetime inasmuch as a displaced atom can exhibit the properties of a recombination center. Experimental evidence[39,65] has indicated that the number of such recombination centers is proportional to the exposure with the result that the lifetime may be written

$$\frac{1}{\tau(x)} = \frac{1}{\tau_o} + \lambda'(x)\theta(t) \qquad \text{(III-26)}$$

where

$$\theta(t) = \int_o^t \dot{N}_\alpha(t)dt = \dot{N}_\alpha t \qquad \text{(III-27)}$$

is the integrated α-particle flux time or exposure, $\lambda' = \bar{v}\sigma_{CD}n_D(x)$, $\bar{v}$ is the average charge carrier velocity, and σ_{CD} is the capture cross section of the defect center for the minority carriers. The spatial variation of the minority carrier diffusion length is then given by

$$\frac{1}{L^2(x)} = \frac{1}{L_o^2} + K(x)\theta(t) \qquad \text{(III-28)}$$

where $K(x)$ is commonly designated as the diffusion length degradation constant and is equal to $\lambda'(x)/D$.

A knowledge of $L(x)$ in the base and surface regions of the diode is required in order to determine the exposure induced changes in short circuit current. In an effort to facilitate an analytical calculation of the short circuit current, it would be necessary to divide the base region of the diode into a number of sub-regions each with a different effective diffusion length, $\tilde{L}$, whereas a single average diffusion length should be adequate for the surface region. Referring to Fig. III.2, a possible division of the base region is indicated by the dotted lines. This technique will be discussed in greater detail in Section V. For the purposes of this section the effects of bombardment upon the energy conversion efficiency are estimated from the experimental results of Section V for α-particle bombardment of Si solar cells.

C. Operating Performance of an Alpha-Voltaic Device.

The geometry found to be the most suitable for an α-voltaic device is shown in Fig. III.3(a). The surface region is substantially thicker than that of a conventional solar cell, and the front surface is completely covered with a thin metal contact. In practice broad area metal contacts of this type have been prepared with a thickness of approximately 0.2 microns. This leads to only a negligible degradation of the α-particle energy upon passing through the metal region.

A bidirectional bombardment scheme in which α particles are incident upon both faces of a broad area junction diode was also considered (see Fig. C.1). In this device the thickness of both base regions is approximately equal to the range of the incident α particles. The major portion of the damage produced by the α particles is therefore contained in the junction or in close proximity to it in which case the charge carriers created in the base regions would have to diffuse through these highly damaged regions in order to be collected at the junction. The charge collection efficiency would therefore decrease quite rapidly with increasing α-particle exposure, whereas the unidirectional geometry limits the highly damaged region to a position in the base region far removed from the junction. This results in a more gradual decrease in the charge collection efficiency. The deleterious changes occurring in the dark I-V characteristics are also expected to be more pronounced for the bidirectional bombardment scheme because the ideal diffusion current and junction recombination-generation current are quite sensitive to the minority carrier lifetimes in the base region close to the junction and in the junction respectively.

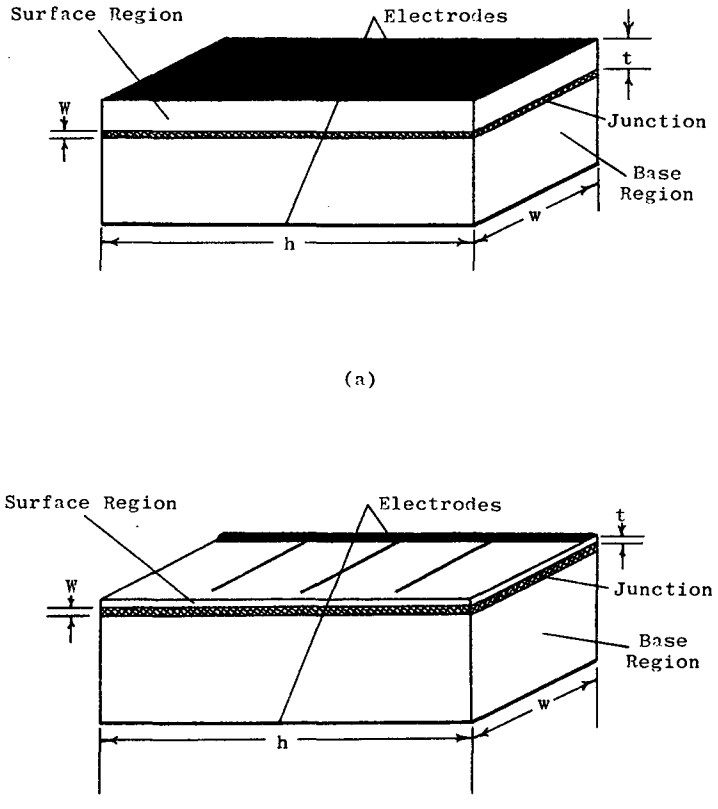

Fig. III.3. Diode geometry for (a) a particle-voltaic device and (b) a solar cell.

These considerations led to the choice of the α-voltaic device geometry presented in Fig. III.3. No attempt has been made to optimize the surface region thickness, t, although there is no doubt that such an optimum does exist. The thickness of the surface region determines the position of the highly damaged material relative to the junction, and therefore controls the charge collection efficiency. It is also quite obvious that the optimum thickness will in general be a function of the exposure, and this fact makes the optimization process of questionable value.

In the succeeding paragraphs calculations are carried out for a Si α-voltaic device exposed to an incident alpha flux which is characterized by a source strength in curies. In practice the α particles from a radioisotope would not produce a beam of particles normal to the surface. The particles would in fact enter at all possible angles to the surface for a source in direct contact with the surface. In this case only half the source activity would be effective in the energy conversion process, whereas the other half of the activity would be lost. This situation could be remedied by sandwiching the source between two α-voltaic devices to produce an α-voltaic capsule. Effects resulting from the non-normal incidence of the α particles will be discussed as the need arises.

1. Alpha Generated Current. The current arising from the electron-hole pairs created along the α-particle track was obtained from the irradiated I-V characteristic as determined from the solution of the minority carrier diffusion equation in the surface and base regions where $G(x) = \dot{N}_\alpha g(x)$ was used as the source term for electron-hole pairs. The detailed steps of this solution can be found in Appendix C. The alpha

generated current is found to consist of terms from the surface region, the junction, and the base region. The analysis was carried out for a p-on-n α-voltaic device in which case

$$I_{G/q\dot{N}_\alpha} = L_n\left\{\left[X_n(d_1)\frac{M_n(d_1)}{K_n(d_1)} - L_n X'_n(d_1)\right] - \left[X_n(0) - \gamma_n L_n X'_n(0)\frac{1}{K_n(d_1)}\right]\right\}$$

$$+ \left[H(d_2)-H(d_1)\right] + L_{pI}\left\{\left[X_p(d_2)\frac{R_p(D)}{P_p(D)} + L_{pI}X'_p(d_2)\right]\right.$$

$$\left. - \left[X_p(d_3) + L_{pI}X'_p(d_3)\right]\frac{R_p(0)}{P_p(D)}\right\} \qquad \text{(III-29)}$$

where $D = d_3 - d_2$, $t = d_4 - d_3$,

$$X_n(x) = a+bx+c(x^2+2L_n^2)+d(x^3+6xL_n^2)+f(x^4+12L_n^2x^2+24L_n^4), \qquad \text{(III-30)}$$

$$M_n(x) = \gamma_n \sinh\left(\frac{x}{L_n}\right) + \cosh\left(\frac{x}{L_n}\right), \qquad \text{(III-31)}$$

$$K_n(x) = \gamma_n \cosh\left(\frac{x}{L_n}\right) + \sinh\left(\frac{x}{L_n}\right), \qquad \text{(III-32)}$$

$$H(x) = ax + \frac{b}{2}x^2 + \frac{c}{3}x^3 + \frac{d}{4}x^4 + \frac{f}{5}x^5, \qquad \text{(III-33)}$$

$$P_p(x) = \Delta_1 \cosh\left(\frac{x}{L_{pI}}\right) + \Delta_2 \sinh\left(\frac{x}{L_{pI}}\right), \qquad \text{(III-34)}$$

$$R_p(x) = \Delta_1 \sinh\left(\frac{x}{L_{pI}}\right) + \Delta_2 \cosh\left(\frac{x}{L_{pI}}\right), \qquad \text{(III-35)}$$

$$\Delta_1 = \cosh\left(\frac{t}{L_{pII}}\right) + \left(\frac{L_{pII}}{L_{po}}\right) \sinh\left(\frac{t}{L_{pII}}\right), \qquad \text{(III-36)}$$

$$\Delta_2 = \left(\frac{L_{pI}}{L_{po}}\right) \cosh\left(\frac{t}{L_{pII}}\right) + \left(\frac{L_{pI}}{L_{pII}}\right) \sinh\left(\frac{t}{L_{pII}}\right), \qquad \text{(III-37)}$$

and $X_p(x)$ is given by Eq. (III-30) with n replaced by p. Equation (III-29) includes the current contribution from region I of the base region but not that of region II (see Fig. III.2). This simplification was discussed in Appendix C where it was found there that approximately 4% of

the electron-hole pairs are produced in region II, and therefore the contribution from this region can be neglected. For an actual alpha source the α particles which enter the diode at oblique angles lead to the production of electron-hole pairs closer to the surface than for the normal incidence case with the result that the charge collection efficiency and associated particle generated current are modified. For angles of incidence close to the normal the charge collection efficiency is increased over that for normal incidence while for grazing angles it is decreased.

The irradiated I-V characteristic obtained in Appendix C is

$$I = I_o(e^{\lambda V_j}-1) - I_G \qquad \text{(III-38)}$$

where the first term is the low injection level diffusion term and represents the dark I-V characteristic for the ideal p-n junction device analyzed in Appendix C. In practice the dark I-V characteristic for a Si p-n junction diode is found to deviate markedly from the ideal exponential relation given in Eq. (III-38).

2. Dark I-V Characteristic. Equation (III-38) is valid for an ideal diode; that is, a diode in which the non-ideal contributions to the current are negligible in comparison to the low injection level diffusion current. Silicon is one material in which the non-ideal current contributions cannot be neglected, and therefore it is necessary to modify Eq. (III-38) so as to account for the specific mechanisms responsible for the additional current.

Appendix A presents a detailed discussion of a number of mechanisms which give rise to additional current contributions. The dominant non-ideal current contributions for a particle-voltaic device (see Fig. III.3(a))

are expected to be the shunt conductance current at low applied voltages and the junction generation-recombination current, I_{rg} (see Appendix A), in the intermediate voltage region. This is a very reasonable assumption in light of the fact that Si power rectifiers[63] and Si diodes with small area-shallow diffused junctions ($\geq$ 10μ junction depth[53]) have been shown to exhibit a non-ideal current term of this type over appropriate voltage intervals (the voltage interval is dependent upon the material properties, shunt resistance, and temperature of the diode). Silicon solar cells (i.e., a Si diode with a broad area-shallow diffused junction, $\approx$ 1μ junction depth, as shown in Fig. III.3(b)), on the other hand, have been found to possess a non-ideal current contribution that cannot be attributed to electron-hole pair recombination or generation in the junction (see Section IV).

The junction depth for an α-voltaic device need not be excessively small as for a solar cell since the production of electron-hole pairs by an α particle extends substantially farther into the diode than for the electron-hole pair production by the photons of the solar spectrum. This means that the surface region material can be of higher purity for an α-voltaic device.

In light of these facts we felt justified in assuming that the dark I-V characteristics for the Si broad area-shallow junction α-voltaic devices analyzed in this section contain shunt conduction and junction recombination-generation currents in addition to the low injection level diffusion current (henceforth referred to as the three component I-V characteristic). The properties used in the calculation of these dark I-V characteristics are listed in Table III.III(a) and the characteristics are plotted in Fig. A.4 of Appendix A.

Table III.III. Typical material properties and associated reverse saturation current for a silicon p-on-n alpha-voltaic device.

T(°K)	200[a]	250[a]	300[b]	300[a]	300[c]	350[a]	400[a]
$t(\mu)$	10	10	10	10	10	10	10
$N_D(cm^{-3})$	1.00×10^{16}	1.00×10^{16}	1.00×10^{16}	1.00×10^{16}	1.00×10^{16}	1.00×10^{16}	1.00×10^{16}
$n_n(cm^{-3})$	9.84×10^{15}	9.84×10^{15}	1.00×10^{16}	1.00×10^{16}	1.00×10^{16}	1.00×10^{16}	1.00×10^{16}
$p_{no}(cm^{-3})$	1.23×10^{-7}	2.43×10^{-1}	4.40×10^{3}	4.40×10^{3}	4.40×10^{3}	5.44×10^{6}	1.20×10^{9}
τ_p (sec)	1.00×10^{-6}	1.00×10^{-6}	1.00×10^{-5}	1.00×10^{-6}	1.00×10^{-7}	1.00×10^{-6}	1.00×10^{-6}
$D_p(cm^2/sec)$	4.57	5.10	5.95	5.95	5.95	5.86	5.47
$L_p(\mu)$	21.4	22.6	77.2	24.4	7.72	24.2	23.4
$N_A(cm^{-3})$	2.01×10^{16}	2.01×10^{16}	2.01×10^{16}	2.01×10^{16}	2.01×10^{16}	2.01×10^{16}	2.01×10^{16}
$p_p(cm^{-3})$	1.97×10^{16}	1.99×10^{16}	2.00×10^{16}	2.00×10^{16}	2.00×10^{16}	2.01×10^{16}	2.01×10^{16}
$n_{po}(cm^{-3})$	6.14×10^{-8}	1.20×10^{-1}	2.20×10^{3}	2.20×10^{3}	2.20×10^{3}	2.73×10^{6}	6.04×10^{8}
τ_n (sec)	1.00×10^{-7}	1.00×10^{-7}	1.00×10^{-6}	1.00×10^{-7}	1.00×10^{-8}	1.00×10^{-7}	1.00×10^{-7}
$D_n(cm^2/sec)$	10.4	14.7	16.3	16.3	16.3	16.6	16.0
$L_n(\mu)$	10.2	10.2	40.5	12.8	4.05	12.8	12.6
$s_n(cm/sec)$	1.00×10^{2}	1.00×10^{2}	1.00×10^{2}	1.00×10^{2}	1.00×10^{2}	1.00×10^{2}	1.00×10^{2}
I_o (amps)	1.18×10^{-22}	2.48×10^{-16}	9.23×10^{-13}	4.68×10^{-12}	1.94×10^{-11}	5.80×10^{-9}	1.26×10^{-6}

N_D, N_A, n_n, p_p — obtained from the assumed room-temperature values of n_n and p_p.

p_{no}, n_{po} — obtained from the values of n_n and p_p and the temperature dependence of n_i^2 [F. J. Morin and J. P. Maita, Phys. Rev. 96, 28 (1954)].

τ_p, τ_n — assumed values.

D_p, D_n — determined from the room-temperature values for mobility [M. B. Prince, Phys. Rev. 93, 1204 (1954)], the measured temperature dependence of lattice scattering mobility [G. W. Ludwig and R. L. Watters, Phys. Rev. 101, 1699 (1956)], and the theoretically predicted temperature dependence of the ionized impurity scattering mobility [E. Conwell and V. F. Weisskopf, Phys. Rev. 77, 388 (1950)].

s_n, s_p — assumed values.

(a) Representative of moderately pure material.

(b) Material of higher purity than (a).

(c) Material of lower purity than (a).

3. Irradiated I-V Characteristic. The I-V characteristics of a Si device under α-particle bombardment were calculated from Eq. (III-38) for both of the cases--an ideal dark characteristic and the three component characteristic (that is, $I_{SH} + I_{rg} + I_d$) mentioned above. The material properties used in the calculation of the alpha generated current, $I_{G\alpha}$, are listed in Table III.III. The values of Table III.III(a) are representative of moderately pure Si and therefore of the most practical interest, whereas Table III.III(b) and (c) presents values of the properties for Si of higher and lower purity. The incident α particles were assumed to be monoenergetic with an energy of 5 MeV in the calculation of $I_{G\alpha}$. This assumption should be reasonably well satisfied with such alpha emitters as Po^{210} or Am^{241}. Table III.IV lists the calculated charge carrier collection efficiencies, and Table III.V the calculated α-particle generated currents for a Si α-voltaic device with the material properties given in Table III.III.

The maximum power output and associated maximum efficiency were graphically determined using the calculated irradiated I-V characteristics. The maximum power output calculated for an α-voltaic device exhibiting a three component dark I-V characteristic is given in Table III.V for a number of α-particle source strengths.

In general the maximum power output will increase as the angle of incidence of the α-particle beam is rotated from the normal since the electron-hole pairs are then produced closer to the junction and are more readily collected. At some angle which approaches a grazing condition the electron-hole pairs are produced so close to the surface that a substantial portion are lost through recombination processes prior to their reaching the junction. These two effects tend to balance

Table III.IV. Charge collection properties of a Si p-on-n alpha-voltaic device under 5 MeV alpha particle bombardment

T(°K)	200[a]	250[a]	300[b]	300[a]	300[c]	350[a]	400[a]
$t(\mu)$	10^3	10	10	10	10	10	10
τ_n(sec)	10^{-7}	10^{-7}	10^{-6}	10^{-7}	10^{-8}	10^{-7}	10^{-7}
τ_p(sec)	10^{-6}	10^{-6}	10^{-5}	10^{-6}	10^{-7}	10^{-6}	10^{-6}
$L_n(\mu)$	10.2	12.1	40.5	12.8	4.05	12.9	12.6
$L_p(\mu)$	21.4	22.6	77.2	24.4	7.72	24.2	23.4
$N_{eh,max}$(eh/a)	1.41×10^6	1.41×10^6	1.41×10^6	1.41×10^6	1.41×10^6	1.41×10^6	1.41×10^6
$N_{eh,SR}$(eh/a)	3.66×10^5	3.84×10^5	4.41×10^5	4.01×10^5	1.97×10^5	3.97×10^5	3.82×10^5
$N_{eh,J}$(eh/a)	6.15×10^4	6.15×10^4	6.15×10^4	6.15×10^4	6.15×10^4	6.15×10^4	6.15×10^4
$N_{eh,BR}$(eh/a)	6.69×10^5	6.99×10^5	8.87×10^5	7.05×10^5	4.29×10^5	7.04×10^5	7.12×10^5
Q	0.779	0.813	0.987	0.829	0.486	0.826	0.821

(a) Representative of moderately pure material.

(b) Material of higher purity than (a).

(c) Material of lower purity than (b).

Table III.V. Short-circuit current (in mA) and maximum power output (in μW) for a silicon p-on-n alpha-voltaic device under 5-MeV alpha particle bombardment.

A_α (curies)	P_{in} (μ W)		T (°K)						
			200[a]	250[a]	300[b]	300[a]	300[c]	350[a]	400[a]
1	1.48×10^{4}	I_{sc}	3.25	3.39	4.12	3.46	2.04	3.45	3.42
		P_{max}	2.21×10^{3}	1.86×10^{3}	1.95×10^{3}	1.45×10^{3}	7.03×10^{2}	1.01×10^{3}	5.94×10^{2}
0.1	1.48×10^{3}	I_{sc}	3.25×10^{-1}	3.39×10^{-1}	4.12×10^{-1}	3.46×10^{-1}	2.04×10^{-1}	3.45×10^{-1}	3.42×10^{-1}
		P_{max}	2.05×10^{2}	1.66×10^{2}	1.69×10^{2}	1.22×10^{2}	5.28×10^{1}	7.73×10^{1}	3.65×10^{1}
10^{-2}	1.48×10^{2}	I_{sc}	3.25×10^{-2}	3.39×10^{-2}	4.12×10^{-2}	3.46×10^{-2}	2.04×10^{-2}	3.45×10^{-2}	3.42×10^{-2}
		P_{max}	1.85×10^{1}	1.42×10^{1}	1.43×10^{1}	9.50	3.70	5.37	1.69
10^{-3}	1.48×10^{1}	I_{sc}	3.25×10^{-3}	3.39×10^{-3}	4.12×10^{-3}	3.46×10^{-3}	2.04×10^{-3}	3.45×10^{-3}	3.42×10^{-3}
		P_{max}	1.63	1.15	1.13	6.83×10^{-1}	2.40×10^{-1}	3.13×10^{-1}	4.23×10^{-2}
10^{-4}	1.48	I_{sc}	3.25×10^{-4}	3.39×10^{-4}	4.12×10^{-4}	3.46×10^{-4}	2.04×10^{-4}	3.45×10^{-4}	3.42×10^{-4}
		P_{max}	1.40×10^{-1}	8.58×10^{-2}	7.76×10^{-2}	4.33×10^{-2}	1.23×10^{-2}	1.13×10^{-2}	4.97×10^{-4}
10^{-5}	1.48×10^{-1}	I_{sc}	3.25×10^{-5}	3.39×10^{-5}	4.12×10^{-5}	3.46×10^{-5}	2.04×10^{-5}	3.45×10^{-5}	3.42×10^{-5}
		P_{max}	1.15×10^{-2}	5.78×10^{-3}	3.37×10^{-3}	1.78×10^{-3}	3.54×10^{-4}	1.81×10^{-4}	2.57×10^{-6}

(a) Representative of moderately pure material.

(b) Material of higher purity than (a).

(c) Material of lower purity than (a).

one another for an isotropic distribution so that the calculations of the maximum output power in this section (i.e., normal incident beam of α-particles) are expected to be representative of an actual α-voltaic device of equivalent activity.

In Fig. III.4 the initial maximum conversion efficiency calculated for an α-voltaic device with an ideal dark I-V characteristic is compared with that for a device with a three component dark I-V characteristic as a function of the α-particle source strength at temperatures of 200 and 300°K. The device with the "harder" characteristic (i.e., lower current passed at a given voltage) is seen to yield the best efficiency for energy conversion. Also included for comparison are typical results from Section V for the measured conversion efficiency of p-on-n Si solar cells under 4 MeV α-particle bombardment. The solid points represent measurements made at 200°K and the other points are for 275°K. The substantially lower values of the measured conversion efficiency result from the very soft dark I-V characteristics possessed by solar cells. Fig. III.5 presents a comparison of the temperature dependence of η_{max} for devices with the two types of dark I-V characteristics for three α-particle source strengths. At the higher temperatures the maximum efficiencies for both device types are seen to approach one another. This results from the fact that at the higher temperatures the ideal contribution to the dark I-V characteristic becomes the dominant contribution; that is, the dark I-V characteristic becomes approximately ideal over the current range which corresponds to the α-particle source strengths considered here. The initial efficiencies calculated for the different degrees of material purity (i.e., the three sets of minority carrier lifetimes characterizing the three degress of purity in Table

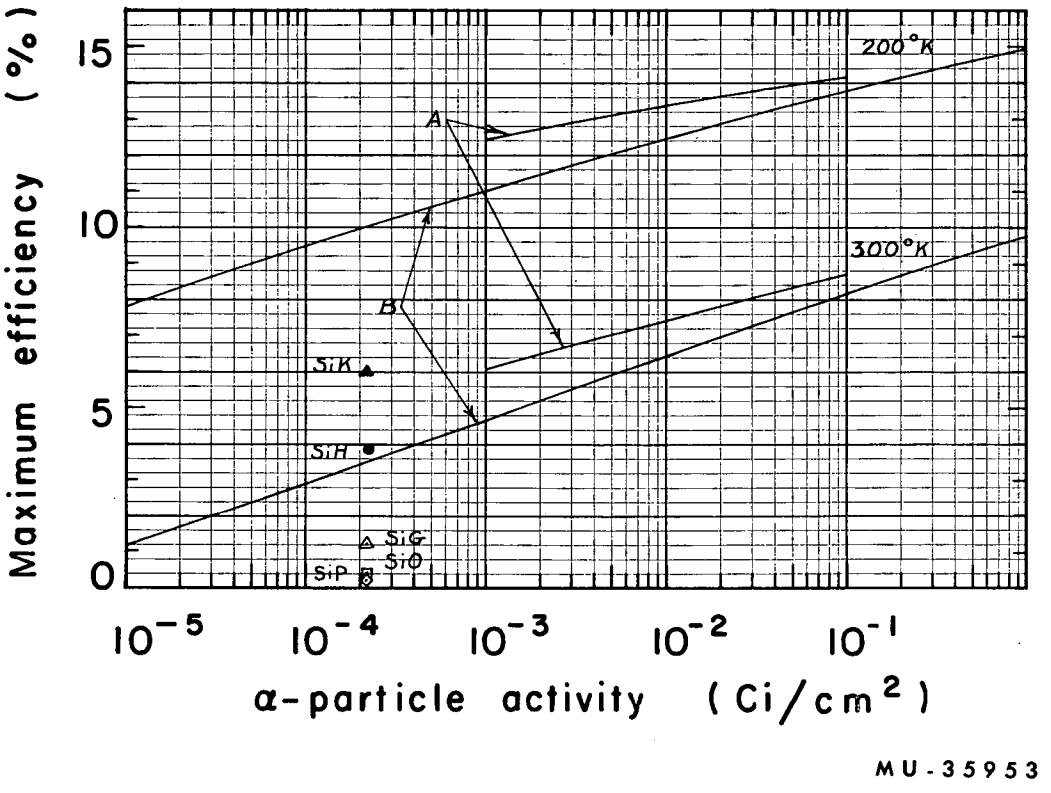

Fig. III.4. Initial maximum conversion efficiency for p-on-n Si α-voltaic devices with (A) ideal and (B) three-component dark I-V characteristics.

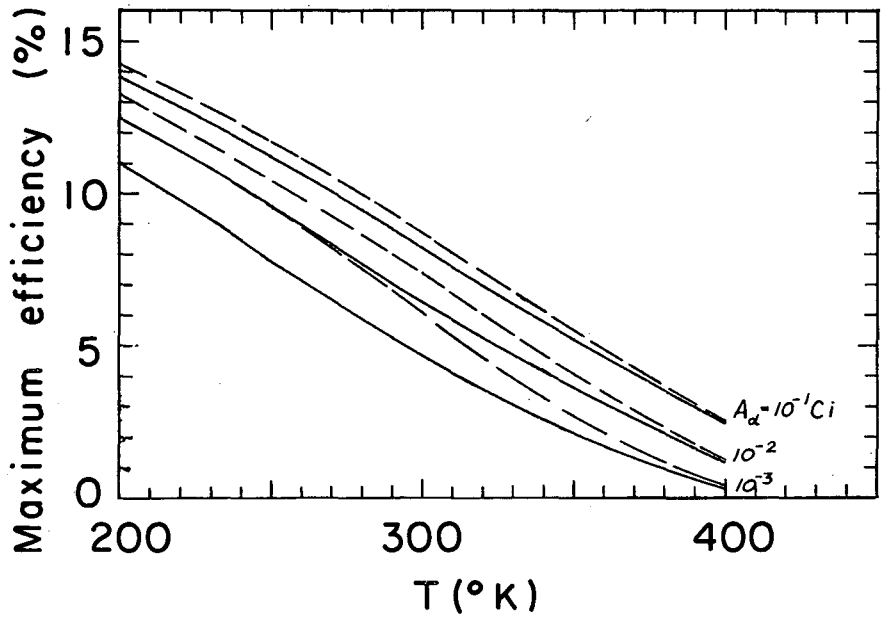

MU-35954

Fig. III.5. Initial maximum conversion efficiency vs temperature for a p-on-n Si α-voltaic device (the solid and dashed curves correspond to diodes possessing ideal and three component dark I-V characteristics respectively).

III.III) are compared in Fig. III.6 as a function of source strength. These results show that the use of high purity material in the preparation of an α-voltaic device results in a sizable improvement in device performance. In a practical situation this effect would become less important since the high purity material is more expensive to produce.

4. Bombardment Induced Changes in Device Performance. The results quoted above apply only to the initial or predamaged state of a Si α-voltaic device. The defect centers which originate from bombardment produce a decrease in the minority carrier lifetime in that portion of the bulk material traversed by the incident α particles. The minority carrier lifetime is related to the defect center concentration through Eq. (III-26). Therefore the spatial variation of the minority carrier lifetime is proportional to the number of defect centers produced per unit track length per α particle, where this is shown in Fig. III.2. From this figure we see that it is reasonable to consider a single average defect concentration in the surface region ($0 \leq x \leq 10\mu$), whereas the base region must be divided into lightly damaged ($11\mu \leq x \leq 24\mu$), heavily damaged ($24\mu \leq x \leq 27\mu$), and undamaged ($27\mu \leq x$) sub-regions each possessing an appropriately determined average defect center concentration. The more regions considered the better would be the accuracy of this approach. However the bombardment produced changes in minority carrier lifetime cannot be directly calculated from Eq. (III-26) because the defect center capture cross sections for holes and electrons are not known.

An alternate technique can be employed which considers changes in the diffusion length during exposure (see Eq. (III-28)). In this case

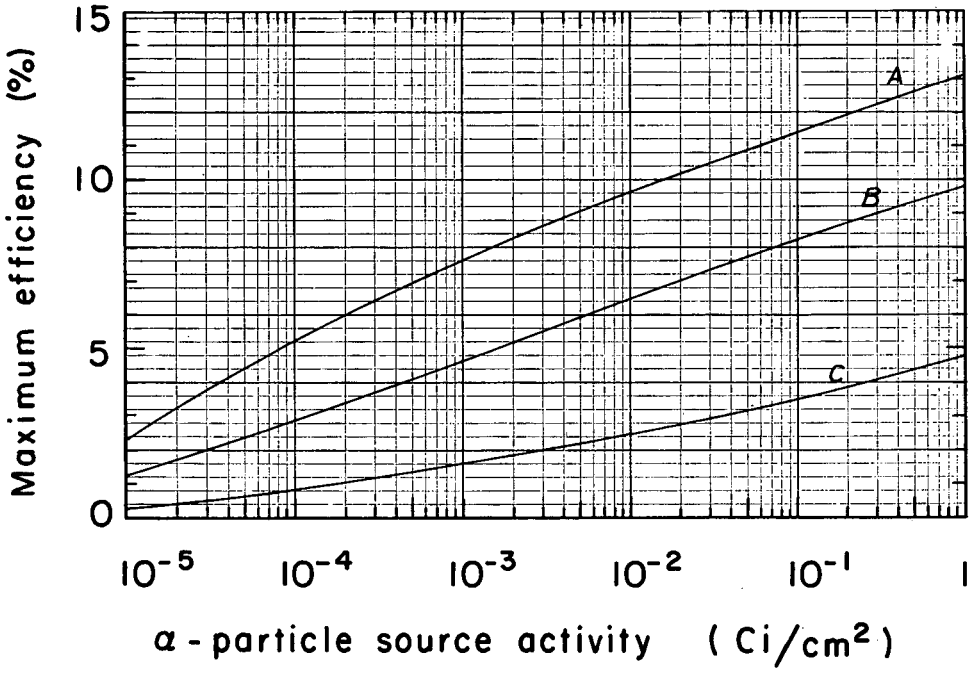

Fig. III.6. Initial conversion efficiency for p-on-n Si α-voltaic devices of various purities at 300 °K (curves A, B, and C correspond to the material properties of columns (b), (a) and (c) respectively of Table III.III).

the diffusion length degradation constant, K(x), is proportional to the number of defect centers produced per unit track length. Using the value of K measured at a particular α-particle energy E_α (and corresponding position x) it is then possible to normalize the spatial distribution for the K(x) at this point and proceed with the determination of the required average defect center concentrations. This technique is considered in more detail in Section V.

For the present discussion it is sufficient to use the results of Section V which deal with the bombardment induced changes of the maximum conversion efficiency for p-on-n Si solar cells. The behavior of a p-on-n Si α-voltaic device should be very similar. The results to be used here were obtained from the measurements at 200 and 275 °K. The effective curve shown by the dotted line in Fig. V.19 was used in calculating the bombardment induced changes in conversion efficiency for a moderately pure p-on-n Si α-voltaic device at 250 °K. Figure III.7 shows the decrease in maximum efficiency with time for four separate source strengths, and it is quite evident that the useful lifetime of the device becomes impractically short for the stronger alpha sources.

The non-normal α-particle flux encountered for an actual α-particle source would result in an even faster decrease in the maximum conversion efficiency during exposure. This results from the fact that the defect centers are produced closer to the junction by those α particles with a low angle of incidence, and therefore the severely damaged regions produced at the end of the α-particle tracks are no longer localized to a portion of the base regions far removed from the junction as is the case for a normal incident beam of α particles.

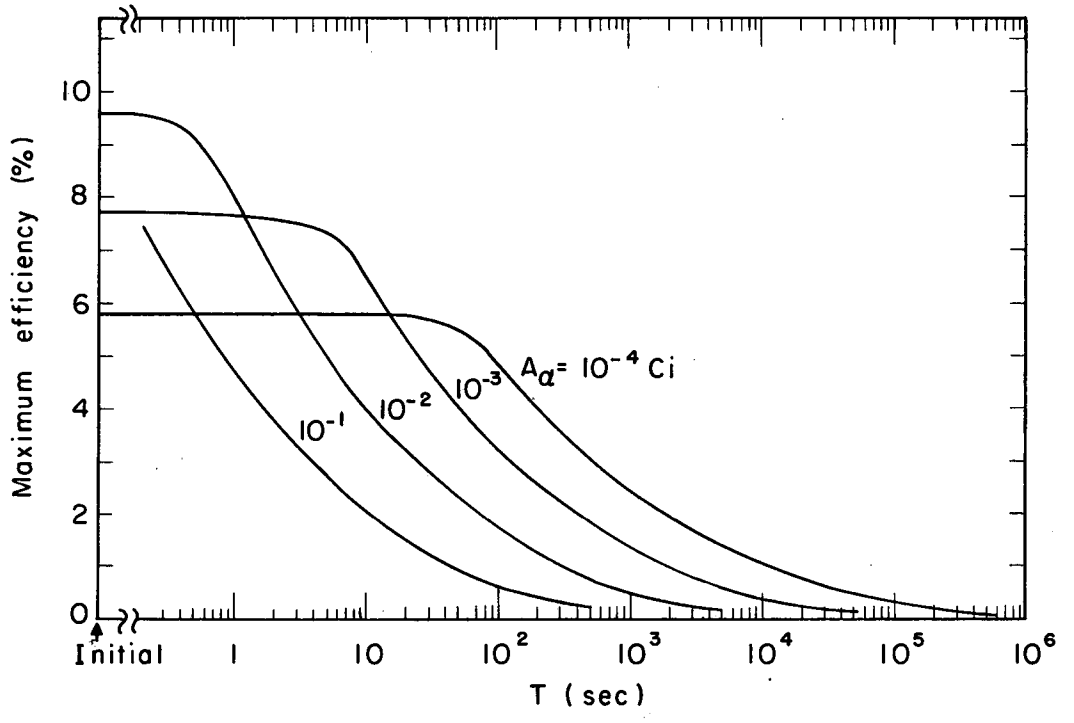

Fig. III.7. Maximum conversion efficiency for a Si p-on-n α-voltaic device vs exposure.

IV. DARK CURRENT-VOLTAGE CHARACTERISTICS FOR SILICON AND GALLIUM ARSENIDE SOLAR CELLS

A. Theory.

In the preceding section it was noted that the ease with which current is passed by a forward biased semiconductor diode has a substantial effect upon the energy conversion capability of the diode under α-particle bombardment. A diode with a soft forward I-V characteristic was shown to yield a lower power output for a fixed power input than one with a hard characteristic.

The forward I-V characteristic of a semiconductor diode is generally assumed to consist of an ideal diffusion term and a non-ideal term which is found to be present in most actual diodes. The various contributions to the non-ideal term are described in the following paragraphs and a detailed discussion of the mechanisms responsible for these contributions to this term can be found in Appendix A.

The diffusion current passed by a p-n junction has been treated in detail by Shockley.[56] The I-V characteristic obtained by Shockley is just the so called ideal term mentioned earlier and is given by

$$I_d(V_j) = I_o(e^{\lambda V_j}-1), \qquad \text{(IV-1)}$$

where the reverse saturation current, I_o, is

$$I_o = qA_x \left[n_{po}\left(\frac{D_n}{L_n}\right) + p_{no}\left(\frac{D_p}{L_p}\right) \right] . \qquad \text{(IV-2)}$$

Equation (IV-1) implies a negligible internal series resistance of the diode since the voltage applied to the diode is $V = V_j + IR_s$. This current is a lower limit for the current which can be passed by a semiconductor diode and is therefore an example of a hard I-V characteristic. Suitably prepared Ge diodes have been shown to obey Eq. (IV-1) at room

temperature and above.[58] However, for Si and GaAs diodes as well as Ge diodes at low temperature, the measured I-V characteristics are found to deviate from Eq. (IV-1).

In the limiting situation where the injected minority carrier concentration is large compared to the equilibrium majority carrier concentration, i.e., high level injection, Sah, Noyce, and Shockley[53] have found the diffusion current to be of the form

$$I_d = \sqrt{2}\, qA_x\left(\frac{D_p+D_n}{L_o}\right)n_i \exp(\lambda V_j/2). \qquad \text{(IV-3)}$$

Therefore, at high injection levels the exponential dependence of the current upon voltage is seen to be $\lambda/2$ or half that for low level injection (cf. Eq. A-21).

A number of mechanisms which contribute additional current in an actual diode have been discussed in the literature. The current resulting from a given mechanism will be designated as a current contribution to the non-ideal term of the I-V characteristic. Thus the total current passed by a semiconductor diode is

$$I = I_o(e^{\lambda V_j}-1) + \Sigma_n\, I_n(V_j), \qquad \text{(IV-4)}$$

where $I_n(V_j)$ represents the non-ideal current contribution to the I-V characteristic resulting from mechanism n and the sum is the non-ideal term.

The specific mechanism responsible for the major contribution to the non-ideal term is dependent upon the type of device in question. The device geometry, material properties, surface condition, and ambient temperature determine the voltage range over which a particular mechanism is dominant.

Shunt Conductance Current. All semiconductor diodes have a common contribution to the I-V characteristic, and this is the shunt conductance current characterized by a shunt resistance, R_{SH}, in parallel with the p-n junction. The I-V characteristic in this case is

$$I = I_{SH} + I_o(e^{\lambda V_j} - 1), \qquad \text{(IV-5)}$$

where $I_{SH} = V_j/R_{SH}$. This term can be large in comparison with the ideal current over a substantial portion of the voltage range, since the reverse saturation current for a Si diode at room temperature is on the order of 10^{-12} amperes and that for GaAs is even smaller. The current contribution of the shunt conductance path can be even more important at lower temperatures.

Junction Recombination-Generation Current. Another process contributing to the non-ideality of a device is the current arising from the generation or recombination of electron-hole pairs in the junction.[53] The thermal generation of electron-hole pairs is important for a junction under a large reverse bias where these thermally produced pairs are swept from the junction and contribute to the current. In the forward bias region of operation, electron-hole pair recombination is of importance, since the carriers injected into the junction from one field-free region of the diode have a finite probability for recombination before reaching the other field-free region. The net result of this process is an increase in the current flowing through the diode at a fixed voltage. This contribution to the I-V characteristic for a linear variation of potential in the junction is given by

$$I_{rg} = \frac{2qn_i A_x W(V_j)}{\sqrt{\tau_{po}\,\tau_{no}}} \quad \frac{\sinh(\frac{\lambda V_j}{2})}{\lambda(\psi_D - V_j)} \quad f(b), \qquad \text{(IV-6)}$$

where $W(V_j)$ is the junction thickness. It is therefore to be expected that this will be the dominant contribution to the non-ideal term for a diode with short minority carrier lifetimes and a thick junction. From Eq. (IV-6) it can be seen that in the intermediate voltage region (i.e., $\lambda V_j > 1$ but $V_j < \psi_D$) the exponential dependence of current upon voltage is $\lambda/2$.

Surface Inversion Layer Current. It is well known that contamination of a semiconductor surface by adsorbed gases can lead to the formation of a surface inversion layer.[12,19,44,60] This consists of a thin surface region of the opposite conductivity type to that of the bulk material. In the specific case of Si a p-type layer can be produced in n-type material when exposed to an oxygen rich atmosphere, and an n-type inversion layer results when p-type material is exposed to water vapor. Therefore a p-n junction is formed in the process, and the current resulting from this junction must be included in the I-V characteristic for the diode. Cutler and Bath[15] have calculated the contribution of a surface inversion layer current to the I-V characteristic of a diode. Under the assumption that the length of the inversion layer is not limited (this is not a good approximation for shallow diffused junctions), they find the diode forward I-V characteristic to be

$$I = I_o(e^{\lambda V_j}-1) + I_L(e^{\lambda V_j}-\lambda V_j-1)^{1/2} \qquad \text{(IV-7)}$$

where $I_L = 2w^2LJ_s/\lambda\rho$ and L is the inversion layer thickness. Equation (IV-7) shows that the inversion layer current also exhibits a $\lambda/2$ exponential dependence on voltage in the intermediate voltage region (i.e., $\lambda V_j > 1$). Therefore the general shape of the generation-recombination and inversion layer current is approximately the same whereas their

magnitudes can be quite different. As stated previously, the relative magnitude of any of these contributions is a characteristic of the particular diode in question.

Tunneling Current. In the case of a diode with a very thin junction and high impurity atom concentration, the dominant contribution to the non-ideal term is expected to be the so-called "excess current" and this is indeed found to be the situation for tunnel diodes.[13,20] The "excess current" arises from either the direct tunneling of the charge carriers through the junction between energy states in the conduction and valence bands or via the intermediary localized energy levels in the forbidden energy gap. The current resulting from this tunneling process as calculated by Chynoweth et al.,[13] is

$$I_T = AN_T \exp\left[-\alpha_T W_o q^{1/2}([E_{fno}-E_{fpo}] - qV_j)\right] \qquad \text{(IV-8)}$$

where N_T is the concentration of impurity energy levels, W_o is the junction width for unity contact potential, and the constant α_T, defined in Appendix A, exhibits a very weak dependence upon temperature. The constant A although not determined by Chynoweth et al., must in conjunction with N_T account for the current going to zero at $V_j = 0$. The constant A depends upon the transition frequency between the impurity level energy states in the forbidden energy gap and the available energy states in the valence band which are situated at the same energy. As the applied bias, V_j, is increased, the localized impurity energy levels located at fixed positions in the forbidden energy gap are shifted relative to the available energy states in the valence band. This leads to a voltage dependence of N_T, and therefore the exact nature of the distribution of impurity levels in the forbidden energy gap must be known in order to quantitatively determine the current. The distribution

of available energy states in the valence band has an energy dependence of $C(E-E_{vp})^{1/2}\exp[\lambda(E-E_{fpo})]$ for a non-degenerate semiconductor. This factor tends to smooth out any structure in the distribution of impurity levels, and the total current must therefore be proportional to the integral of $I_T(V)$ at E over the energy interval of overlap for the two distributions (the position of the impurity level distribution being dependent upon junction bias). Then

$$I_T = \int_{E_{vn}}^{E_{vp}} T(E)C(E-E_{vp})^{1/2}\exp\lambda(E-E_{fpo})N_T(E,V_j)dE, \qquad \text{(IV-9)}$$

where $E_{vn} = E_{vp} - (\psi_D - V_j)$, $N_T(E,V_j)$ designates the concentration of impurity levels at energy E for a junction bias of V_j, and T(E) is the transition probability at energy E which is given by Eq. (A-44) of Appendix A. The total number of available valence band energy states in the energy interval of overlap is dependent upon temperature through the exponential factor $\exp\lambda(E-E_{fpp})$. It is therefore expected that the magnitude of the tunneling current contribution to the non-ideal term will decrease with decreasing temperature, whereas the exponential dependence upon voltage is approximately independent of temperature as deduced from Eq. (IV-8). At low temperatures the band of available states in the valence band is comparatively narrow so that the tunneling current I-V characteristic is expected to have a structure similar to that present in the distribution of impurity levels.

Sheet Resistance. In the preceding discussion it has been assumed that the entire junction experiences an identical bias, V_j. This situation is, however, not realized for a solar cell where a voltage gradient is developed in the surface region when current flows along the path from the junction to the electrode strips on the front surface.

The potential variation over the cross sectional area at the junction-surface region boundary has been studied by Wysocki.[68] He found that, as the current increased, the effective area of the junction (the fraction of the area which contributes to current flow) decreased. Therefore the current is found to increase more slowly than the ideal exponential term at $\lambda V_j > 1$.

Non-Uniformity of Material Properties. Queisser[58] has shown that non-uniformity of material properties in the surface region and junction result in regions of the junction possessing different I-V characteristics. Therefore this spatial non-uniformity of the junction characteristic is of substantial importance when considered along with the fractional use of the junction area. In particular Queisser found the I-V characteristic of the junction region immediately below the electrical contacts to be quite different from that of the regions far removed from the contacts. At large applied bias and associated current, the effective junction area includes only those regions in the vicinity of the electrical contacts; and therefore it is to be expected that the solar cell I-V characteristic can be markedly affected.

Recent work by Wolf and Rauschenbach[66] has shown that the I-V characteristic of a Si solar cell in the temperature range of 300 to 400°K can be relatively well represented by an expression containing two exponential terms and the shunt conductance term,

$$I(V) = \frac{(V-IR_s)}{R_{SH}} + I_{o1}[\exp(\frac{\lambda}{A}[V-IR_s])-1] + I_o[\exp(\lambda[V-IR_s])-1] \quad \text{(IV-10)}$$

where the last term on the right hand side of Eq. (IV-10) is the ideal diffusion term, I_{o1} is the effective reverse saturation current for the non-ideal term, and A is the junction non-ideality factor normally

assumed to be between 1 and 3.[40,66] They were unable to draw any conclusions relative to the mechanism producing the non-ideal exponential term in Eq. (IV-10) while concluding that the ideal diffusion term was indeed present for the p-on-n Si solar cells tested.

In the work reported in this section the temperature range of interest was extended down to either 100 or 200 °K, and the solar cell and junction I-V characteristics were measured for p-on-n and n-on-p Si solar cells and p-on-n GaAs solar cells. The results were analyzed using the two exponential model of Wolf and Rauschenbach, where an attempt has been made to relate each of the exponential terms to one or more of the basic mechanisms discussed above.

B. Experimental Method.

The current voltage characteristics were measured for Si and GaAs solar cells in the temperature range 90 °K to 360 °K. Both p-on-n and n-on-p Si cells were used, whereas only p-on-n GaAs cells were available. The majority of the cells were treated only with a distilled water and/or ethyl alcohol wash. One exception to this was GaAs A-20 which received an etch of the cell edges with a solution of $HNO_3/HF/H_2O$ in 1:1:1 proportions followed by a distilled water wash. In this case the etch was required in order to reduce the shunt conductance current to an acceptable value. Also given an edge etch were cells Si3A and SiL. These cells were etched with CP4* etch in order to observe the effect of such an etch upon the I-V characteristic. The method of preparation along

* 5 parts concentrated HNO_3, 3 parts each CH_3COOH and 48 percent HF; sometimes contains trace amounts of Br.

with a detailed description of each cell tested is given in Table IV.I.

The solar cell I-V characteristics were measured in a light tight vacuum chamber at a pressure of about one micron of mercury. The chamber is shown in Fig. IV.1. The pressure was measured with a Hastings thermocouple type gauge.

The vacuum chamber was designed in such a way that the I-V characteristic of a sample cell could be measured at a number of temperatures. The solar cells were soldered to a platinum sheet and placed in a sample holder which was in turn bolted to the bottom of the fluid container. Platinum was chosen because of the fact that its coefficient of expansion is approximately equal to that of Si. This made possible tests on a majority of the Si cells at liquid nitrogen temperature without complete destruction of the cell. The platinum sheet was bolted to the sample holder at only one point in order to allow it to freely contract or expand relative to the brass sample holder. In order to attain the desired temperatures, the fluid container was filled with either liquid nitrogen ($\simeq 90\,^{\circ}K$), dry ice and ethyl alcohol ($\simeq 200\,^{\circ}K$), distilled water ice ($\simeq 273\,^{\circ}K$), or distilled water heated by a 100 watt blade type heater element ($\simeq 360\,^{\circ}K$). The solar cell was in good thermal and electrical contact with the vacuum chamber body so that the chamber became part of the electrical circuit. The sample holder was positioned in the chamber such that it could be subjected to a light source (a GE 1493 tungsten lamp). A teflon sheet was placed between the solar cell and lamp in order to yield a more diffuse light source than that of the lamp alone. An infrared filter was not used in conjunction with the light source, and as a result heating of the sample cells became an important factor at high light source intensities.

Table IV.I. Properties and preparation of sample solar cells.

Cell	Type	Size (cm×cm)	Contact	Rated solar efficiency (%)	Preparation	Symbol used in figures
SiM	IRCS0510E10-p-n	0.5×1.0	Gridded	10	D. W. & E. A. wash	△
SiN	IRCS0510E11-p-n	0.5×1.0	Gridded	11	D. W. wash	□
Si51CB	Hoffman 51C-p-n	0.5×1.0	Ungridded	8	D. W. & E. A. wash	○
Si3A	IRCS0510E10-p-n	0.5×1.0	Gridded	10	D. W. & E. A. wash	▽
Si3A	IRCS0510E10-p-n	0.5×1.0	Gridded	10	Etched in CP-4 and D. W. & E. A. wash	▼
Si1B	IRCS1020E8-p-n	1.0×2.0	Gridded	8	D. W. wash	▲
Si1D	IRCS1020E8-p-n	1.0×2.0	Gridded	11	D. W. wash	●
SiL	IRCS1020E11-n-p	1.0×2.0	Gridded	11	D. W. & E. A. wash	◐
SiL	IRCS1020E11-n-p	1.0×2.0	Gridded	11	Etched in CP-4 and D. W. & E. A. wash	◑
SiF	IRCS1020E8-n-p	1.0×2.0	Gridded	8	D. W. & E. A. wash	■
GaAs A-20	RCAXSC100-p-n	1.0×2.0	Gridded	4	Etched and D. W. wash	◇
GaAs A-22	RCAXSC100-p-n	1.0×2.0	Gridded	4	D. W. & E. A. wash	◆

Manufacturers estimates of device properties:

Si p-on-n; junction depth of 1μ to 2μ, $L_n \approx 1\mu$, $\rho_n \approx 1\ \Omega$ cm, $L_p \approx 10\mu$ to 100μ, $s_n \approx 5000$ cm/sec

Si n-on-p; junction depth of 1μ to 2μ, $L_p \approx 1\mu$, $\rho_p \approx 1\ \Omega$ cm, $L_n \approx 10\mu$ to 100μ

GaAs p-on-n; junction depth = $1\mu \pm 10\%$ (never more than 1.5μ), $\overline{p_p} \approx 2.3\times10^{19}$ cm^{-3},
$L_n \approx 0.5$ to 1.0μ, $s_n \approx 1000$ to 5000 cm/sec, $n_n \approx 10^{17}$ cm^{-3},
$L_p \approx 1 \rightarrow 3\mu$ (zinc diffusion).

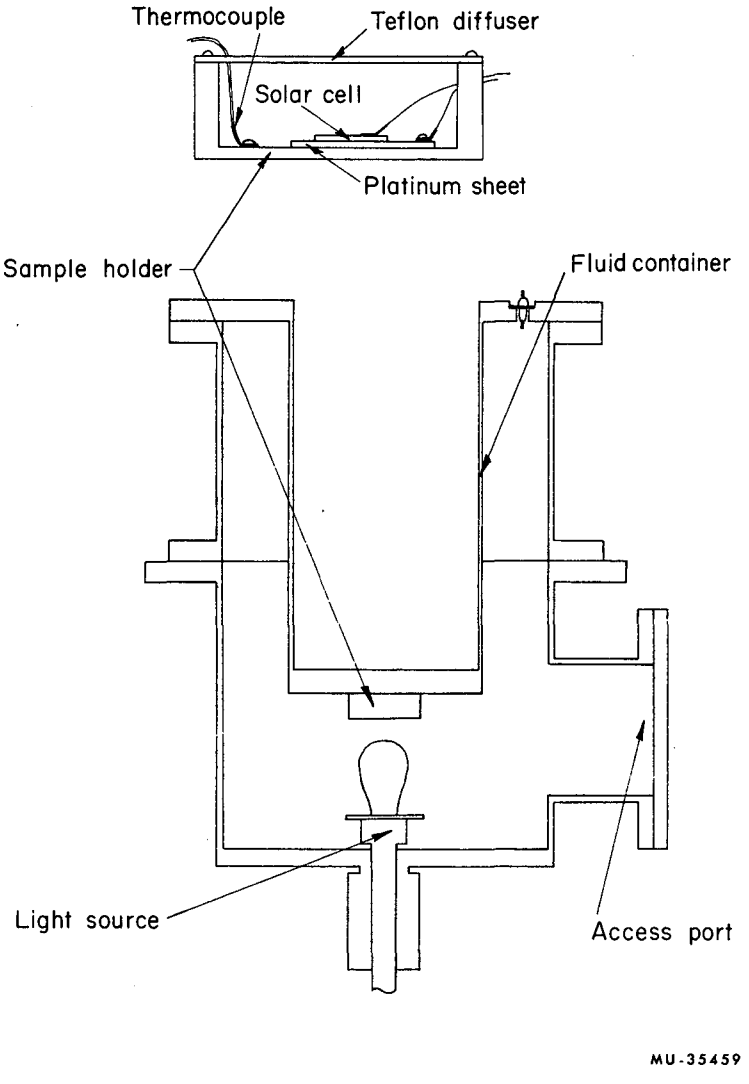

Fig. IV.1. Diagram of vacuum chamber and associated parts.

The sample temperature was continuously monitored by feeding the output of a copper-constantan thermocouple to a strip chart recorder. The thermocouple was attached to the inner wall of the sample holder.

The current-voltage characteristics of the solar cells were measured at the four previously mentioned temperatures using the circuit shown in Fig. IV.2 and the equipment shown in Fig. IV.3. Measurement of the forward bias region of the I-V characteristic was limited to currents less than 200 milliamps. The voltage drop across the cell was measured by an electrometer voltmeter with the output of the voltmeter being used to drive one co-ordinate of an X-Y recorder. The current was obtained from the measured voltage drop developed across one of a set of precision resistors which could be placed in series with the sample solar cell. This voltage was also measured with an electrometer voltmeter, and the meter output was used to feed the other co-ordinate of the X-Y plotter. In this way the current-voltage characteristics were displayed on an X-Y recorder. The measuremental uncertainties associated with this system are presented in Table IV.II. The I-V characteristic obtained in this way includes the internal series resistance effects and as a result is referred to as the diode current-voltage characteristic.

In the forward bias voltage range where the series resistance is of importance, it was necessary to also measure the I-V characteristic of the junction alone. Providing the series resistance is not too great, this can be achieved by using a light source of adequate strength. In this work a tungsten lamp, powered by a regulated DC power supply, was employed where the intensity of the light source was increased in a stepwise manner. The short circuit current and open circuit voltage were measured at each setting of light source intensity. As mentioned in

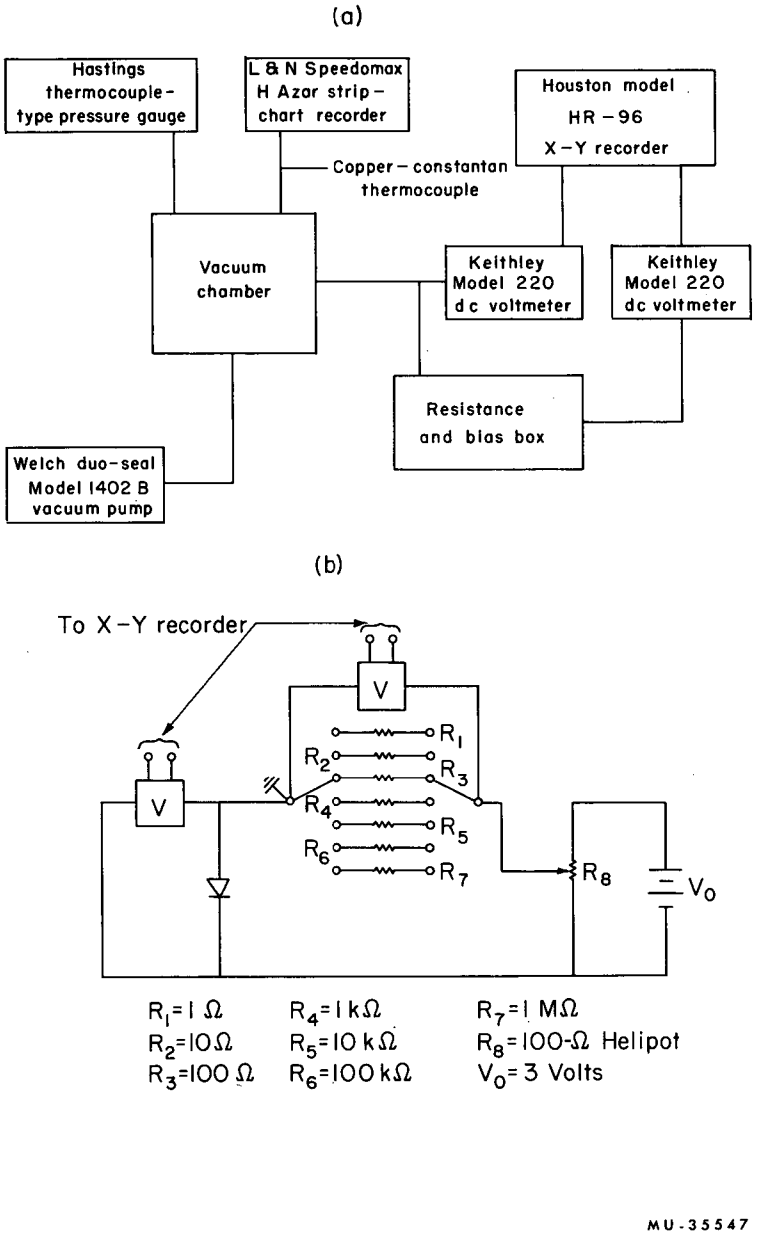

Fig. IV.2. (a) Block diagram and (b) circuit diagram used in the measurement of the diode I-V characteristics.

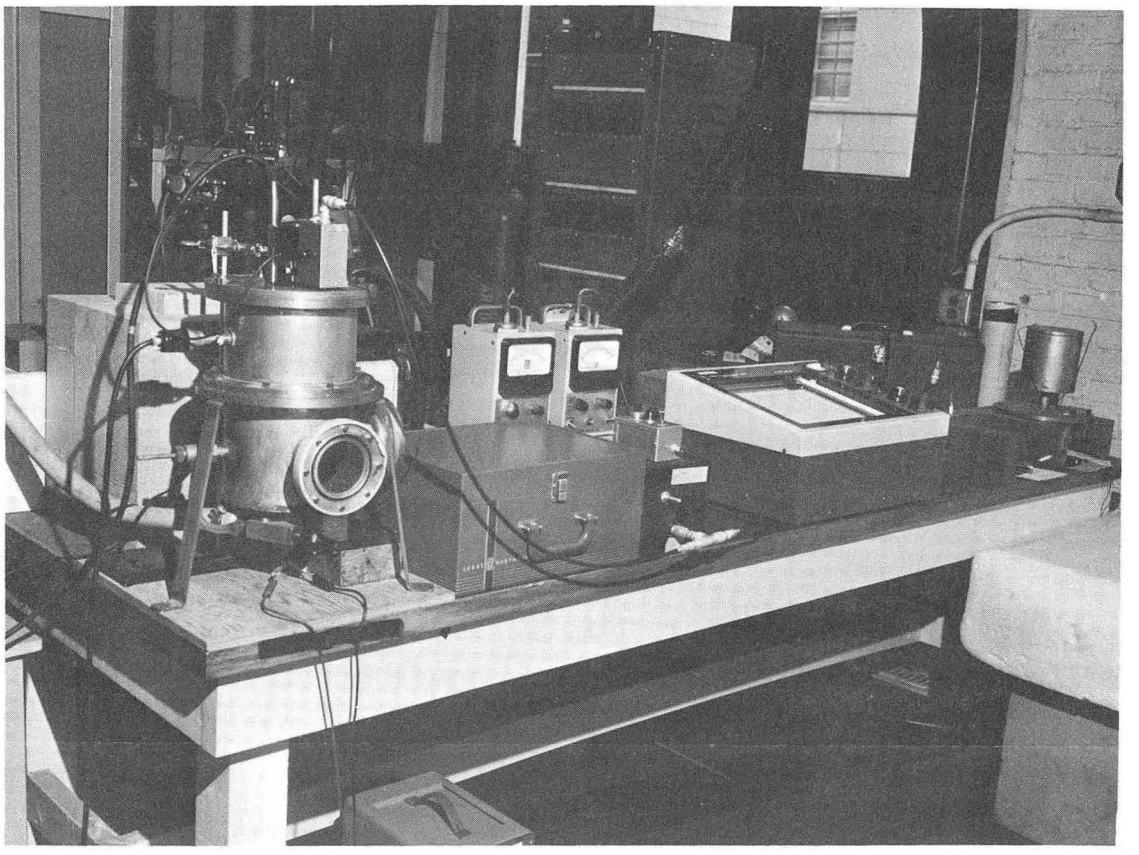

ZN-4825

Fig. IV.3. Apparatus used in the measurement of the diode I-V characteristics.

Table IV.II. Estimated systematic and random uncertainties associated with the measuring apparatus.

Measured quantity		I-V Characteristic		
		Diode (low voltage)	Diode (intermediate and high voltage)	Junction (high voltage)
		(a)	(b)	(c)
V_j,	Random	±0.5%	±0.5%	±0.5%
	Systematic	±0.5%	±0.5%	±0.5% (d)
V_I,	Random	±0.5%	±0.5%	±0.5% (e)
	Systematic	±0.5%	±0.5%	±2% (f)
R_I,	Random	±0.1%	±0.1%	---
		(g)	(h)	(i)
V_j,	Random	±0.1 mV	±0.3 mV	±0.4 to 0.5 mV
	Systematic	$\lesssim$+0.3 mV	$\lesssim$+0.6 mV	$\lesssim$+0.6 mV
V_I,	Random	±2%	±2%	±0.1 mV
	Systematic	---	---	$\lesssim$+0.3 mV
R_I,	Random	±0.1%	±0.1%	±0.1%

(a) X-Y plotter with inputs fed by two Keithley VTVM's.
(b) X-Y plotter with inputs fed by two Keithley VTVM's.
(c) Voltage measured with Keithley and current with clip-on milliameter.
(d) Keithley VTVM readings corrected using calibration curve.
(e) Random error increased on lowest scale.
(f) Specified by the manufacturer of the instrument.
(g) Voltage measured with Digitec and current with Keithley.
(h) Voltage measured with Digitec and current with Keithley.
(i) Voltage measured with Digitec and current with Digitec.

Section III, the I-V characteristic of a solar cell under illumination is equal to the sum of the dark I-V characteristic and the current resulting from the collection of the electron-hole pairs produced by the light source,

$$I(V) = I_d(V) - I_L \,, \qquad \text{(IV-11)}$$

where $I_d(V_j)$ is the junction dark I-V characteristic, I_L is the light generated current, and $V = V_j + IR_s$. The junction dark I-V characteristic is equal to the diode dark I-V characteristic if either $R_s = 0$ or $IR_s \ll V_g$. The open circuit voltage produced by a given light source intensity is obtained from Eq. (IV-11) with $I = 0$,

$$I_d(V_{oc}) = I_L. \qquad \text{(IV-12)}$$

Therefore the junction I-V characteristic can be obtained providing that it is possible to achieve the necessary range in I_L. The short circuit current is obtained from Eq. (IV-11) with $V = 0$,

$$I_{sc} = I_d(-I_{sc}R_s) - I_L, \qquad \text{(IV-13)}$$

which is indeed equal to $-I_L$ for sufficiently small values of the series resistance. Therefore the junction dark I-V characteristic was obtained in a point-by-point manner. The circuit used to measure the junction dark I-V characteristic is presented in Fig. IV.4 and the equipment shown in Fig. IV.5. The open circuit voltage was measured with an electrometer voltmeter, and the short circuit current was either measured directly with a clip on milliammeter or was obtained from the voltage drop developed across a calibrated precision resistance (this voltage was measured by an electrometer voltmeter-digital voltmeter combination). The resistance employed was always small enough so as to satisfy the condition that $I_d(-I_{sc}R_s) \ll I_L$. The measuremental uncertainties associated with this system are also presented in Table IV.II.

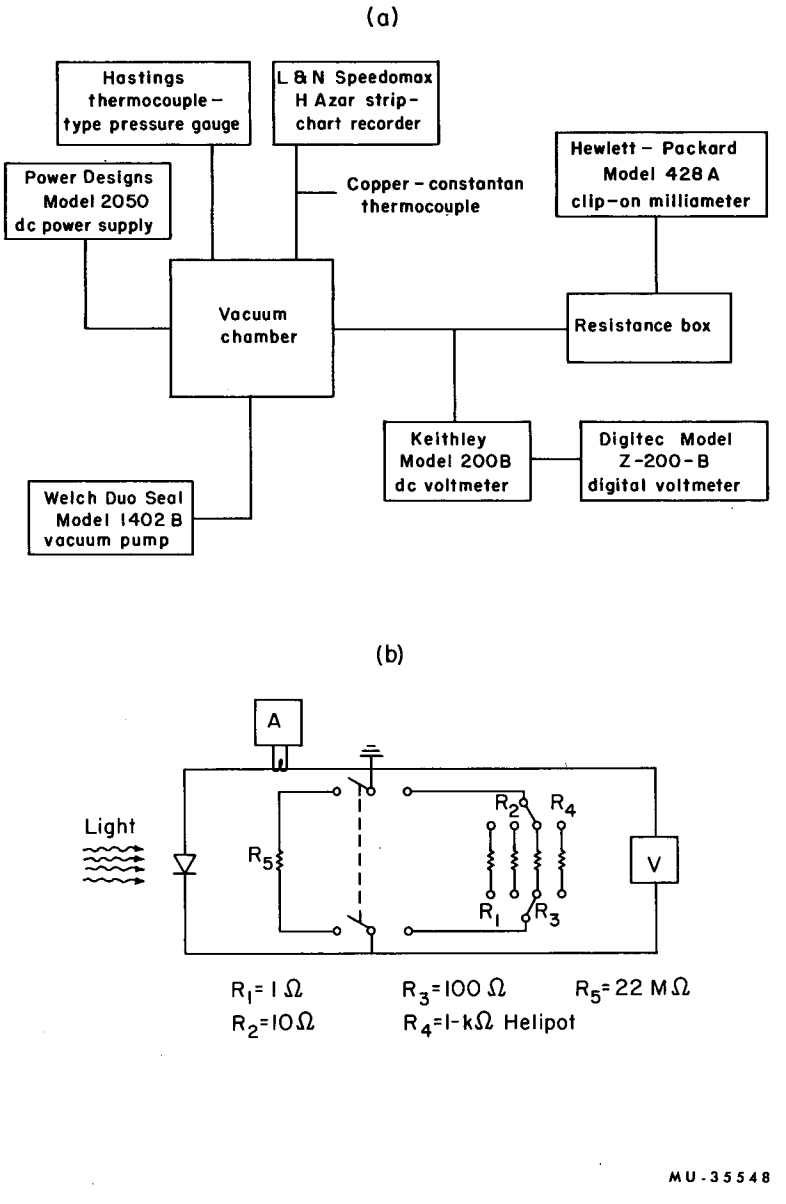

Fig. IV.4. (a) Block diagram and (b) circuit diagram of equipment used in the measurement of the junction I-V characteristics.

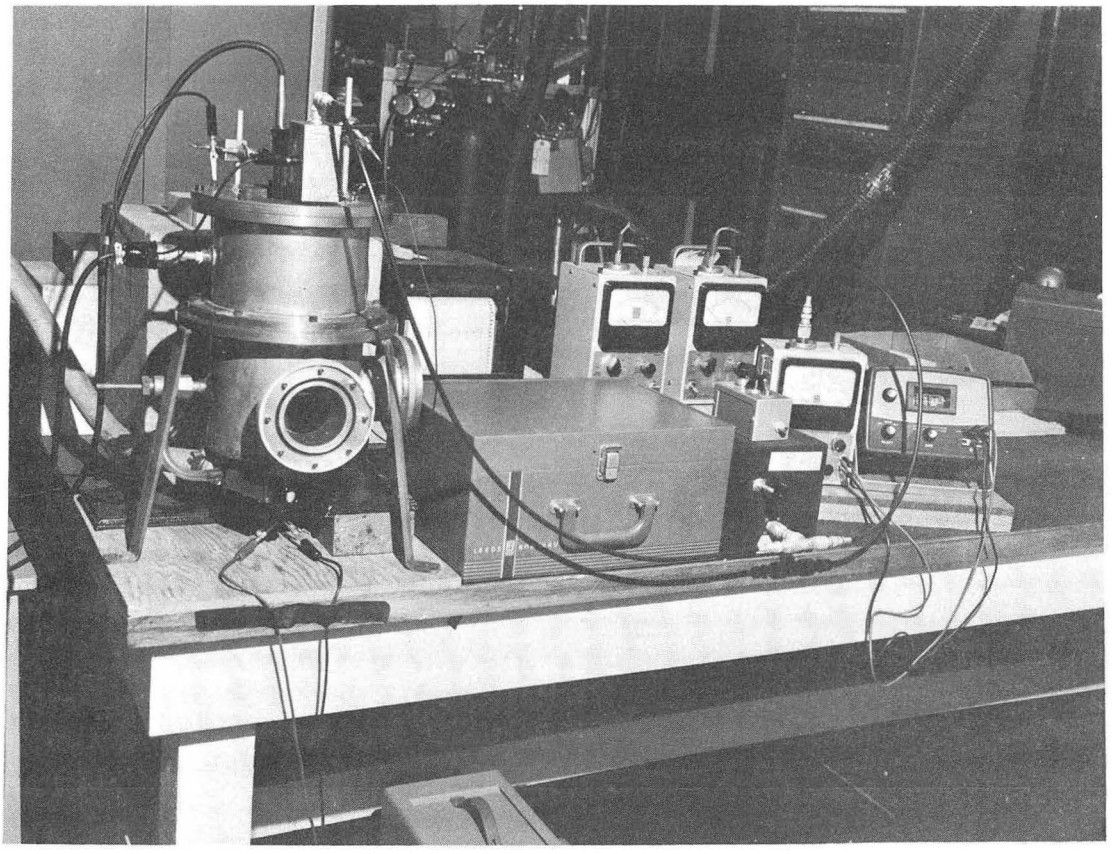

ZN-4826

Fig. IV.5. Apparatus used in the measurement of the junction I-V characteristics.

The solar cell temperature was found to increase at the higher light source intensities as a result of infrared heating produced by the tungsten lamp. In order to minimize the effects of this heating upon the measured I-V characteristic, the majority of cells tested were allowed to return to thermal equilibrium prior to the measurement of V_{oc} and I_{sc} for each point.

C. Results and Discussion.

The experimentally measured diode and junction dark I-V characteristics for the three cell types were compared with Eq. (IV-10) with $R_s = 0$; and the constants R_{SH}, I_{o1}, δ, I_o, and λ_m were chosen so as to obtain a best fit of the experimental data. The value of R_s was then obtained from the displacement of the diode dark I-V characteristic with respect to the junction dark I-V characteristic.

For small currents the dark I-V characteristic can be approximated by (the magnitude of the current for which this is a valid approximation is a function of the test temperature, see Table IV.III)

$$I(V_j) = \frac{V_j}{R_{SH}} + I_{o1}(\delta V_j) + I_o \lambda V_j \qquad \text{(IV-14)}$$

where λ/A has been replaced by δ. The motivation for this step will become evident when the temperature dependence of the non-ideal exponential term is discussed. The third term on the right hand side of Eq. (IV-14) is negligible and can be neglected. Then the slope of the I-V characteristic at the origin is

$$\frac{dI(0)}{dV_j} = \frac{1}{R_{SH}} + \delta I_{o1} = \Lambda$$

or

$$\frac{1}{R_{SH}} = \Lambda - \delta I_{o1}. \qquad \text{(IV-15)}$$

Table IV.III. Typical temperature dependence of the different voltage regions for the three cell types tested. [a]

Cell type	Temp(°K)	Voltage region (V)		
		Intermediate	Transition	High
Si p-on-n	90	$V \lesssim 0.85$	$0.85 \lesssim V \lesssim -$	—
(SiM)	200	$V \lesssim 0.65$	$0.65 \lesssim V \lesssim -$	—
	275	$V \lesssim 0.45$	$0.45 \lesssim V \lesssim -$	—
	360	$V \lesssim 0.30$	$0.30 \lesssim V \lesssim -$	—
Si n-on-p	200	$V \lesssim 0.60$	$0.60 \lesssim V \lesssim 0.75$	$0.75 \lesssim V$
(SiL)	275	$V \lesssim 0.45$	$0.45 \lesssim V \lesssim 0.60$	$0.60 \lesssim V$
	360	$V \lesssim 0.25$	$0.25 \lesssim V$ —	—
GaAs p-on-n	200	$V \lesssim 1.00$	$1.00 \lesssim V \lesssim -$	—
(GaAs A-22)	275	$V \lesssim 0.80$	$0.80 \lesssim V \lesssim -$	—
	360	$V \lesssim 0.50$	$0.50 \lesssim V \lesssim -$	—

(a) The low-voltage region for all the cells tested corresponds to $V \lesssim 0.10$ V.

It is then possible to obtain the shunt resistance providing I_{ol} and δ are known. However, it was sometimes impossible to obtain a positive value for R_{SH} once I_{ol} and δ had been determined. This is a result of the inadequacies in the assumed two-exponential model. Figure IV.6 presents the I-V characteristic for SiM at 274°K where the linear slope through the origin is indicated and where the deviation from linearity with increasing voltage can be seen. Applying the method of least squares to the four or six lowest voltage points, the value of Λ and its variance were obtained as outlined in Appendix E.

In line with our earlier statements, the first exponential term in Eq. (IV-10) is expected to result from one or more of the mechanisms responsible for the non-ideal current term. Both I_{rg} and the inversion layer current exhibit an exponential dependence corresponding to A = 2 in the intermediate voltage region (i.e. $\lambda V_j/2 > 1$ and $V_j < \psi_D$). The exponential dependence for these two current contributions is therefore dependent upon temperature, whereas the exponential dependence of the tunneling current is approximately independent of temperature. Combining Eqs. (IV-15) and (IV-10) yields

$$I(V) = \Lambda V_j + I_{ol}(e^{\delta V_j} - \delta V_j - 1) + I_o(e^{\lambda V_j} - 1) \qquad \text{(IV-16)}$$

where as before $V_j = V - IR_s$.

The measured junction characteristic satisfies the condition that $V = V_j$, since the effect of the series resistance is not present. For a broad area junction device with two thick field free regions (i.e. the n- and p-type regions on either side of the junction) and a uniform junction, the true junction I-V characteristic is indeed measured using the light source technique described previously. As we mentioned in

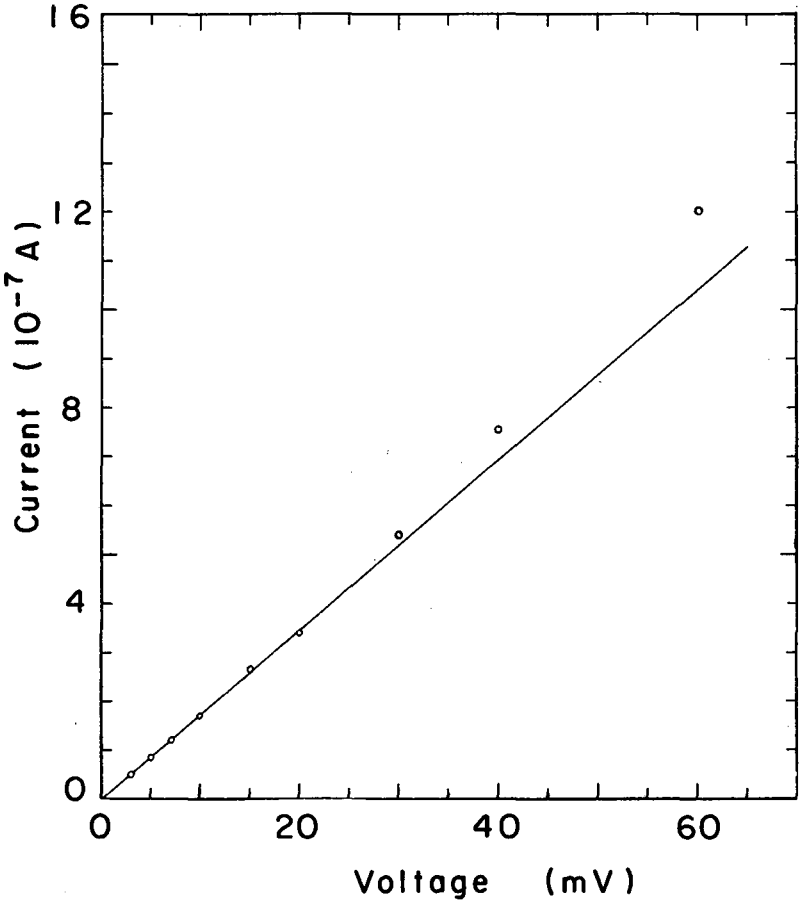

Fig. IV.6. The forward I-V characteristic in the low-voltage region for SiM at 274 °K.

Section IV.A, the solar cell junction was found to be non-uniform[58] so that the measured junction I-V characteristic is an effective one given by

$$I(V_j) = \int_{A_x} J(x,y;V_j)dxdy \qquad \text{(IV-17)}$$

where the integration is carried out over the cross-sectional area of the junction. For solar cell geometry the additional complication of a thin surface region arises. The surface region-junction boundary is not, in general, an equipotential surface so that the measured I-V characteristic, assuming the junction to be spatially uniform, is still an effective one given by

$$I(V_j) = \int_{A_x} J(V_j(x,y))dxdy \,. \qquad \text{(IV-18)}$$

The I-V characteristic measured for a solar cell under illumination is therefore the effective I-V characteristic of the surface region-junction combination which in the limit of low surface region series resistance (i.e., for low surface region resistivity or gridded electrical contacts) reduces to the effective I-V characteristic of the junction alone.

The current in the intermediate voltage region is low enough ($\lesssim 5X10^{-4}$ amps) so that the surface region-junction boundary is approximately an equipotential plane, and the measured I-V characteristic in this voltage range is essentially that of the junction. Returning to Eq. (IV-16), it can be seen that for $\delta V_j > 1$

$$[I(V_j) - \Lambda V_j] \simeq I_{o1}e^{\delta V_j} + I_o e^{\lambda V_j} \qquad \text{(IV-19)}$$

where the ideal term is not important until high voltages are attained. The voltage at which the ideal term makes a perceptible contribution to the I-V characteristic can be determined from the point at which a log plot of the quantity $[I(V_j) - \Lambda V_j]$ deviates from linearity. This effect

is shown in Fig. IV.7 for SiM at 274°K. The values of δ and I_{ol} were determined from plots of this type using those points which fall on a straight line in the voltage region where $(\delta V_j + 1) \lesssim 0.05 e^{\delta V_j}$. This last condition is satisfied as long as $\delta V_j \gtrsim 4.25$.

Having obtained the values of R_{SH}, I_{ol}, and δ as outlined in the preceding steps, it was then possible to compare the additional contribution to the current (the increase in current at high voltages) with the ideal diffusion term. For most of the cells tested this was accomplished by subtracting the non-ideal current term from the measured current. The I-V characteristic obtained in this way (results could only be obtained over a limited voltage range as shown in Fig. IV.7) was used to determine the constants I_o and λ_m of the ideal exponential term. For the case of the n-on-p Si solar cells the ideal contribution to the current was determined directly from the high voltage region of the measured I-V characteristic, and then this term was subtracted from the total in order to obtain the non-ideal contribution and the constants I_{ol} and δ. These values for I_{ol} and δ were in turn used to determine R_{SH} from the measured value of Λ.

1. <u>P-on-N Si Cells</u>. Diode and junction I-V characteristics were measured for $0.5cm^2$ (0.5cm by 1cm) and $2cm^2$ (1cm by 2cm) p-on-n Si solar cells. Initially the two cell sizes were chosen in the hope that the different surface-to-volume ratios might indicate the relative importance of the surface currents (both shunt conductance and inversion layer) to the I-V characteristic. The surface-to-volume ratios for these two size cells are

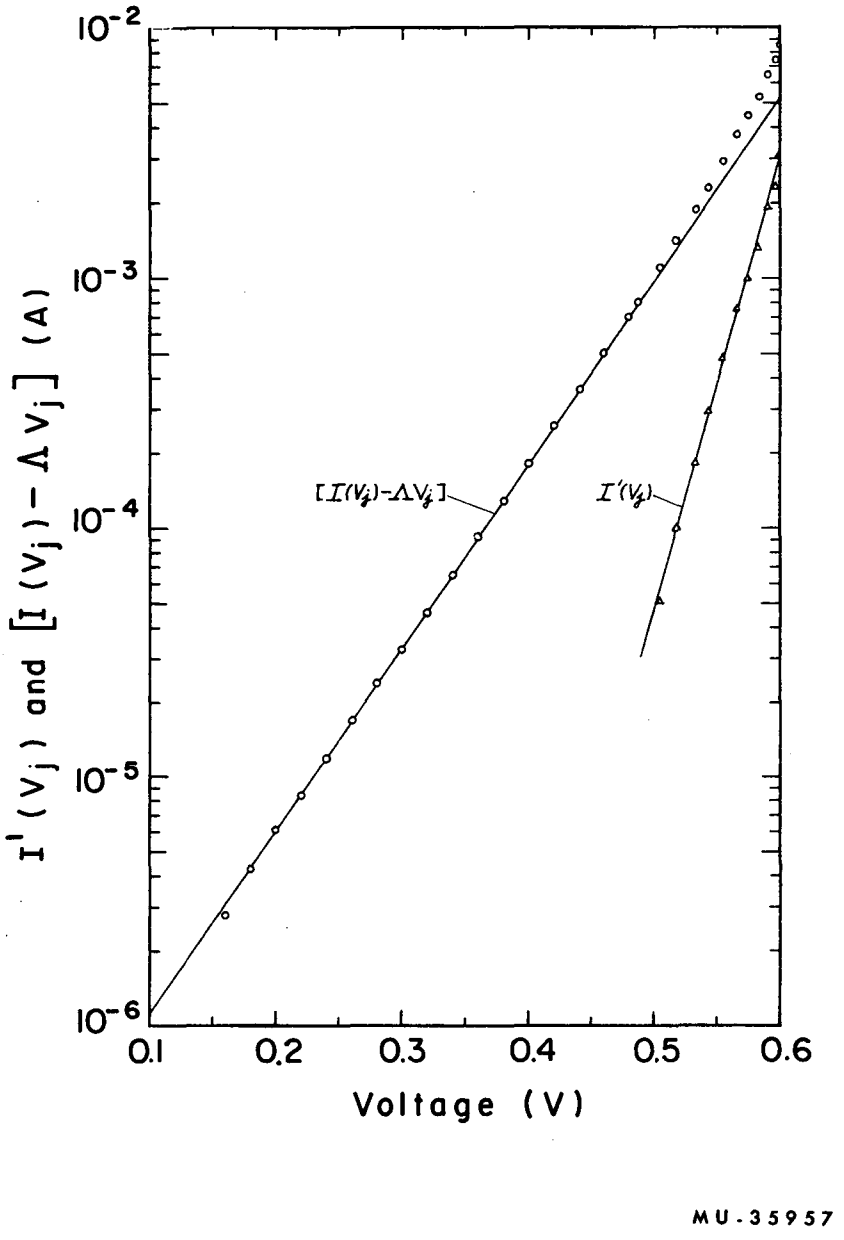

Fig. IV.7. The junction I-V characteristic in the intermediate and high-voltage regions for SiM at 274 °K.

$$\left(\frac{S}{V}\right)_{0.5cm^2} = 6 \text{ cm}^{-1}$$

and

$$\left(\frac{S}{V}\right)_{2cm^2} = 3 \text{ cm}^{-1}.$$

It was not possible to draw any conclusions in this regard, since the non-ideal current term was found to vary by more than a factor of two within each set of cells of a given size.

An attempt was made to minimize this variation in each group by giving some of the cells an edge etch prior to measurement of the I-V characteristic at ice bath. The effect of such an etching process proved to be minimal, and in fact for a number of the cells the current at a given voltage was found to increase as well as decrease in what appeared to be a random manner after consecutive etches. The cells which exhibited this type of behavior were then discarded, and the measured characteristics are not presented here. Results are reported for one cell of each type which showed a consistent current decrease after two consecutive etches. It can be seen from Table IV.I that the majority of cells were tested with only an ethyl alcohol and distilled water wash.

The calculational technique used to obtain the constants R_{SH}, I_{o1}, δ, I_o and λ_m was outlined above and sample plots presented for SiM at 274°K. A least squares fit was used to estimate the experimental error associated with the determination of these constants. The variance in the Λ was determined from Eqs. (E-9) and (E-16) of Appendix E. The variances in I_{o1} and δ were determined from Eqs. (E-9) and (E-10). It was then possible to determine the variance in R_{SH} using Eq. (E-2). The variances in I_o and λ_m were more difficult to ascertain since the I-V

characteristic to be fit with the ideal exponential form was obtained by subtracting the non-ideal current contributions from the measured junction I-V characteristic which resulted in a different variance for each data point. The variances in δ, I_{o1}, and R_{SH} are conveyed to these points through Eq. (E-17) where $I'_j(V_j)$ is the I-V characteristic to be fit with the ideal term $I_o(e^{\lambda V_j}-1)$. The variance of a given data point was determined from Eq. (E-18), and the variances in I_o and λ_m were determined from Eqs. (E-19) and (E-20). Representative experimental errors for each type of cell tested are presented in Table IV.IV.

The errors quoted in Table IV.IV for SiM are representative of the set of p-on-n Si cells tested with the exception of the ideal junction characteristic measurements where the error is less for the $2cm^2$ cells, since I_j/I'_j is smaller for these cells, Also for the junction characteristics measured using the clip-on milliameter, the error in the measured values of current is approximately ±2%. Although this increases the value of σ_{I_i}/I_i in Eq. (E-18) with a resulting increase in $\ln I'_i$, it will not result in a sizable increase in $\sigma_{\ln I_o}$ and σ_{λ_m}, as uncertainties in I_{o1} and δ produce the dominant contribution in Eq. (E-18). Applying this fitting technique to the I-V characteristics measured at the various test temperatures, the values of the fitting constants were obtained. The fit at the four temperatures for SiM are shown in Fig. IV.8 where it is seen that a reasonably good fit can be obtained at 364 °K and 274 °K, whereas a small deviation exists at 202 °K and the fit is relatively poor at 90 °K. The I-V characteristic measured at 90 °K is seen to exhibit a structure. Figure IV.9 presents the fit obtained for SilB at the four temperatures, and it is seen that the results are qualitatively the same as for SiM. In these figures the solid dots indicate the deviation of

Table IV.IV. Typical errors in the I-V characteristic fitting parameters for the three cell types

Cell	SiM		SiL (unetched)		GaAs A-22	
Fitting constants	T=274°K	Error (±%)	T=274°K	Error (±%)	T=357°K	Error (±%)
$A(10^{-6}A/V)$(a)	17.2	3.80	1.54	3.20	5.14	3.70
$R_{SH}(k\Omega)$	70.7	4.80	1.06×10^{3}	7.4	3.21×10^{2}	6.30
$\delta(V^{-1})$	17.0	0.35	20.3	1.30	15.6	0.48
$I_{o1}(A)$	2.04×10^{-7}	1.90	2.63×10^{-8}	9.5	1.29×10^{-7}	2.70
$\lambda_m(V^{-1})$	41.2	4.0	45.7	5.0	28.6	8.9
$\log I_o$	-13.265	3.0	-13.216	4.3	-11.464	7.0
$R_s(\Omega)$ (b)	1.80	10.0	1.00	8.0	1.16	8.0

(a) In some cases this error is larger owing to a poor signal-to-noise ratio.

(b) Total error including all uncertainties

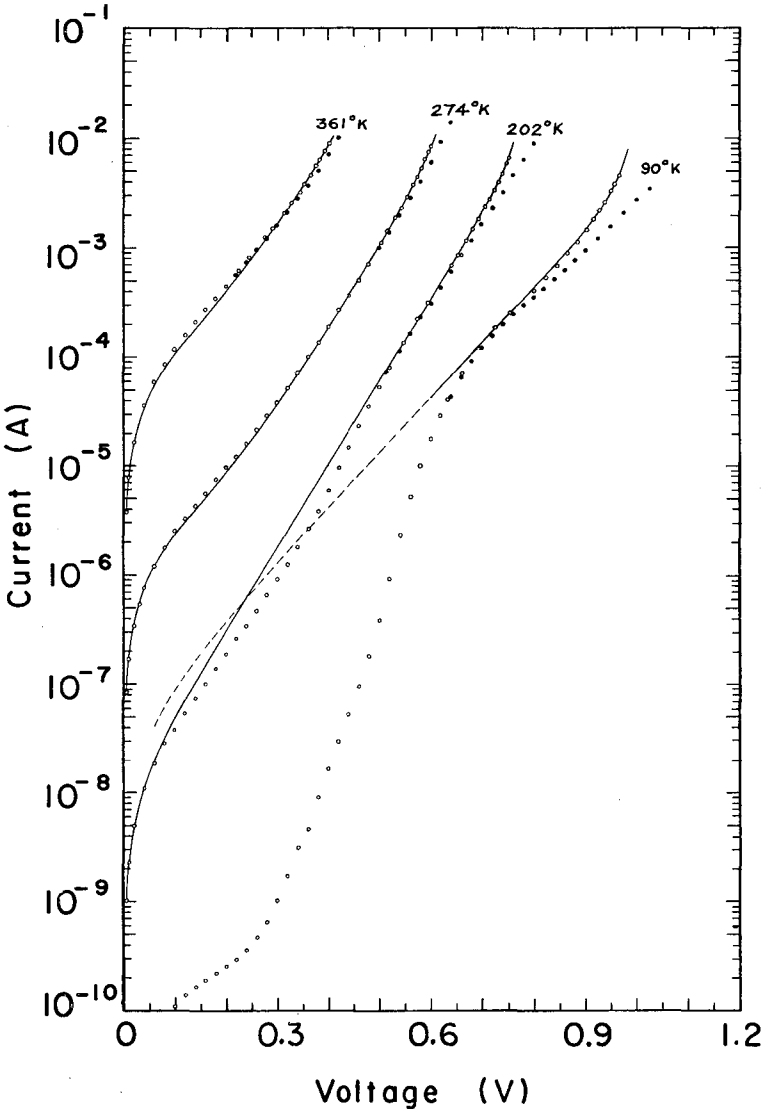

Fig. IV.8. The diode and junction I-V characteristics for SiM.

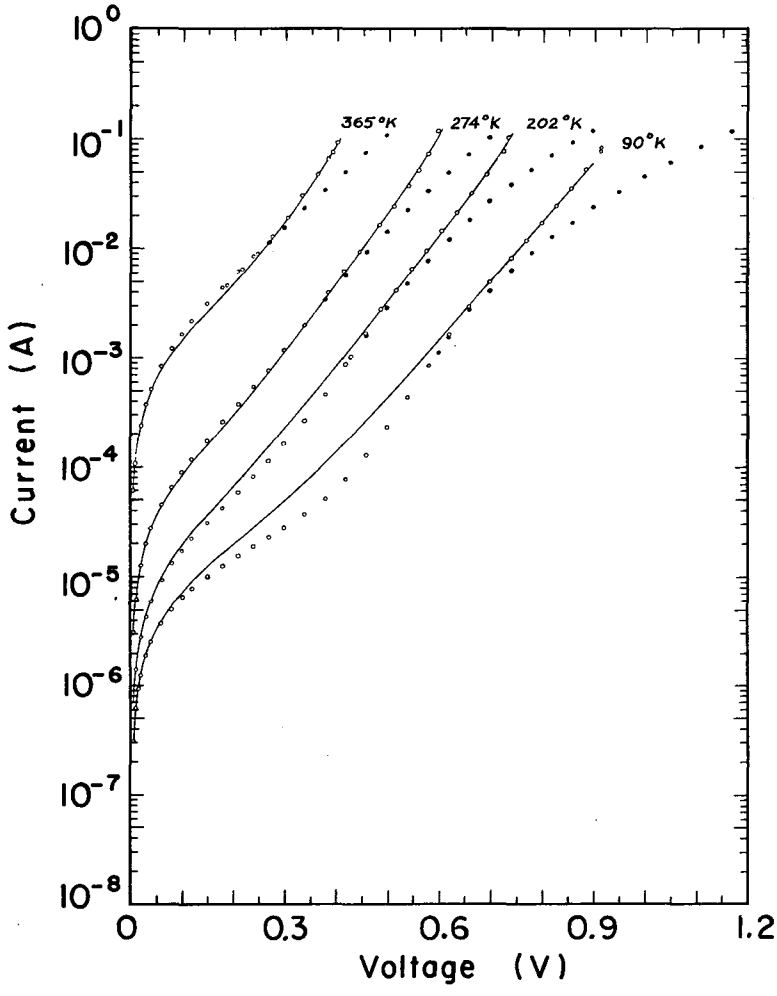

Fig. IV.9. The diode and junction I-V characteristics for SilB.

diode characteristic from the junction characteristic. The values of R_{SH}, I_{o1}, δ, I_o, and λ_m used to fit the measured I-V characteristics are listed in Table IV.V for both sizes of the p-on-n Si solar cell.

The results show that it was impossible to fit the set of I-V characteristics for each cell using a constant value for A which we would expect for a current contribution controlled by the process of electron-hole pair recombination (this includes the high and low injection level diffusion currents, the junction recombination-generation current, and the inversion layer current). The factor $\delta=\lambda/A$ is however relatively insensitive to temperature which is the characteristic behavior of the tunneling current. At the lower test temperatures the low voltage portion of the I-V characteristics appears to be controlled by a mechanism which is a much stronger function of voltage than at the higher test temperatures. The structure in the I-V characteristic for SiM at 90°K (that is, the inflective nature of the curve) is consistent with a tunneling current controlled non-ideal current term. The tunneling current term for a single intermediary energy state (i.e. one dominant type of impurity center) increases with increasing applied bias through the barrier penetration probability given by the exponential term in Eq. (IV-8) until the tunneling process no longer corresponds to conservation of energy. Referring to Fig. A.2(b) this situation corresponds to the case of $E_{fp} < E$ of impurity center B. The current then levels out or decreases depending upon the distribution of the other impurity energy levels in the forbidden gap and the magnitude of the other current terms contributing to the I-V characteristic. For the specific I-V characteristic under consideration (that of SiM at 90°K), the current increases at a more rapid rate once again as the ideal diffusion current term comes into play.

Table IV.V. I-V characteristic fitting parameters for the p-on-n and n-on-p silicon and p-on-n gallium arsenide solar cells.

Cell	Temp (°K)	$\lambda=q/kT$ (V^{-1})	I_{o1} (A)	δ (V^{-1})	A	I_o (A)	λ_m (V^{-1})	R_{SH} (KΩ)
Si M	90	129	4.00×10^{-8}	11.6	11.1	5.39×10^{-25}	51.4	--
	202	57.5	9.47×10^{-9}	17.5	3.29	6.80×10^{-23}	59.7	3.17×10^{3}
	274	42.4	2.04×10^{-7}	17.0	2.49	5.44×10^{-14}	41.2	7.07×10
	361	32.2	1.26×10^{-5}	15.8	2.03	7.03×10^{-10}	36.2	1.73
Si 51CB	201	57.7	2.53×10^{-8}	16.2	3.57	1.09×10^{-20}	53.0	5.32×10^{2}
	274	42.4	5.15×10^{-7}	15.2	2.78	5.48×10^{-14}	41.2	3.92×10
	357	32.5	2.00×10^{-5}	14.9	2.19	2.69×10^{-10}	37.2	1.48
Si N	92	126	3.95×10^{-7}	8.59	14.7	7.82×10^{-29}	60.0	--
	206	56.3	6.10×10^{-8}	14.3	3.94	8.70×10^{-22}	57.1	--
	274	42.4	5.04×10^{-8}	19.0	2.23	3.91×10^{-15}	46.0	4.03×10^{2}
	361	32.2	3.90×10^{-6}	17.8	1.81	1.66×10^{-8}	32.6	4.24
Si 3A	204	56.9	2.82×10^{-8}	15.9	3.58	9.79×10^{-22}	56.2	6.66×10^{2}
	274	42.4	2.65×10^{-7}	16.5	2.57	7.71×10^{-15}	44.0	7.95×10
	362	32.1	1.18×10^{-5}	15.8	2.03	6.83×10^{-9}	32.2	2.42
Si 3A etch	92	126	5.35×10^{-8}	11.1	11.4	1.33×10^{-31}	67.1	--
	204	56.9	2.23×10^{-9}	18.7	3.04	4.28×10^{-22}	57.6	--
	274	42.4	4.32×10^{-8}	19.1	2.22	2.03×10^{-14}	42.2	5.73×10^{2}
	362	32.1	3.68×10^{-6}	18.7	1.72	5.41×10^{-9}	32.0	6.14
Si 1B	90	129	8.10×10^{-7}	12.5	10.4	--	--	1.87×10^{10}
	202	57.5	3.16×10^{-6}	13.9	4.14	1.05×10^{-20}	56.9	1.03×10^{10}
	274	42.4	1.03×10^{-5}	15.2	2.79	1.41×10^{-13}	41.9	2.14
	365	31.8	1.23×10^{-4}	15.8	2.01	3.40×10^{-8}	31.9	1.02×10^{-1}
Si 1D	89	130	1.90×10^{-6}	10.1	12.9	1.44×10^{-27}	60.0	--
	202	57.5	1.67×10^{-6}	13.1	4.40	3.15×10^{-22}	60.0	--
	273	42.5	1.69×10^{-5}	12.7	3.34	2.38×10^{-14}	46.1	9.01
	365	31.8	6.30×10^{-5}	16.0	1.99	2.79×10^{-8}	32.0	3.97×10^{-1}
Si L	202	57.5	4.77×10^{-10}	19.6	2.93	1.47×10^{-20}	55.7	1.03×10^{5}
	274[a]	42.2	2.63×10^{-8}	20.3	2.09	6.09×10^{-14}	45.7	1.06×10^{3}
	360	32.2	3.07×10^{-6}	22.4	1.44	3.15×10^{-8}	35.1	1.12×10
Si L etch	202[a]	57.5	2.02×10^{-10}	22.3	2.58	5.57×10^{-21}	56.8	--
	274[a]	42.4	1.85×10^{-8}	21.5	1.97	2.32×10^{-13}	42.4	2.92×10^{3}
	360[a]	32.2	3.07×10^{-6}	22.3	1.45	2.86×10^{-8}	35.3	9.76
Si F	202	57.5	9.48×10^{-9}	16.8	3.43	--	--	1.61×10^{4}
	273[a]	42.5	1.55×10^{-7}	17.3	2.46	1.84×10^{-13}	43.7	1.94×10^{2}
	356[a]	32.6	9.10×10^{-6}	16.3	2.00	1.24×10^{-7}	32.6	5.39
GaAs A-20	204	56.9	1.03×10^{-4}	3.41	16.7	1.46×10^{-28}	55.5	--
	273	42.5	5.59×10^{-7}	6.14	6.92	5.52×10^{-20}	43.0	--
	365	31.8	3.40×10^{-6}	10.5	3.04	2.12×10^{-12}	30.8	--
GaAs A-22	202	57.5	1.26×10^{-13}	22.6	2.54	1.21×10^{-29}	54.7	3.89×10^{5}
	274	42.4	6.35×10^{-11}	20.3	2.09	7.33×10^{-21}	42.5	2.35×10^{4}
	357	32.5	1.29×10^{-7}	15.6	2.08	3.44×10^{-12}	28.6	3.21×10^{2}

a. Runs for which I_o and λ_m were determined directly.

The diffusion reverse saturation current was calculated from a modified form of Eq. (IV-2) using material properties typical of those encountered in a p-on-n Si solar cell. Equation (IV-2) was corrected to account for the thin surface region of a solar cell with the result that the diffusion reverse saturation current is given by (see Appendix A)

$$I_o = qA_x n_{po}\left(\frac{D_n}{L_n}\right)\frac{\left[\gamma_n \sinh\left(\frac{t}{L_n}\right)+\cosh\left(\frac{t}{L_n}\right)\right]}{\left[\gamma_n \cosh\left(\frac{t}{L_n}\right)+\sinh\left(\frac{t}{L_n}\right)\right]} + qA_x p_{no}\left(\frac{D_p}{L_p}\right). \qquad \text{(IV-20)}$$

The material properties used in the calculation are listed in Table IV.VI. The measured and calculated values of the diffusion reverse saturation current are compared in Fig. IV.10 for the $0.5cm^2$ cells and in Fig. IV.11 for the $2cm^2$ cells. The magnitude and temperature dependence are seen to be in good agreement for both cell sizes. In addition the values of λ_m are compared with $\lambda = q/kT$ in Figs. IV.12 and IV.13 for the two cell sizes. Again the agreement is seen to be good at all temperatures except liquid nitrogen where the measured points fall quite close to the curve for A = 2. This is in agreement with the prediction of Sah, Noyce, and Shockley[53] for the high injection level condition of a diode (see Appendix A) where the current is given by

$$I_d = q2^{3/2}\left(\frac{D_n+D_p}{L_o}\right)A_x n_i \exp(\lambda V_j/2), \qquad \text{(IV-21)}$$

where $L_o^{-2} = (D_n^{-1} + D_p^{-1})/(\tau_{po} + \tau_{no})$. The constant in Eq.(IV-21) was calculated using $L_o = 1.01\text{X}10^{-3}cm$ and $n_i = 8.88\text{X}10^{-15}cm^{-3}$ in addition to the same set of material properties employed in the calculation of I_o for these cells (see Table IV.VI). The calculated values and the experimental results are tabulated below, and the agreement is seen to be relatively good in view of the rather large experimental errors.

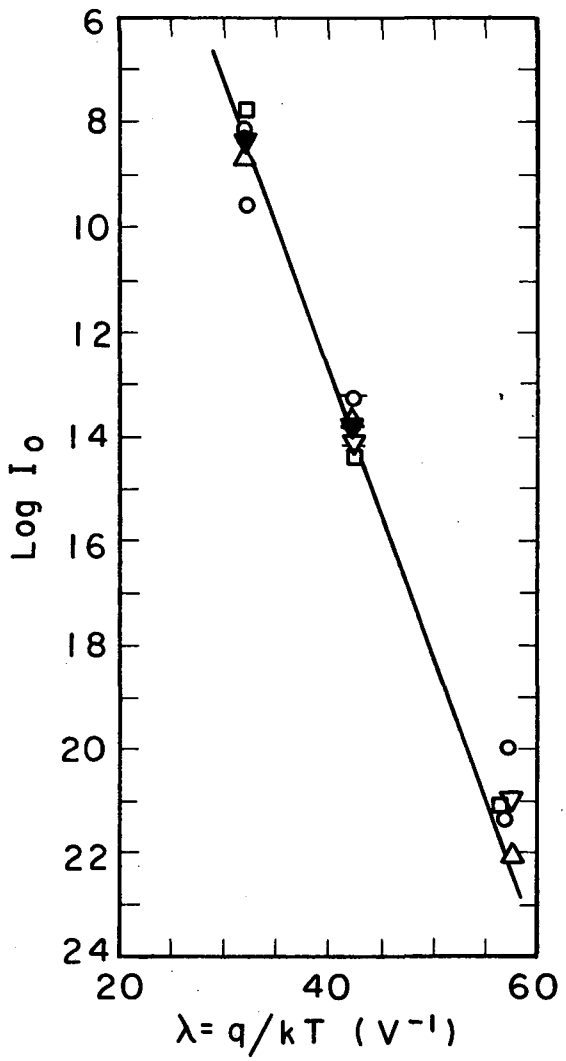

Fig. IV.10. The diffusion reverse saturation current for the 0.5-cm^2 p-on-n Si solar cells.

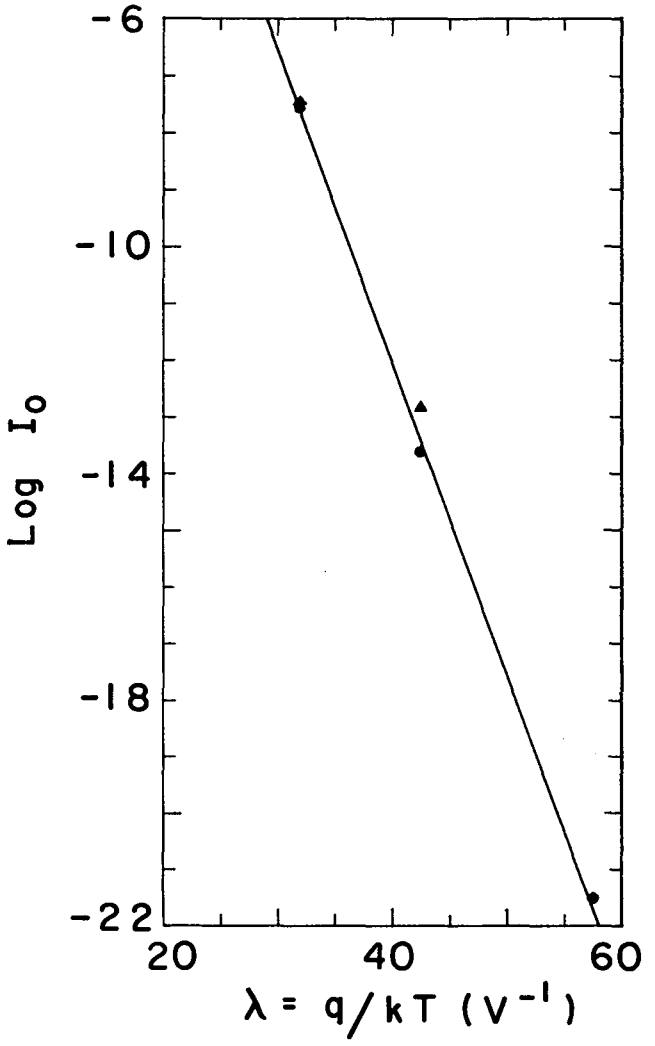

Fig. IV.11. The diffusion reverse saturation current for the 2-cm^2 p-on-n Si solar cells.

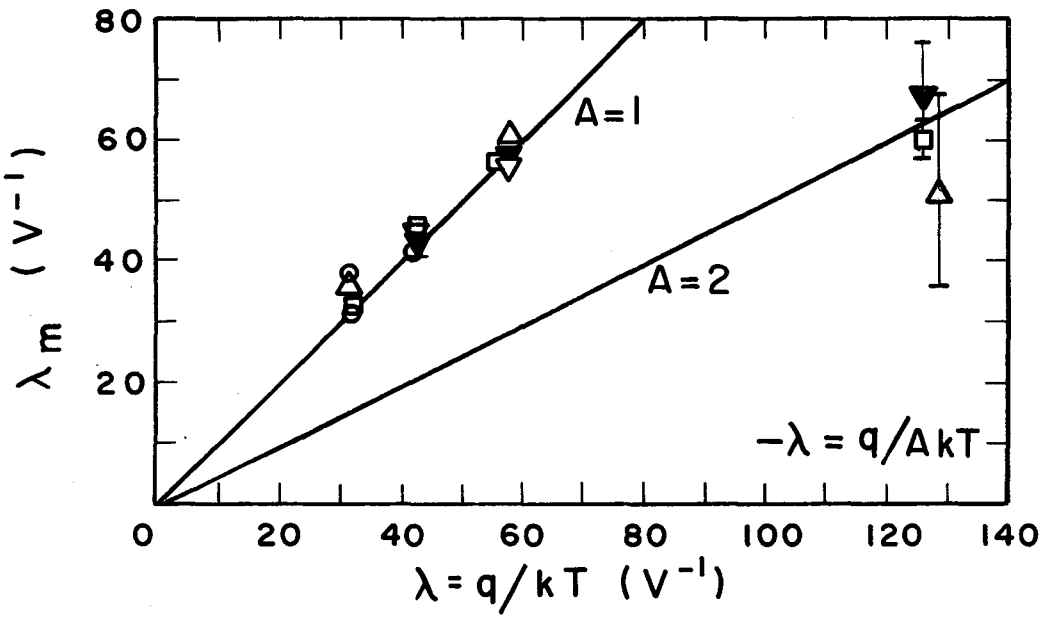

MU-35831

Fig. IV.12. The ideal exponential factor, λ_m, for the 0.5-cm^2 p-on-n Si solar cells.

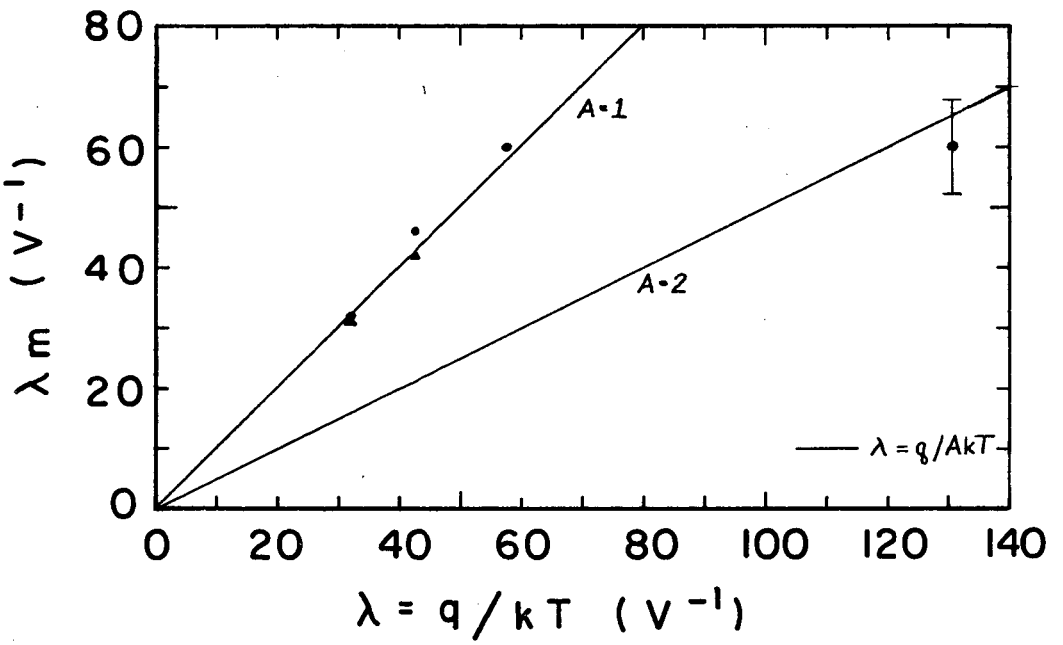

MU-35959

Fig. IV.13. The ideal exponential factor, λ_m, for the 2-cm^2 p-on-n Si solar cells.

Table IV.VI. Diffusion reverse saturation current and typical material properties for p-on-n and n-on-p silicon solar cells.

Cell type	p-on-n				n-on-p			
T(°K)	200	250	300	350	200	250	300	350
t(cm)	2.00×10^{-4}	2.00×10^{-4}	2.00×10^{-4}	2.00×10^{-4}	2.00×10^{-4}	2.00×10^{-4}	2.00×10^{-4}	2.00×10^{-4}
$N_D(cm^{-3})$	1.00×10^{16}	1.00×10^{16}	1.00×10^{16}	1.00×10^{16}	1.50×10^{17}	1.50×10^{17}	1.50×10^{17}	1.50×10^{17}
$n_n(cm^{-3})$	9.84×10^{15}	9.84×10^{15}	1.00×10^{16}	1.00×10^{16}	1.50×10^{17}	1.50×10^{17}	1.50×10^{17}	1.50×10^{17}
$p_{no}(cm^{-3})$	1.23×10^{-7}	2.43×10^{-1}	4.40×10^{3}	5.44×10^{6}	1.21×10^{-8}	2.39×10^{-2}	4.40×10^{2}	5.44×10^{5}
τ_p (sec)	1.00×10^{-6}	1.00×10^{-6}	1.00×10^{-6}	1.00×10^{-6}	5.00×10^{-8}	5.00×10^{-8}	5.00×10^{-8}	5.00×10^{-8}
$D_p(cm^2/sec)$	4.57	5.10	5.95	5.86	2.73	3.44	3.88	4.15
L_p(cm)	2.14×10^{-3}	2.26×10^{-3}	2.44×10^{-3}	2.42×10^{-3}	3.70×10^{-4}	4.15×10^{-4}	4.40×10^{-4}	4.55×10^{-4}
$N_A(cm^{-3})$	4.44×10^{17}	4.44×10^{17}	4.44×10^{17}	4.44×10^{17}	2.01×10^{16}	2.01×10^{16}	2.01×10^{16}	2.01×10^{16}
$p_p(cm^{-3})$	3.19×10^{17}	3.72×10^{17}	4.00×10^{17}	4.14×10^{17}	1.97×10^{16}	1.99×10^{16}	2.00×10^{16}	2.01×10^{16}
$n_{po}(cm^{-3})$	3.78×10^{-9}	6.42×10^{-3}	1.10×10^{2}	1.31×10^{5}	6.14×10^{-8}	1.20×10^{-1}	2.20×10^{3}	2.73×10^{6}
τ_n (sec)	5.00×10^{-8}	5.00×10^{-8}	5.00×10^{-8}	5.00×10^{-8}	1.00×10^{-6}	1.00×10^{-6}	1.00×10^{-6}	1.00×10^{-6}
$D_n(cm^2/sec)$	4.78	6.33	7.80	8.94	1.00x10	1.47x10	1.63x10	1.66x10
L_n(cm)	4.89×10^{-4}	5.64×10^{-4}	6.24×10^{-4}	6.70×10^{-4}	3.22×10^{-3}	3.83×10^{-3}	4.04×10^{-3}	4.08×10^{-3}
s(cm/sec)	5.00×10^{3}	5.00×10^{3}	5.00×10^{3}	5.00×10^{3}	5.00×10^{3}	5.00×10^{3}	5.00×10^{3}	5.00×10^{3}
$J_o(amp\,cm^{-2})$	4.65×10^{-23}	9.59×10^{-17}	1.86×10^{-12}	2.28×10^{-9}	4.42×10^{-23}	1.00×10^{-16}	1.92×10^{-12}	2.41×10^{-9}

N_D, N_A, n_n, p_p — obtained from the assumed room-temperature values of n_n and p_p.

p_{no}, n_{po} — obtained from the values of n_n and p_p and the temperature dependence of n_i^2 [F. J. Morin and J. P. Maita, Phys. Rev. 96, 28 (1954)].

τ_p, τ_n — assumed values.

D_p, D_n — determined from the room-temperature values for mobility [M. B. Prince, Phys. Rev. 93, 1204 (1954)], the measured temperature dependence of the lattice scattering mobility [G. W. Ludwig and R. L. Watters, Phys. Rev. 101, 1699 (1956)], and the theoretically predicted temperature dependence of the ionized impurity scattering mobility [E. Conwell and V. F. Weisskopf, Phys. Rev. 77, 388 (1950)].

s_n, s_p — assumed values.

Cell	log I_o, calculated	log I_o, measured
Si1D	-28.488	-26.84 ± 3.19
SiM	-29.100	-24.27 ± 6.47
SiN	-29.100	-28.11 ± 1.28
Si3A	-29.100	-30.88 ± 3.76

The parameters δ and I_{ol} for the non-ideal exponential term are presented in Figs. IV.14 and IV.15 in the form of ratios to their ice bath values. Figure IV.14 shows $\delta(T)/\delta(273\,^{\circ}K)$ for both large and small cells where the solid line corresponds to $\delta=\lambda/2$ as is expected for inversion layer and junction recombination-generation currents over the intermediate voltage region. The results are seen to exhibit a nearly temperature independent behavior with $\delta(T)$ for the individual cells showing both slight increases and decreases with increasing temperature. The results are in better agreement with the temperature dependence expected of tunneling currents. Figure IV.15 presents the results obtained for the ratio $[I_{ol}(T)/I_{ol}(273\,^{\circ}K)]$ where the curve represents the current ratio calculated for the non-ideal term consisting entirely of the I_{rg}. The current due to recombination of electron-hole pairs in the junction is given by Eq. (IV-6) with

$$n_i = \sqrt{N_v N_c}\, e^{-\frac{E_g}{2kT}} = 2\left(\frac{2\pi m_e k}{h^2}\right)^{\frac{3}{2}} T^{\frac{3}{2}} \exp\left(-\frac{E_g}{2kT}\right). \qquad \text{(IV-22)}$$

In the intermediate voltage region, Eq. (IV-6) becomes

$$I_{rg} \approx CT^{5/2} e^{-\frac{E_g}{2kT}} \exp\left(\frac{\lambda V_j}{2}\right) = I_{ol,rg} \exp\left(\frac{\lambda V_j}{2}\right) \qquad \text{(IV-23)}$$

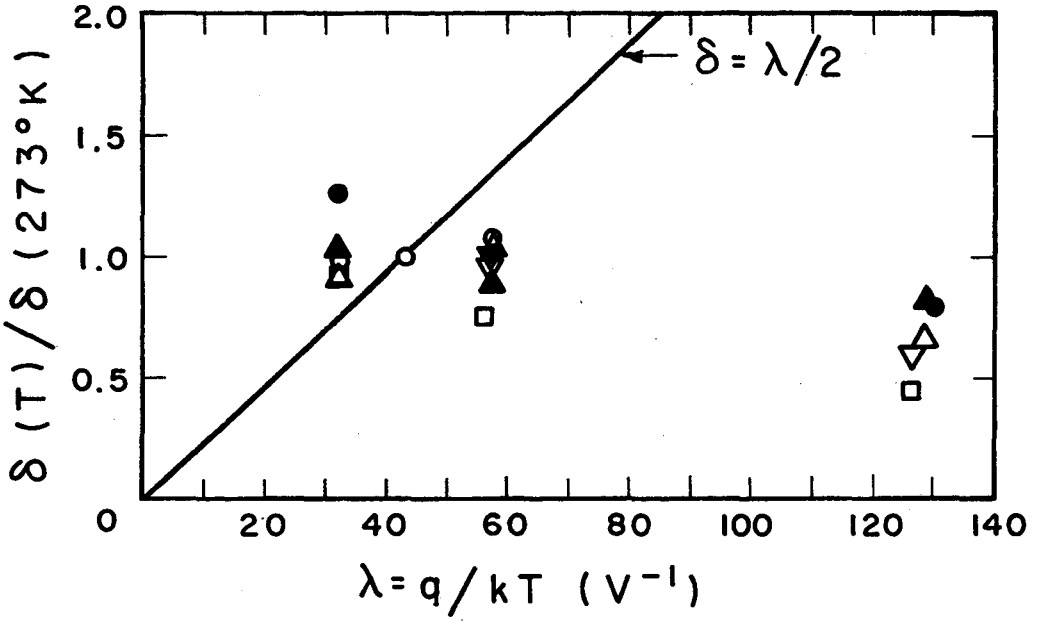

MU-35832

Fig. IV.14. $\delta(T)/\delta(273\,^{\circ}K)$ for both sets of p-on-n Si solar cells.

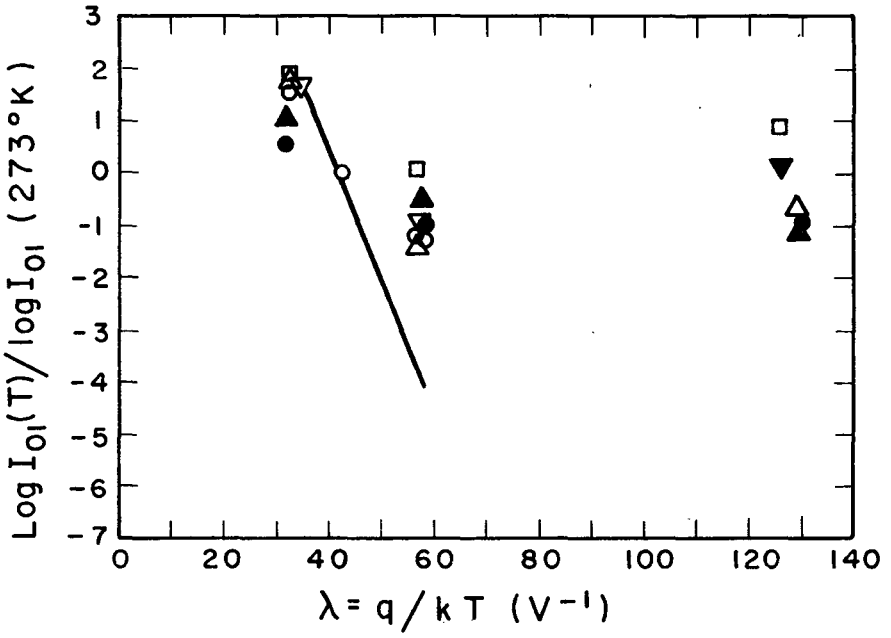

MU-35838

Fig. IV.15. Log $[I_{01}(T)/I_{01}(273\,°K)]$ for both sets of p-on-n Si solar cells.

where

$$C = \frac{2A_x\left(\frac{2\pi mk}{h^2}\right)^{3/2} kW(V_j)}{\sqrt{\tau_{po}\tau_{no}}(\psi_D - V_j)} f(b), \qquad \text{(IV-24)}$$

and all the terms in C are relatively insensitive to temperature. Therefore the effective reverse saturation current ratio is given by

$$\frac{I_{rg}(T)}{I_{rg}(T_{IB})} = \left(\frac{T}{T_{IB}}\right)^{5/2} \exp\left(\frac{E_g}{2k}[T^{-1} - T_{IB}^{-1}]\right). \qquad \text{(IV-25)}$$

It can be seen that the experimentally measured points deviate substantially from the calculated curve. It is quite evident from Figs. IV.14 and IV.15 that the edge etch was not able to produce a non-ideal I-V characteristic which closely approximated either that for a surface layer current or a junction recombination-generation current. Table IV.V shows that the magnitude of δ and I_{ol} do however change subsequent to the etch for Si3A with I_{ol} decreasing by about a factor of five and δ increasing by approximately 15%. As far as the results for this one cell can be interpreted as being representative of the set, it is evident that the non-ideal current term is related in some degree to the surface state of the device. The temperature dependence of δ, the structure in the low temperature I-V characteristics, and the changes subsequent to etching indicate that the dominant contribution to the non-ideal current term is a tunneling current which, apparently, is at least partially controlled by the surface state of the device.

2. <u>N-on-P Si Cells</u>. It was found that in a number of the test runs for the n-on-p cells the magnitude of the non-ideal current term was much less than the ideal current term. This made it possible to directly fit the high voltage region of the measured I-V characteristic with the

ideal exponential relation. Therefore the errors associated with the determination of λ_m and I_o for these n-on-p test cells were much less than those associated with the fitting technique used for the p-on-n Si solar cells (i.e., fitting the difference between the measured current and the non-ideal exponential current with the ideal exponential relationship). Typical errors associated with such a fitting process are listed in Table IV.IV for SiL (unetched) at 274°K. The non-ideal term of the I-V characteristic was then obtained by subtracting the ideal current from the measured characteristic. After correcting for the slope through the origin as in Eq. (IV-17), the method of least squares was used to find I_{ol} and δ. For the case of SiL at 274°K the errors listed in Table IV.IV are seen to be quite close to those for the p-on-n Si cells. Figure IV.16 shows the fit obtained for SiL at 202, 274, and 360°K. These fitted I-V characteristics are seen to deviate only slightly from the measured points but still enough to show a weak structure which becomes more pronounced as the temperature decreases.

In Fig. IV.17 a comparison is made between $\delta=\lambda/2$ and the values obtained from the measured characteristics for the two n-on-p Si cells. As for the p-on-n cells the experimental results show that the exponential factor, δ, is only slightly temperature dependent. The experimentally determined ratio of the effective reverse saturation current, $I_{ol}(T)/I_{ol}$ (273°K), is compared in Fig. IV.18 with that for I_{rg} as calculated from Eq. (IV-25). The agreement is good at the higher temperatures, but a substantial deviation was found to exist at 202°K. Despite the agreement at high temperature, it is highly improbable that I_{rg} is the dominant contribution to the non-ideal term in light of the discrepancy in the observed temperature dependence of δ.

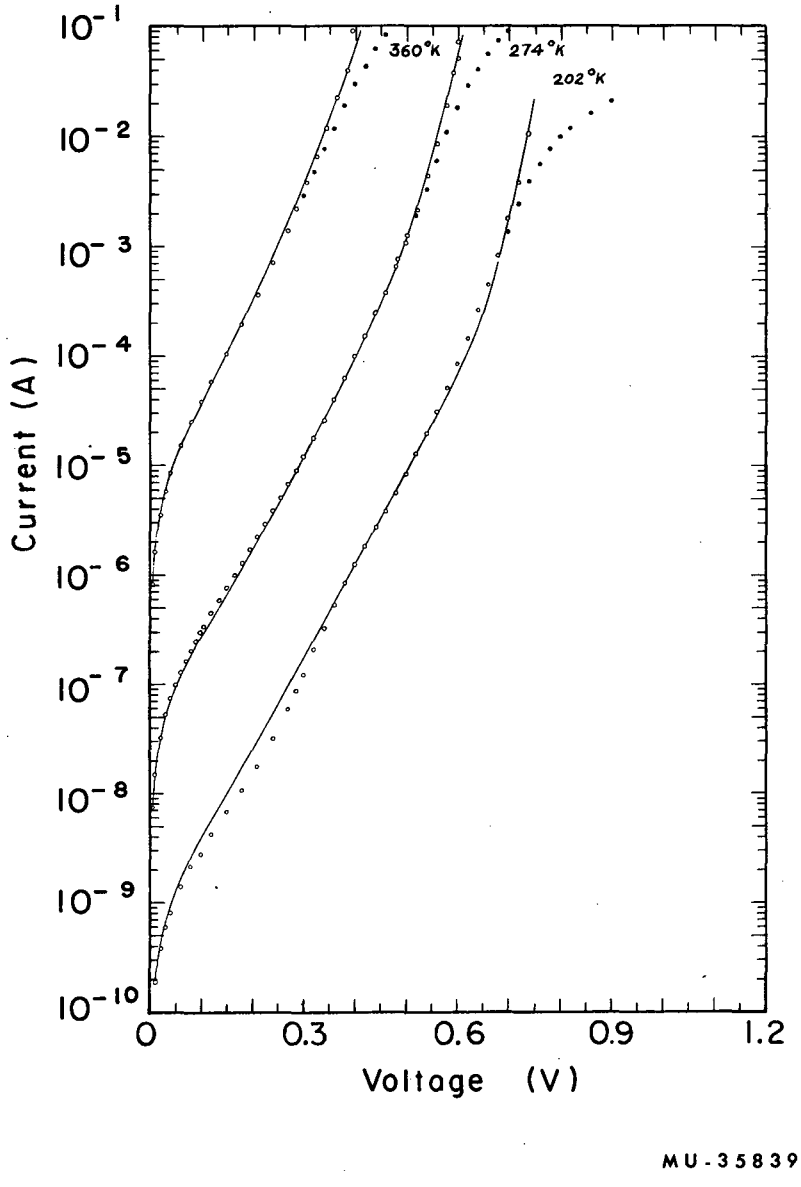

Fig. IV.16. The diode and junction I-V characteristics for SiL.

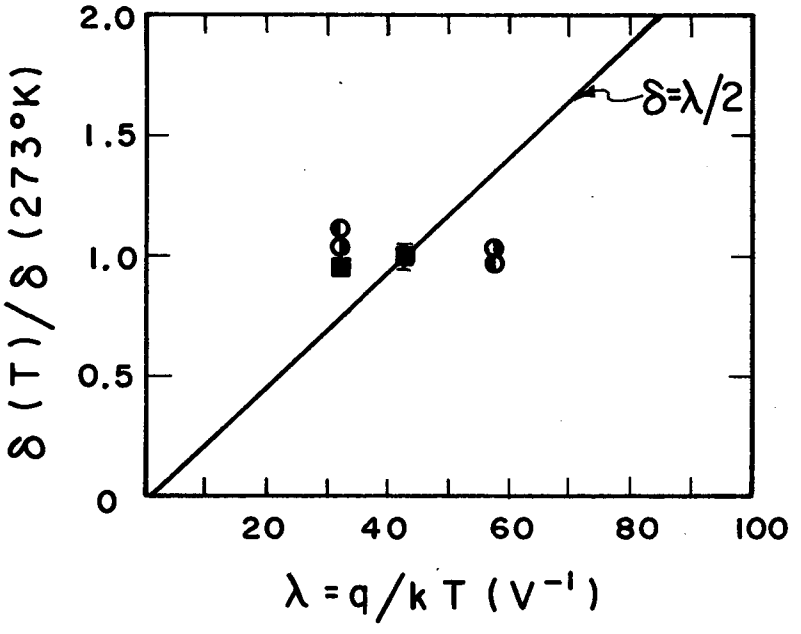

MU-35833

Fig. IV.17. $\delta(T)/\delta(273°K)$ for the n-on-p Si solar cells.

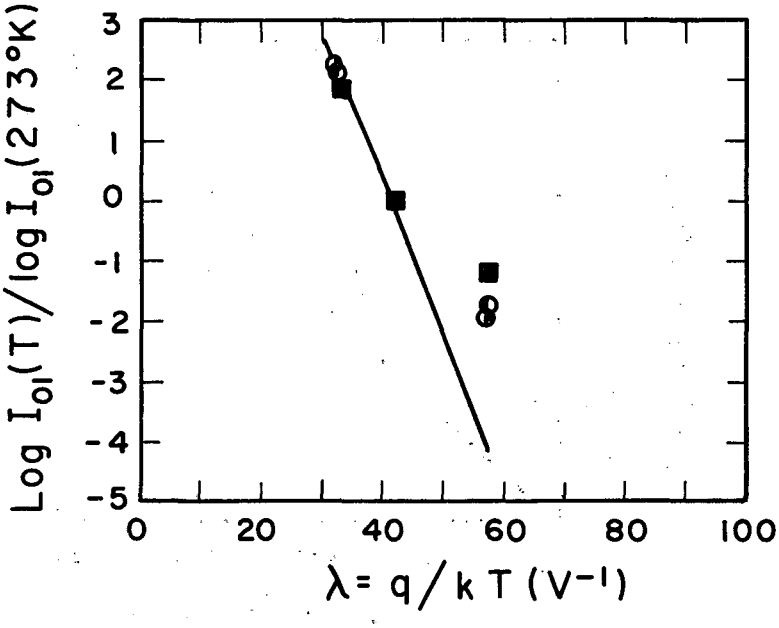

Fig. IV.18. Log $[I_{01}(T)/I_{01}(273°K)]$ for the n-on-p Si solar cells.

The values of R_{SH}, I_{o1}, δ, I_o and λ_m used to fit the I-V characteristics for the n-on-p Si cells are listed in Table IV.V. It is evident from Figs. IV.17 and IV.18 and Table IV.V that the edge etch on SiL had little effect upon either the magnitude or temperature dependence of I_{o1} and δ.

The diffusion reverse saturation currents obtained from the measured characteristics for both cells are compared in Fig. IV.19 with the current calculated from Eq. (IV-20) (indicated by the solid curve) and the agreement is seen to be relatively good. The material properties used for the calculation are listed in Table IV.VI. The exponential factor λ_m is compared with $\lambda=q/kT$ in Fig. IV.20, and the agreement here is quite good.

3. P-on-N GaAs Cells. The three terms of the I-V characteristics measured for the GaAs cells were determined in the same manner as for the p-on-n Si cells. The errors encountered are of the same order of magnitude as those existing for the p-on-n Si cells and are listed in Table IV.IV for GaAs A-22 at 357°K.

The material properties typical of the GaAs solar cells used in this study are not as well known as those for the Si cells, and as a result the magnitude of the measured diffusion reverse saturation currents was not directly compared with theoretical calculations based upon Eq. (IV-20). As an alternative the temperature dependence of I_o was compared with that predicted by Eq. (IV-2) using $n_{po} = n_i^2/N_A$, $p_{no} = n_i^2/N_D$, $D_{n,p} = (kT/q)\mu_{e,h}$ and $n_i^2 = N_c N_v \exp(-E_g/kT) = aT^3 \exp(-E_g/kT)$. Also making use of the carrier mobility temperature dependence for GaAs; that is, $\mu_e \alpha T^{-1}$ and $\mu_h \alpha T^{-2.1}$,[32] Eq. (IV-2) becomes

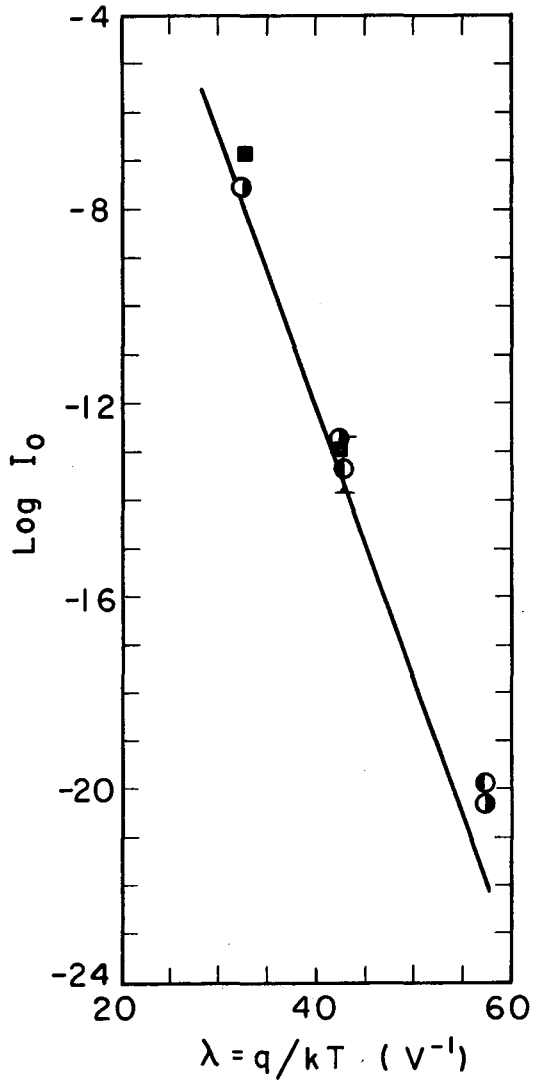

Fig. IV.19. The diffusion reverse saturation current for the n-on-p Si solar cells.

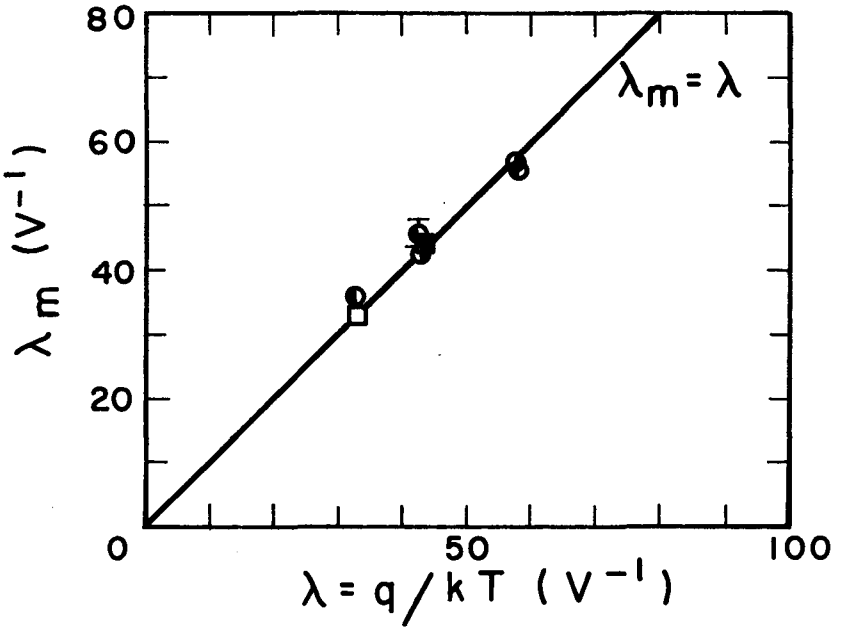

Fig. IV.20. The ideal exponential factor, λ_m, for the n-on-p Si solar cells.

$$I_o \simeq CT^3 \exp(-\frac{E_g}{kT}), \qquad \text{(IV-26)}$$

and the ratio of the diffusion reverse saturation current at temperature T to that at ice bath is

$$\frac{I_o(T)}{I_o(273\,°K)} = (\frac{T}{273\,°K})^3 \exp[\lambda(273\,°K)E_g(273\,°K)-\lambda(T)E_g(T)]\,. \qquad \text{(IV-27)}$$

A linear temperature dependence was assumed for the forbidden energy gap using the experimentally measured values of $E_g(300\,°K) = 1.40$ eV and $E_g(90\,°K) = 1.47$ eV.[32] A linear extrapolation was made using this data to find E_g at 350 and 400 °K. In Fig. IV.21 the measured ideal exponential factor, λ_m, is compared with $\lambda=q/kT$ (indicated by the solid curve) and the agreement is seen to be good. The temperature dependence of the reverse saturation current as given by Eq. (IV-27) (the solid curve in Fig. IV.22) and the measured values are seen to be in relatively good agreement.

In Fig. IV.23 the ratio $\delta(T)/\delta(273\,°K)$ for the two cells tested is compared with that for $\delta=\lambda/2$. The results for GaAs A-20 show no resemblance to the theoretical curve and in fact show a marked deviation from the results of all the other cells tested. This behavior may possibly arise from the presence of some form of shunt conductance current path which could not be treated properly with a simple shunt conductance. Further application of the edge etch technique described in Section IV.B might have brought about a similarity in the I-V characteristics for this cell and those of GaAs A-22. The results for GaAs A-22 are seen to be in good agreement with the theoretical curve above 274°K but show a deviation at 200 °K. The non-ideal effective reverse saturation current ratio is presented in Fig. IV.24 where the results for gaAs A-22 also agree well with the theoretical curve above

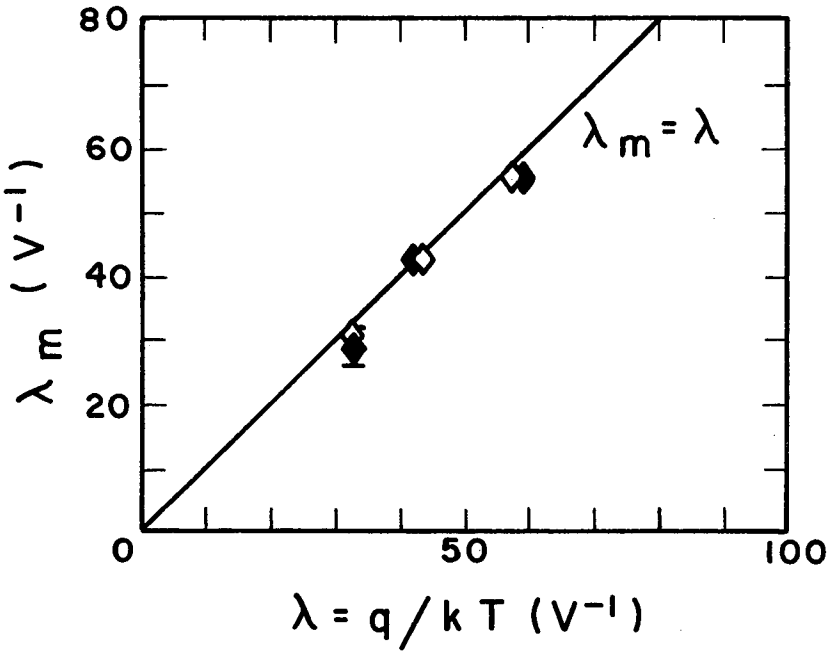

Fig. IV.21. The ideal exponential factor, λ_m, for the p-on-n GaAs solar cells.

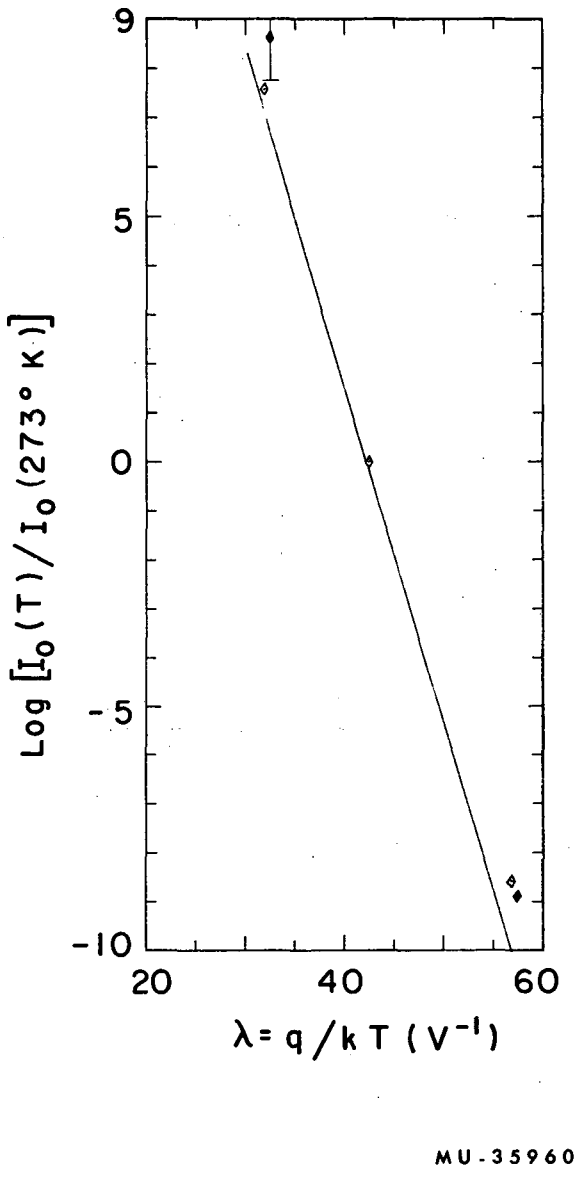

Fig. IV.22. Log $[I_o(T)/I_o(273\,°K)]$ for the p-on-n GaAs solar cells.

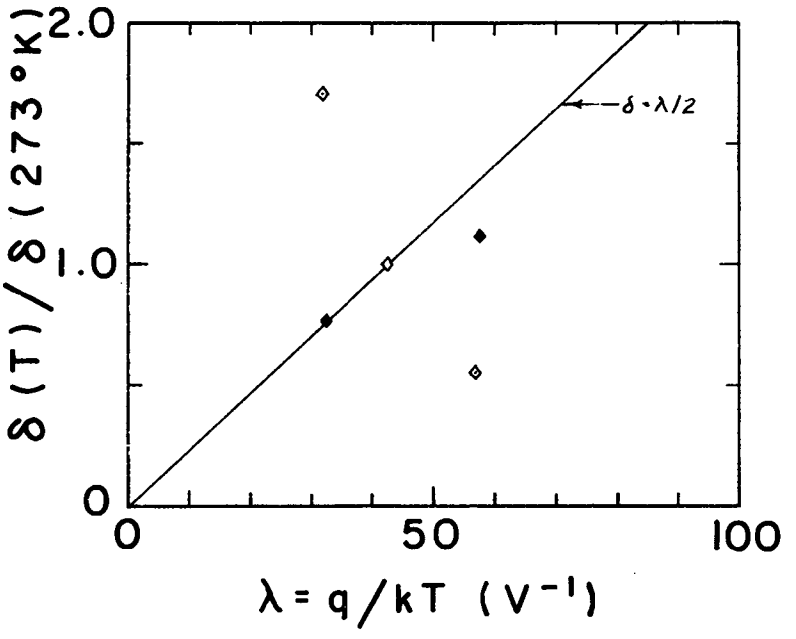

MU-35961

Fig. IV.23. $\delta(T)/\delta(273\,^{\circ}K)$ for the p-on-n GaAs solar cells.

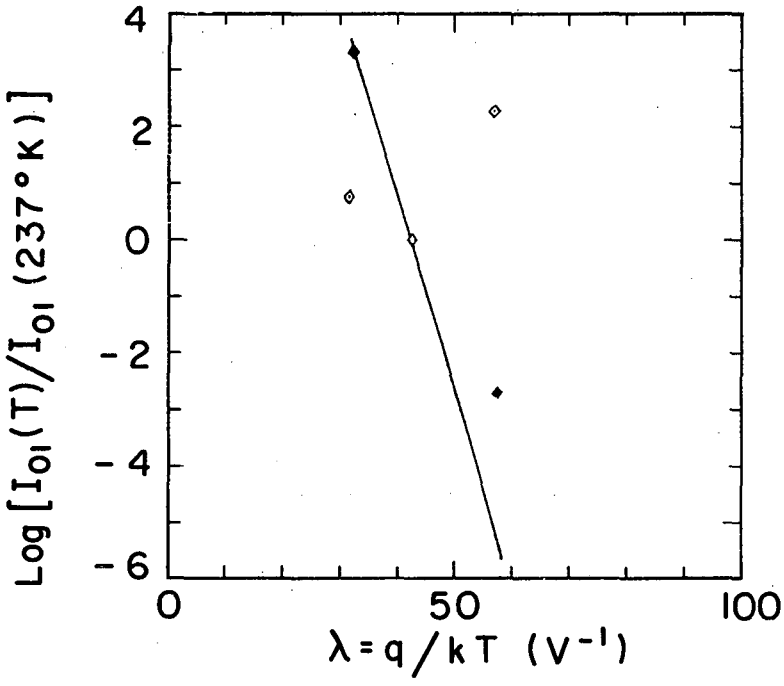

MU-35962

Fig. IV.24. Log $[I_{ol}(T)/I_{ol}(273\,°K)]$ for the p-on-n GaAs solar cells.

274°K and show a substantial deviation at 200°K. The theoretical curve as calculated from Eq. (IV-25) applies to the I_{rg}. It is therefore apparent that an additional non-ideal current contribution becomes important for $T \lesssim 250°K$. The results for GaAs A-20 are again seen to be in poor agreement with the calculated curve. The values of R_{SH}, I_{o1}, δ, I_o, and λ_m used to fit the I-V characteristics for the p-on-n GaAs solar cells are listed in Table IV.V, and the curves thus obtained are shown in Fig. IV.25. It was possible to fit the measured I-V characteristics reasonably well although a structure in the curve is noticeable at the lowest temperature.

4. Series Resistance. As mentioned earlier the series resistance of each cell was obtained from the displacement of the diode I-V characteristic with respect to the junction I-V characteristic; that is, the difference between the diode and junction voltages which correspond to an identical current. Therefore the series resistance is given by

$$R_s = \frac{V_d - V_j}{I} \quad . \qquad \text{(IV-28)}$$

A number of the cells tested exhibited a series resistance which was dependent upon current (see Fig. IV.26). This behavior is a result of the fact that the surface region-junction interface is not an equipotential surface. As the current is increased, the effective area of the junction decreases (this was discussed in Section IV.A) as does the length of the surface region path through which the current must pass. In this way the contribution to the series resistance arising from the surface region decreases with increasing bias. For large short circuit currents and the corresponding forward biased currents only the junction area in close proximity to the electrode strips is effective in

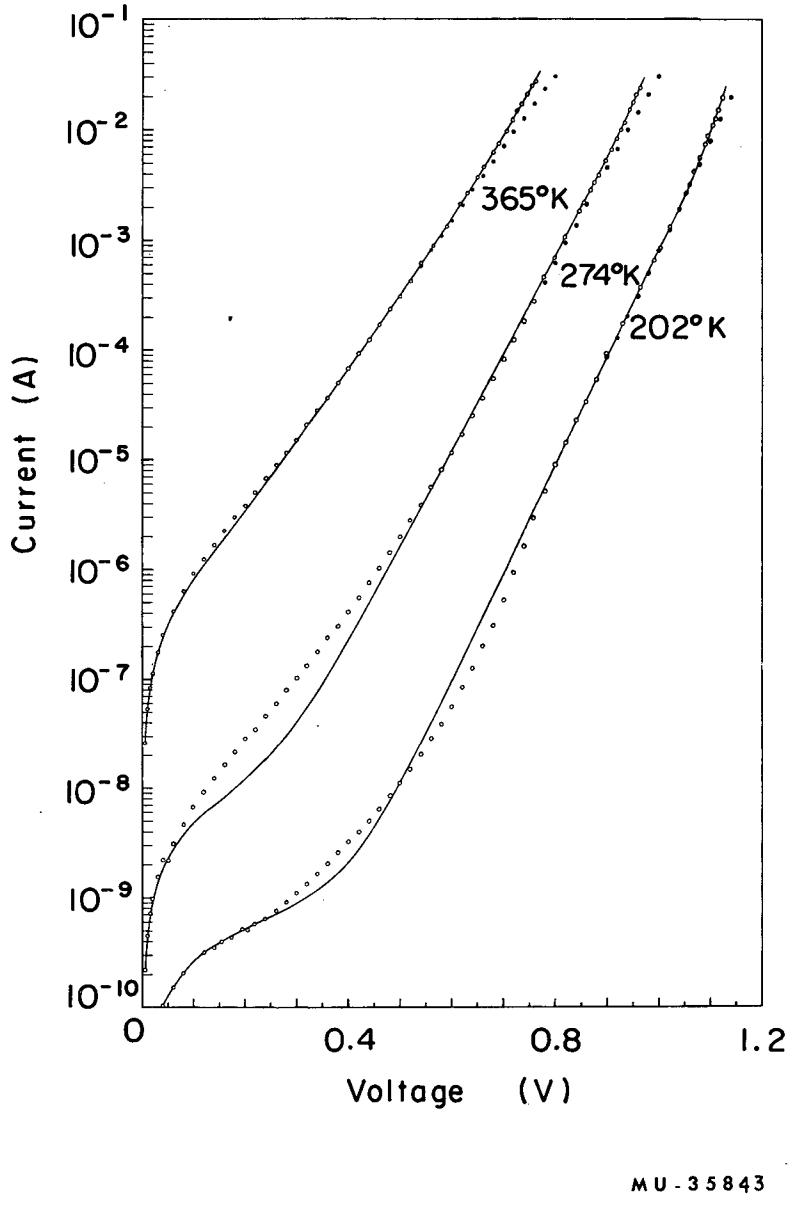

Fig. IV.25. The diode and junction I-V characteristics for GaAs A-22.

contributing to the current. In this current limit, the measured effective series resistance will approach that of the contacts, the base region, and the portion of the surface region near the contact strips.

The results obtained for SiM are presented in Fig. IV.26 where it can be seen that the effective series resistance decreases as the current increases and tends toward a constant value. This indicates that a voltage in excess of open circuit voltage must be applied to the surface region-junction combination in order to pass a current equal in magnitude to the short circuit current. The errors indicated are total errors including both random and systematic uncertainties. The results are in agreement with the expected temperature dependence, although the magnitude of the change cannot be explained on the basis of resistivity changes alone. In Fig. IV.27 the effective series resistance is presented for one cell from each of the four cell classes tested. Both GaAs and Si p-on-n cells show the same qualitative shape, while wihin experimental error the n-on-p Si cell exhibits a constant series resistance. The saturation series resistance (that is, the series resistance determined in the high current limit) for each of the cells tested is presented in Table IV.VII. The series resistances measured for Si51CB are seen to be greater than those for the other p-on-n Si cells which is to be expected since Si51CB was the only ungridded cell tested.

D. Conclusions.

We had initially hoped for a unique determination of the mechanism responsible for the non-ideal term in the dark I-V characteristic. This was not realized and it is only possible to draw tentative conclusions

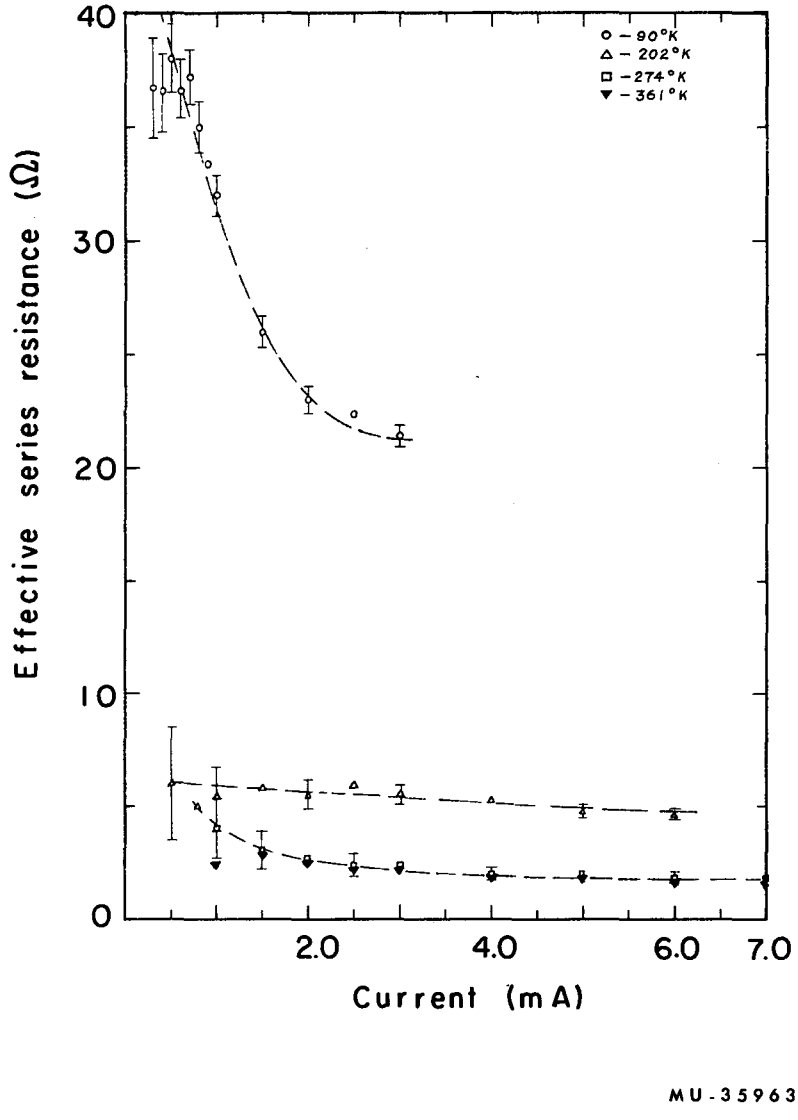

Fig. IV.26. The effective series resistance of SiM. (Key in Table V.I.)

Table IV.VII. Series resistance of the p-on-n and n-on-p silicon solar cells and the p-on-n gallium arsenide solar cells.

	Temperature (°K)			
Cell	90	200	275	360
SiM	21.0±1.7	4.80±0.60	1.80±0.36	1.80±0.27
Si51CB	----	32.0±1.6	4.30±0.34	2.30±0.21
SiN	20.0±1.5	6.00±0.66	2.10±0.48	1.20±0.25
Si3A	----	11.2±1.1	3.20±0.64	1.40±0.31
Si3A (etch)	37.0±2.9	12.0±0.9	2.75±0.50	1.70±0.31
Si1B	2.50±0.22	1.40±0.12	1.00±0.09	0.81±0.06
Si1D	5.40±0.60	1.50±0.11	1.00±0.10	0.65±0.06
SiL	----	6.50±0.88	1.00±0.15	0.63±0.07
SiL (etch)	----	6.30±0.63	0.95±0.19	0.65±0.07
SiF	----	42.0±1.6	2.30±0.09	0.70±0.04
GaAsA-20	----	2.20±0.42	1.80±0.45	1.60±0.24
GaAsA-22	----	0.90±0.27	1.00±0.20	1.16±0.16

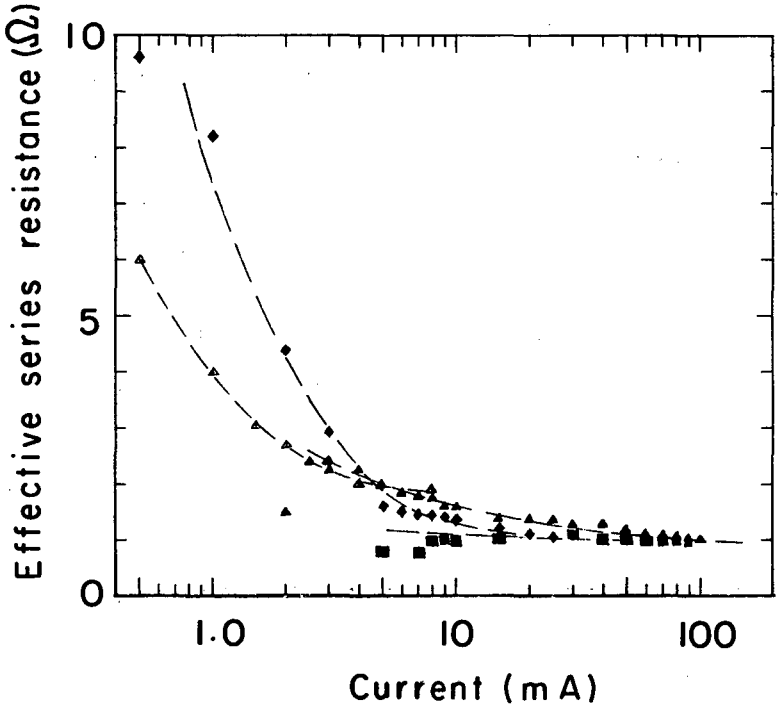

Fig. IV.27. The effective series resistance for the Si n-on-p and p-on-n and the GaAs p-on-n solar cells at 274°K. (Key in Table V.I.)

in regard to the current contributions to the non-ideal term for each cell type.

For all the cell types tested the ideal current term was isolated from the measured I-V characteristic and found to be in relatively good agreement with theory. The deviation of the measured ideal current term from the simple exponential relation employed for the ideal term in Eq. (IV-10) arising from the incomplete use of the junction (associated with the IR_s voltage drop in the surface region) was not discernible since the limiting effective junction area was estimated to be of the order of 10 to 20% of the total junction area (the electrical contacts cover approximately 10% of the front surface). Variations of this order of magnitude fall well within the quoted experimental error.

The junction recombination-generation current mechanism and/or the surface inversion layer current mechanism were found to make a minor contribution to the measured non-ideal current term for the p-on-n Si solar cells. The observed temperature dependence of the non-ideal exponential factor was found to be approximately that expected for the tunneling current mechanism, although the magnitude of the measured curve could not be compared with theory inasmuch as the analysis of this mechanism is as yet incomplete.

It is evident that the edge etch produced a substantially greater change in the effective reverse saturation current than in the non-ideal exponential factor for the p-on-n Si cells. These results are consistent with a tunneling current mechanism which is dependent upon the surface state of the diode, since it is possible that the concentration of energy states contributing to the tunneling process undergoes a sizable change upon etching, whereas the barrier penetration probability remains

virtually unchanged. This indicates that the tunneling process must be, in part, associated with energy states existing in a surface inversion layer or in the surface region. The latter is a possibility, since it was not practicable to completely eliminate etching of those regions of the front surface bordering the cell edges. It therefore appears reasonable to assume that the non-ideal current term is primarily due to the tunneling current mechanism for the p-on-n Si solar cells.

The results obtained for the n-on-p Si solar cells were also not consistent with the junction recombination-generation current mechanism, although the discrepancy was not as great as for the p-on-n Si cells. The temperature dependence of the non-ideal exponential factor, δ, indicates that the non-ideal current term may well be controlled by the tunneling current mechanism. The negligible effect of the edge etch upon the effective reverse saturation current and the non-ideal exponential factor for the n-on-p Si solar cells is consistent with a current mechanism primarily controlled by the bulk material properties.

The non-ideal term measured for one of the p-on-n GaAs solar cells was found to agree well with the junction recombination-generation mechanism at the two higher test temperatures. The results show that another current producing mechanism enters at 200 °K, and the measured temperature dependence of the non-ideal exponential factor indicates that this may be the tunneling current mechanism. It was therefore concluded that the non-ideal term was composed of these two current producing mechanisms which is in agreement with the conclusions arrived at by M. F. Lamorte[35] in a study of the solar energy conversion properties of GaAs solar cells.

It also seems quite reasonable to conclude that, for the case of solar cells possessing tunneling current controlled non-ideal current terms, the incomplete use of the junction will have a marked effect upon the measured I-V characteristic of this term. This results from the non-uniform surface region properties of solar cells as observed by Queisser[49] who measured the I-V characteristics for various regions of the junction.

The reported values of the shunt resistances must be regarded as only approximate, since their determination is quite sensitive to the form of the non-ideal current term in the limit of zero applied bias. The form obtained from the second term in Eq.(IV-10) is substantially different from that for I_{rg} and the form for a tunneling current is not even known in the low voltage limit.

The series resistance of the ungridded p-on-n Si solar cell was found to be greater than that for the gridded cells. This is to be expected, since the gridded cell makes more effective use of the junction area thus allowing a larger current to be passed at a given voltage than its ungridded counterpart. The observed temperature dependence of the series resistance was greater than that expected from resistivity considerations alone. The rather high series resistance measured for some of the cells at low temperatures possibly arises from poor electrical contacts, since in a number of the test runs at LN temperature the surface or base region electrodes separated from the cell and produced an open circuit.

V. ALPHA PARTICLE BOMBARDMENT OF SILICON AND GALLIUM ARSENIDE SOLAR CELLS

A. Theory.

In Section III the performance of an α-voltaic device was analyzed for an incident alpha flux normal to the diode surface. For the practical situation described in this section; namely, a Si or GaAs solar cell exposed to a thin film of alpha emitting material but not in direct contact with it, the angular distribution of the incident α-particles is neither isotropic nor normal incident but falls somewhere between these two limits. In addition, for the experimental work described in this section the source is circular and the test cell rectangular, resulting in no radial symmetry. However, in the latter part of this section the α-particle flux incident upon a test cell is calculated by replacing the rectangular cell with a circular disk of the same area. This has the effect of overestimating the magnitude of the α-particle flux incident upon the test cell.

In light of this symmetrizing step and the fact that an exact determination of the stopping power law for a general angular distribution of the incident α-particles is quite complicated, we decided to analyze the experimental results of this section on the basis of the formulation of Appendix B. The effects of the incident α-particle angular distribution and spectrum width are estimated in Section V.C as the need arises.

The electronic and atomic collision stopping power curves were calculated in the same manner as described in Section III.B. The energy as a function of track length for 4MeV α particles (this is the energy of the α-particles employed in this work, see Section V.C) was then determined from a numerical integration of the stopping power curve of

Fig. B.18, and the result is presented in Fig. B.20 of Appendix B. This figure was then used in conjunction with Fig. B.10 to obtain the spatial variation of the electronic stopping power $[dE_\alpha(x)/dx]_{el}$ which is represented by the solid curve in Fig. V.1. As in Section III.B the electronic stopping power was approximated by a polynomial in x (see Eq. (III-22)) where the method of least squares was used to find the best fit which is shown by the dotted curve in Fig. V.1. The energy required to produce an electron-hole pair was again assumed to be a constant along the α-particle track length (the value of 3.55 eV was again used) so that the spatial production of electron-hole pairs is given by

$$g_\alpha(x) = \frac{1}{\epsilon}[dE_\alpha/dx]_{el} = a+bx+cx^2+dx^3+fx^4 \qquad \text{(V-1)}$$

where the values of the constants obtained from the least squares fit for $\bar{E}_{\alpha o}$ = 4MeV are listed in Table III.II. The results of Appendix B were again used in the calculation of the spatial production of lattice displacements. The method of calculation was outlined in Section III.B where the spatial lattice displacement production rate was found to be

$$\dot{\delta N}_D(x) = \dot{N}_\alpha n_D(x)\delta x. \qquad \text{(V-2)}$$

Figure B.16 of Appendix B shows the number of lattice displacements produced by an α particle of energy E_α per unit track length. Using this, the spatial production of lattice displacements per incident α particle, $n_D(x)$, was determined and is shown in Fig. V.2. Following the suggestions put forth on pages 25 and 29 of Section III.C, the average number of lattice displacements produced per incident α particle were determined for the surface region and base region from Fig. V.2. Consideration of Fig. V.2 resulted in the decision to divide the base region into three sub-regions (a lightly damaged region, a high damaged region, and

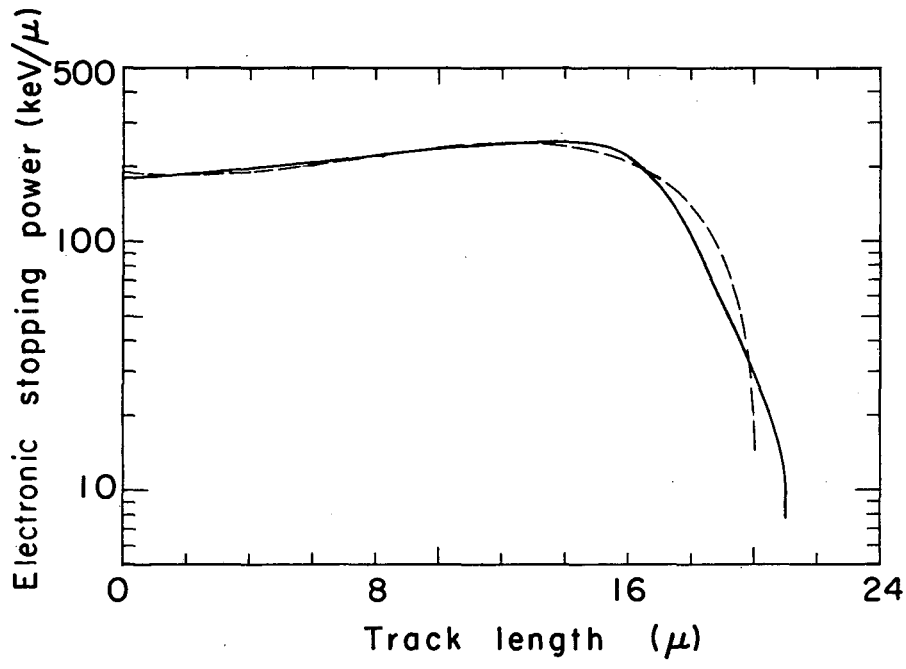

Fig. V.1. Electronic stopping power for 4-Mev α-particle stopping in Si (the dashed curve represents the polynomial fit).

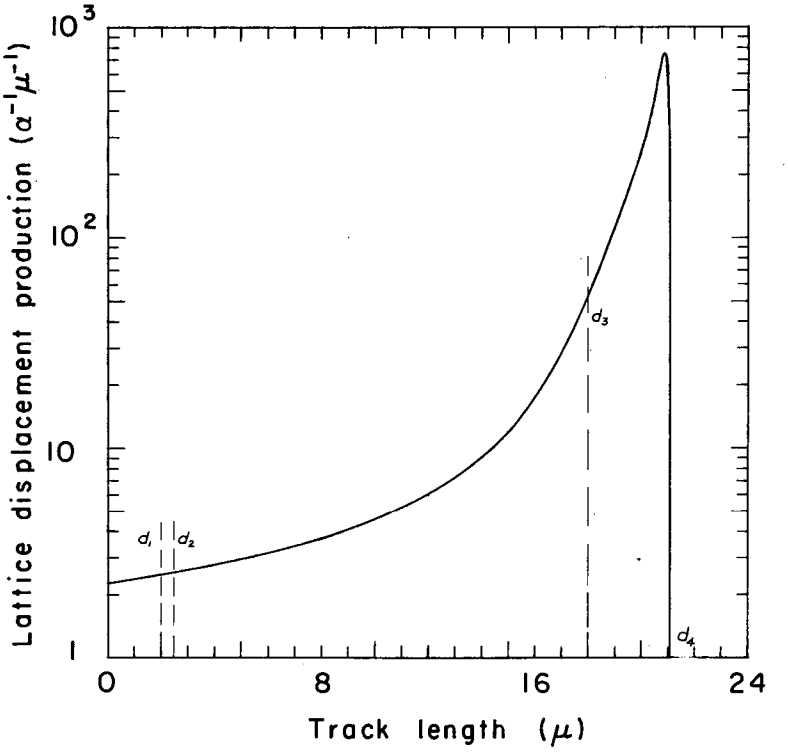

Fig. V.2. Lattice displacement production, $n_D(x)$, for 4-Mev α-particle stopping in Si.

an undamaged region) each with a different average lattice displacement production, whereas the surface region was characterized by a single average lattice displacement production. The division of the base region is indicated by the dotted lines in Fig. V.2. The average values are then found to be

$$\begin{aligned}
\bar{n}_D &= 2.38\bar{\mu}^{-1} \text{ for } 0 < x < d_1 \text{ (surface region)} \\
\bar{n}_D &= 8.88\bar{\mu}^{-1} \text{ for } d_2 < x < d_3 \text{ (lightly damaged base region)} \\
\bar{n}_D &= 249\bar{\mu}^{-1} \text{ for } d_3 < x < d_4 \text{ (highly damaged base region)} \\
\bar{n}_D &= 0 \text{ for } d_4 < x \text{ (undamaged base region).}
\end{aligned} \tag{V-3}$$

The I-V characteristic for a solar cell under α-particle bombardment was obtained from a solution of the minority carrier diffusion equation applied to the surface region and base region where $\dot{N}_\alpha g_\alpha(x)$ was used as the minority carrier source term. Details of this development can be found in Appendix C. The surface region and the three subregions of the base region were characterized by different effective diffusion lengths. In Section III.B the effective diffusion length $\tilde{L}$ was found to be related to the average defect center concentration (assumed equal to the lattice displacement concentration, $\bar{n}_D \frac{\theta(t)}{A_x}$, through the relation

$$\frac{1}{\tilde{L}^2} = \frac{1}{L_o^2} + \bar{K}\theta(t) \tag{V-4}$$

where $\bar{K} = \bar{v}\sigma_{CD}\bar{n}_D/DA_x$. The alpha generated current was found to consist of independent terms from the surface region, the junction, and the lightly damaged sub-region of the base region. The analysis was carried out for a p-on-n solar cell with the result that the alpha generated current is

$$I_{G\alpha}/q\dot{N}_{\alpha} = L_n \left\{ [X_n(d_1)\frac{M_n(d_1)}{K_n(d_1)} - L_n X'_n(d_1)] - \frac{[X_n(0)-\gamma_n L_n X'_n(0)]}{K_n(d_1)} \right\}$$

$$+ [H(d_2)-H(d_1)] + L_{pI} \left\{ [X_p(d_2)\frac{R_p(D)}{P_p(D)} + L_{pI} X'_p(d_2)] \right.$$

$$\left. - [X_p(d_3)+L_{pI} X'_p(d_3)]\frac{R_p(0)}{P_p(D)} \right\} \qquad \text{(V-5)}$$

where $D = (d_3 - d_2)$, $t = (d_4 - d_3)$, and the remaining quantities are defined by Eqs. (III-30) through (III-37). In the derivation of Eq. (V-5), the current contribution from the highly damaged sub-region of the base region has been neglected. This is quite reasonable for the damaged state of the solar cell, since this region then becomes a strong sink for excess electron hole pairs. Even in the undamaged state this leads to a minor correction. Consider, for example, the situation of a material with an infinite diffusion length (this will overestimate the actual contribution from the highly damaged sub-region which is the farthest removed from the junction) in which case the fractional contribution from this sub-region is

$$F_I = 1 - \frac{H(d_3)}{H(d_4)} = 1 - \frac{1.075X10^6}{1.123X10^6} = 0.043, \qquad \text{(V-6)}$$

where Eq. (III-33) gives H(x) and the fitting constants of Table III.II were used in the calculation. The error introduced by neglecting the highly damaged sub-region current contribution will therefore always be less than about 4%.

In the undamaged state (that is, $L_{pII} = L_{pI} = L_{po}$) Eq. (V-5) simplifies to

$$\left(I_{G\alpha}/\dot{N}_{\alpha}q\right)\Big| = L_n\left\{\left[X_n(d_1)\frac{M_n(d_1)}{K_n(d_1)} - L_n X'_n(d_1)\right] - \frac{[X_n(0)-\gamma_n L_n X'_n(0)]}{K_n(d_1)}\right\}$$

$$\lim \theta = 0$$

$$+ [H(d_2)-H(d_1)] + L_{po}\left[U_p(d_2)-U_p(d_3)\exp\left(-\frac{D}{L_{po}}\right)\right] \qquad \text{(V-7)}$$

where $U_p(x) = X_p(x) + L_p X'_p(x)$.

At an exposure level for which the base region properties are substantially changed while the surface region properties are virtually unaffected (this condition is indeed realized since the surface region has a much higher impurity level and correspondingly shorter minority carrier lifetime than the base region), Eq. (V-5) can be simplified. For $L_{pII} \lesssim t/2 = 1.5\mu$, Δ_1 and Δ_2 become

$$\Delta_1 \approx \cosh\left(\frac{t}{L_{pII}}\right)\left(1+\frac{L_{pII}}{L_{po}}\right) \approx \cosh\left(\frac{t}{L_{pII}}\right) \qquad \text{(V-8)}$$

and

$$\Delta_2 \approx \cosh\left(\frac{t}{L_{pII}}\right)\left(\frac{L_{pI}}{L_{po}}+\frac{L_{pI}}{L_{pII}}\right) \approx \frac{L_{pI}}{L_{pII}}\cosh\left(\frac{t}{L_{pII}}\right) \qquad \text{(V-9)}$$

since $L_{pII} < L_{pI} < L_{po}$. Also if $L_{pI} \lesssim D/2 = 7.75\mu$, we find that

$$P_p(D) \approx \cosh\left(\frac{t}{L_{pII}}\right)\cosh\left(\frac{D}{L_{pI}}\right)\left[1+\frac{L_{pI}}{L_{pII}}\right] \approx \cosh\left(\frac{t}{L_{pII}}\right)\cosh\left(\frac{D}{L_{pI}}\right)\left(\frac{L_{pI}}{L_{pII}}\right), \qquad \text{(V-10)}$$

$$P_p(0) \approx \cosh\left(\frac{t}{L_{pII}}\right), \qquad \text{(V-11)}$$

and

$$R_p(D) \approx \cosh\left(\frac{t}{L_{pII}}\right)\cosh\left(\frac{D}{L_{pI}}\right)\left[1+\frac{L_{pI}}{L_{pII}}\right] \approx \cosh\left(\frac{t}{L_{pII}}\right)\cosh\left(\frac{D}{L_{pI}}\right)x\left(\frac{L_{pI}}{L_{pII}}\right). \qquad \text{(V-12)}$$

Then the base region contribution to the alpha generated current becomes

$$(I_{C\alpha}/\dot{N}_\alpha q)_{BR}=L_{pI}\left\{ [X_p(d_2)+L_{pI}X'_p(d_2)] - \frac{[X_p(d_3)+L_{pI}X'_p(d_3)]}{\cosh(\frac{D}{L_{pI}})}\left(\frac{L_{pII}}{L_{pI}}\right)\right\}$$

$$= L_{pI}[X_p(d_2)+L_{pI}X'_p(d_2)] - \frac{L_{pII}}{\cosh(\frac{D}{L_{pI}})}[X_p(d_3)+L_{pI}X'_p(d_3)] . \qquad (V\text{-}13)$$

Therefore, in this limit that $L_{pII} < L_{pI} < L_{po}$, $L_n \simeq L_{no} \simeq d_1$, $L_{pII} \lesssim t/2$, and $L_{pI} \lesssim D/2$ the alpha generated current is given by

$$(I_{C\alpha}/\dot{N}_\alpha q)=L_n\left\{ [X_n(d_1)\frac{M_n(d_1)}{K_n(d_1)} - L_nX'_n(d_1)] - \frac{[X_n(0)-\gamma_nL_nX'_n(0)]}{K_n(d_1)}\right\}$$

$$+[H(d_2)-H(d_1)]+\left\{L_{pI}[X_p(d_2)+L_{pI}X'_p(d_2)]\right.$$

$$\left. - \frac{L_{pII}}{\cosh(\frac{D}{L_{pI}})}[X_p(d_3)+L_{pI}X'_p(d_3)]\right\} . \qquad (V\text{-}14)$$

Further consideration of the condition that $L_{pI} < (d_3-d_2) \approx R_\alpha$ allows us to approximate $g_\alpha(x)$ with the constants g_{os} and g_{ob} for the surface and base regions respectively, since the electronic stopping power is nearly constant over the first few microns of the α-particle track (see Fig. V.1). Therefore, the base region contribution to the alpha generated current becomes

$$(I_{C\alpha}/q\dot{N}_\alpha)_{BR} \approx L_{pI}g_{ob}\left[1-\left(\frac{L_{pII}}{L_{pI}}\right)\frac{1}{\cosh(\frac{D}{L_{pI}})}\right] \approx L_{pI}g_{ob} \qquad (V\text{-}15)$$

and Eq. (V-14) becomes

$$\frac{I_{G\alpha}}{q\dot{N}_\alpha} = L_n g_{os} \frac{[M_n(d_1)-1]}{K_n(d_1)} + [H(d_2)-H(d_1)] + L_{pI} g_{ob} \quad . \tag{V-16}$$

The current contributions from the surface region and the junction region are approximately constant for medium exposure levels so that these two terms can be replaced by a constant, I_c. Then using Eq. (V-4) in Eq. (V-16) yields

$$\frac{1}{(I_{G\alpha}-I_c)^2} = \frac{1}{q^2(g_{ob}\dot{N}_\alpha)^2} \left[\frac{1}{L_{po}^2} + \bar{K}\theta \right] \tag{V-17}$$

and when $\frac{1}{L_{po}^2}$ is small in comparison to $\bar{K}\theta$ (using $L_{pI} < L_{po}$ in Eq. (V-4)), Eq.(V-17) becomes

$$I_{G\alpha} = I_c + \frac{q g_{ob} \dot{N}_\alpha}{\bar{K}^{1/2}} \theta^{-1/2} = I_c + K_1 \theta^{-1/2} \quad . \tag{V-18}$$

Therefore I_c and $\bar{K}$ can be obtained from a plot of $I_{G\alpha}$ versus $\theta^{-1/2}$. The applicability of these limiting equations will be discussed in connection with the experimental results presented in Section V.C.

B. Experimental Method.

Irradiations were performed using p-on-n and n-on-p Si solar cells and p-on-n GaAs solar cells, which were purchased from commercial sources. The Si cells were IRC type 1020 with rated solar efficiencies of 9% and 11%, while the GaAs cells were RCA type XSC100 with a rated solar efficiency of approximately 4%. Prior to mounting in the irradiation chamber, all the sample cells received identical treatment. Thesample cells first received an ethyl alcohol wash which was followed by a distilled water rinse, and finally they were dried in an air jet.

The air jet was used in order to insure the removal of all liquid from the narrow region between the rear surface of the cell and the mounting plate.

Before being placed in the bombardment chamber, the sample cells were soldered onto a two-inch square copper or brass mounting plate using a conducting silver impregnated glue. The copper mounting plates were 3/32-inch thick and the brass mounting plates 1/16-inch thick. Owing to the fact that the irradiation chamber was situated in a glove box, it was considered desirable to perform the preparation and soldering steps outside of the glove box. Subsequent to soldering, the mounting plate and attached cell were passed into the glove box and bolted to the top of the irradiation chamber.

The irradiation chamber consisted of a cylindrical brass vacuum chamber with a source holder containing the source affixed to the chamber base. Through the chamber top was passed a rod and an attached shield plate. The shield could be inserted between the sample cell and source by rotation of the rod in a sealastic fitting. The irradiation chamber is shown in Fig. V.3 and V.4. When measurements were made at 200°K, it was necessary to heat the rod and sealistic fitting with heating tape in order to maintain the desired chamber pressure.

An operating pressure of approximately 100 microns was chosen to insure negligible α-particle energy loss in the path length between source and sample and to minimize the possibility of water vapor adsorption on the sample cells during irradiation.

An Americium 241 α-particle source was used for the irradiations. The source material was plated onto the central portion of a platinum disk and covered with a 0.35 mil Al foil. The disk was then mounted

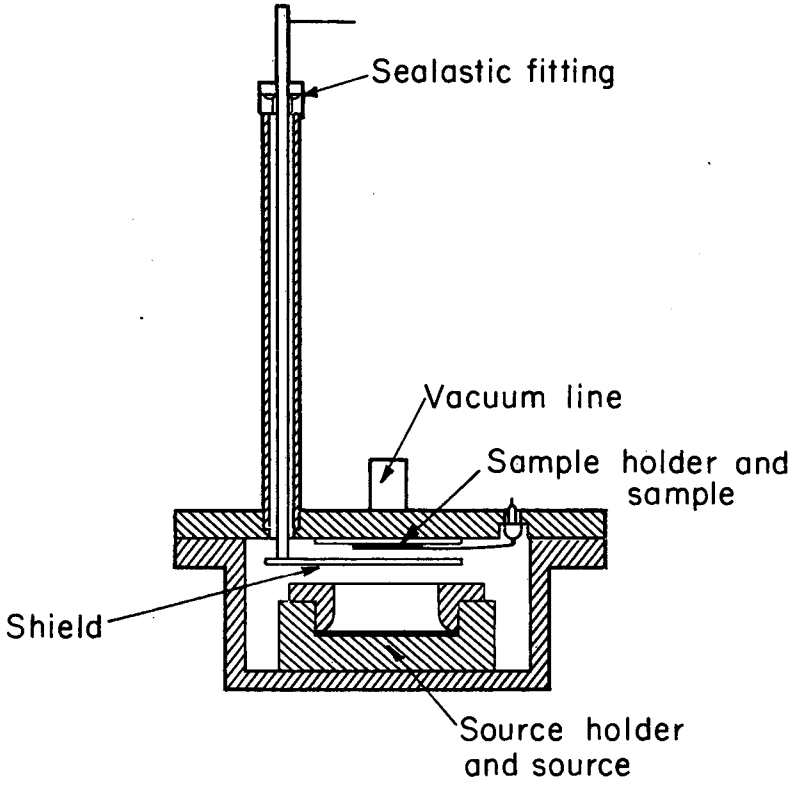

Fig. V.3. Diagram of irradiation chamber.

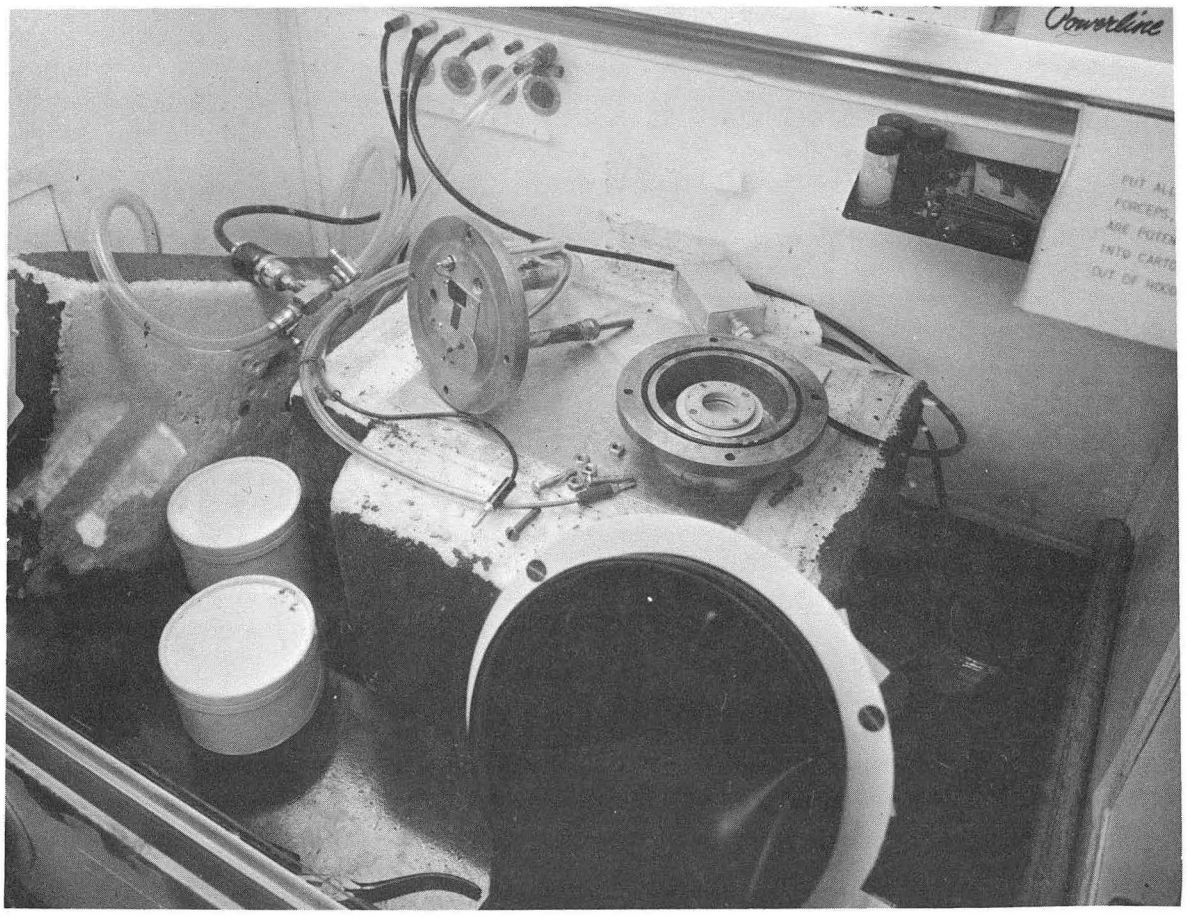

ZN-4828

Fig. V.4. Photograph of the irradiation chamber, the fluid container, and the glove box interior.

into the source holder unit and held in place with a retaining ring. The source was calibrated in position in the vacuum chamber and found to have an activity of (5.3±0.1) millicuries.[48] The calibration was accomplished by attaching to the chamber bottom a long cylindrical unit containing an ORTEC SBDJ025 Si solid-state detector. The solid state detector was attached to a rod (located on the central axis of the cylindrical body) which had approximately two inches of axial travel. This allowed the detector to be situated far enough from the source so that the electronic counting equipment employed was not saturated. Counting rates were measured for a number of source-detector separations and used in conjunction with a machine calculation to determine the source strength.

Both the Si and GaAs solar cells were irradiated at temperatures of 273°K and 200°K. A styrofoam container was used to hold the irradiation chamber in either a distilled water and ice solution at 273°K or a dry ice and ethyl alcohol solution at approximately 200°K. The operating temperature, radiation exposure level, and other properties for each cell are presented in Table V.I.

The initial plan was to irradiate the solar cells until the short circuit current had decreased by a factor of five which should correspond to a decrease in maximum efficiency of more than an order of magnitude. This was easily realized in a one-day run for the p-on-n Si cells, whereas the n-on-p Si cells required a two-day exposure time. For the p-on-n GaAs cells, an exposure time of ten days was required in order to attain the desired reduction in short circuit current. Three of the p-on-n Si cells were irradiated for longer than one day.

Table V.I. Properties and test conditions of sample solar cells.

Cell	Type	Rated solar[(a)] efficiency (%)	Test temp (°K)	Exposure level (a's) ($\times 10^{12}$)	Symbol used in figures
Si P	p-on-n	11	275	0.753	◇
Si H	p-on-n	11	200	5.94	○
Si 4	p-on-n	11	275	1.21	▽
Si G	p-on-n	11	200	0.812	△
Si O	p-on-n	9	275	1.11	□
Si R	n-on-p	11	275	1.27	●
Si 10	n-on-p	11	275	5.40	◆
Si K	n-on-p	9	200	1.35	▲
Si J	n-on-p	11	200	1.40	■
GaAs A-21	p-on-n	4	275	7.11	◐
GaAs A-22	p-on-n	4	200	5.60	◑

Manufacturers' estimates of device properties:

Si p-on-n; junction depth of 1μ to 2μ, $L_n \approx 1\mu$, $\rho_n \approx 1\Omega$cm., $L_p \approx 10\mu$ to 100μ, $s_n \approx 5{,}000$ cm/sec.

Si n-on-p; junction depth of 1μ to 2μ, $L_p \approx 1\mu$, $\rho_p \approx 1\Omega$cm., $L_n \approx 10\mu$ to 100μ

GaAs p-on-n; junction depth = 1μ ± 10% (never more than 1.5μ), $\bar{p}_p \approx 2.3\times10^{19}$cm.$^{-3}$, $L_n \approx 0.5 \rightarrow 1.0\mu$, $s_n \approx 1{,}000 \rightarrow 5{,}000$ cm sec^{-1}, $n_n \approx 10^{17}$cm.$^{-3}$, $L_p \approx 1 \rightarrow 3\mu$. (Zinc diffusion)

(a) Cells are rated at 100mW/cm^2 input photon energy flux. At an equivalent input energy flux for an alpha-voltaic device the results of Section III predict $\eta_{max} = 14.5\%$.

Each experimental run started when the shield plate was rotated so as to expose the sample cell to the alpha flux. At this time the open circuit voltage and short circuit current were measured in rapid succession. This was followed by a number of consecutive measurements of the short circuit current during the time interval when this short circuit current changes rapidly. The open circuit voltage was read less frequently during the same time interval. At such time as it became possible, the complete I-V characteristic was swept out with an X-Y recorder. Periodic measurements of the open circuit voltage and short circuit current continued between measurements of the complete I-V characteristics. In addition the short circuit current was continuously monitored using a Bristol circular recorder. The short circuit current was measured by way of the voltage drop across a calibrated precision resistance. The open circuit voltage was measured with the circular recorder for values less than 100 mV and with an electrometer-voltmeter digital-voltmeter combination for values greater than 100 mV. In effect, the electrometer voltmeter was used as an impedence transformer, since the digital voltmeter had a relatively low input impedence but a much greater accuracy. In the measurement of the complete I-V characteristics the output of two electrometer voltmeters were used to drive the co-ordinates of an X-Y recorder. The random and systematic uncertainties arising from the use of these measuring devices are listed in Table V.II. The circuit used is shown in Fig. V.5 and the equipment used in Fig. V.6.

The dark I-V characteristics were measured two or more times prior to and subsequent to irradiation for most of the cells. The purpose of this was to observe any inherent drift in the I-V characteristic of a

Table V.II. Uncertainties associated with the measurement of the dark and irradiated I-V characteristics.

Measured quantity	Open-circuit voltage and short circuit current[a]	I-V Characteristic	
		Dark[b]	Irradiated[c]
V(V < 100 mV)			
Random	±0.2% of F.S.	±0.2% of F.S.	±0.5% of F.S.
Systematic	≈0.5 mV	≈0.5 mV	≈0.5%
V(V > 100 mV)			
Random	±0.4 to 0.5 mV	±0.4 to 0.5 mV	±0.5% of F.S.
Systematic	≲0.3 mV	≲0.3 mV	≈0.5%
$I(I < 5\times10^{-8}A)$			
Random	———	±0.5% of F.S.	±0.5% of F.S.[d]
Systematic	———	≈2%	≈5% (e)
$V_I(I > 5\times10^{-8}A)$			
Random	±0.2% of F.S.	±0.2% of F.S.	———
Systematic	≈0.5 mV	≈0.5 mV	———
R_I, Random	±0.25%	±0.25%	———

(a) Voltage measured with circular recorder (V < 100 mV) or Digitec (V > 100 mV) and current with circular recorder.
(b) Voltage measured with circular recorder (V < 100 mV) or Digitec (V > 100 mV) and current with EH Meter ($I < 5\times10^{-8}A$) or circular recorder ($I > 5\times10^{-8}A$).
(c) XY Recorder with inputs fed by a Keithley and an EH meter.
(d) Oscillations were observed at times thus leading to larger errors.
(e) Corrected for by calibration with the circular recorder.

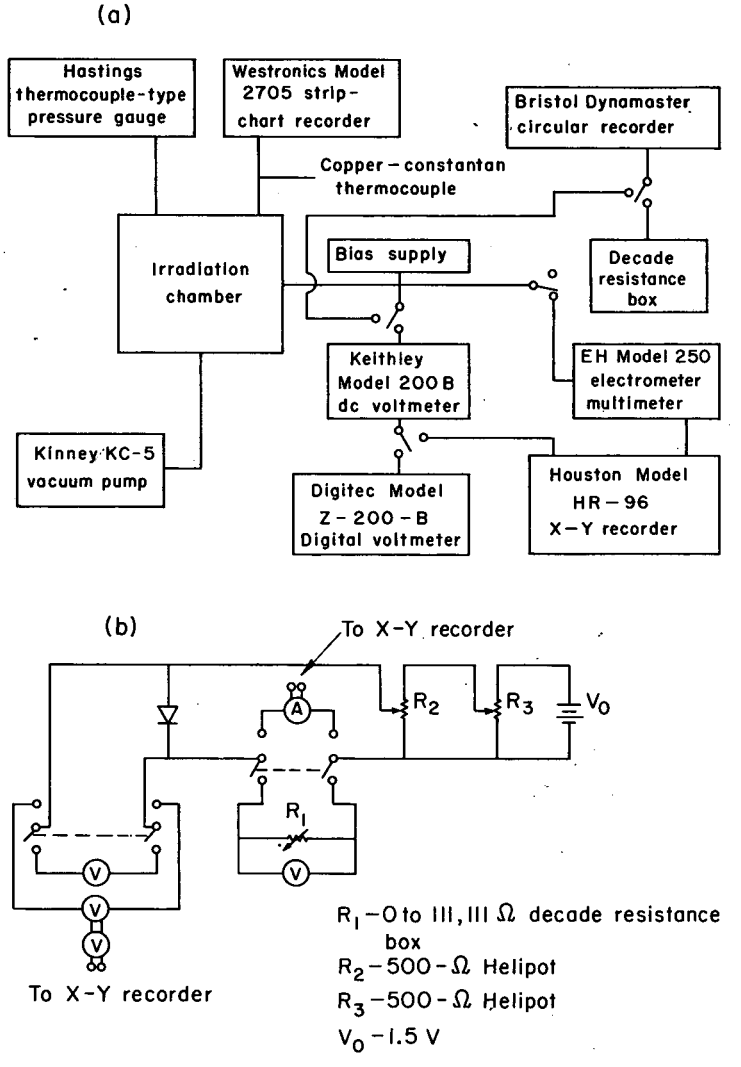

Fig. V.5. (a) Block diagram and (b) circuit diagram of equipment used in the measurement of the dark and irradiated I-V characteristics.

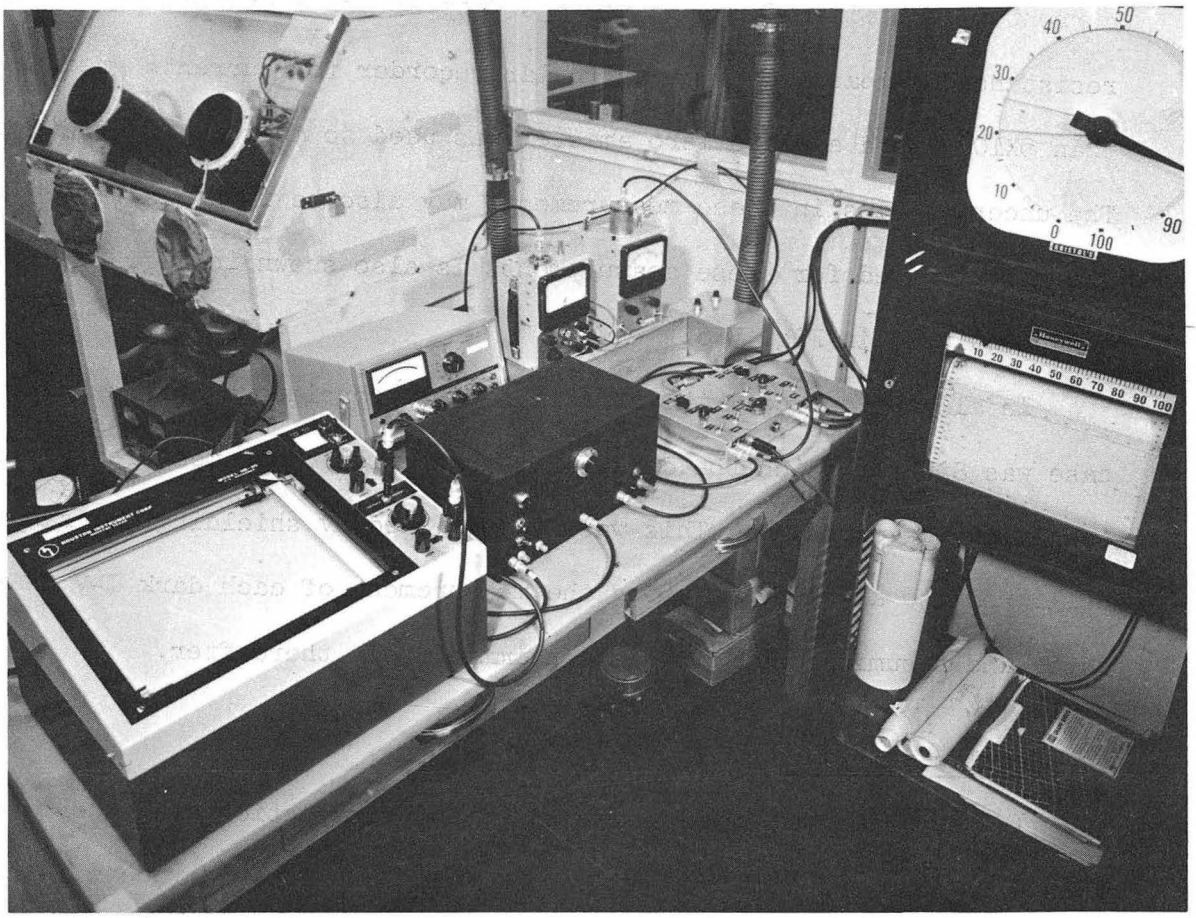

ZN-4829

Fig. V.6. The apparatus used in the measurement of the dark and irradiated I-V characteristics.

given cell. In these measurements the voltage was measured with the circular recorder for values up to 100 mV and with the electrometer voltmeter-digital voltmeter combination for values above 100 mV. The current was obtained from the voltage drop across a calibrated precision resistance as measured by the circular recorder for currents greater than $5X10^{-8}$A and a micromicro ammeter was used to measure lower currents. The uncertainties in these measurements may also be found in Table V.II. The circuit used for these measurements is also shown in Fig. V.5 and the equipment used in Fig. V.6.

In all but one cell the irradiation was continuous. This special case was SiH for which the dark I-V characteristic was measured periodically during exposure. This was accomplished by shielding the sample cell from the alpha flux during the measurement of each dark I-V characteristic and resuming the irradiation immediately thereafter.

C. Results and Discussion.

The experimental results presented in this section are, whenever possible, compared with theoretical calculations for a device with solar cell geometry (see Fig. III.3). The short circuit current calculations are based upon an incident α-particle flux that is normal to the front surface of the solar cell and is assumed to be monoenergetic. Subject to these conditions the short circuit current was calculated using Eq. (V-5) and the electron-hole pair production rate, $g_\alpha(x)$, obtained from the calculated electronic stopping power presented in Fig. V.1.

Prior to the presentation of these results, it is necessary to investigate the departure of the actual situation (that is, a radioisotope alpha source) from the idealized case used in the calculations.

1. Alpha Source Angular Distribution and Energy Spectrum. The α-particle flux incident upon an incremental area of the solar cell surface is not in practice isotropic as a result of the finite size of the alpha source employed and of the separation existing between the alpha source and the target solar cell. This separation in conjunction with the size of the source and the cell determines a maximum angle of incidence relative to the surface normal. For the purpose of this discussion (to be of a semi-quantitative nature) it is acceptable to replace the rectangular solar cell by a disk of equal area. The effective radius of the solar cell is then 0.314 inches, and the diameter of the source is 0.625 inches. The spacing between the solar cell and source is 0.672 inches (for the 1/16-inch thick brass mounting plates) and may be in error by as much as 0.031 inches. This geometrical configuration and the associated maximum angles of incidence are shown in Fig. V.7(a). Also shown in this figure is the maximum angle of incidence for the alpha flux incident upon an actual test cell. It can therefore be seen that replacing the solar cell by an effective disc was not a bad approximation. Figure V.7(b) presents a rough estimated of the angular distributions (in three dimensions they would be cones) expected at the outer edges and at the center of the solar cell. The maximum angle of incidence occuring at the edge is approximately 43°, and the axis of the cone is at approximately 25° to the inward normal at the surface. At the center of the cell the cone axis is perpendicular to the surface, and the angle of incidence ranges up to 25°. From the approximate angular distributions of Fig. V.7(b), it is seen that the majority of incident α particles travel in a direction closer to normal incidence than to the 43° maximum. The 25° limiting deviation should therefore be a more suitable

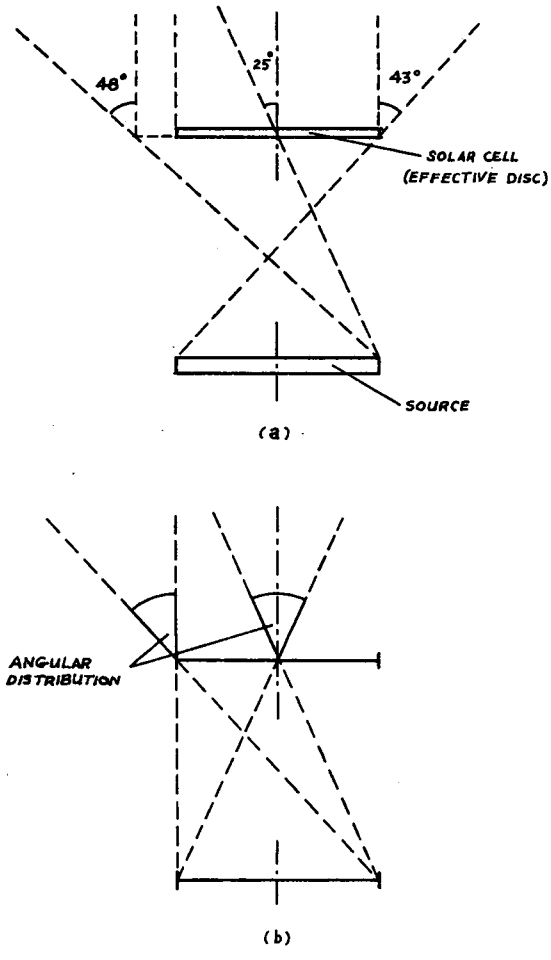

Fig. V.7. Source-solar cell geometry and approximate angular distributions for the incident α particles.

approximation to a mean angle of deviation from the normal than 43°. The perpendicular depth of penetration, R', for an α particle incident at this angle is related to the range by

$$R' = R_\alpha \cos(\theta_{mean}) \simeq 20.3 \cos(25°) = 18.4\mu. \qquad (V\text{-}19)$$

This two-micron difference should have a relatively minor effect upon the calculated electron-hole pair production rate, $g_\alpha(x)$ (this can be seen from Fig. V.1), whereas it may have a substantial effect upon the calculated lattice displacement production rate, $n_D(x)\dot{N}_\alpha$, over the latter portion of the α-particle track (this can be seen from Fig. V.2). As will become evident later, the calculated lattice displacement rate is only used in a quantitative manner when analyzing changes in the short circuit current occurring at high exposure levels. Only those regions of the solar cell within eight microns or so of the surface are important for high exposures (the remaining material has been damaged so highly that it contributes little to the short circuit current), and thus the effect of the spread in the incident alpha flux is minimized. The effect of this angular spread will be discussed later in connection with the measurement of the diffusion length degradation constant.

The incident α-particle spectrum is shown in Fig. V.8. Included for comparison is the basic α-particle spectrum for Am-241.* It is evident that the actual spectrum is not a delta function and in fact the width at half maximum is ±400keV. This corresponds to a ±2 micron

---

* This spectrum was furnished by Nuclear Diode Inc. along with the Si surface barrier detector used in measuring it.

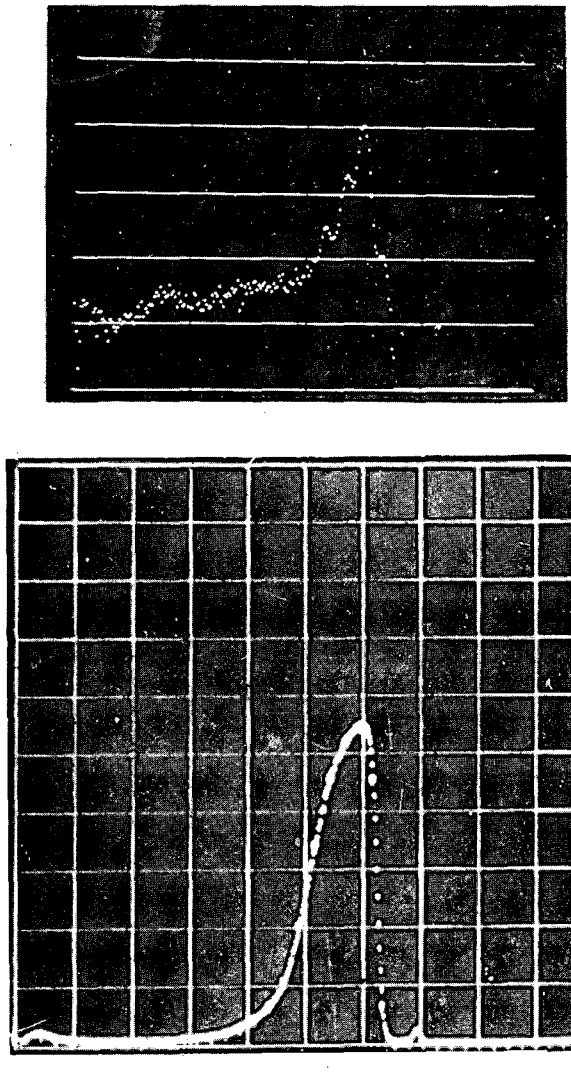

Fig. V.8. Energy spectrum for (a) the α particles emitted from Am^{241} and (b) the α particles incident upon the solar cells (at 50 volts detector bias). Relative abundances of α's from Am^{241} are 5.534 Mev (0.35%), 5.500 Mev (0.23%), 5.477 Mev (85%), 5.435 Mev (12.6%), 5.378 Mev (1.7%); from D. Strominger, J. M. Hollander and G. T. Seaborg "Table of Isotopes," Rev. Mod. Phys. 30, 585 (1958).

uncertainty in the range of the α particle; and, therefore, the comments made above with regard to the effect of the incident α-particle angular spread upon the calculations of $g_\alpha(x)$ and $n_D(x)$ apply equally well in connection with the energy spread.

2. Initial Energy Conversion Properties. The short circuit current for the Si solar cells in the undamaged state was calculated from Eq. (V-7) for temperatures of 200°, 250°, and 300°K. The material properties listed in Table IV.VI (properties representative of commercially available Si solar cells) were used in the calculation along with the polynomial fitting constants for a 4MeV α particle (see Table III.II). Table V.III presents the total charge collection efficiency and the number of electron-hole pairs collected per incident α particle by each region of the diode. The calculations were performed for both p-on-n and n-on-p Si solar cells.

As stated in Section V.B, the open circuit voltage was measured immediately upon initiation of the test run. The first measurement of the short circuit current took place as soon as possible after the open circuit voltage was obtained. The short circuit current was measured by applying a reverse bias to the diode sufficient to null out the voltage developed by the diode. This process took on the order of 10 to 30 seconds with the result that an extrapolation of the experimental results was required in order to determine the initial value of the short circuit current. The extrapolation process was aided through the use of the initial dark I-V characteristic and the initial value of the open circuit voltage (see Eq. (IV-12)). The results of this extrapolation technique are shown in Fig. V.9 for SiJ. Table V.IV lists the measured short circuit currents obtained for all the cells tested along with the

Table V.III. Calculated charge collection efficiency for p-on-n and n-on-p silicon solar cells under 4 MeV alpha particle bombardment.

	p-on-n			n-on-p		
	200	250	300	200	250	300
d_1(cm)	2.00×10^{-4}	2.00×10^{-4}	2.00×10^{-4}	2.00×10^{-4}	2.00×10^{-4}	2.00×10^{-4}
d_2(cm)	2.50×10^{-4}	2.50×10^{-4}	2.50×10^{-4}	2.50×10^{-4}	2.50×10^{-4}	2.50×10^{-4}
R_a(cm)	2.03×10^{-3}	2.03×10^{-3}	2.03×10^{-3}	2.03×10^{-3}	2.03×10^{-3}	2.03×10^{-3}
L_n(cm.)	4.89×10^{-4}	5.64×10^{-4}	6.24×10^{-4}	3.22×10^{-3}	3.83×10^{-3}	4.04×10^{-3}
L_p(cm.)	2.14×10^{-3}	2.26×10^{-3}	2.44×10^{-3}	3.70×10^{-4}	4.15×10^{-4}	4.40×10^{-4}
N_{eh}	1.12×10^{6}	1.12×10^{6}	1.12×10^{6}	1.12×10^{6}	1.12×10^{6}	1.12×10^{6}
$N_{eh,SR}$	9.17×10^{4}	9.41×10^{4}	9.58×10^{4}	7.18×10^{4}	7.48×10^{4}	7.70×10^{4}
$N_{eh,J}$	2.72×10^{4}	2.72×10^{4}	2.72×10^{4}	2.72×10^{4}	2.72×10^{4}	2.72×10^{4}
$N_{eh,BR}$	6.94×10^{5}	7.09×10^{5}	7.28×10^{5}	7.77×10^{5}	8.08×10^{5}	8.11×10^{5}
$N_{eh,T}$	8.13×10^{5}	8.31×10^{5}	8.51×10^{5}	8.76×10^{5}	9.11×10^{5}	9.15×10^{5}
Q	0.724	0.740	0.757	0.780	0.811	0.814

d_1 - assumed

$d_2 = d_1 + W$, assumed $W = 0.5\,\mu$

L_n, L_p - see Table IV.7.

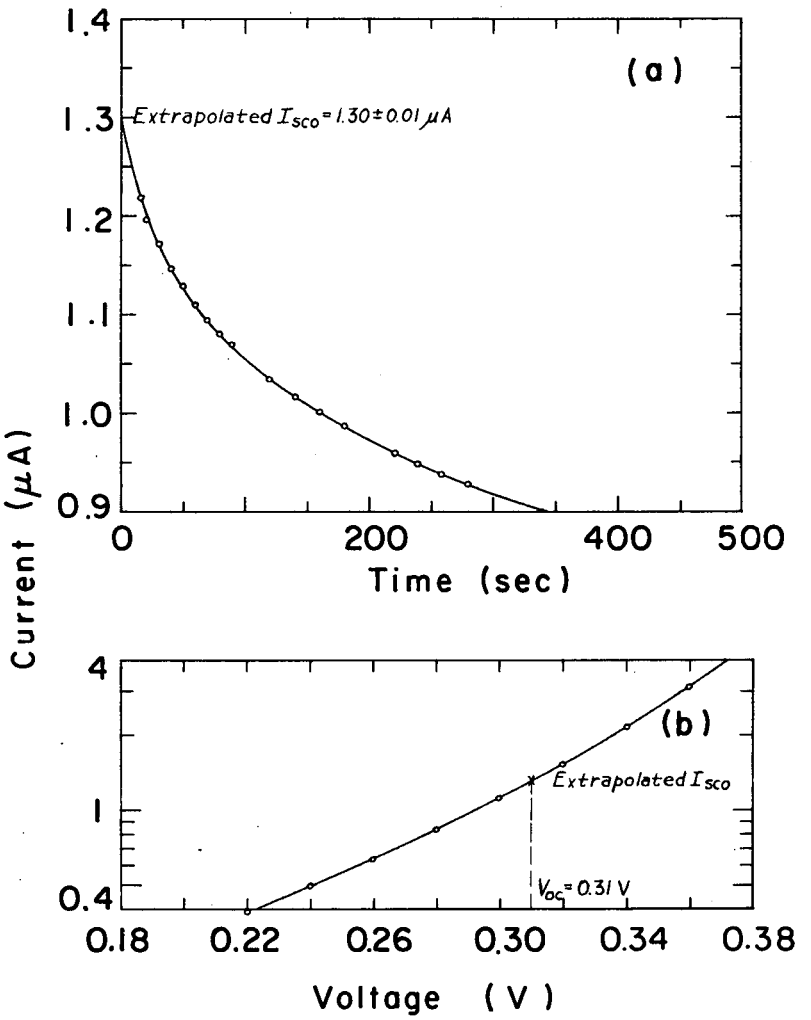

Fig. V.9. Extrapolation technique used to determine I_{sco}. The curves are (a) the extrapolation of the short-circuit current to zero time and (b) the comparison of $V_{oc,o}$ and I_{sco} with the initial dark I-V characteristic.

Table V.IV. Initial energy conversion properties for the silicon and gallium arsenide solar cells under 4 MeV alpha particle bombardment.

Cell	T(°K)	$\dot{N}_a$(a/sec)	$I_{sco,meas}$ (μA)	$I_{sco,calc}$ (μA)	Q_o, meas	Q_o, calc	$V_{oc,o}$ (mV)	$V_{mp,o}$ (mV)	$I_{mp,o}$ (μA)	$P_{max,o}$ (W)	$\eta_{max,o}$ (%)
Si P	275	8.2×10^{6}	1.29	1.105	0.860	0.749	27.1	14.6	0.670	9.76×10^{-9}	0.186
Si 4	275	8.5×10^{6}	1.37	1.145	0.884	0.749	---	---	---	---	---
Si O	275	8.2×10^{6}	1.31	1.105	0.873	0.749	58.0	35.0	0.650	2.28×10^{-8}	0.434
Si G	200	8.2×10^{6}	1.31	1.070	0.873	0.724	133	80.0	0.793	6.34×10^{-8}	1.21
Si H	200	8.6×10^{6}	1.41	1.120	0.898	0.724	286	195	1.087	2.12×10^{-7}	3.85
Si R	275	8.0×10^{6}	1.30	1.170	0.890	0.812	101	55.0	0.697	3.83×10^{-8}	0.749
Si 10	275	8.0×10^{6}	1.28	1.170	0.877	0.812	---	---	---	---	---
Si K	200	8.2×10^{6}	1.29	1.151	0.860	0.780	353	290	1.074	3.11×10^{-7}	5.94
Si J	200	8.2×10^{6}	1.30	1.151	0.867	0.780	310	214	0.950	2.05×10^{-7}	3.90
GaAs A-21	275	8.2×10^{6}	0.198	0.266[a]	0.151	0.203[a]	226	155	0.158	2.45×10^{-8}	0.467
GaAs A-22	200	8.2×10^{6}	0.330	0.266[a]	0.252	0.203[a]	680	565	0.300	1.70×10^{-7}	3.23

(a) Calculated from Eq. (5.21) with $d_1 = 1\mu$, $L_n = 1\mu$ and $L_p = 2\mu$.

short circuit currents calculated from Eq. (V-7). The calculated and measured values of the charge collection efficiency are compared in Fig. V.10(a) for the p-on-n Si solar cells and in Fig. V-10(b) for the n-on-p Si solar cells. It can be seen from this comparison that the minority carrier lifetime and associated diffusion length in the base region must be greater than the assumed value, since we feel the spread in the incident α-particle energy spectrum and angular distribution cannot account for a discrepancy of this magnitude. We shall later find that the charge collection efficiency for the base region can be used to estimate the diffusion length in that region.

The measured values of the initial open circuit voltage are also listed in Table V.IV. The initial values of the open circuit voltage and short circuit current were used in conjunction with the initial dark I-V characteristic to construct the initial irradiated I-V characteristic. (see Figs. V.16 and V.17) From the Irradiated I-V characteristics constructed in this manner the initial values of maximum power, voltage at maximum power, current at maximum power, and maximum efficiency have been determined; and the results are presented in Table V.IV. As expected from theoretical considerations the efficiency increases with a decrease in temperature for all three types of cells tested. The maximum efficiency is found to be consistently higher for the n-on-p Si solar cells that for the p-on-n Si solar cells even though the charge collection efficiency is approximately the same for these two cell types. The superior performance of the n-on-p Si solar cells arises from the hard dark I-V characteristics exhibited by these cells as compared to the p-on-n Si cells. The results also support the contention stated in Section III.A that the maximum efficiency should

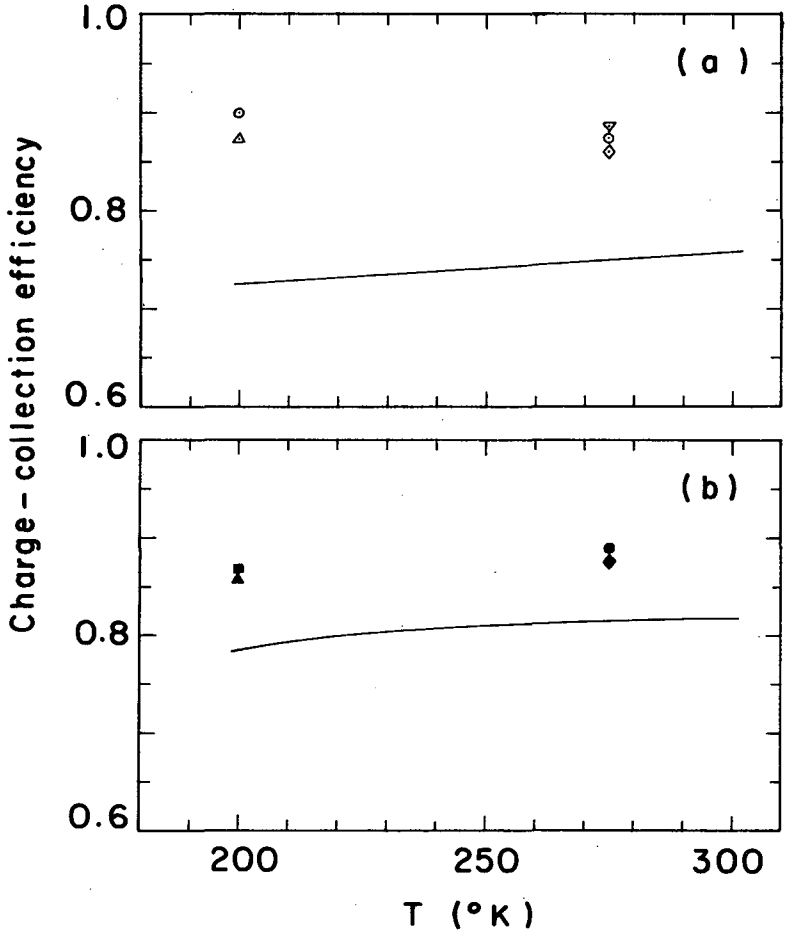

Fig. V.10. Comparison of measured and calculated charge-collection efficiencies for (a) the p-on-n Si solar cells and (b) the n-on-p Si solar cells.

increase as the forbidden energy gap increases. This is evident from the results presented in Table V.IV when it is noted that the GaAs solar cells ($E_g \approx 1.35$eV) yield maximum efficiencies comparable to those of the Si solar cells ($E_g \simeq 1.1$eV) at much lower values of the short circuit current. Therefore, the maximum conversion efficiency of a GaAs solar cell with a short circuit current in excess of one μA would be greater than that for a Si solar cell with an equivalent short circuit current.

3. Bombardment Induced Changes in Device Performance. The lattice displacements produced in a solar cell during α-particle bombardment give rise to a decrease in the minority carrier lifetime and mobility in that portion of the material traversed by the α particles. The changes in minority carrier lifetime are in general observed at substantially lower exposure levels than the changes in mobility.[44,84] These changes in the material properties are responsible for the observed degradation in the power conversion properties of the Si and GaAs solar cells tested. The results for the exposure induced changes in short circuit current are presented in Figs. V.11 through V.14.

Prior to a detailed discussion of these results, one important point should be made. Despite the fact that the electronic properties of a material are quite sensitive to radiation damage, a device composed of said material with relatively high impurity concentration can exhibit an apparent resistance to radiation damage, from a device standpoint. This type of behavior will be encountered when considering the experimental results for the GaAs solar cells. We have determined the sensitivity of a device to radiation damage from the exposure induced

changes in its performance, whereas the sensitivity of the material to radiation damage is determined from the measured values of the diffusion length degradation constant (see Eq. (V-4).

Short Circuit Current. We see in Fig. V.11 that the test runs for the p-on-n Si solar cells at both 200°K and 275°K yield nearly identical results for the fractional change in short circuit current with exposure. In addition, the approximate equality of measured values of the initial short circuit current for these cells indicates that the minority carrier diffusion lengths are very nearly the same at the two test temperatures. Therefore, it is evident that the type of radiation damage produced is the same at both temperatures. This type of a temperature independent behavior has been observed for the electron bombardment produced A-center in n-type Si.[64] As a result of the techniques used in the preparation of Si solar cells, the surface region possesses a much higher impurity concentration than the base region with the result that the base region is the first to exhibit radiation damage. This means that the base region is primarily responsible for the observed degradation in short circuit current and the other energy conversion properties. Bearing this in mind, it is evident that the location within the energy gap of these energy states arising from the bombardment induced recombination centers (those lattice displacements which act as recombination centers, hereafter referred to as the defect recombination centers or DRC's) must lie well below the Fermi level which is situated below but near the bottom of the conduction band for the n-type material used in these p-on-n cells. Therefore the DRC energy states must also lie well below the bottom of the conduction band. A DRC energy state located near the bottom of the conduction band would have a finite

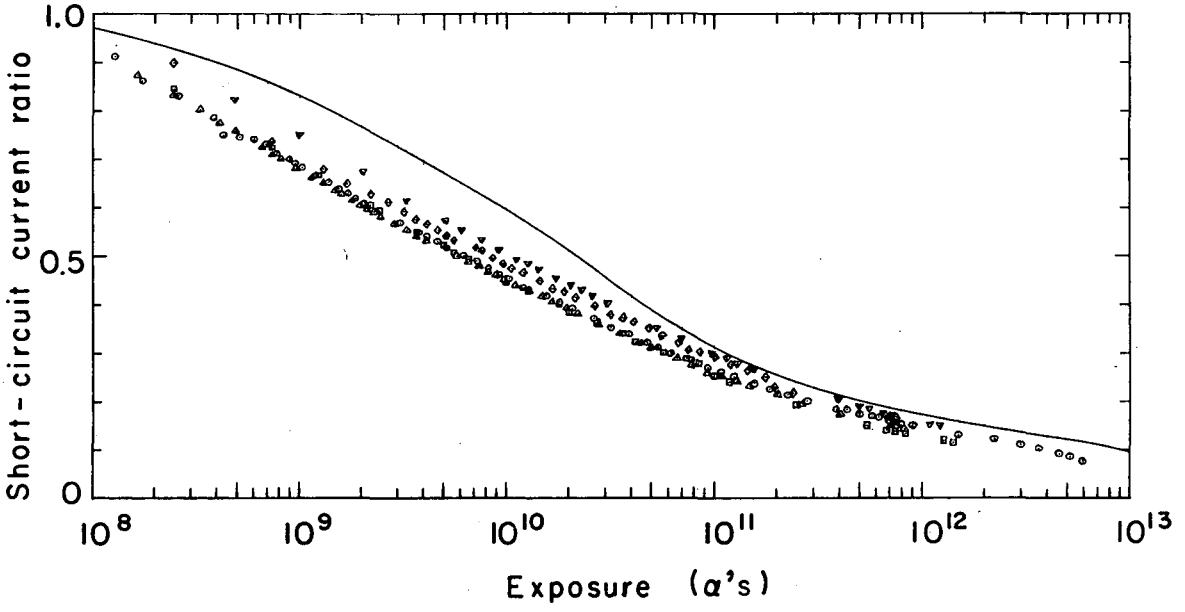

Fig. V.11. Short-circuit current ratio, I_{sc}/I_{sco}, vs exposure for the p-on-n Si solar cells. (Key in Table V.I.)

probability of being unoccupied by electrons and therefore incapable of contributing to hole recombination. This probability (that is, the Fermi-Dirac distribution function) would then exhibit a temperature dependence in contrast to the observed results. The solid curve in Fig. V.11 represents a calculation of I_{sc}/I_{sco} which is discussed below (see page 147).

The results for the n-on-p Si solar cells as depicted in Fig. V.12 show a marked temperature dependence. It is unlikely that this difference is attributable to different initial minority carrier lifetimes at the two temperatures since the measured initial short circuit currents are nearly identical for both temperatures. There is no a priori basis for believing that the DRC's produced in the base p-type material are identical to those produced in the base material of the p-on-n cells. We cannot therefore use the results obtained for these cells to further isolate the position of the DRC energy states produced in the p-on-n cells by the α particles. In order to explain the behavior of the n-on-p cells, the DRC energy states produced in the base p-type material must be situated near the top of the valence band whereupon the temperature will affect the probability of occupancy for these energy states. Assuming the DRC produced at 200°K and 275°K to be identical, the greater resistance to radiation damage at 275°K can only be realized for DRC energy states lying above the Fermi energy, since in this situation the number of empty energy states decreases with increasing temperature. As mentioned above, it is not possible to exclude the possibility of a temperature dependence in the nature or production rate of the DRC. Therefore, the results presented thus far do not allow us to choose between these possibilities with any reasonable degree of certainity.

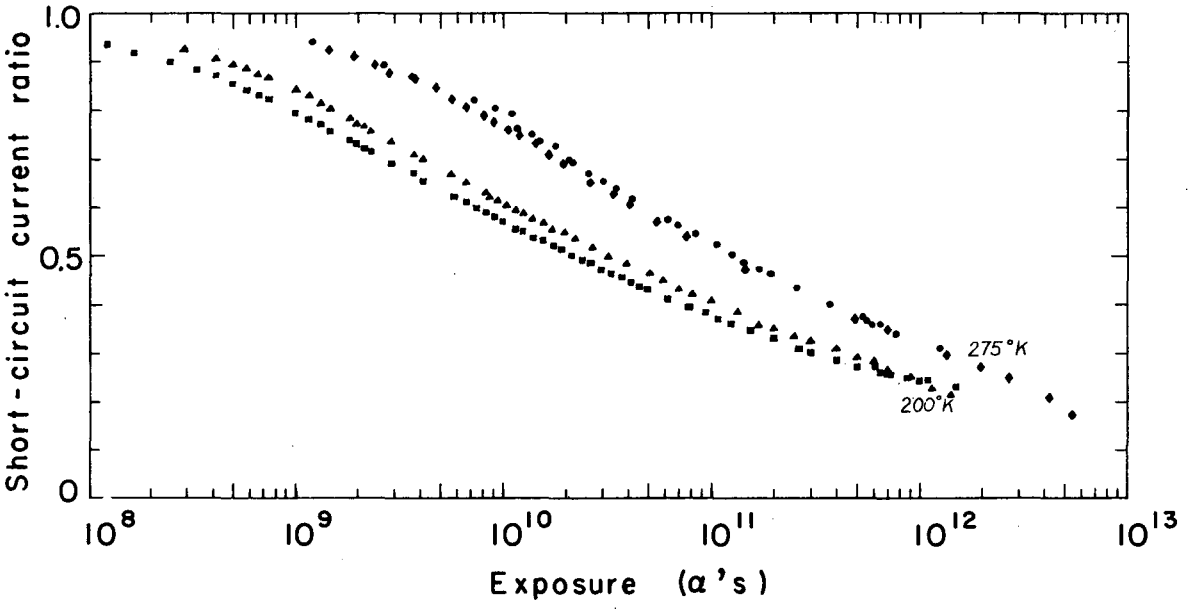

Fig. V.12. Short-circuit current ratio, I_{sc}/I_{sco}, vs exposure for the n-on-p Si solar cells. (Key in Table V.I.)

It is difficult to draw conclusions about the temperature dependence of the device radiation resistance for the p-on-n GaAs solar cells inasmuch as only one cell was tested at each temperature. Therefore the spread in data for GaAs cells at a fixed temperature is not know. If for the time being we assume the spread in data for these cells to be approximately the same as that for the p-on-n Si cells, it is apparent from Fig. V.13 that the cell tested at 275°K is more resistant to radiation damage from a device standpoint. This behavior is consistent with an initial base region diffusion length for GaAs A-22 in excess of that for GaAs A-21, and the existence of such a situation can be inferred from the greater initial short circuit current for GaAs A-22. In view of these facts, it is not possible to obtain any information relative to a temperature dependence in the nature and production rate of the DRC or of the position of the DRC energy states in the forbidden energy gap.

In Fig. V.14 a comparison is made for all the cell types tested. The p-on-n GaAs solar cells exhibit the strongest device radiation resistance which is in part a result of the short initial diffusion lengths of these cells as deduced from their low initial short circuit currents. The n-on-p Si solar cells show less resistance to radiation damage than the p-on-n GaAs cells and the p-on-n Si solar cells are the least resistant. The n-on-p Si cells possess base region diffusion lengths that are only slightly less than those of the p-on-n Si cells (see Table V.VII). Therefore the large difference in device radiation resistance for the p-on-n and n-on-p Si solar cells cannot be entirely attributed to differences in the initial diffusion lengths. The basic nature of the DRC and/or their production rate must be different for

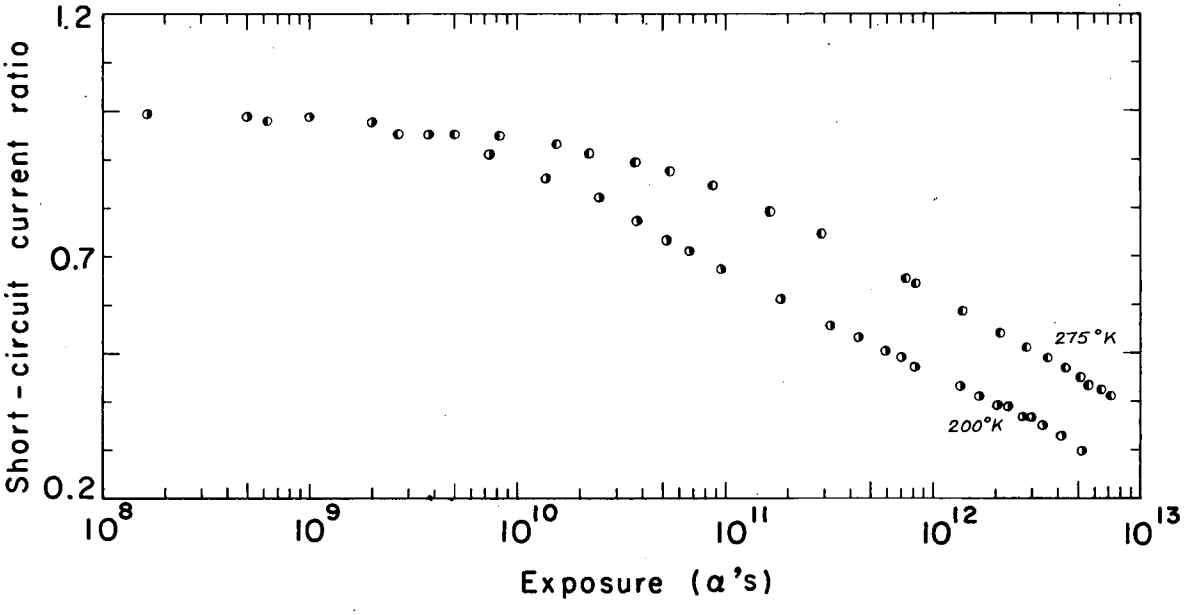

Fig. V.13. Short-circuit current ratio, I_{sc}/I_{sco}, vs exposure for the p-on-n GaAs solar cells. (Key in Table V.I.)

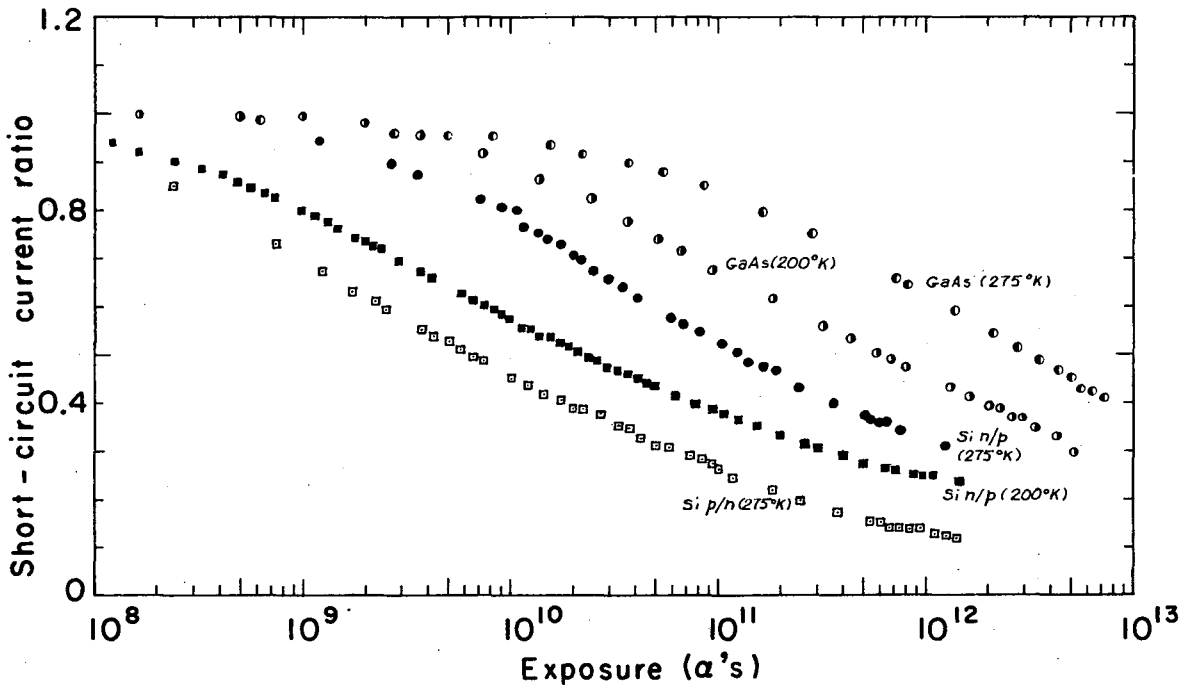

Fig. V.14. Comparison of the short-circuit current ratio, I_{sc}/I_{sco}, for representative cells of each type.

these two cell types. This will be returned to when we consider the experimentally measured values of the diffusion length degradation constant. In connection with the present discussion, it should be pointed out that although the p-on-n GaAs solar cells are the most resistant to device radiation damage, the measured short circuit currents are lowest for these cells at intermediate exposure levels ($\theta \gtrsim 10^{11}$ α's).

In Fig. V.11 a comparison was made between the experimental results and a calculation of I_{sc}/I_{sco} for a p-on-n Si solar cell at 250 °K based upon a modified form of Eq. (V-5). The calculation was simplified by assuming the electron-hole pair production rates in the surface and base regions to be spatially uniform and given by g_{os} and g_{ob} respectively. In this case Eq. (V-5) becomes

$$I_{G\alpha}/q\dot{N}_{\alpha} = L_n g_{os} \frac{[M_n(d_1)-1]}{K_n(d_1)} + [H(d_2)-H(d_1)] + L_{pI} g_{ob} \frac{[R_p(D)-R_p(0)]}{P_p(D)} \quad . \quad (V\text{-}20)$$

In the calculation the properties listed in Table IV.VI were used for the initial properties, except that the surface region thickness was set equal to 1.5×10^{-4} cm. The reason for this change will become evident when we estimate the initial diffusion lengths in the base and surface regions. The changes of the diffusion lengths in the surface region and the sub-regions of the base region were calculated using Eq. (V-4) upon normalization of the K(x) curve ($K(x) \alpha n_D(x)$ of Fig. V.2) to the experimentally measured values of $\tilde{K}$ (see Table V.V). The values of $\bar{K}$ for the surface region and the subregions of the base region were found to be

$$\overline{K}_p = \frac{1}{d_1}\int_o^{d_1} K(x)dx \approx 2.08X10^{-13}\ \mu^{-2}\alpha^{-1}$$

$$\overline{K}_{nI} = \frac{1}{D}\int_{d_2}^{d_3} K(x)dx \approx 1.55X10^{-12}\ \mu^{-2}\alpha^{-1}$$

$$\overline{K}_{nII} = \frac{1}{t}\int_{d_3}^{d_4} K(x)dx \approx 4.34X10^{-11}\ \mu^{-2}\alpha^{-1} \qquad \text{(V-21)}$$

$$\overline{K}_{nIII} = 0.$$

The experimental results and the curve calculated using Eqs. (V-20) and (V-21) are seen to be in qualitative agreement where the calculated curve is consistently above the measured values. This is a result of the averaging process used for the three sub-region analysis. The three sub-region model underestimates the amount of damage produced over the latter part of the α-particle track, and as a result the experimentally measured short circuit current decreases at a faster rate that the calculation. The averaging process however leads to an overestimate of the DRC concentration in sub-region I with the result that at intermediate exposure levels ($\theta \gtrsim 10^{11}$ α's) the calculation and experimental results are seen to be in relatively good agreement. Finally at high exposure levels ($\theta \gtrsim 10^{12}$ α's) the experimental results decrease at a faster rate than the calculation. This indicates that either the DRC introduction rate was underestimated for the surface region or the DRC concentration is high enough to produce substantial changes in the diffusion coefficient in the base region. It is highly probable that the calculation could be brought into better agreement with experiment by dividing the base region into a greater number of sub-regions.

Open Circuit Voltage. The fractional change in open circuit voltage with increasing exposure for a given solar cell is expected to be slower than the fractional change in short circuit current. The relation between $I_{G\alpha}$ and V_{oc} as obtained from Eq. (III-12) is

$$V_{oc} = \frac{1}{\delta} \ln\left(\frac{I_G}{I_{ol}} + 1\right). \qquad \text{(V-22)}$$

where $\delta = \lambda/A$. Figure V.15 shows that $V_{oc}/V_{oc,o}$ does indeed decrease more slowly than I_{sc}/I_{sco} for each of the three cell types.

Maximum Efficiency. During the initial period of a test run, it was not possible to obtain the complete irradiated I-V characteristics; and therefore it was necessary to construct the characteristics in this exposure interval using the same method we previously employed to determine the initial irradiated I-V characteristics. The plots of I_{sc}/I_{sco} and $V_{oc}/V_{oc,o}$ were used to get the intercepts at a given exposure level, and they were connected using the initial dark I-V characteristic of the solar cell, since this was observed to change only slightly over this exposure interval. Figures V.16 and V.17 show the irradiated I-V characteristics obtained for SiH (p-on-n) and SiJ (n-on-p) respectively where the solid dot curves are the constructed I-V characteristics, and the other curves are the measured I-V characteristics.

It was then possible to graphically calculate the exposure induced changes in the maximum power, voltage at maximum power, current at maximum power and maximum efficiency. The maximum efficiency determined from the constructed and measured irradiated I-V characteristics is presented in Figs. V.18, V.19, and V.20 as a function of exposure in the form of $\eta_{max}/\eta_{max,o}$. As expected from our previous discussion of the exposure induced changes in short circuit current, it is found that

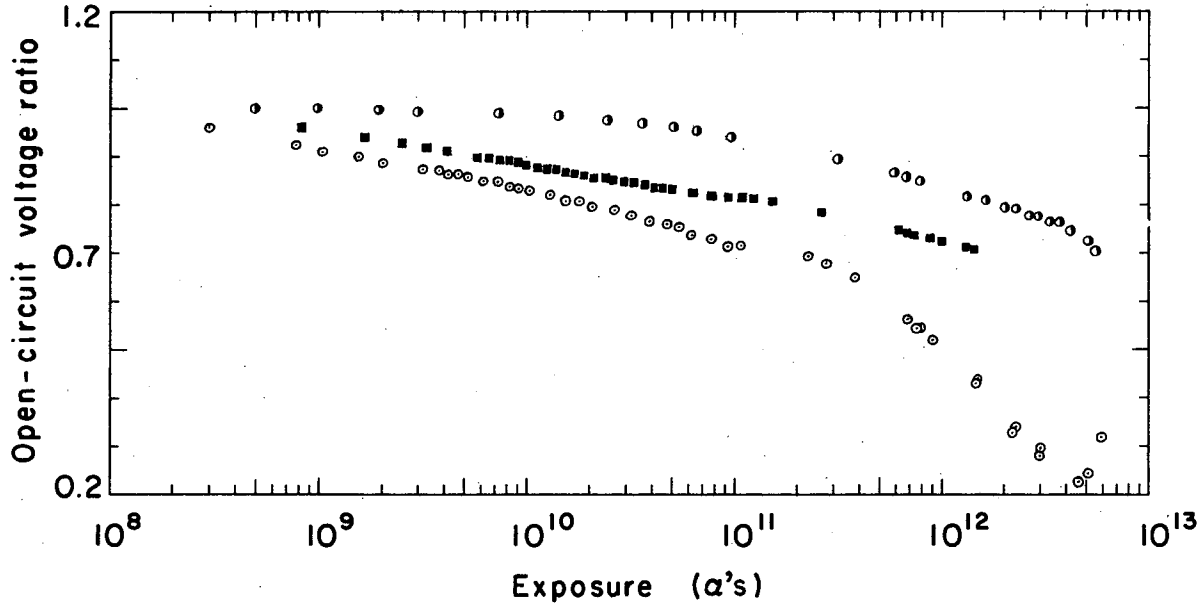

Fig. V.15. Open-circuit voltage ratio, $V_{oc}/V_{oc,o}$, vs exposure for representative cells of each type. (Key in Table V.I.)

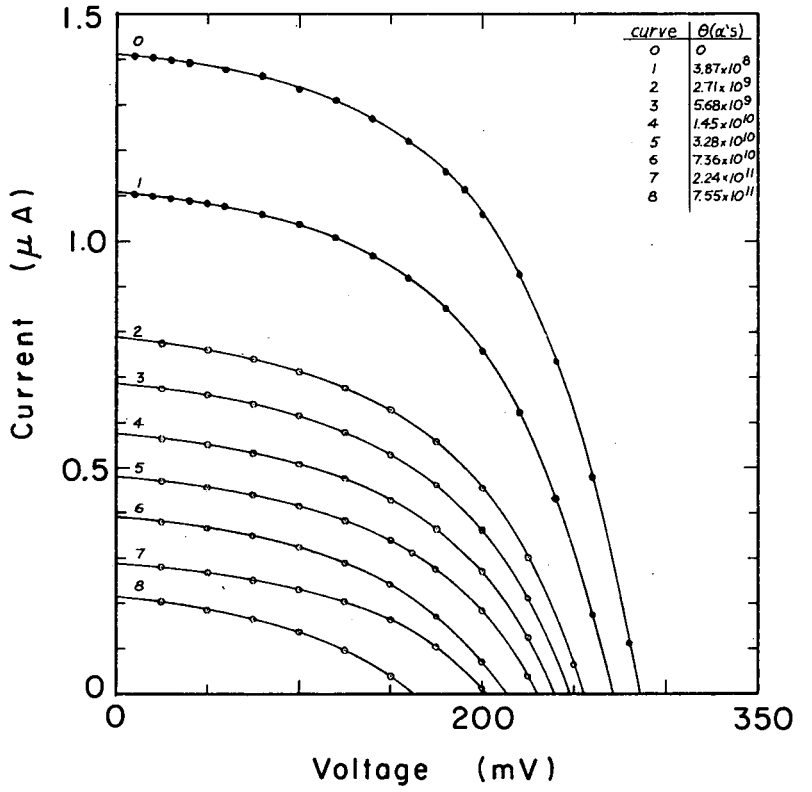

Fig. V.16. The irradiated I-V characteristics for SiH at 200°K.

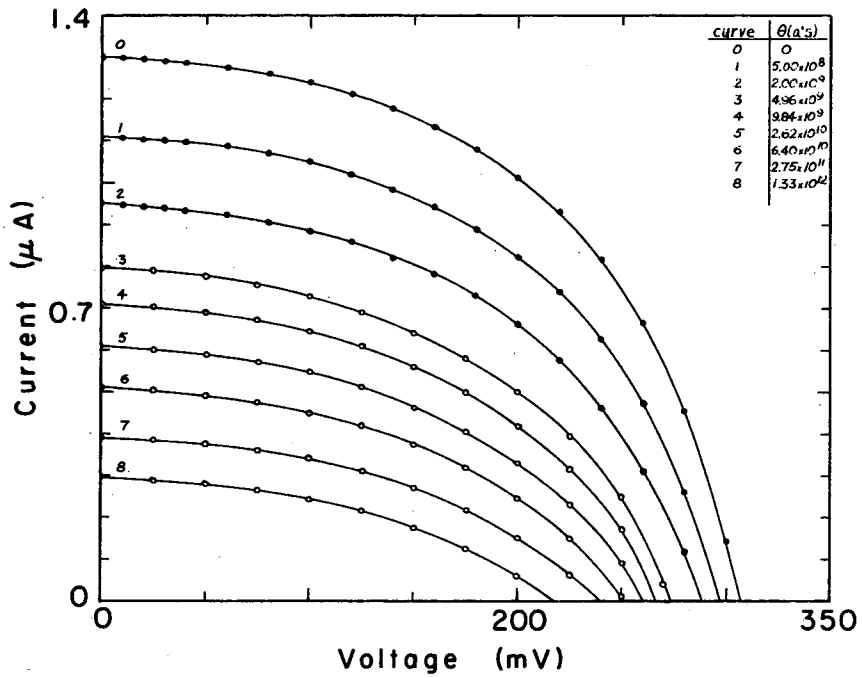

Fig. V.17. The irradiated I-V chacteristics for SiJ at 200 °K.

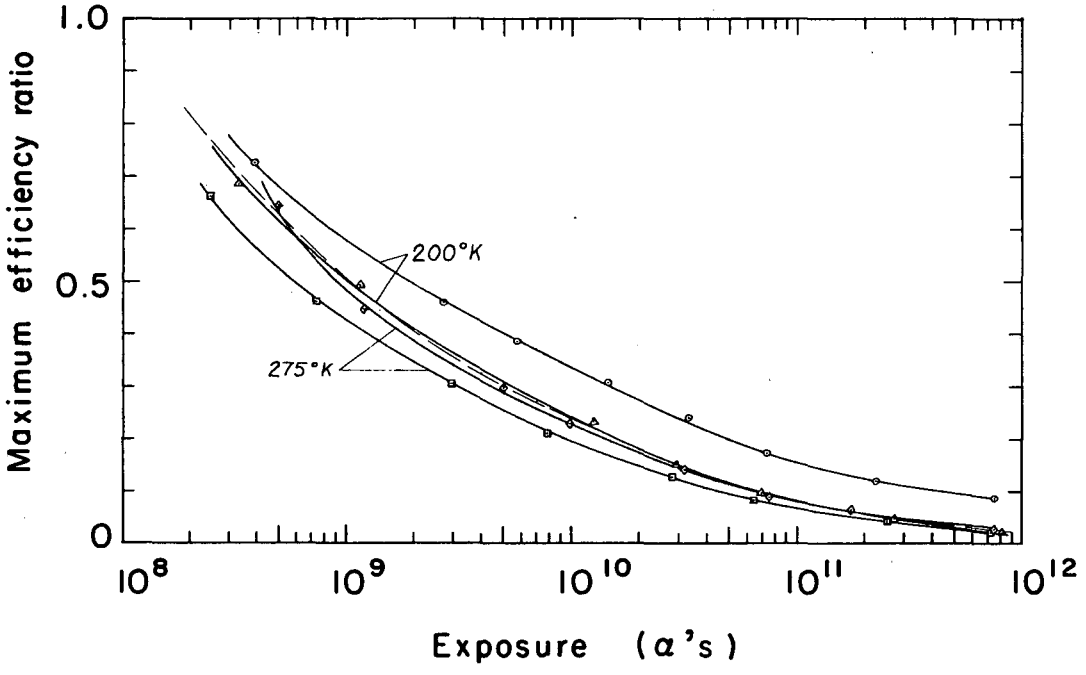

Fig. V.18. Maximum efficiency ratio, $\eta_{max}/\eta_{max,o}$, vs exposure for the p-on-n Si solar cells. (Key in Table V.I.)

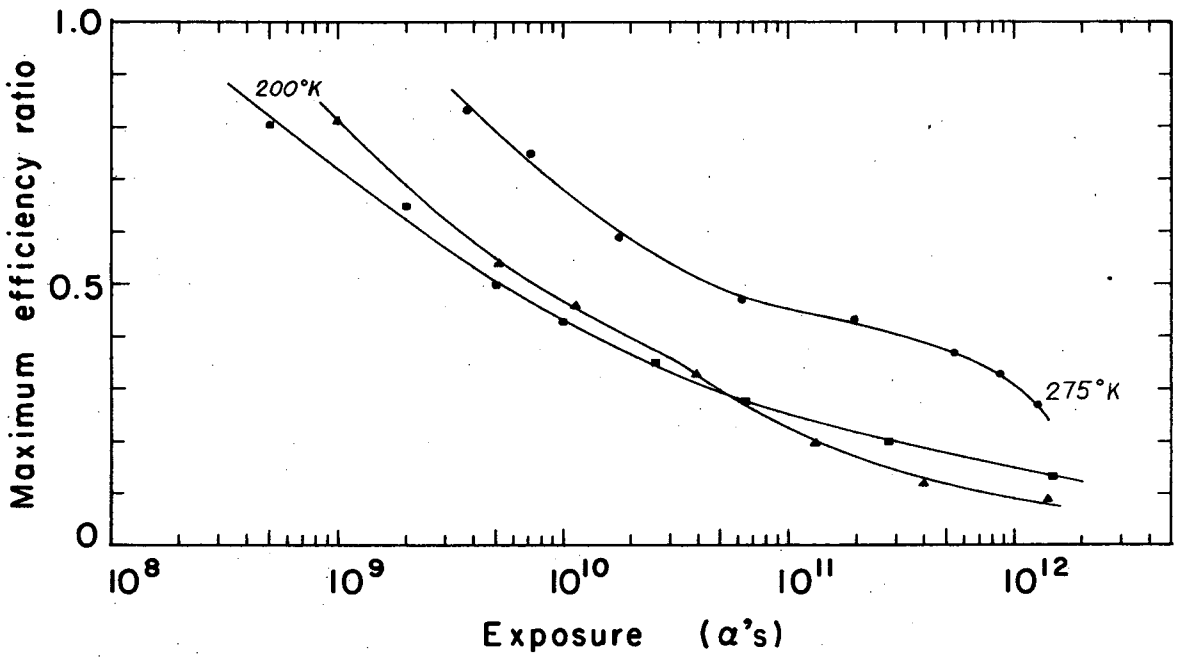

Fig. V.19. Maximum efficiency ratio, $\eta_{max}/\eta_{max,o}$, vs exposure for the n-on-p Si solar cells. (Key in Table V.I.)

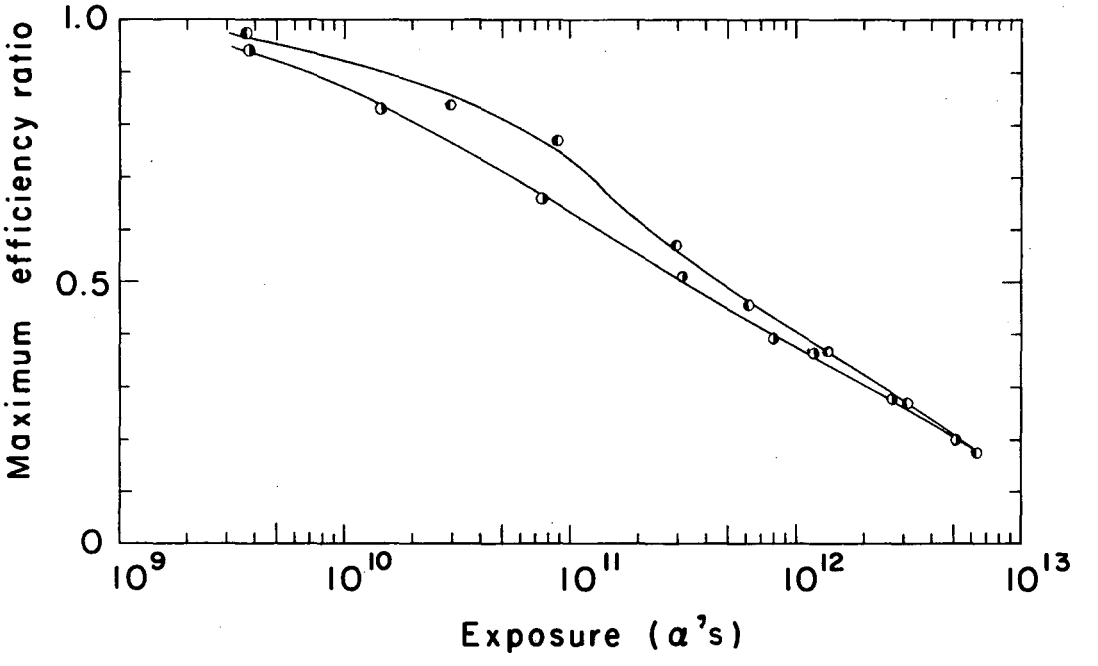

Fig. V.20. Maximum efficiency ratio, $\eta_{max}/\eta_{max,o}$, vs exposure for the p-on-n GaAs solar cells. (Key in Table V.I.)

the p-on-n GaAs solar cells and the p-on-n Si solar cells show the highest and lowest device radiation resistance respectively. In addition to changes in the alpha generated current (the alpha generated currents are equivalent to the short circuit current for the low currents encountered), the changes in the dark I-V characteristic arising from bombardment also contribute to the observed changes in maximum efficiency. This can be seen from the curve for SiR (n-on-p) in Fig. V.19 where $\eta_{max}/\eta_{max,o}$ begins to level off at $\theta \approx 10^{11}\alpha$'s, whereas I_{sc}/I_{sco} continues to decrease. This behavior resulted from a substantial improvement in the dark I-V characteristic at this exposure level (this was observed from the shape of the irradiated I-V characteristic). The dark I-V characteristic then proceeded to degenerate with the result that $\eta_{max}/\eta_{max,o}$ underwent a sharp decrease at $\theta \approx 10^{12}\alpha$'s. The maximum efficiencies for cells SiH, SiJ, and GaAs A-22 are shown in Fig. V.21 to demonstrate the fact that, although the initial maximum efficiency is the lowest for the GaAs cell, this cell would yield the greatest energy output (that is, $E_{out} = \int P_{max}(\theta)d\theta$) for exposure levels in excess of $10^{9}\alpha$'s. The harder dark I-V characteristic of the GaAs solar cell is responsible for its superior performance.

4. Diffusion Length Degradation Constant. The diffusion length degradation constant as defined in Eq. (III-28) is a continuously varying function of position where the form of this variation should have roughly the form of the lattice displacement production per α particle shown in Fig. V.2. It is evident therefore that K(x) cannot be determined from the measured changes in short circuit current unless the current contributions from every half micron or so along the α-particle track were isolated from the total current. At high exposure levels

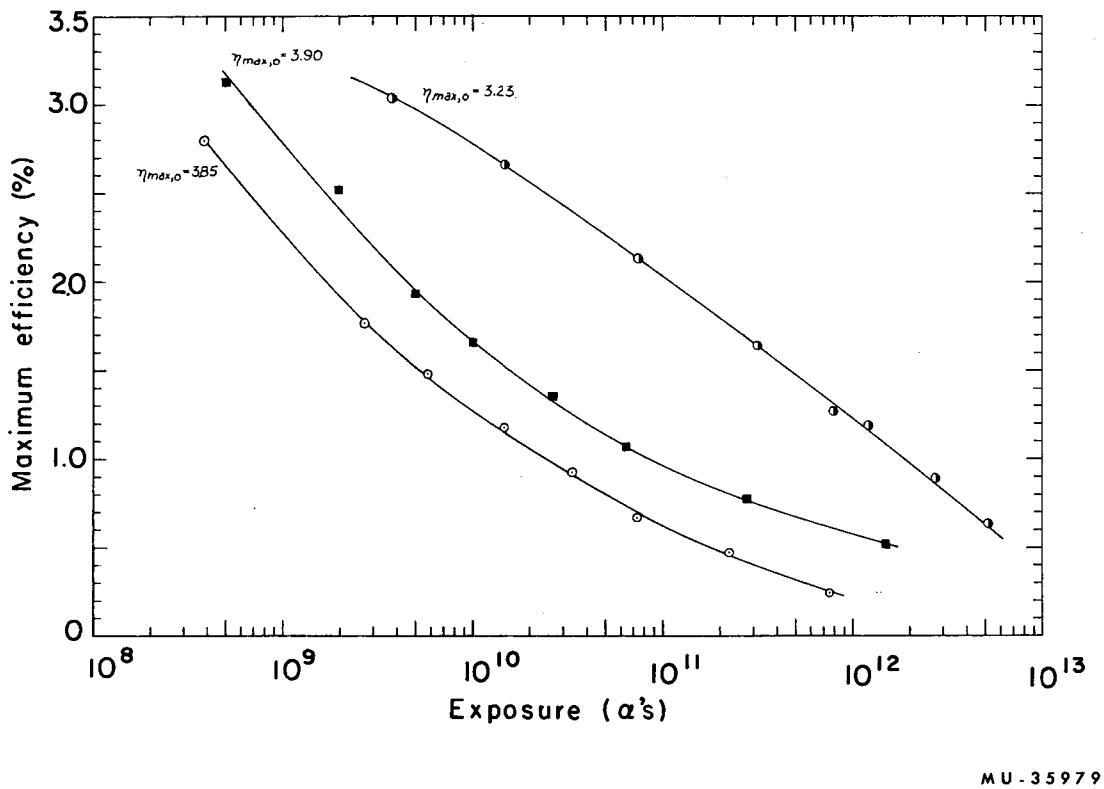

Fig. V.21. Comparison of the maximum efficiency for cells SiH (p-on-n), SiJ(n-on-p), and GaAs A-22 (p-on-n). (Key in Table V.I.)

($\theta \gtrsim 10^{11}\alpha$'s) a situation is realized for the Si solar cells in which the base region contribution to the short circuit current arises from that portion of the base region within a few mincrons of the junction-base region interface. This situation exists for all values of θ in the case of the GaAs solar cells, since they possess very short initial diffusion lengths. Now K(x) undergoes a relatively small change over the first few microns of the base region so that for these limiting cases an effective diffusion length degradation constant can be determined for this spatial interval. The effective diffusion length and effective diffusion length degradation constant are related by

$$\frac{1}{\tilde{L}^2} = \frac{1}{L_o^2} + \tilde{K}\theta(t). \qquad \text{(V-23)}$$

This is a measured effective diffusion length and is not the same as the calculated effective diffusion length defined in Eq. (V-9). In Section V.A it was found that the diffusion length degradation constant is related to the short circuit current through Eq. (V-18) providing that the exposure level has not reached the point where radiation damage in the surface region gives rise to a decrease in I_c (for all cell types this corresponds to $\theta \simeq 10^{12}\alpha$'s) but, in the case of the Si solar cells, has exceeded an exposure level of $\theta = 10^{11}\alpha$'s so that the conditions $L_{pI} < D$ and $L_{pI} < L_{po}$ will be satisfied. The second of these inequalities is in fact never satisfied for the GaAs solar cells with the result that Eq. (V-17) must be used for these cells. In light of the initial diffusion length estimated later in this section (see Table V.VII) it is permissible to use Eq. (V-18) in analyzing the short circuit current changes for the Si solar cells. Recalling that the short circuit current and α generated current are equal for the low current values encountered, we recognize that

$$I_{sc} = I_c + K_1 \theta^{-1/2} \qquad \text{(V-24)}$$

where $I_c = I_{SR} + I_J$, I_{SR} and I_J are the surface region and junction contributions to the alpha generated current respectively, and $K_1 = qg_{ob}\dot{N}_\alpha/\tilde{K}^{1/2}$.

Si Cells. Figure V.22 presents plots of I_{sc} versus $\theta^{-1/2}$ for SiJ (n-on-p) and SiO (p-on-n). A substantial linear region is seen to exist for both cells in agreement with Eq. (V-24). All the Si cells tested exhibited such a linear region where the experimental points were observed to fall below the linear curve at both high ($\theta \gtrsim 10^{12}\alpha$'s) exposure levels as can be seen in Fig. V.23 for SilO (n-on-p) and SiH (p-on-n) and low exposure levels as is evident from both figures. The deviation in the high exposure level limit is attributable to bombardment induced changes in I_{SR} and correspondingly I_c. As is expected the n-type surface region material undergoes damage faster than the p-type surface region ($\tilde{K}_n(Si) > \tilde{K}_p(Si)$, see Table V.V) which is evident from the observed decrease in I_c at lower exposure levels for the n-on-p cell. At low exposure levels the finite extent of the source term (extending only to the depth of the α-particle range) leads to measured short circuit currents less than that predicted by Eq. (V-24) where the source term was assumed to be a constant throughout the base region. In addition, the spatial variation in the diffusion length would lead to a smaller contribution to the short circuit current than predicted by Eq. (V-24), since it was derived using a constant diffusion length in sub-region I of the base region. The values of the diffusion length degradation constants and I_c determined for the Si solar cells are listed in Table V.V along with the exposure interval, estimated base region

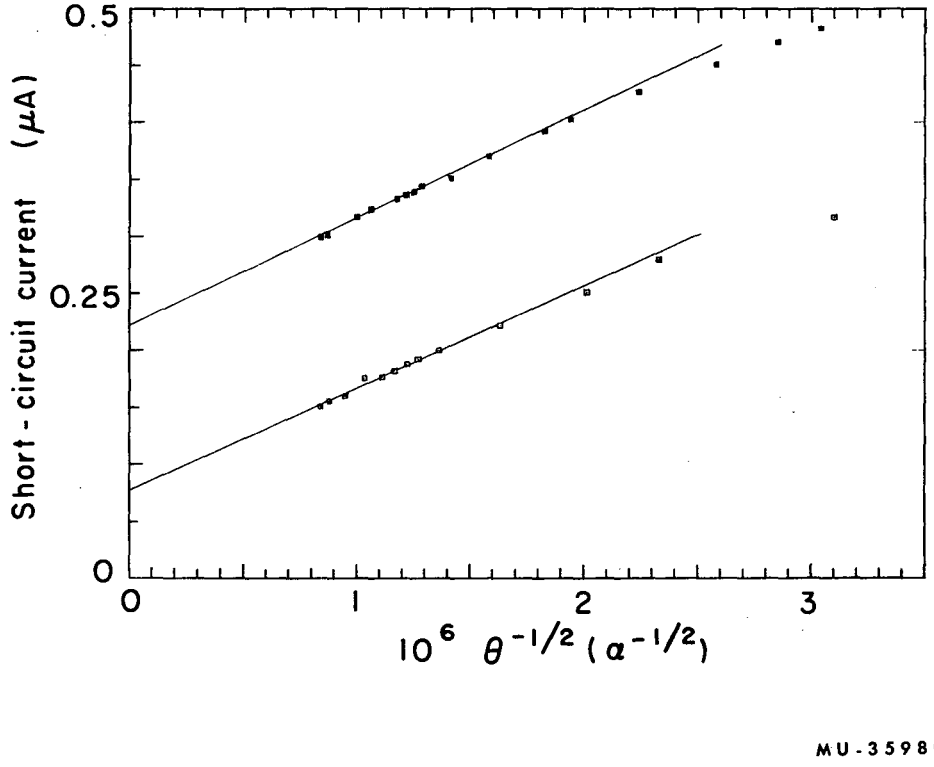

Fig. V.22. Plots of the short-circuit current, I_{sc}, vs $\theta^{-1/2}$, for SiO (p-on-n) and SiJ(n-on-p) used to determine I_c and K_1. (Key in Table V.I.)

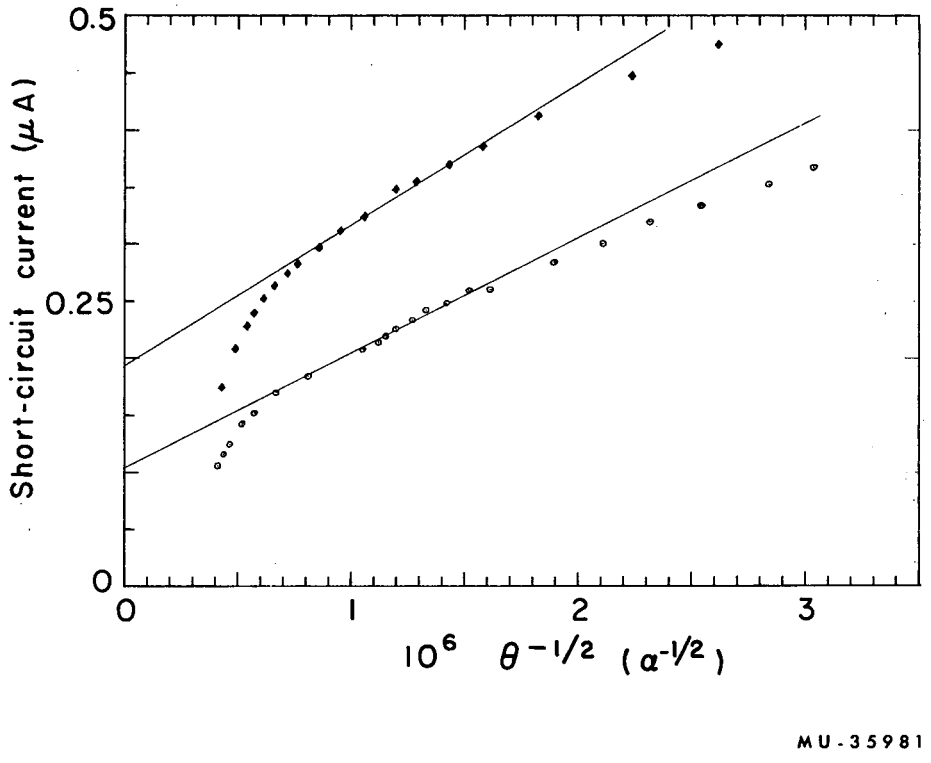

Fig. V.23. Plots of the short-circuit current, I_{sc}, vs $\theta^{-1/2}$ for SiH (p-on-n) and SilO (n-on-p) used to determine I_c and K_1. (Key in Table V.I.)

Table V.V. Silicon and gallium arsenide device and material properties determined from the bombardment-induced changes in short-circuit current.

Cell	T (°K)	$\dot{N}_\alpha$ (α's sec^{-1})	$I_{c,meas}$ (μA)	$I_{c,calc}$ (1) (μA)	K_1^{-2} (A^{-2} α^{-1})	$q\dot{N}_\alpha g_{ob}$ ($\mu A/\mu$)	$\tilde{K}$ (cm^{-2} α^{-1})	θ_i (α's)	θ_f (α's)	L_{BRi} (2) (μ)	L_{BRf} (2) (μ)	$\overline{E}_\alpha$ (MeV)
					p—on—n							
Si P	275	8.2×10^{6}	0.099	0.132	100	0.0764	5.8×10^{-5}	2.92×10^{11}	7.53×10^{11}	2.38	1.49	3.3
Si O	275	8.2×10^{6}	0.078	0.132	121	0.0764	7.1×10^{-5}	2.48×10^{11}	1.29×10^{12}	2.29	1.01	3.3
Si 4	275	8.5×10^{6}	0.107	0.137	86	0.0791	6.8×10^{-5}	3.95×10^{11}	1.09×10^{12}	2.18	1.30	3.3
Si G	200	8.2×10^{6}	0.090	0.132	128	0.0764	7.5×10^{-5}	2.66×10^{11}	8.12×10^{11}	2.19	1.27	3.3
Si H	200	8.6×10^{6}	0.104	0.136	98	0.0801	7.9×10^{-5}	3.87×10^{11}	1.49×10^{12}	1.96	1.00	3.3
					n—on—p							
Si R	275	8.0×10^{6}	0.270	0.130	39	0.0745	2.2×10^{-5}	3.72×10^{11}	1.25×10^{12}	3.41	1.85	3.3
Si 10	275	8.0×10^{6}	0.194	0.130	66	0.0745	3.7×10^{-5}	4.00×10^{11}	1.34×10^{12}	2.58	1.40	3.3
Si K	200	8.2×10^{6}	0.190	0.132	62	0.0764	3.6×10^{-5}	3.00×10^{11}	7.00×10^{11}	3.01	1.95	3.3
Si J	200	8.2×10^{6}	0.222	0.132	111	0.0764	6.5×10^{-5}	2.65×10^{11}	1.00×10^{12}	2.36	1.24	3.3
					p—on—n							
GaAs A-21	275	8.2×10^{6}	0.084	—	500	0.0835	3.5×10^{-4}	1.57×10^{10}	7.16×10^{11}	1.20	0.55	3.0
GaAs A-22	200	8.2×10^{6}	0.120	—	600	0.0835	4.9×10^{-4}	1.48×10^{10}	6.80×10^{11}	1.94	0.48	3.0

(1) I_c for the silicon cells was calculated assuming $d_1 = 1.5\ \mu$, $d_2 = 2\ \mu$, and using the diffusion lengths given in Table V.III, in conjunction with the curves of Figs. V.26 and V.27 and I_J from Table V.VII.

(2) The diffusion lengths were estimated from $L_{BR}(\theta) = (q\dot{N}_\alpha g_{ob})^{-1} [I_{sc}(\theta) - I_c]$.

diffusion lengths at the extremes of the interval, and the average α-particle energy.*

An error analysis was performed on SiO and the results assumed to be typical of all the cells. A least squares fit was applied to the data of Fig. V.22 using only the points in the interval $0.8X10^{-6} \lesssim \theta^{-1/2} \lesssim 2X10^{-6}$. The slope and intercept and their associated variances resulting from the spread in the data were found to be $I_c = 0.078 \pm 0.006\mu A$ and $K_1 = 0.091 \pm 0.004\mu A\ \alpha^{1/2}$. These results are quite sensitive to the specific points chosen for the least squares fit. We feel however that the set of points selected is close enough to the proper set that any uncertainties arising from this choice will yield accuracy errors less than or on the order of the precision errors. The precision error in the measurement of I_c was determined from the spread in data points and the variance in $\theta^{-1/2}$ which is

$$(\sigma_{\theta-1/2})^2 = (\frac{\partial\theta^{-1/2}}{\partial \dot{N}_\alpha})^2(\sigma_{\dot{N}_\alpha})^2 = (-\frac{1}{2}\theta^{-1/2})^2(\frac{\sigma_{\dot{N}_\alpha}}{\dot{N}_\alpha})^2 \qquad (V\text{-}25)$$

or

$$(\frac{\sigma_{\theta-1/2}}{\theta^{-1/2}}) = \frac{1}{2}(\frac{\sigma_{\dot{N}_\alpha}}{\dot{N}_\alpha}) = \pm 2.2\%$$

---

* The measured value of $\tilde{K}$ is most heavily weighted by K(x) within the first diffusion length from the junction. Therefore $\bar{E}_\alpha$ was determined from Fig. B.20 at a position

$$x = d_2 + \frac{1}{2}(L_{BRi} + L_{BRf}).$$

The error in E_α corresponding to $\pm\frac{1}{2}(L_{BRi} + L_{BRf})$ was found to be approximately ± 0.3MeV.

where $(\sigma_{\dot{N}_\alpha}/\dot{N}_\alpha) = \pm 4.4\%$ (see Appendix E). The variance in $\theta^{-1/2}$ will be greatest for the upper limit of the interval employed so that a somewhat conservative estimate of $\sigma_{\theta-1/2} = \pm .004 \times 10^{-6} A\, \alpha^{1/2}$. Since the effective diffusion length degradation constant is

$$\tilde{K} = \left(\frac{1}{K_1}\right)^2 (q\dot{N}_\alpha g_{ob})^2, \qquad \text{(V-26)}$$

the variance is given by

$$\left(\frac{\sigma_{\tilde{K}}}{\tilde{K}}\right)^2 = 4\left[\left(\frac{\sigma_{K_1}}{K_1}\right)^2 + \left(\frac{\sigma_{\dot{N}_\alpha}}{\dot{N}_\alpha}\right)^2 + \left(\frac{\sigma_{g_{ob}}}{g_{ob}}\right)^2\right]. \qquad \text{(V-27)}$$

The variances in K_1 and $\dot{N}_\alpha$ have already been specified so that the only variance remaining to be determined is $\sigma_{g_{ob}}$. The value of g_{ob} used in the calculation of $\tilde{K}$ was 20% below the curve of Fig. V.1 at the junction-base region interface ($d_2 = 2\mu$) and 30% high at a position 8μ into the base region. The errors present at positions farthest removed from the junction are not as important as those close to the junction, since these remote regions are not as effective in contributing to the alpha generated current as the portion of the base region within a diffusion length or so of the junction (the base region diffusion lengths encountered are on the order of one to three microns). We therefore thought it reasonable to weight the deviation at position x by the factor $\exp(-x/L_{BR})$ where the source term can be fairly well approximated by $g_\alpha(x) = (50.1 + 1.4x) \times 10^3$ eh/μ over the interval $2\mu \lesssim x \lesssim 10\mu$. The average spread deviation in this interval is then found to be

$$D = \frac{\int_{d_2}^{l'} [g_\alpha(x) - g_{ob}]^2 \exp(-\frac{x}{L_{BR}})dx}{\int_{d_2}^{l'} \exp(-\frac{x}{L_{BR}})dx}$$

$$= \frac{(1.4\text{X}10^{3})^{2}}{[1 - \exp(-\frac{l'-d_2}{L_{BR}})]} \left\{ [(t-d_2)^2 - 2L_{BR}(t-d_2) + 2L_{BR}^2] \right.$$

$$\left. - [(l'-t)^2 + 2L_{BR}(l'-t) + 2L_{BR}^2] \exp(-\frac{l'-d_2}{L_{BR}}) \right\} \qquad \text{(V-28)}$$

where t is the position at which $g_{\alpha}(x) = g_{ob}$. For $L_{BR} \approx 3\mu$ (representative of the values encountered at higher $\theta^{-1/2}$), the variance in g_{ob} is found to be $\sigma_{g_{ob}}/g_{ob} \approx D^{1/2}/g_{ob} \approx \pm 5.5\%$. Then the precision error in $\tilde{K}$ is $\sigma_{\tilde{K}}/\tilde{K} \approx \pm 16\%$. We have not as yet considered the systematic error introduced by the angular and energy spread of the source employed in the experimental work. From our previous discussion of these properties of the source, it is evident the value of g_{ob} used in the above analysis is smaller than the actual electron-hole pair source term. It is difficult to ascertain the magnitude of this error, but we feel that a total error of about ± 25% might easily be realized.

In order to check the justification of the approximations used in deriving Eq. (V-24) we shall look at the case of SiJ in detail. The diffusion length in the exposure interval over which $L_{nI} \approx K_1\theta^{-1/2}$ was estimated from the relation that $L_{nI}g_{ob} \approx [I_{sc}(\theta) - I_c]$ where g_{ob} is the average electron-hole pair production rate for the interval $d_2 = 2\mu$ to 10μ (all diffusion lengths were found to be less than 10μ for $\theta > 10^{11}\alpha$'s). In particular it was found that $L_{nI} = 2.36\mu$ at $\theta = 2.65\text{X}10^{11}\alpha$'s and $L_{nI} = 1.24\mu$ at $\theta = 1.00\text{X}10^{12}\alpha$'s for SiJ.

The value of D is 16μ for the assumed value of $d_2 = 2\mu$ and therefore $D/L_{nI} > 2$ is indeed satisfied for all $\theta \gtrsim 2.65\text{X}10^{11}\alpha$'s. In addition the average values of K in sub-regions I and II of the base region as

calculated from $n_D(x)$ given in Fig. V.2 lead to an expected diffusion length ratio of

$$\frac{L_{nII}}{L_{nI}} \approx \left(\frac{K_{nI}}{K_{nII}}\right)^{1/2} \approx 0.189 \qquad \text{(V-29)}$$

with the result that $L_{nII} \approx 0.45\mu < t/2 = 1.5\mu$ at $\theta = 2.65X10^{11}\alpha's$. Therefore the conditions that $L_{nII} < t/2$ and $L_{nII} < L_{nI}$ are also satisfied for this cell. The condition that $L_{nI} < L_{no}$ is satisfied as can be seen from Table V.VII for the estimated initial diffusion lengths. The next condition to be checked is that of

$$\left(\frac{L_{nII}}{L_{nI}}\right) \frac{1}{\cosh\left(\frac{D}{L_{nI}}\right)} \ll 1, \qquad \text{(V-30)}$$

and for the two exposure level limits we find that this term is equal to .0002 at $\theta = 2.65X10^{11}\alpha's$ and essentially zero at $\theta = 1.00X10^{12}\alpha's$. Therefore the neglect of this term is justified, and the only approximation left to be considered is that of the assumed constancy of the electron-hole pair source term. The validity of this approximation was ascertained by comparing the $\tilde{K}$ and I_c values obtained from Fig. V.22 with those obtained from Eq. (V-14) where the second term in the base region contribution is neglected in comparison to the first. Then

$$I_{sc}(\theta) - I_c = L_{nI}(\theta)\left[X_{nI}(d_2) + L_{nI}(\theta)X_n'(d_2) \right] \qquad \text{(V-31)}$$

where $X_n(x) = a+bx = (50.1+1.4x)x10^3 eh/\mu$ is a good representation of the electron-hole pair production rate from the solar cell surface to a depth of approximately 10μ. Using this form for $X_n(x)$ and the fact that $L_n(\theta) \approx \tilde{K}\theta^{-1/2}$, Eq. (V-31) becomes

$$I_{sc}(\theta) = I_c + \left[\frac{q\dot{N}_\alpha(a+bd_2)}{\tilde{K}^{1/2}}\right]\theta^{-1/2} + \left[\frac{q\dot{N}_\alpha b}{K}\right]\theta^{-1}. \qquad (V\text{-}32)$$

Therefore we used the method of least squares to fit the experimental data with a polynomial of the form

$$I_{sc}(\theta) = I_c + K_1\theta^{-1/2} + K_2\theta^{-1/2} \qquad (V\text{-}33)$$

with the result that the fitting constants were found to be I_c=0.210μA, $K_1 = 0.113\mu A\ \alpha^{1/2}$, and $K_2 = -7.10X10^{3}\mu A\ \alpha$. The value of I_c is in good agreement with $I_c = 0.222\pm0.017\mu A$ given in Table V.V. The negative value of K_2 is unacceptable in light of the arguments made leading to Eq. (V-36); namely, the assumed constancy of the diffusion length in the base region. As mentioned previously the downward concavity of the curve is a result of the decrease in diffusion length with distance from the junction. The effective diffusion length degradation constant as found from K_1 is $\tilde{K} = 3.80X10^{-5}cm^{-2}\alpha^{-1}$ as compared with the value of $(6.48\pm1.04)X10^{-5}cm^{-2}\alpha^{-1}$ given in Table V.V. The substantial discrepancy between these two values is a result of the improper weighting of the experimental data at large $\theta^{-1/2}$ through the constant K_2. We therefore feel that the least squares fit with Eq. (V-24) yields the most meaningful results.

From the results presented in Table V.V we find that K_n for the p-on-n Si solar cells shows no preceptible temperature dependence within the experimental error. The results for the n-on-p Si cells indicate that K_n is approximately a factor of two greater than K_p(275°K) and only slightly greater than K_p(200°K) if at all.

Comparison with Other Work. Values of the diffusion length degradation constant as measured for electron and proton bombardment of Si solar cells

are listed in Table V.VI. We shall make a direct comparison of our results with the 8.3MeV proton data given in Table V.VI only. At this proton energy Eqs. (B-49) and (B-50) of Appendix B yield $\kappa \simeq 1.5$ and $\zeta \simeq 1.2\text{X}10^{-4}$ for proton stopping in Si. Therefore, it is expected that the scattering process can be represented to a fair degree of accuracy by the classical Rutherford scattering cross section (see Appendix B). In fact, the QM Rutherford scattering cross section must be used for $\kappa < 1$; and since $\sigma_{DR}(QM) < \sigma_{DR}(C)$, the ratio of the lattice displacement production rate for 3.3 MeV α particles and 8.3 MeV protons is therefore expected to be (see Eq. (B-69))

$$R_{LD} \leq \frac{\bar{\nu}_p(8.3\text{MeV})\sigma_{DR,p}(8.3\text{MeV})}{\bar{\nu}_\alpha(3.3\text{MeV})\sigma_{DR,\alpha}(3.3\text{MeV})} \qquad \text{(V-34)}$$

Providing that the same type of defect recombination center is produced by both particle types, the diffusion length degradation constant ratio is identical to that in Eq. (V-34); that is,

$$\frac{K_{n,p}(8.3)}{K_{n,\alpha}(3.3)} = R_{LD} \leq \left(\frac{z_p}{z_\alpha}\right)^2 \left(\frac{E_\alpha}{E_p}\right)\left(\frac{M_p}{M_\alpha}\right)\left(\frac{\bar{\nu}_{R,p}}{\bar{\nu}_{R,\alpha}}\right) = 0.013 \qquad \text{(V-35)}$$

where Eq. (B-67) was used to obtain $\bar{\nu}$. Using the average value of $\tilde{K}_n = 7\text{X}10^{-5}\text{cm}^{-2}\alpha^{-1}$ from Table V.V and the area of diodes tested in this work in Eq. (V-35), the anticipated value of K_n for 8.3MeV protons (assuming identical defect recombination centers) is found to be $K_{n,p}(8.3) \lesssim 2\text{X}10^{-6}\text{p}^{-1}$ is an order of magnitude below the measured values presented in Table V.VI. Similarly the predicted value of $K_{p,p}(8.3) \lesssim 8\text{X}10^{-7}\text{p}^{-1}$ is an order of magnitude below the measured value. It is therefore evident that protons are more effective at producing damage in Si than are α-particles.

Table V.VI. Diffusion length degradation constants for electron and proton bombardment of silicon solar cells.

Cell type	Base region resistivity	Bombarding particle type and energy		
W. Rosenzweig[a]		1-MeV electrons	16.8-MeV protons	130-MeV protons
n-on-p	1Ω cm	$1.8\times10^{-10}e^{-1}$	$8.3\times10^{-7}p^{-1}$	$3.3\times10^{-7}p^{-1}$
n-on-p	10Ω cm	$5.8\times10^{-11}e^{-1}$	---	---
p-on-n	1Ω cm	$2.6\times10^{-9}e^{-1}$	$5.1\times10^{-6}p^{-1}$	$2.0\times10^{-7}p^{-1}$
W. Rosenzweig et al.[b]		1-MeV electrons		
p-on-n	- -	$1.22\times10^{-8}e^{-1}$		
n-on-p	- -	$1.70\times10^{-10}e^{-1}$		
J. A. Baicker and B. W. Faughnan[c]		8.3 MeV protons		19 MeV protons[f]
p-on-n[d]	- -	1.4 to $3.6\times10^{-5}p^{-1}$		1.8 to $12.4\times10^{-5}p^{-1}$
n-on-p	- -	0.6 to $3\times10^{-5}p^{-1}$		0.2 to $0.44\times10^{-5}p^{-1}$
p-on-n[e]	- -	- -		0.28 to $2.4\times10^{-5}p^{-1}$
n-on-p	- -	- -		0.14 to $0.4\times10^{-5}p^{-1}$

(a) W. Rosenzweig, Bell Sys. Tech. J. 41, 1573 (1962).
(b) W. Rosenzweig, H. K. Gummel, and F. M. Smits, Bell Sys. Tech. J. 42, 399 (1963).
(c) J. S. Baicker and B. W. Faughnan, J. Appl. Phys. 33, 3271 (1962).
(d) These values were determined from changes in L.
(e) These values were determined from changes in τ.
(f) These values of K were obtained from the values of λ quoted by Baicker and Faughnan using a diffusion length of $D = 5\ cm^2\ sec^{-1}$.

GaAs Cells. The situation for the p-on-n GaAs solar cells is complicated by the fact that L_{po}^{-2} cannot be neglected in comparison to $\tilde{K}\theta$ (these cells possess substantially shorter base region diffusion lengths than the Si cells) as was the case for the Si solar cells. Let us for the time being return to Eq. (V-5) for the alpha generated current where it is possible to use for $X(x)=a+bx$ as a result of the short initial diffusion lengths. Using the estimates of the initial diffusion lengths in the base region listed in Table V.VII, we find that $D/L_{pI} \gtrsim 4$ so that the base region contribution to the alpha generated current becomes

$$\left(\frac{I_{G\alpha}}{qN_{\alpha}}\right)_{BR} = L_{pI}[X_p(d_2)+L_{pI}X'_p(d_2)]-\left(\frac{\Delta_1}{\Delta_1+\Delta_2}\right)\frac{L_{pI}[X_p(d_3)+L_{pI}X'_p(d_3)]}{\cosh\left(\frac{D}{L_{pI}}\right)} \quad (V\text{-}36)$$

where $\cosh\left(\frac{D}{L_{pI}}\right) \gtrsim 30$ for $D/L_{pI} \gtrsim 4$. Making use of the supplementary fact that $L_{pII} < L_{pI} \simeq L_{po}$, it can be shown that $\Delta_1/(\Delta_1+\Delta_2) \lesssim 1/2$ and therefore $\Delta_1\cosh\left(\frac{D}{L_{pI}}\right)/(\Delta_1+\Delta_2) \lesssim 1/60$. In addition $b < a$, $L_{pI} \simeq 2\mu$, and we have chosen $d_2 = 1.5\mu$ so that

$$\left[X_p(d_3)+L_{pI}X'_p(d_3)\right] \simeq \left[X_p(d_2)+L_{pI}X'_p(d_2)\right] \quad . \quad (V\text{-}37)$$

Therefore the second term in Eq. (V-36) can be neglected and the alpha generated current becomes

$$\left(\frac{I_{G\alpha}}{qN_{\alpha}}\right) \simeq L_n g_{os}\left[\frac{M_n(d_1)-1}{K_n(d_1)}\right] + [H(d_2)-H(d_1)] + L_{pI}g_{ob} \quad (V\text{-}38)$$

where it has further been assumed that the electron-hole pair source terms in the surface and base regions can be approximated by the constants g_{os} and g_{ob} respectively.

We shall one again assume the surface region and junction contributions to the alpha generated current to be reasonably constant over the early

stages of exposure. Then the measured short circuit current for the GaAs solar cells ($I_{sc} < 10^{-6}$ amps) is

$$I_{sc} = I_c + L_{pI}(q\dot{N}_\alpha g_{ob}) \tag{V-39}$$

or

$$(I_{sc}-I_c)^{-2} = (q\dot{N}_\alpha g_{ob})^{-2} L_{pI}^{-2} = (q\dot{N}_\alpha g_{ob})^{-2}[L_{po}^{-2} + \tilde{K}\theta]$$

$$= (I_{sco}-I_c)^{-2} + K_1^{-2}\theta \ . \tag{V-40}$$

Finally let us rewrite this equation in the form

$$I_{sc}(\theta) = I_c + K_1[\theta + \theta_o]^{-1/2} \tag{V-41}$$

where $\theta_o = K_1^2(I_{sco} - I_c)^{-2}$. This is analagous to Eq. (V-24), and the values of I_c and K_1 can be obtained from a plot of I_{sc} versus $[\theta+\theta_o]^{-1/2}$. Since θ_o depends upon I_c and K_1, it is first necessary to estimate I_c and K_1 and then determine first corrections from the plot of I_{sc} versus $[\theta+\theta_o]^{-1/2}$. This iteration process is to be continued until only minor changes are observed in the values of I_c and K_1 from one iteration to the next. In the application of this technique a number of points must be kept in mind. The initial short circuit current must lie above the curve of Eq. (V-41), since the analysis leading to this equation did not properly account for the increase in the electron-hole pair production rate with depth of penetration. Soon after the start of bombardment the minority carrier diffusion length in the base region undergoes a substantial decrease over that portion of the base region associated with the latter portion of the α-particle track. As mentioned in the discussion of the results for the Si solar cells, this situation leads to a lower measured value of the short circuit current than predicted

by Eq. (V-41). At sufficiently high exposure levels the measured short circuit current must decrease below that predicted by Eq. (V-41) as a result of the decrease in I_c. A knowledge of the exposure level at which the current contribution from the surface region begins to diminish is of the utmost importance if one is to achieve a precise determination of K_1 and to a lesser degree of I_c.

The curves resulting from the aforementioned iterative technique are shown in Fig. V.24 for the two GaAs cells tested, and the measured values of I_c and $\tilde{K}$ are listed in Table V.V. The curves for both cells exhibit the anticipated shape although the choice of the data points used for the determination of I_c and K_1 is a rather nebulous affair. In an effort to be consistent the measured value of $\tilde{K}$ for the base region (i.e. $\tilde{K}_n \approx 3.5X10^{-4}$ $cm^{-2}\alpha^{-1}$ for GaAs A-21) was used to estimate the value of $\tilde{K}$ for the p-type surface region. This was accomplished by assuming $\tilde{K}_n$ for GaAs to be approximately two to three times that of $\tilde{K}_p$ as was found to be the case for Si. We therefore expect to observe a noticeable decrease in the measured short circuit current at an exposure level where $\tilde{K}_p\theta \simeq L_{no}^{-2}$. Using the estimated initial surface region diffusion lengths listed in Table V.VII, this condition is seen to correspond to $\tilde{K}_p\theta \simeq 1$ or $\theta \simeq 1X10^{11}$ which corresponds to a value of $10^6[\theta+\theta_o]^{1/2} \simeq 1.0$ which is in reasonably good agreement with the curve in Fig. V.24. This kind of semi-quantitative agreement is also realized for GaAs A-22. It is only possible to give rough estimates for the possible errors in I_c and $\tilde{K}$ when this iterative process is used. We feel that the value of K_1^{-2} may be in error by as much as ±30%. I_c is less sensitive to the set of data points chosen for the fit, and the error in this quantity is estimated to be on the order of ±10%.

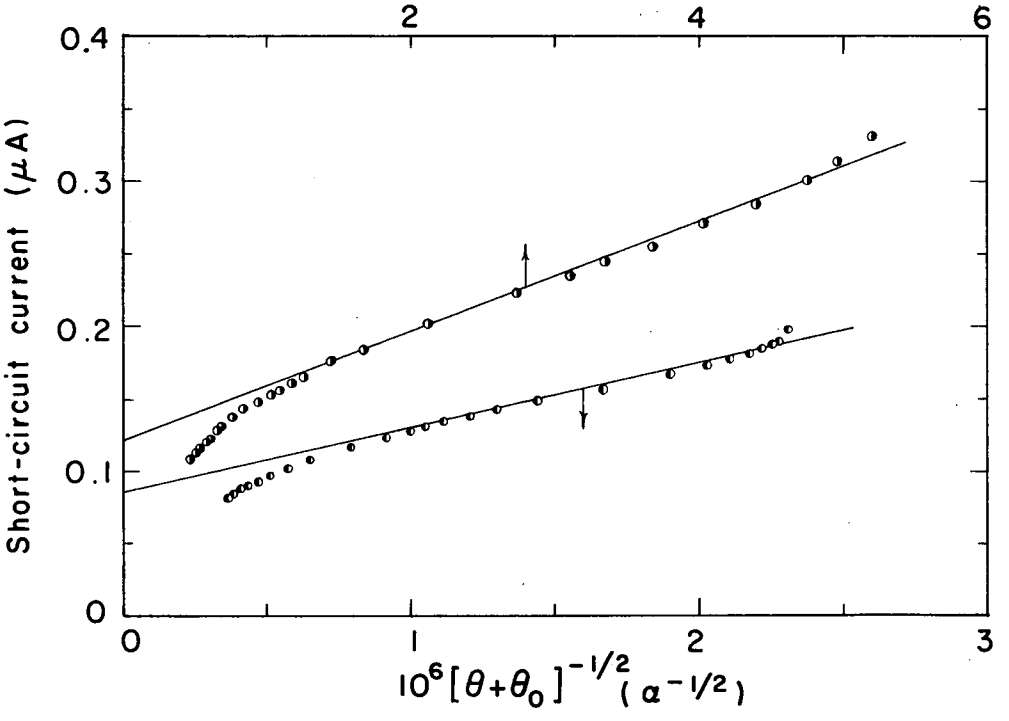

Fig. V.24. Plots of the short-circuit current, I_{sc}, vs $(\theta+\theta_o)^{-1/2}$ for GaAs A-22 and GaAs A-21 used to determine I_c and K_1. (Key in Table V.I.)

A more precise determination of I_c and $\tilde{K}$ might be realized using what might be called a self-consistent iterative technique. This would include a determination of I_c and K_1 following the technique outlined above. The additional steps are then as follows: (1) Calculate the bombardment induced changes in I_{SR} from the initially determined value of $\tilde{K}_n$ using

$$I_{SR}(\theta) = I_{sc}(\theta) - I_J - \tilde{K}_n\theta \,, \qquad \text{(V-42)}$$

(2) Use the charge collection efficiency corresponding to a given $I_{SR}(\theta)$ in conjunction with the curves of Fig. V.27 to obtain $L_{SR}(\theta)$, (3) Plot $\left[L_{SR}(\theta)\right]^{-2}$ as a function of θ and determine $\tilde{K}_p$ for the surface region, (4) From $\tilde{K}_p$ and the estimated value of L_{no} determine the exposure level at which noticeable changes in I_c occur, and then (5) Modify the set of points used to determine the initial $\tilde{K}_n$ and I_c accordingly and repeat the complete sequence of steps. It is also possible that the technique could be further improved through the use of $X(x) = a+bx$ and the polynomial fit of $I_{sc}(\theta)$ discussed in connection with Eq. (V-31).

It is reasonable to assume that this technique could be applied to the data for SiH and SiIO in order to estimate the diffusion length degradation constants for the highly doped surface regions of these cells. In the application of this technique to any of the cells tested it is important to know the surface region thickness; and as this was not measured in the present work (once the solar cells were passed into the glove box for the irradiation, they could not be removed), the experimental results were not analyzed using this more sophisticated technique.

Electron-Hole Pair Production in GaAs. In the process of obtaining $\tilde{K}$ from the measured value of K_1, it was necessary to estimate the electron-hole pair production rate in GaAs. There was no experimental data available for the stopping power of α particles in GaAs so that it

was necessary to use the information available for Ge. We feel this is not a bad approximation, since Ga and As bracket Ge in the periodic table and the data for Ge was only used for high α-particle energies where the complex nature of minimum excitation energy transitions is of minor importance. Gobeli[27] measured the range-energy curve for 0.7 to 5 MeV α-particle stopping in Ge and found that

$$R(\mu) = 1.95\ [E(\text{MeV})]^{1.34} + 1.72. \qquad \text{(V-43)}$$

This relation was used to construct the stopping power curve presented in Fig. V.25 where the assumed average stopping powers in the surface and base regions are shown. The electron-hole pair production rates associated with these averages are $g_{os} = 6.05\text{X}10^{4}$ eh/μ and $g_{ob} = 6.35\text{X}10^{3}$ eh/μ and hold for $d_1 = 1\mu$ and $d_2 = 1.5\mu$. The surface region thickness was chosen to coincide with the nominal thickness specified by the manufacturer. In order to determine the electron-hole pair production rate from the stopping power, it was necessary to assume a value of ϵ for GaAs, since the only measured value for GaAs, that of $\epsilon = 6.3$ eV, is known to be in error.* It has been found from the measured values of ϵ for a number of insulating and semiconducting materials that the quantity $(\epsilon - E_g)$ is approximately a constant value.[43] The value for ϵ was then obtained from

$$\epsilon = E_g + (\epsilon - E_g) \simeq 1.4 \text{ eV} + 2.6 \text{ eV} = 4.0 \text{ eV} . \qquad \text{(V-44)}$$

This value of ϵ led to the g_{os} and g_{ob} quoted above. g_{ob} was in turn used to find the values of I_c and $\tilde{K}$ listed in Table V.V, and both were

---

* H. Pfister, Z. Naturforschg. 12, 217 (1957). The value of ϵ was measured using low energy electron bombardment of GaAs diodes (junction depth $\simeq 10\mu$). The incomplete charge carrier collection resulting from the relatively impure material employed led to a high value for ϵ.

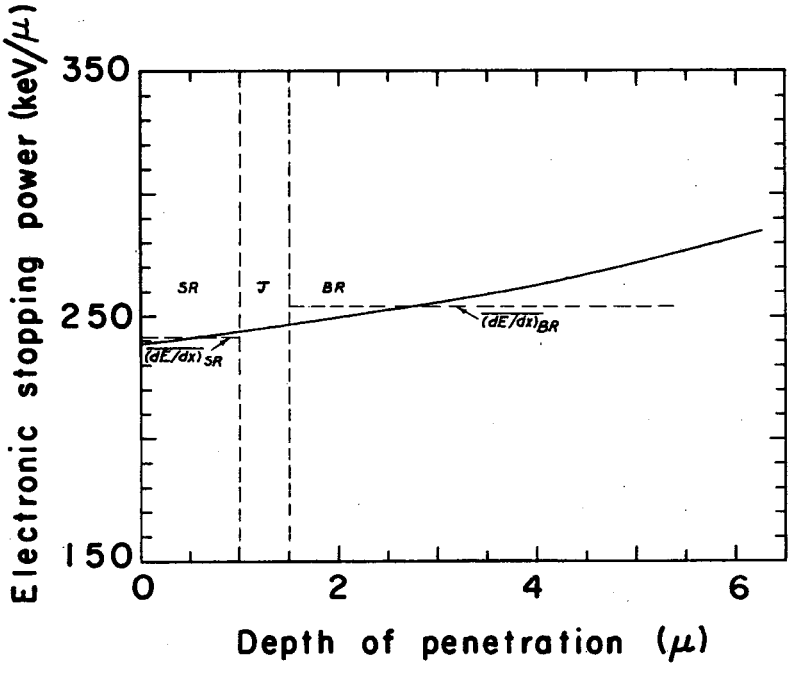

Fig. V.25. Stopping power for 4-Mev α-particles in Ge from Gobeli.[27]

used in estimating the initial diffusion lengths given in Table V.VII. On the basis of these approximations, it is estimated that $\sigma_G/G \approx \pm 15\%$. Therefore, the error in $\tilde{K}$ for GaAs is expected to be about $\pm 35\%$ not including the systematic error resulting from the angular and energy spread of the alpha source.

A comparison of the results presented in Table V.V shows that n-type GaAs exhibits a much greater sensitivity to radiation damage than either type Si material. Inasmuch as data was available on only two cells, it is not possible to draw any meaningful conclusions as to the temperature dependence of $\tilde{K}_n$ for GaAs.

5. Initial Diffusion Length Estimates. Having determined the initial surface region plus junction contribution to the short circuit current, it was then possible to estimate the initial diffusion lengths in the surface and base regions for each test cell. The initial base region diffusion length, L_{BRo}, was estimated comparing the measured $(I_{sco} - I_c)$ with that calculated from the base region contribution to Eq. (V-7). The calculations were performed for various values of d_2 but with the identical $d_3 = 18\mu$, and the corresponding charge collection efficiencies are shown in Fig. V.26 with d_2 as a parameter. The estimated values of L_{BRo} are presented in Table V.VII along with the base region charge collection efficiency. The initial surface region diffusion lengths, L_{SRo}, were estimated from $(I_c - I_J)$ (the junction width was assumed to be 0.5μ in all cases) and the surface region contribution to the alpha generated current as given in Eq. (V-16). The calculations were carried out for various values of d_1, and the results are presented in Fig. V.27 with d_1 as a parameter. The estimated values of L_{SRo} are listed in Table V.VII along with the measured surface region charge collection efficiency. The value of d_1 which yields the most reasonable estimates of L_{SRo} for the

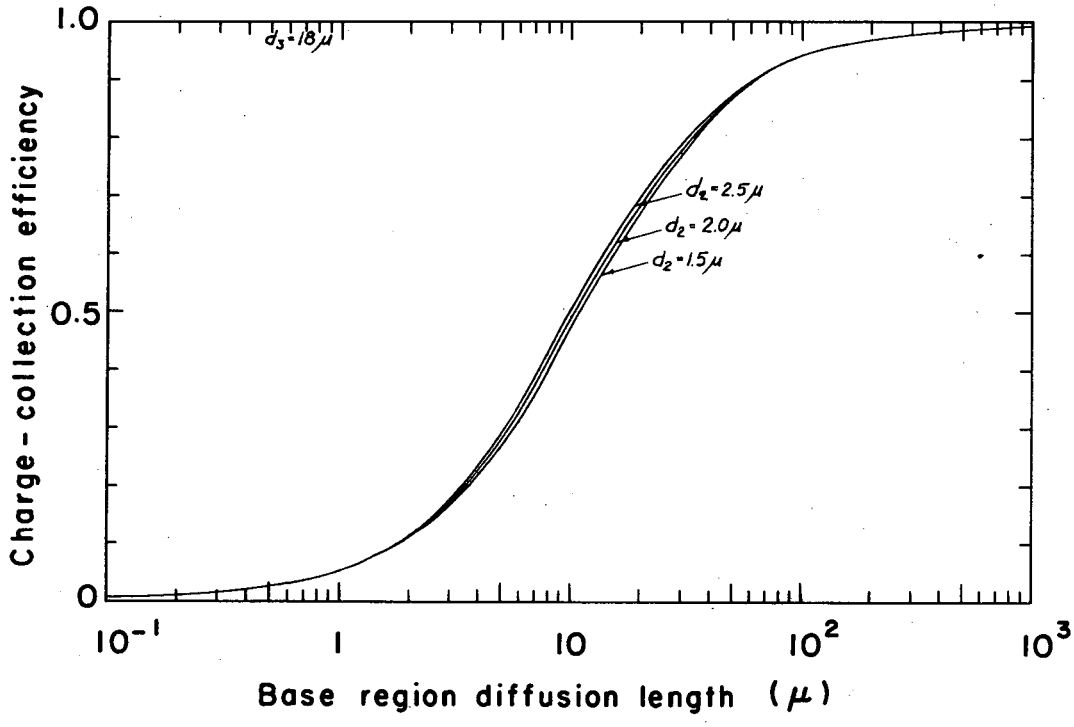

Fig. V.26. Base region charge collection efficiency, Q_{BR}, from Eq. (V-7) for α-particle stopping in Si.

Table V.VII. Initial charge collection efficiencies and initial diffusion length estimates for the surface and base regions of the silicon and gallium arsenide solar cells.

Cell	I_{sco} (μA)	I_c (μA)	$I_{sco}-I_c$ (μA)	d_1 (μ)	I_J (μA)	I_{SR} (μA)	$I_{SR,max}$ (μA)	Q_{SR}	L_{SRo} (μ)	d_2 (μ)	$I_{BR,max}$ (μA)	Q_{BR}	L_{BRo} (μ)
Si P	1.29	0.099	1.191	1.0	0.0341	0.0649	0.0668	0.971	--	1.5	1.372	0.869	51
				1.5	0.0345	0.0645	0.1008	0.640	1.14	2.0	1.337	0.892	59
				2.0	0.0349	0.0641	0.1353	0.474	1.01	2.5	1.303	0.915	71
Si O	1.31	0.078	1.232	1.0	0.0341	0.0439	0.0668	0.657	0.78	1.5	1.372	0.899	62
				1.5	0.0345	0.0435	0.1008	0.432	0.67	2.0	1.337	0.923	77
				2.0	0.0349	0.0431	0.1353	0.318	0.65	2.5	1.303	0.946	107
Si 4	1.37	0.107	1.263	1.0	0.0353	0.0717	0.0692	--	--	1.5	1.422	0.888	58
				1.5	0.0358	0.0712	0.1045	0.681	1.27	2.0	1.385	0.913	69
				2.0	0.0362	0.0708	0.1403	0.505	1.08	2.5	1.352	0.934	88
Si H	1.41	0.104	1.306	1.0	0.0357	0.0683	0.0701	0.974	--	1.5	1.440	0.906	67
				1.5	0.0362	0.0678	0.1057	0.641	1.14	2.0	1.401	0.931	85
				2.0	0.0366	0.0674	0.1419	0.475	1.01	2.5	1.368	0.955	125
Si G	1.31	0.090	1.220	1.0	0.0341	0.0559	0.0668	0.836	1.43	1.5	1.372	0.889	58
				1.5	0.0345	0.0555	0.1008	0.551	0.91	2.0	1.337	0.914	70
				2.0	0.0349	0.0551	0.1353	0.408	0.85	2.5	1.303	0.936	90
Si R	1.30	0.269	1.031	2.0	0.0340	0.2350	0.1320	--	--	2.5	1.271	0.811	33
				3.0	0.0349	0.2341	0.2000	--	--	3.5	1.202	0.859	42
				4.0	0.0358	0.2332	0.2705	0.861	--	4.5	1.136	0.909	66
Si 10	1.28	0.194	1.086	2.0	0.0340	0.1600	0.1320	--	--	2.5	1.271	0.855	43
				3.0	0.0349	0.1591	0.2000	0.795	4.60	3.5	1.202	0.903	60
				4.0	0.0358	0.1582	0.2705	0.585	2.80	4.5	1.136	0.956	125
Si K	1.29	0.190	1.100	2.0	0.0349	0.1551	0.1353	--	--	2.5	1.303	0.845	41
				3.0	0.0358	0.1542	0.2056	0.751	3.60	3.5	1.232	0.894	53
				4.0	0.0367	0.1533	0.2777	0.553	2.50	4.5	1.163	0.946	105
Si J	1.30	0.222	1.078	2.0	0.0349	0.1871	0.1353	--	--	2.5	1.303	0.826	36
				3.0	0.0358	0.1862	0.2056	0.907	--	3.5	1.232	0.875	47
				4.0	0.0367	0.1853	0.2777	0.669	3.70	4.5	1.163	0.927	80
GaAs A-21	0.198	0.084	0.114	1.0	0.0403	0.0437	0.0795	0.550	0.50	1.5	1.194	0.095	1.37(a)
				1.5	0.0408	0.0432	0.1198	0.361	0.36	2.0	1.153	0.099	1.34(b)
GaAs A-22	0.330	0.120	0.210	1.0	0.0403	0.0797	0.0795	--	--	1.5	1.194	0.176	2.51(a)
				1.5	0.0408	0.0792	0.1198	0.661	1.20	2.0	1.153	0.182	2.48(b)

(a) Estimated from $I_{BRo} \approx q\dot{N}_a g_{ob} L_{BRo}$, where $g_{ob} \approx 6.35 \times 10^4$ eh/μ

(b) Estimated from $I_{BRo} \approx q\dot{N}_a g_{ob} L_{BRo}$, where $g_{ob} \approx 6.45 \times 10^4$ eh/μ

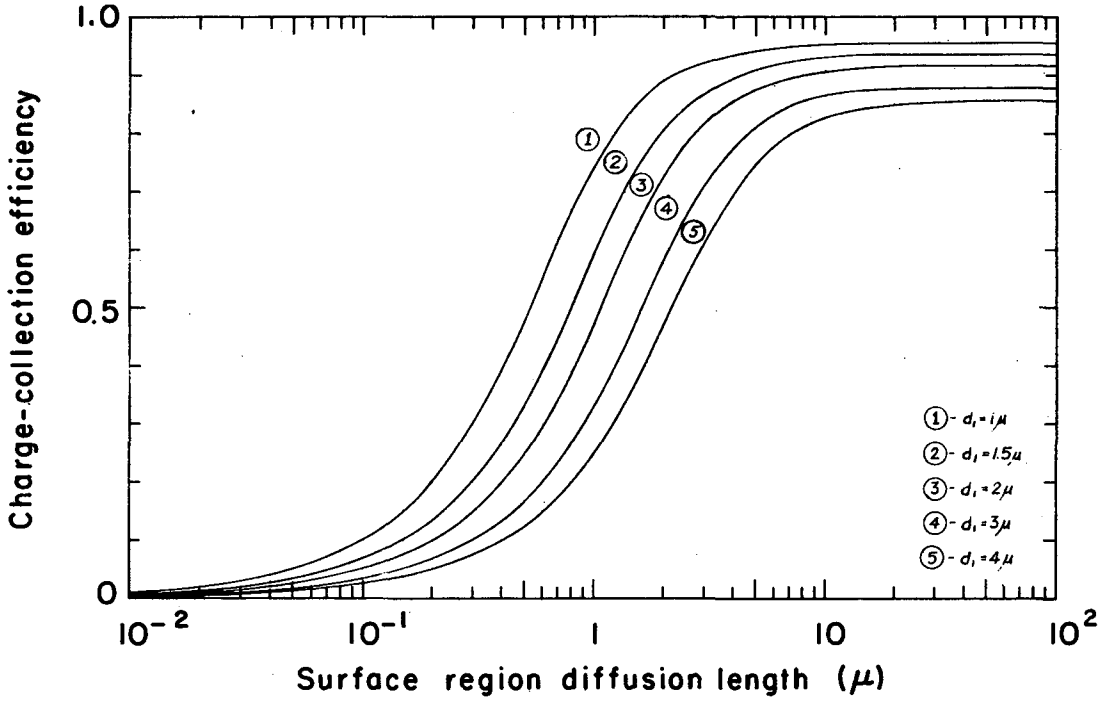

Fig. V.27. Surface region charge-collection efficiency, Q_{SR}, from Eq. (V-16) for α-particle stopping in Si.

p-on-n Si cells is 1.5μ which is within the 1 to 2μ interval estimated by the manufacturer. A surface region thickness on the order of 3.0μ is required in order to account for the larger values of I_c measured for the n-on-p Si cells, since the junction current contribution is expected to be approximately the same for both types of Si cells. The values of L_{SRo} obtained in this manner are also higher than expected on the basis of the manufacturers' estimates. These discrepancies for the n-on-p Si cells cannot be resolved at the present time. The GaAs cells most probably have a junction depth of slightly over 1μ as this situation leads to estimates of L_{SRo} in good agreement with the 0.5 to 1μ quoted by the manufacturer.

6. Bombardment Induced Changes in the Dark I-V Characteristics. In our previous discussion the bombardment induced changes in the short circuit current were attributed to decreases in the minority carrier lifetimes and corresponding diffusion lengths of the surface layer and base region. It is therefore quite clear that such changes should also lead to an increase in the current arising from the various mechanisms contributing to the dark I-V characteristic. From Eq. (IV-2) of Section IV.A we can see that the ideal term of the dark I-V characteristic should increase with increasing exposure, since it depends upon L_n^{-1} and L_p^{-1}. The junction recombination-generation current increases as τ_{no} and τ_{po} decrease as can be seen from Eq. (IV-6). These two currents should therefore undergo noticeable changes at roughly the same exposure level. In addition, a surface inversion layer current, if present, will be modified at approximately this same exposure level, since it depends at least in part upon the bulk material properties. It is also possible that a fraction of the defect recombination centers produced during bombardment participate in the tunneling mechanism and thus produce an

increase in this current contribution to the non-ideal term of the dark I-V characteristic. The exposure level at which this increase occurs need not be the same as that required to produce changes in the three current mechanisms mentioned above. This is to be expected inasmuch as the initial magnitude of the tunneling current depends upon the initial concentration of impurity atoms which possess energy states capable of contributing to the tunneling process, whereas the currents controlled by the diffusion and recombination processes are controlled by the initial concentration of recombination centers. The concentrations of these two types of impurity centers are not in general the same.

The dark I-V characteristics measured prior and subsequent to bombardment are shown in Figs. V.28 through V.30 for one cell of each type at the two test temperatures. Only diode I-V characteristics (see Section IV for the definition of the diode and junction I-V characteristic) are presented as it was not possible to measure junction I-V characteristics subsequent to bombardment owing to the substantial reduction in the minority carrier lifetime of the base region and, to a lesser degree, of the surface layer. Therefore the magnitude of these changes in I_o could not be ascertained, and in addition changes in R_{SH} were not determined, since the reliability of these values would be questionable as mentioned in the Section IV.D. The values of I_{o1} and δ for the non-ideal current term were however estimated from the measured dark I-V characteristics, and the results are presented in Table V.VIII. The technique used to estimate I_{o1} and δ can best be described by making reference to the pre-bombardment dark I-V characteristic of SiG of Fig. V.28. The current shows an initially rapid increase at low applied bias. This is followed by what is approximately a simple exponential

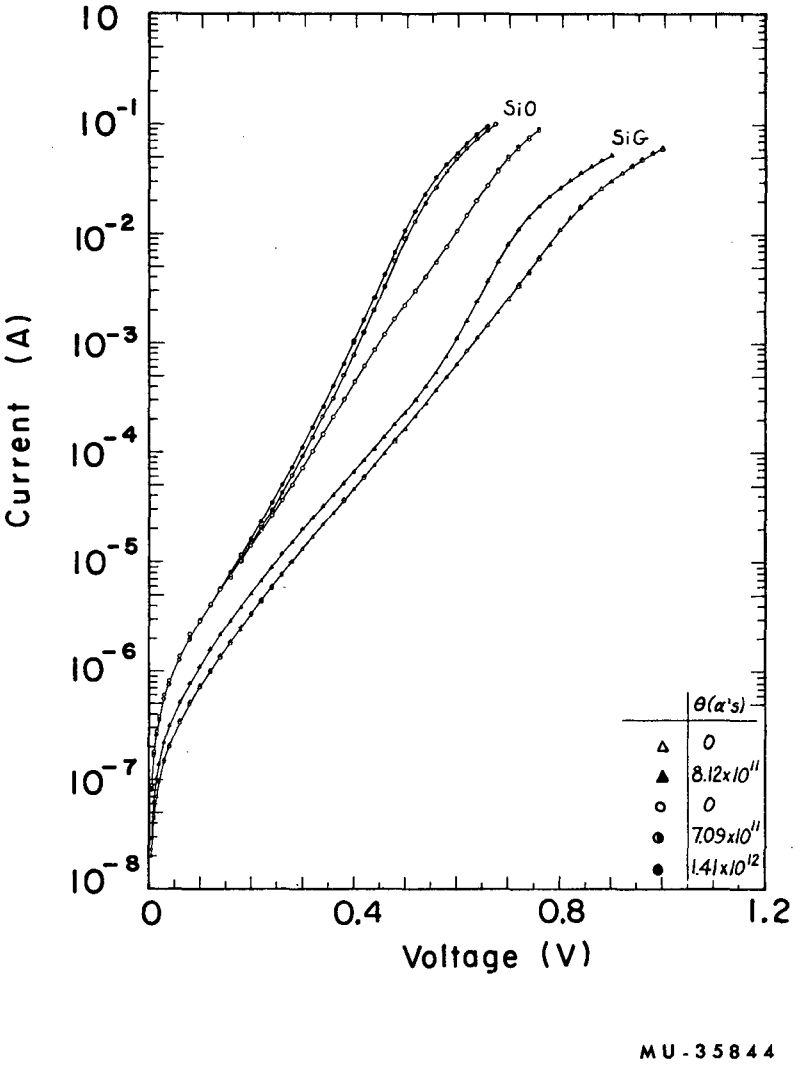

Fig. V.28. Pre- and postbombardment dark I-V characteristics for p-on-n cells SiG and SiO.

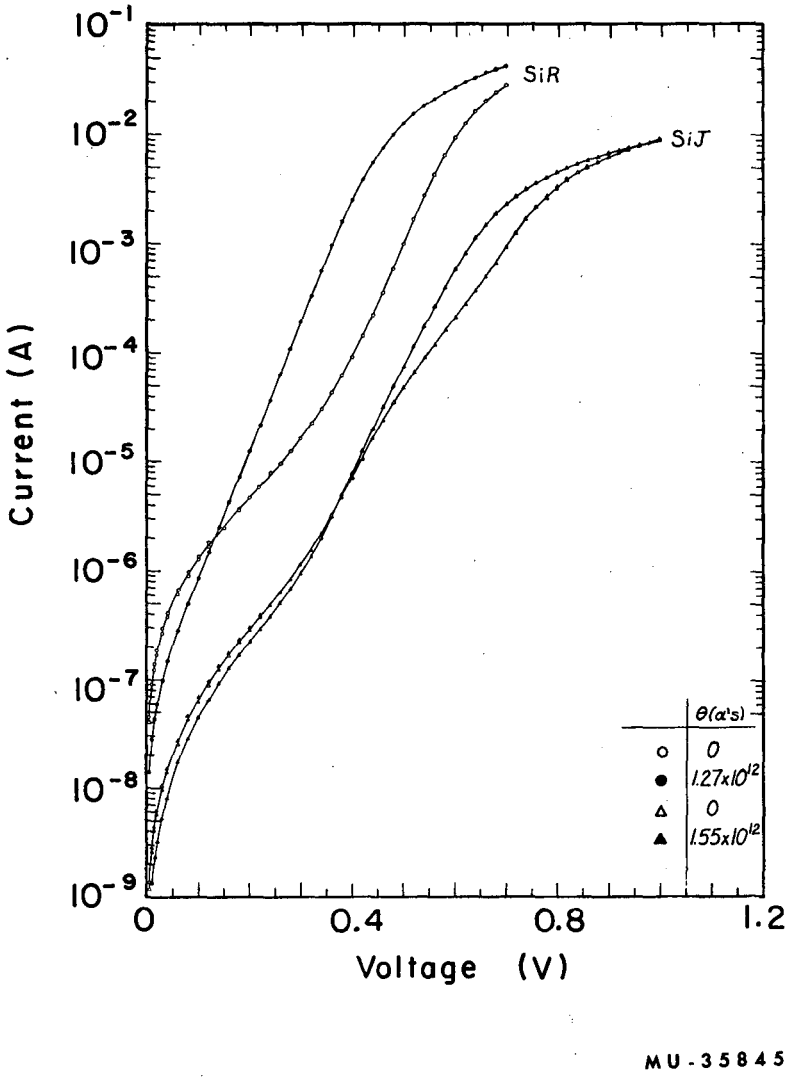

Fig. V.29. Pre- and postbombardment dark I-V characteristics for n-on-p cells SiR and SiJ.

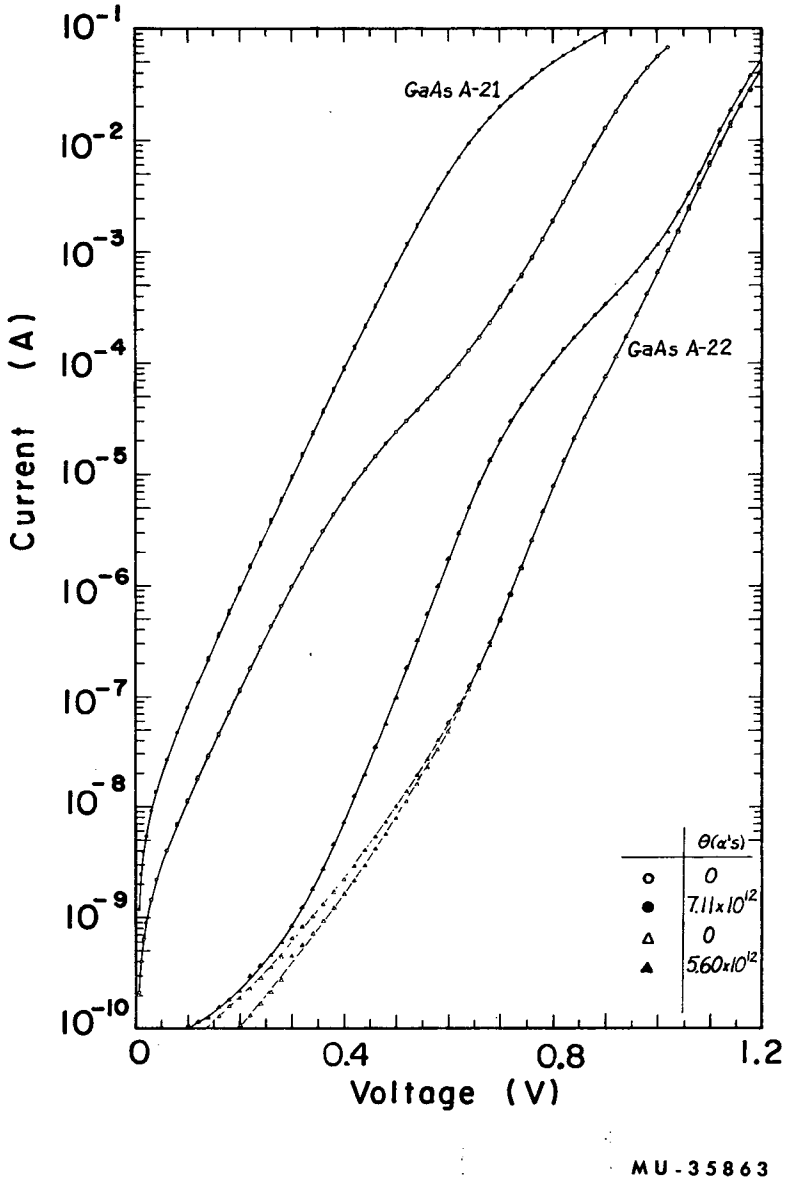

Fig. V.30. Pre- and postbombardment dark I-V characteristics for the GaAs solar cells.

Table V.VIII. Values of I_{o1}, δ, and A for the solar call pre- and post-bombardment dark I-V characteristics.

Cell	T(°K)	$\lambda(V^{-1})$	θ(a's)	I_{o1}(A)	$\delta(V^{-1})$	A
Si P	275	42.5	0	1.45×10^{-6}	16.0	2.66
			7.53×10^{11}	1.63×10^{-6}	16.3	2.61
Si 4	275	42.5	0	1.40×10^{-6}	14.5	2.93
			1.21×10^{12}	1.85×10^{-6}	15.4	2.75
Si O	275	42.5	0	3.53×10^{-7}	17.7	2.40
			7.09×10^{11} (a,b)	2.00×10^{-7}	20.5	2.07
			1.41×10^{12} (a,b)	2.17×10^{-7}	20.8	2.04
Si G	200	58.0	0	3.00×10^{-7}	12.5	4.62
			8.12×10^{11}	4.85×10^{-7}	12.3	4.72
Si H	200	58.0	0	1.53×10^{-8}	16.2	3.58
			3.72×10^{11}	1.38×10^{-8}	16.0	3.63
			1.49×10^{12} (c)	--	--	--
			2.99×10^{12}	2.16×10^{-9}	20.8	2.79
			5.95×10^{12}	5.19×10^{-11}	27.3	2.12
Si R	275	42.5	0 (d)	1.50×10^{-8}	21.9	1.94
			1.27×10^{12}	5.65×10^{-8}	26.7	1.59
Si 10	275	42.5	0 (a)	2.65×10^{-7}	15.3	2.78
			5.40×10^{12}	4.00×10^{-7}	25.0	1.70
Si K	200	58.0	0	6.28×10^{-10}	20.2	2.87
			1.35×10^{12}	3.00×10^{-10}	27.6	2.10
Si J	200	58.0	0 (a)	2.48×10^{-9}	20.0	2.90
			1.55×10^{12}	7.80×10^{-10}	23.1	2.51
GaAs A-21	275	42.5	0 (a)	1.27×10^{-9}	22.3	1.91
			7.11×10^{12}	9.10×10^{-9}	23.1	1.84
GaAs A-22	200	58.0	0	2.57×10^{-15}	27.2	2.13
			5.60×10^{12}	6.80×10^{-14}	28.3	2.05

(a) Was not possible to find semilog region of sizable extent.

(b) Despite the fact that I_{o1} decreased, the current at a given voltage either increased or remained unchanged.

(c) Was not possible to isolate a simple exponential in the intermediate voltage region.

(d) The values are of questionable reliability, since the selected semilog region was quite short.

dependence over a substantial voltage interval, and then at high applied bias the ideal exponential term begins to make its appearance only to be overshadowed by the IR_s internal voltage drop with the result that the I-V characteristic tails off at high voltage (this behavior is even more evident in the post-bombardment I-V characteristic for SiG). From our previous experience at fitting the dark I-V characteristics of similar solar cells in Section IV, we knew that a good estimate of I_{ol} and δ for the non-ideal term of the dark I-V characteristic could be obtained from the slope and the intercept (extrapolating the curve to V=0) of that portion of the measured I-V characteristic exhibiting a simple exponential behavior. Some of the characteristics exhibited an approximately simple exponential dependence over more than one voltage interval as is the case for the pre-bombardment I-V characteristic of SiR. The GaAs A-21 pre-bombardment and GaAs A-22 post-bombardment I-V characteristics exhibited an even more complex behavior. In determining the appropriate region to use in these cases, the low voltage portion of the I-V characteristic was not employed (this is the voltage region where the shunt conductance current would make a contribution) and likewise that portion at higher voltages where the ideal current term begins to make itself felt. Comments relating to any difficulty encountered in determining I_{ol} and δ for a given I-V characteristic are included as footnotes to Table V.VIII.

Ideal Current Term. The figures show that the current at high voltage does show a substantial increase after bombardment for all cell types with the exception of the post-bombardment I-V characteristic for GaAs A-22. The complex shape of this characteristic may result from bombardment induced changes in resistivity (presumably in the base region)

which nearly offset the increase expected in the ideal term. The results are threfore in general agreement with the theoretical prediction that the ideal term should increase substantially with exposure. At very high voltages the current tail-off is seen to be more pronounced for the post-bombardment than for the pre-bombardment I-V characteristics (in particular see the characteristics for SiJ, Fig. V.29). This behavior indicates that the series resistance increased during exposure. On the basis of the theoretical calculation for the lattice displacement production per α particle (see Fig. V.2), we expect the increase in series resistance to be primarily associated with radiation damage to the base region.

Non-Ideal Current Term. In discussing bombardment induced changes in the intermediate voltage portion of the I-V characteristic, it is necessary to consider each cell type separately. From Fig. V.30 and Table V.VIII it is seen that for the GaAs cells δ is nearly independent of exposure, while I_{o1} undergoes a substantial increase and in addition $A \approx 2$. This type of behavior can be accounted for on the basis of all the mechanisms discussed in Section IV in connection with the non-ideal current term.

The n-on-p Si cells exhibit quite unexpected changes in their dark I-V characteristics. We see from Fig. V.29 that in contrast to predictions based upon any of the current producing processes mentioned thus far the current decreased with exposure in the low voltage region. This behavior may be compatible with a current producing mechanism associated with surface states which at a sufficiently high exposure level are "passivated" or rendered incapable of further contribution to the current passed by the solar cell. In addition we see from Table

V.VIII that the post-bombardment values for δ correspond more closely to an A of 2 than for the pre-bombardment situation. It is not unreasonable to expect the junction recombination-generation current to make a substantial contribution to the non-ideal term subsequent to bombardment, since it is inversely proportional to the minority carrier lifetime (this has been found to decrease substantially during exposure), and in addition the other contribution to the non-ideal term is found to be diminished subsequent to bombardment.

The p-on-n Si solar cell dark I-V characteristics behave in a more conventional manner under bombardment (at least at the lower exposure levels, $\theta \lesssim 10^{12}$ α's) as can be seen in Fig. V.28. The bombardment produced changes in the I-V characteristics are found to be much less pronounced in the low and intermediate voltage regions than in the high voltage region. In addition the data of Table V.VIII shows that little change is produced in δ during exposure and therefore A has a negligible tendency towards 2 if any. One p-on-n Si cell (SiH) received an unusually large α-particle dose. The dark I-V characteristics were measured periodically during exposure and a number are shown in Fig. V.31. It is evident from these characteristics that the current in the high voltage region undergoes a more rapid change with exposure than the current at low and intermediate voltages. Therefore, the mechanism responsible for the major contribution to the non-ideal current term is not controlled by the bulk material minority carrier lifetimes. In the high voltage region where the ideal current is dominant, the current is seen to increase initially and then decrease. This behavior is consistent with a bombardment induced increase in the base region contribution to the internal series resistance inasmuch as this would lead to a delayed

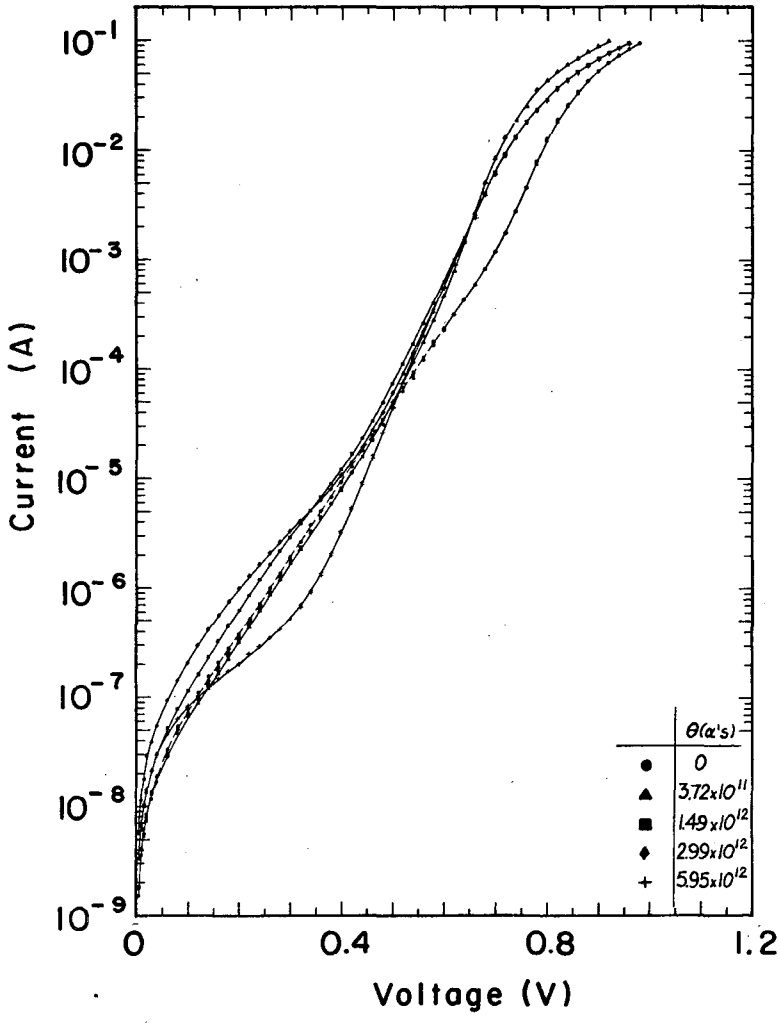

Fig. V.31. The dark I-V characteristics at a number of exposure levels for SiH.

decrease in the current, as observed. The dark I-V characteristic is finally found to undergo an abrupt and substantial change in the intermediate voltage region which is in no way consistent with the changes in a junction recombination-generation current arising from a decrease in the minority carrier lifetimes. This behavior is similar to that exhibited by the n-on-p Si cells at lower exposure levels. Comments made relative to the behavior of the n-on-p cells apply equally well here. The final I-V characteristic possesses a non-ideal term with a sizeable contribution from the junction recombination-generation current as is evident from the value for A in Table V.VIII.

D. Conclusions.

All the cell types exhibited an increased maximum conversion efficiency at the lower test temperature which is in agreement with theory. A comparison of the maximum efficiency and corresponding short circuit current for the Si and GaAs solar cells indicated that the maximum efficiency increased with increasing forbidden energy gap of the material, and this is also in agreement with theoretical predictions.

The measured maximum efficiencies for the Si solar cells fell well below theoretical predictions. This behavior was attributed to the very "soft" I-V characteristics exhibited by the Si solar cells.

The GaAs solar cells were found to exhibit the greatest device radiation resistance with the n-on-p and p-on-n Si cells showing decreased resistance in that order. The device radiation resistance of the p-on-n Si solar cells was independent of temperature (in the range of 200 °K to 275°K), while that for the n-on-p Si cells was found to be greater at 275°K. The behavior of the p-on-n GaAs cells is apparently the same as for the n-on-p Si cells, although it is not possible to draw any firm

conclusions in this regard as only one cell of this type was irradiated at each temperature. The apparent temperature dependence for the GaAs cells may be attributable to the unequal initial diffusion lengths of the two cells.

The initial values of the maximum efficiency were found to be only slightly greater for the Si cells than for the GaAs cells. However, the total energy output ($E_{tot} = \int P_{max}(\theta)d\theta$) was found to be the greatest for the GaAs cells as a result of their greater device radiation resistance.

The diffusion length degradation constant was used as a measure of the material radiation resistance. The diffusion length degradation constants for p-type Si, approximately $3X10^{-5}cm^{-2}\alpha^{-1}$ at 275°K and $5X10^{-5}cm^{-2}\alpha^{-1}$ at 200°K, were less than those of both the n-type Si, approximately $7X10^{-5}cm^{-2}\alpha^{-1}$ at 275°K and 200°K, and the n-type GaAs, approximately $4.9X10^{-4}cm^{-2}\alpha^{-1}$ at 200°K and $3.5X10^{-4}cm^{-2}\alpha^{-1}$ at 275°K. Therefore p-type Si is the most resistant to radiation damage. The ratio of diffusion length degradation constants for Si at 275°K, $\tilde{K}_p/\tilde{K}_n \simeq 2.5$, is in good agreement with the results for protons where this ratio is approximately 3. This is the primary reason why the n-on-p Si cells exhibit a greater device radiation resistance than the p-on-n Si cells.

The substantially greater sensitivity of the n-type GaAs to radiation damage is consistent with the argument that, in addition to the production of Frenkle defects which are common to both materials, the displaced Ga or As lattice atoms can in general be replaced by atoms of the other type and thereby create additional lattice defects. This replacement process is not of importance in Si since all the lattice atoms are alike.

The device radiation resistance of the GaAs solar cells is superior to that of the Si cells despite its inferior material radiation resistance as compared to both n- and p-type Si. This is possible, since the initial diffusion lengths of the GaAs cells are very much shorter than those of the Si cells. Therefore a greater exposure is required for the GaAs cells in order to realize changes in the base region diffusion length.

The bombardment induced changes in the dark I-V characteristics for these three cell types could only be explained in a qualitative manner. For all three cell types the increased current in the high voltage portion of the I-V characteristic was attributed to an increase in the ideal current arising from a decrease in the minority carrier lifetime resulting from bombardment. In the intermediate voltage region the results were different for the three cell types. The GaAs cells exhibited a substantial increase in current over the entire voltage range suggesting that the non-ideal current term is minority carrier lifetime controlled as is the case for the junction recombination-generation current. For the n-on-p Si cells a decrease in the current was observed over the low voltage interval. A similar behavior was observed for the one p-on-n Si cell which had received an extended exposure. It is felt that this type of behavior can only be attributable to changes in the surface state of the cell.

Subsequent to exposure, the non-ideal term of the dark I-V characteristic was observed to have an exponential dependence approximately equal to that predicted for the junction recombination-generation current for most of the cells tested. Considering these results, we feel that a surface state controlled non-ideal current contribution is eliminated during exposure leaving the junction recombination-generation current contribution which is greatly enhanced as a result of the bombardment.

VI. SUMMARY

We have seen that the energy conversion efficiency of a particle-voltaic device is controlled by its charge collection efficiency and dark I-V characteristic. The charge collection efficiency for a given device is controlled by surface and volume charge carrier recombination as is, in part, the dark I-V characteristic.

The energy conversion properties for an idealized Si α-voltaic device were calculated. For this device the dominant current contribution to the non-ideal term was assumed to be the junction recombination-generation current. At room temperature the maximum efficiency was calculated to be about 12% for a device exposed to a 100 mC alpha source. The useful lifetime for such a device (that is, the time required for the maximum efficiency to decrease by an order of magnitude) was estimated to be one minute.

The dark I-V characteristics were measured for p-on-n and n-on-p Si and p-on-n GaAs solar cells at various test temperatures in the range of 90°K to 360°K. The ideal contribution to the I-V characteristic was isolated for all three cell types. It was, however, not possible to separate out the effects of surface region sheet resistance due to the large experimental errors encountered. The non-ideal current term was best described by the mechanism of charge carrier tunneling through the junction for the p-on-n Si cells. In light of the effect of chemical etching upon the non-ideal current term, it became evident that the tunneling mechanism is, at least in part, associated with the surface energy states of the device. The non-ideal current term for the n-on-p Si cells was also found to be consistent with a tunneling current mechanism. However the non-ideal current term for these cells was closer

to a junction recombination-generation current than for the p-on-n cells. In addition the n-on-p Si cells were affected to a lesser degree by chemical etching than the p-on-n cells. One of the p-on-n GaAs cells tested possessed a non-ideal current term which was in good agreement with a junction recombination-generation current for temperatures above 250 °K while showing a substantial deviation below this temperature.

The energy conversion properties of Si and GaAs solar cells under α-particle bombardment were measured at 200 °K and 275° K. The GaAs solar cells were found to be more resistant to radiation damage from a device standpoint than either type of Si cell, and this was attributed to the lower purity and correspondingly shorter base region diffusion length for the GaAs devices. The greater device radiation resistance of the n-on-p Si cells relative to the p-on-n Si cells results from the fact that p-type Si is more resistant to radiation damage than n-type. The improved radiation resistance of p-type Si at 275 °K relative to that at 200 °K implies that the energy states corresponding to the radiation induced defects must lie above the Fermi level, since it is unlikely that the nature of the defects produced at these two temperatures is different.

The diffusion length degradation constants were also determined for both materials. P-type Si was found to be the most resistant to radiation damage with $K_p(Si) \approx 3X10^{-5} cm^{-2}\alpha^{-1}$ at 275 °K and $5X10^{-5} cm^{-2}\alpha^{-1}$ at 200 °K, followed by n-type Si for which $K_n(Si) \approx 7X10^{-5} cm^{-2}\alpha^{-1}$ at both temperatures, and finally n-type GaAs with $K_n(GaAs) \approx 4X10^{-4} cm^{-2}\alpha^{-1}$. Comparison with the data from proton irradiations showed that the α particles were less effective than the protons in producing electrically active lattice defects.

The bombardment induced changes in the dark I-V characteristics were in qualitative agreement with the changes expected in the ideal term resulting from the decrease in minority carrier lifetime with exposure. The non-ideal terms for the Si cells, however, were observed to undergo changes that were in no way consistent with expectations for tunneling or junction recombination-generation currents controlled by bulk material properties. The results indicate that one of the current contributions to the non-ideal current term (presumably a tunneling current associated with surface energy states) is rendered inactive by α-particle bombardment with an associated "hardening" of the I-V characteristic at low forward applied bias. The post-bombardment I-V characteristics were found to possess a non-ideal current term in good agreement with the junction recombination-generation current providing an exposure level had been reached for the Si cells sufficient to realize the "hardening" phenomenon.

NOMENCLATURE

A	p-n junction non-ideality factor
A_x	p-n junction cross sectional area
a	screening radius
a_o	radius of the first Bohr orbit
b	classical distance of closest approach
C	capacity
c	velocity of light
D_n	electron diffusion coefficient
D_p	hole diffusion coefficient
E_α	α-particle energy
$E_{\alpha o}$	initial α-particle energy
E_{bi}	atomic binding energy of i^{th} electron
E_c	energy at the bottom of the conduction band
E_D	threshold energy for the production of a lattice displacement
E_{fi}	intrinsic Fermi energy
E_{fn}	Fermi energy in n-type material
E_{fno}	equilibrium Fermi energy in n-type material
E_{fp}	Fermi energy in p-type material
E_{fpo}	equilibrium Fermi energy in p-type material
E_g	forbidden energy gap
E_R	energy of k=0 optical phonon for Si
E_v	energy at the top of the valence band
g_α	electron-hole pair production rate per α particle
h	Plancks constant ($\hbar = \frac{h}{2\pi}$)
I	mean ionization potential or total current
I_c	surface region plus junction current

I_d p-n junction diffusion current

I_e electron current

I_G particle generated current

$I_{G\alpha}$ α-particle generated current

I_h hole current

I_i average ionization potential of i^{th} electron

I_{IL} p-n junction inversion layer current

I_L light generated current or $(2\sigma w^2 L J_s/\lambda)^{1/2}$

I_{mp} current at maximum power

I_o reverse saturation current for the ideal diffusion term

I_{ol} effective reverse saturation current for the non-ideal current term

I_{rg} p-n junction recombination-generation current

I_{sc} short circuit current

I_T p-n junction tunneling current

J_n electron current density

J_p hole current density

J_s reverse saturation current density for ideal diffusion term

K diffusion length degradation constant

K_ϵ dielectric constant

k Boltzmann constant

L_n electron diffusion length

L_p hole diffusion length

m rest mass of the electron

$\dot{N}_\alpha$ incident α-particle rate

N_A acceptor atom concentration

N_A^- ionized acceptor atom concentration

N_D donor atom concentration or defect center concentration

N_D^+	ionized donor atom concentration
N_o	atomic density of stopping medium
N_T	concentration of localized energy states contributing to tunneling current
n	electron concentration
n_D	number of displacements per unit track length per α particle
n_i	intrinsic carrier concentration
n_n	electron concentration in n-type material
n_p	electron concentration in p-type material
n_{po}	equilibrium electron concentration in p-type material
P_{max}	maximum power
p	hole concentration or impact parameter
p_m	maximum impact parameter
p_n	hole concentration in n-type material
p_{no}	equilibrium hole concentration in n-type material
p_p	hole concentration in p-type material
Q	semiconductor diode charge collection efficiency
q	magnitude of the electronic charge
R	atomic radius determined from atomic density
R_α	α-particle range
R_c	equivalent solar cell radius
R_h	Rydberg energy for the hydrogen atom
R_o	radius for hard sphere scattering
R_s	internal series resistance
R_{SH}	shunt resistance
r_c	distance of closest approach in coulomb scattering with arbitrary p
s_n	electron surface recombination velocity
s_p	hole surface recombination velocity

T	absolute temperature
T_m	maximum energy transfer in a head-on collision
U_j	ionization energy for j^{th} electron in ground state
V_j	voltage drop across junction
V_{mp}	voltage at maximum power
V_{oc}	open circuit voltage
W	junction width
Z	atomic number
z_m	mean charge on the α particle
β	effective reverse saturation current non-ideality factor or V/c
γ	D/Ls
δ	λ/A, the non-ideal exponential factor
$\mathcal{E}$	electric field
ϵ	energy per electron-hole pair
ϵ_o	permitivity of free space
ζ	screening parameter
η_{max}	maximum conversion efficiency
θ	particle exposure
κ	classicity constant
λ	q/kT
λ'	minority carrier lifetime degradation constant
μ_e	electron mobility
μ_h	hole mobility
ν	number of lattice displacements per primary
ρ	resistivity
σ	cross section or variance

σ_D	cross section for lattice displacement production
$d\sigma$	differential cross section
τ_{no}	lifetime for electrons in highly p-type material
τ_{po}	lifetime for holes in highly n-type material
ψ_D	equilibrium p-n junction contact potential

ACKNOWLEDGMENTS

I want to express my deep gratitude to: Professor T. H. Pigford for his encouragement and patience throughout the course of the work and also his critical review of this report, Professors H. M. Mark and A. M. Portis for the time and effort each spent in reviewing this report, Mr. S. Untermyer for suggesting the particle-voltaic effect as a possible area of investigation, and Mr. B. E. Thinger for assisting with some of the measurements. Thought provoking discussions with Mr. J. G. Poksheva were greatly appreciated as was his assistance with the development of a portion of the measuring apparatus. I also want to thank my wife for her immeasurable patience, understanding, and assistance.

I would like to express appreciation to the Atomic Energy Commission for fellowships received during the preliminary stages of this work.

This work was done under the auspices of the Atomic Energy Commission.

APPENDICES

A. Semiconductor Diode Dark I-V Characteristics.

In this appendix the various contributions to the dark current-voltage characteristic of a semiconductor diode will be discussed in detail.

Diffusion Current. Shockley[56] has shown that the ideal current-voltage characteristic of a p-n junction is obtained from the solution of the minority carrier diffusion equation in the n- and p-type regions on either side of the junction. (A large field exists in the junction region, whereas the p- and n-type regions are essentially field free.) For example, in the n-type region the steady state hole continuity equation is

$$D_p \frac{d^2 \Delta p_n}{dx^2} - \frac{\Delta p_n}{\tau_p} = 0, \qquad \text{(A-1)}$$

where $\Delta p_n = p_n - p_{no}$ is the excess hole concentration and p_{no} is the equilibrium hole concentration in the n-type region. Equation (A-1) is solved subject to the boundary conditions that the excess hole concentration goes to zero at distances from the junction which are large in comparison to the diffusion length,

$$\Delta p_n(x \to \infty) = 0, \qquad \text{(A-2)}$$

and the excess hole concentration at the boundary between the junction and the n-type region is

$$\Delta p_n = p_{no}[\exp(\lambda V_j) - 1] = \Delta p_{no}, \qquad \text{(A-3)}$$

where V_j is the voltage drop across the junction. The excess hole concentration obtained from Eq. (A-1) is

$$\Delta p_n = \Delta p_{no} \exp(-\frac{x}{L_p}) \qquad (A\text{-}4)$$

for $0 \leq x \leq \infty$ which represents the n-type region. The hole current density at the junction boundary (x=o) is given by

$$J_h = -qD_p \frac{d\Delta p_n(0)}{dx} = qp_{no}(\frac{D_p}{L_p})[\exp(\lambda V_j)-1] \quad . \qquad (A\text{-}5)$$

The electron current density, J_e, is obtained in a similar manner with the result that the total current is

$$I_d = I_e + I_h = I_o[\exp(\lambda V_j)-1] \quad , \qquad (A\text{-}6)$$

where

$$I_o/qA_x = n_{po}(\frac{D_n}{L_n}) + p_{no}(\frac{D_p}{L_p}) \qquad (A\text{-}7)$$

is the reverse saturation current and A_x is the junction cross sectional area. In Appendix C the preceding analysis is extended to the case of a thin surface region device where Eq. (A-2) is no longer a valid boundary condition for the surface region, and it becomes necessary to account for the recombination of electron-hole pairs at the surface. The I-V characteristic of a shallow junction diode (i.e., see Fig. A.1) is of the same form as Eq. (A-6) except that the reverse saturation current is obtained from

$$I_o/qA_x = n_{po}(\frac{D_n}{L_n})\frac{[\gamma_n \sinh(\frac{t}{L_n})+\cosh(\frac{t}{L_n})]}{[\gamma_n \cosh(\frac{t}{L_n})+\sinh(\frac{t}{L_n})]} + p_{no}(\frac{D_p}{L_p}) \qquad (A\text{-}8)$$

where $\gamma_n = D_n/L_n s_n$ and t is the thickness of the surface region. Equation (A-8) represents the reverse saturation current for a diode with a thin p-type surface region and a thick n-type base region.

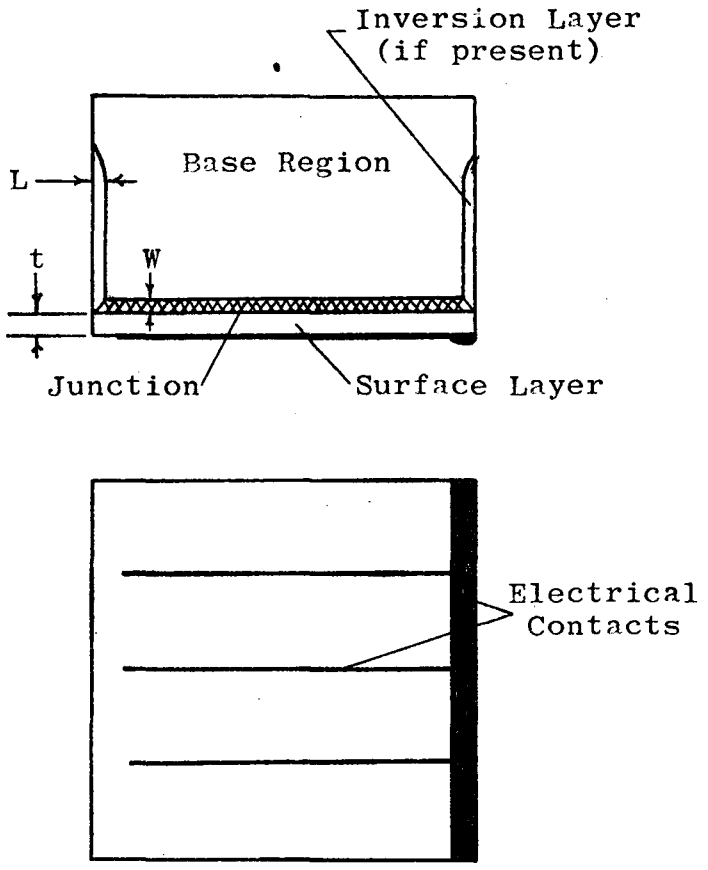

Fig. A.1. Geometry for a shallow-junction semiconductor diode.

Thus far the possible existence of a voltage drop in either the n- or p-type regions has been neglected. Sah, Noyce, and Shockley[53] have considered this case and obtain the I-V characteristic by solving the current equation, continuity equation, and Poisson's equation in both the n- and p-type regions. These equations are

$$K_{\epsilon}\epsilon_{o}\,\mathrm{div}\,\mathcal{E} = q(p-n\pm N), \tag{A-9}$$

$$J_p = qD_p[\lambda\mathcal{E}\,p-\mathrm{grad}p], \tag{A-10}$$

$$J_n = qD_n[\lambda\mathcal{E}\,n+\mathrm{grad}n], \tag{A-11}$$

$$\mathrm{div}(J_p) = -qU, \tag{A-12}$$

and

$$\mathrm{div}(J_n) = qU \tag{A-13}$$

where $\mathcal{E}$ is the electric field, N is the number of ionized donors or acceptors (i.e., + for donors and - for acceptors), and U is the bulk electron-hole pair recombination rate. This recombination rate for non-equilibrium but steady state conditions has been calculated by Shockley and Read[57] for a single recombination center of uniform spatial distribution located at an energy E_t with respect to the top of the valence band and is

$$U = \frac{(pn-n_i^2)}{[(n+n_1)\tau_{po}+(p+p_1)\tau_{no}]}, \tag{A-14}$$

where n_1 and p_1 are the electron and hole concentrations corresponding to the situation where the Fermi level lies at E_t, and τ_{po} and τ_{no} are the minority carrier lifetimes in highly doped n-type and p-type material respectively. The ensuing steps closely follow those of Sah, et al.

excepting for the exclusion of a junction recombination-generation current contribution. At the edge of the junction on the n-region side (x=0)

$$p_n(0)n_n(0) = n_i^2 \exp(\lambda V_j) \tag{A-15}$$

and

$$n_n(0) = p_n(0) + N \tag{A-16}$$

so that

$$p_n(0) = \frac{N}{2}\left[\sqrt{1+(4n_i^2/N^2)\exp(\lambda V_j)} - 1\right] . \tag{A-17}$$

Equation (A-17) is valid so long as the quasi-Fermi levels for the electrons and holes are constant in the junction. Using Eqs. (A-9) through (A-14) and (A-16), it is possible to solve for d^2p_n/dx^2 and then integrate to obtain

$$(dp_n/dx)^2 = L_o^{-2}\left[\frac{1}{2}(p_n^2-p_{no}^2) + (N-p_o)(p_n-p_{no}) - (p_o(N-p_o)\, n_i^2)\ln\frac{(p_n+p_o)}{(p_{no}+p_o)}\right] . \tag{A-18}$$

where

$$p_o = \frac{\tau_{po} n_1 + \tau_{no} p_1 + \tau_{po} N}{\tau_{po}+\tau_{no}} \tag{A-19}$$

and the boundary condition used in the integration was $p_n \to p_{no}$ and $\text{grad}p_n \to 0$ as $x \to \infty$. The same set of equations is also used to find the hole current at the junction edge with the result that

$$J_h(0) = -\frac{qD_p[2p_n(0)+N]dp_n(0)/dx}{[p_n(0)+N]} . \tag{A-20}$$

A similar relation would hold for the p-type region also, although in most practical devices one region has a much higher resistivity than the other and therefore controls the diffusion current. Assume for the

present that this is the n-type material. Then in the case of low level injection (i.e., $p(0) \lesssim N/10$) the current becomes

$$J_{pd}(0) = qp_{no}\left(\frac{D_p}{L_p}\right)\sqrt{\frac{1+b}{2b}}\,(e^{\lambda V_j}-1) \qquad \text{(A-21)}$$

where $b = D_n/D_p$. This is similar to the diffusion theory result obtained above except for the factor $\sqrt{(1+b)/2b}$ which arises from the fact that in the present development an electric field was assumed to exist outside of the junction.

In the case of high level injection (i.e., $p(0) \gtrsim 10N$) the current is given by

$$J_{hd}(0) = \sqrt{2}\,q\left(\frac{D_p}{L_o}\right)p_n(0), \qquad \text{(A-22)}$$

where

$$L_o^{-2} = (1/D_n+1/D_p)/(\tau_{po}+\tau_{no}) \qquad \text{(A-23)}$$

and

$$p_n(0) = n_i\exp(\lambda V_j/2). \qquad \text{(A-24)}$$

Recombination-Generation Junction Current. Sah, Noyce, and Shockley[53] have also considered the effect of carrier generation or recombination in the junction upon the current-voltage characteristic. For an electron-hole pair recombination rate in the junction given by Eq. (A-14), the total current contribution due to recombination or generation in the junction is given by

$$I_{rg} = qA_x\int U(x)dx. \qquad \text{(A-25)}$$

where the integral is carried out over the junction thickness. The electrostatic potential variation in the junction must be known in order to solve Eq. (A-15), since p and n are related to the electrostatic potential, ψ, through

$$p = n_i \exp[\lambda(\phi_p - \psi)] \tag{A-26}$$

and

$$n = n_i \exp[\lambda(\psi - \phi_n)] \tag{A-27}$$

where $q\phi_p$ and $q\phi_n$ are the quasi-Fermi levels in the junction for holes and electrons respectively.

Also $$p_1 = n_i \exp[(E_i - E_t)/kT] \tag{A-28}$$

and $$n_1 = n_i \exp[(E_t - E_i)/kT] \tag{A-29}$$

where

$$E_i = [E_c + E_v - kT\ln(N_c/N_v)]/2 = -q\psi \tag{A-30}$$

is the intrinsic Fermi level.

Then use of Eqs. (A-26) through (A-30) in Eq. (A-14) yields the steady state recombination rate as a function of the electrostatic potential,

$$U = \frac{n_i \sinh \frac{\lambda V_j}{2} \Big/ \sqrt{\tau_{po}\tau_{no}}}{\cosh\left[\lambda\left(\psi - \frac{\phi_p+\phi_n}{2}\right) + \frac{1}{2}\ln\left(\frac{\tau_{po}}{\tau_{no}}\right)\right] + \exp\left[-\frac{\lambda V_j}{2}\right]\cosh\left[\frac{(E_t - E_i)}{kT} + \frac{1}{2}\ln\left(\frac{\tau_{po}}{\tau_{no}}\right)\right]} \tag{A-31}$$

where $V_j = \phi_p - \phi_n$. It was also shown by Sah, et al., that in a diffused diode the electrostatic potential variation in the junction can be approximated, to a reasonable degree, by that of a linear graded junction in which case

$$\psi - \frac{(\phi_p+\phi_n)}{2} = (\psi_D - V_j)x/W \tag{A-32}$$

for $-W/2 < x < W/2$. ψ_D is the equilibrium junction contact potential and W is the junction thickness. Then Eq. (A-31) can be integrated with the result that Sah, et al. found this current contribution to be

$$I_{rg} = \frac{qn_i AW}{\sqrt{\tau_{po}\tau_{no}}} \quad \frac{2\sinh(\lambda V_j/2)}{\lambda[\psi_D - V_j]} \quad f(b) \qquad \text{(A-33)}$$

where

$$f(b) = \int_{z_1}^{z_2} \frac{dz}{z^2+2bz+1} \ , \qquad \text{(A-34)}$$

$$b = \exp[-\lambda V_j/2]\cosh[\frac{(E_t - E_i)}{kT} + \frac{1}{2}\ln(\frac{\tau_{po}}{\tau_{no}})] \ , \qquad \text{(A-35)}$$

and the limits of integration are

$$z_{1,2} = \sqrt{\tau_{po}/\tau_{no}}\exp[\mp \frac{\lambda}{2}(\psi_D - V_j)] \ . \qquad \text{(A-36)}$$

Surface Current. It has been found that contamination of a semiconductor surface can lead to the formation of an inversion layer on the surface which is of opposite conductivity type to that of the bulk material.[12,19,44,60] This inversion layer formation arises from surface energy states which are produced by impurity atom adsorption or structural deformation at the surface. The formation of such a layer requires that a p-n junction or depletion region be present between the inversion layer and the bulk material. Therefore, the total junction area is increased and neglecting I_{rg} the total diode current becomes

$$I = I_o(e^{\lambda V_j} - 1) + I_{IL}(V_j), \qquad \text{(A-37)}$$

where $I_{IL}(V_j)$ is the inversion layer current. The inversion layer current-voltage characteristic has been determined by Cutler and Bath.[15] This development involved the simultaneous solution of the equations for the voltage drop in the surface leakage path

$$dV(x)/dx = -\rho I(x)/wL \qquad \text{(A-38)}$$

where ρ is the resistivity of the surface channel and L is the width of the channel, and for the current flow in the leakage path

$$dI(x)/dx = -J_s w[\exp(\lambda V(x)) - 1] . \qquad (A\text{-}39)$$

where J_s is the reverse saturation current density for the surface barrier formed by the inversion layer. The boundary conditions used in the solution of Eqs. (A-38) and (A-39) were $I(\infty) = 0$ and $V(\infty) = 0$. The total current contribution from the surface barrier is obtained from the solution for $I(x)$ at $x=0$ with $V(0) = V_j$. The current found from Eqs. (A-38) and (A-39) is

$$I_{IL} = \pm I_L(e^{\lambda V_j} - \lambda V_j - 1)^{1/2} \qquad (A\text{-}40)$$

where the plus and minus signs hold for forward and reverse bias respectively and

$$I_L^2 = 2w^2 I J_s/\lambda\rho . \qquad (A\text{-}41)$$

The total current given by Eq. (A-37) then becomes

$$I(V_j) = I_o(e^{\lambda V_j} - 1) \pm I_L(e^{\lambda V_j} - \lambda V_j - 1)^{1/2} . \qquad (A'\text{-}42)$$

Excess Current. Another process whereby the charge carriers can contribute to the current is that of electron or hole tunneling through the junction from one base region to the other. This is indeed dominant current term at small applied bias in tunnel diodes[20] where the carriers tunnel directly from the conduction band in one region into the valence band in the other region. The energy band overlap required for this tunneling mechanism is achieved by doping the material to a very high degree. The resultant energy diagram is shown in Fig. A.2(a).

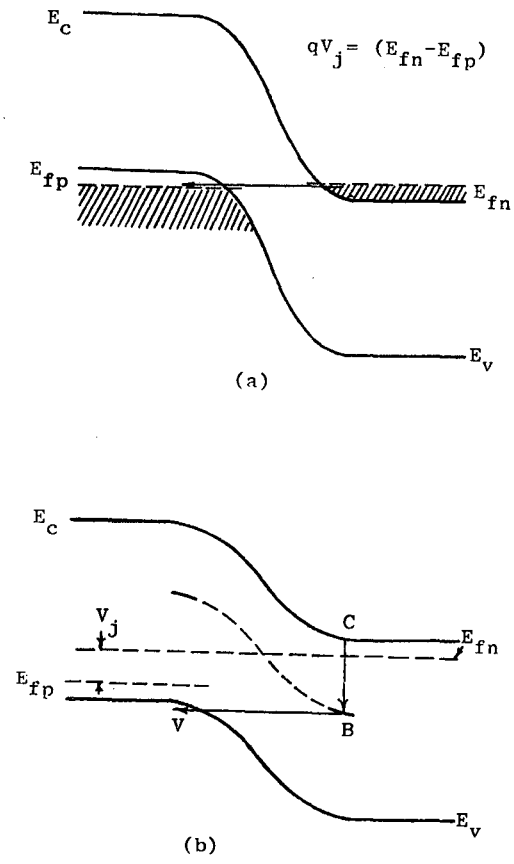

Fig. A.2. Energy band diagrams for a diode with (a) conduction band to valence band tunneling and (b) impurity level to valence band tunneling.

At a lower doping level the conduction band to valence band tunneling is not possible, but carriers may still tunnel from the conduction band in one region through an intermediate localized energy level in the forbidden energy gap into the valence band on the opposite side of the junction. Figure A.2(b) shows the energy diagram for this situation and indicates one possible route for the tunneling process. Chynoweth, et al.,[13] analyzed this mechanism assuming route CBV to be the most probable mechanism for the tunneling process. An electron making a tunneling transition from B to V in Fig. A.2(b) must tunnel through an energy barrier given by

$$E_T = E_g - (E_c - E_{fn}) - (E_{fp} - E_v) - qV_j = (E_{fn} - E_{fp}) - qV_j \qquad \text{(A-43)}$$

assuming the electron ends up at the top of the valence band. The tunneling probability for this transition was found to be

$$P_T = \exp(-\alpha_T E_T^{3/2}/\mathcal{E}) \qquad \text{(A-44)}$$

where $\mathcal{E}$ is the electric field in the junction, α_T is defined by

$$\alpha_T = [4(2m_T)^{1/2}/3eh]\theta \ , \qquad \text{(A-45)}$$

and θ is a numerical factor of the order of unity and m_T is the effective mass for the tunneling process. For a step junction the electric field in the transition region can be approximated by

$$\mathcal{E} = \frac{\psi_D - V_j}{WV_j} = \frac{[\psi_D - V_j]^{1/2}}{W_o} \qquad \text{(A-46)}$$

where W_o is the junction width for unit voltage across it and $q\psi_D = E_{fno} - E_{fpo}$. The transition probability therefore becomes

$$P_T(V_j) = \exp(-\alpha_T W_o q^{1/2} [(E_{fn}-E_{fp}) - qV_j]). \qquad (A-47)$$

For a concentration of occupied energy levels at an energy E_T above the top of the valence band (i.e., levels such as B) of N_T, the tunneling current was then found to be[13]

$$I_T(V_j) = AN_T(V_j)P_T(V_j) = AN_T(V_j)\exp(-\alpha_T W_o q^{1/2}[(E_{fn}-E_{fp})-qV_j]) \qquad (A-48)$$

where A is an undetermined coefficient.

Total Current. In addition to the previously mentioned contributions to the current, it is necessary to consider the possible existence of a shunt conductance path in parallel with the junction. The contribution to the current resulting from this mechanism is

$$I_{SH} = V_j/R_{SH} \qquad (A-49)$$

where R_{SH} is the shunt resistance in parallel with the junction.

The total current is then, in general, the sum of the contributions from all these mechanisms discussed above

$$I = I_d + I_{rg} + I_{IL} + I_T + T_{SH}. \qquad (A-50)$$

The material properties, surface preparation, and device geometry of a semiconductor diode determine which of the terms in Eq. (A-50) dominates at a given temperature and voltage V_j. The current-voltage characteristic of a practical device is given by Eq. (A-50) providing that the internal series resistance of the diode is taken into account. Application of a voltage, V, to the diode results in a junction bias of V_j and an internal voltage drop of IR_s. Therefore Eq. (A-50) becomes

$$I(V) = I_d(V_j) + I_{rg}(V_j) + I_{IL}(V_j) + I_T(V_j) + I_{SH}(V_j) \qquad (A-51)$$

where $V_j = V - IR_s$. Figure A.3 shows the calculated I-V characteristic and its individual current contributions for a p-on-n silicon diode with negligible inversion layer and tunneling currents. The temperature dependence of this particular I-V characteristic is presented in Fig. A.4, where the material properties used in the calculations are representative of moderately pure material (for values used see Table III.III) and the front surface was assumed to be completely covered by an electrode. In a calculation of this type for a solar cell it would be necessary to consider the effect of the non-uniform potential variation in the thin surface region upon the characteristic. Current passing from the junction to the electrode strip (see Fig. A.1) results in a voltage drop in the surface region with the result that the junction-surface region boundary is not an equipotential.[68] The analysis of this situation would be similar to that used in the determination of the inversion layer current.

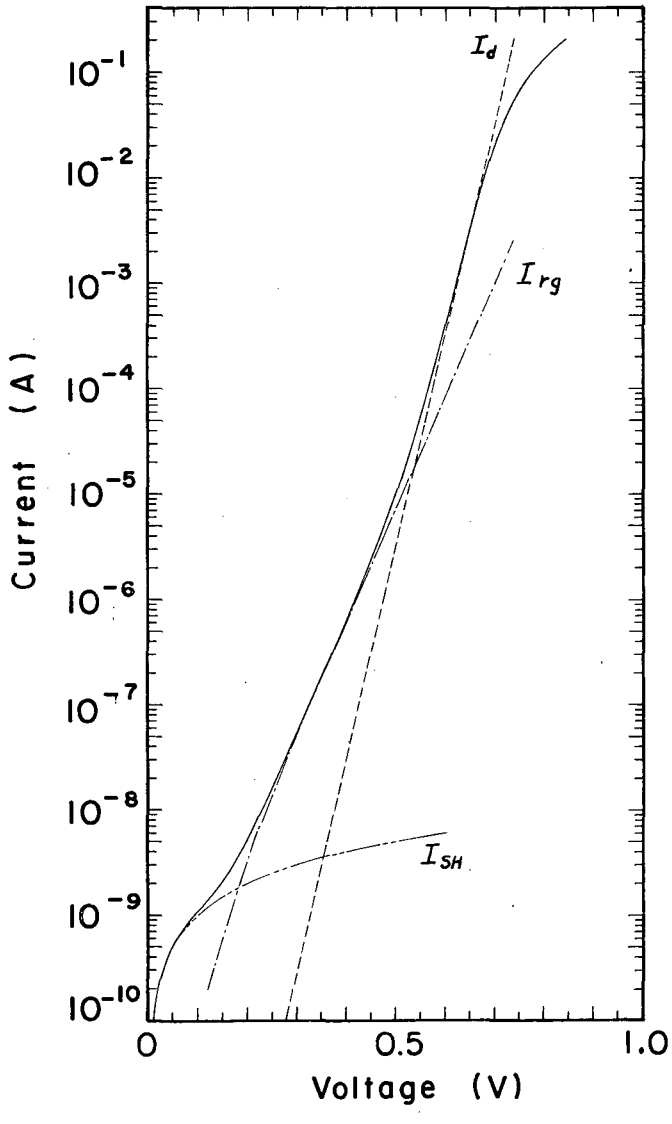

Fig. A.3. I-V characteristic for a broad-area junction diode with broad-area contacts (calculated by use of properties of Table III.III).

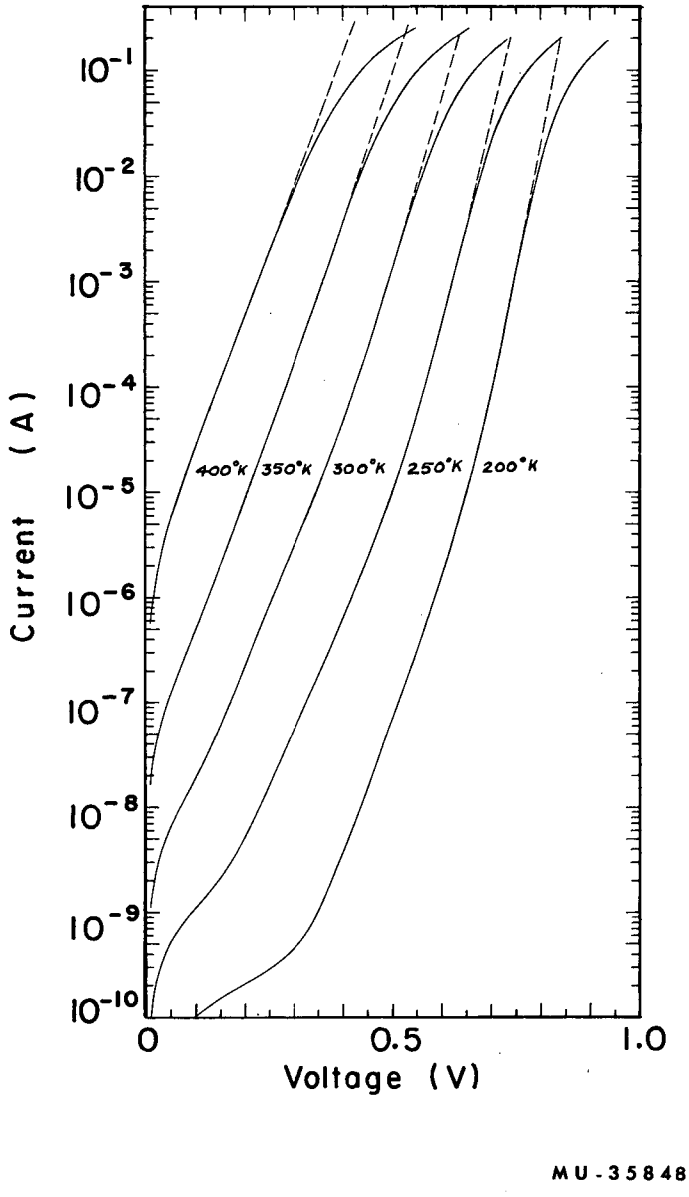

Fig. A.4. Temperature dependence of the I-V characteristic for a broad-area junction diode (calculated by use of properties of Table III.III).

B. Charged Particle Energy Loss in Semiconductors.

In this appendix the various contributions to the total stopping power are considered in detail. These include the stopping power contributions from atomic electron excitation and ionization, valence band to conduction band electron excitation, and classical hard sphere and classical Rutherford atomic collisions. The calculated stopping power curve consisting of these contributions is then used to determine the spatial variation of α-particle energy, E_α, the electronic stopping power, $[dE_\alpha/dx]_{el}$, and the lattice displacement production per α particle, $n_D(x)$.

1. Atomic Electron Excitation and Ionization. A number of models have been proposed to predict the energy loss per unit path length or stopping power for the interaction of heavy charged particles with matter. At sufficiently high particle energies the energy loss is primarily through electron ionization and excitation processes, while at lower energies atomic collisions contribute to the stopping power. The type of particle, its energy, and the type of material encountered determine which of the stopping power equations is applicable.

A quantum mechanical calculation for the excitation of the bound atomic electrons into the energy continuum and/or the empty excited electronic states has been carried out by Bethe.[5] In this treatment the coulomb scattering cross section was calculated using the Born approximation which, according to Bethe, is a valid approach so long as $2z_m/137\beta \ll 1$, where z_m is the mean charge on the energetic particle, Z is the atomic number of the stopping material, and $\beta = V/c$. At sufficiently high particle energies of the incident particle this condi-

tion is satisfied, and the stopping power equation, including relativistic effects, is given by

$$\frac{dE}{dx} = - \frac{4\pi e^4 z_m^2}{mV^2} N_o Z \left[\ln \frac{2mV^2}{I} - \ln(1-\beta^2) - \beta^2 \right] \qquad \text{(B-1)}$$

where N_o is the number of stopping atoms per unit volume and I is the mean ionization potential of the stopping medium.

Also at sufficiently high charged particle energies the mean ionization potential is approximately constant, and empirical values have been determined from experimental measurements of the stopping power. At lower particle energies the mean ionization potential is a function of the charged particle velocity, since excitation of the most tightly bound atomic electrons becomes energetically impossible. If the factor $Z/137\beta$ becomes on the order of unity or larger, the K-shell electrons are no longer ionized. In Fig. B.1 a comparison is made between various relations used to predict I/Z and the experimental results of numerous investigators. The two relations involving constants are seen to yield good agreement with experiment over a very limited range of atomic number, whereas the empirical relation*

$$\frac{I}{Z} = 15.5 - 1.63 \ln Z + 2.22 \times 10^{-5} Z^2 \qquad \text{(B-2)}$$

gives reasonable agreement over the entire range. Bethe defined the dependence of the mean ionization potential upon the energy necessary for excitation and ionization of the individual electrons by the relation

$$Z \ln I = \Sigma_i f_i \ln \bar{E}_i, \qquad \text{(B-3)}$$

---

* Introduced without discussion in the Ph.D. Thesis of J. Erkins, University of California, 1959 (unpublished).

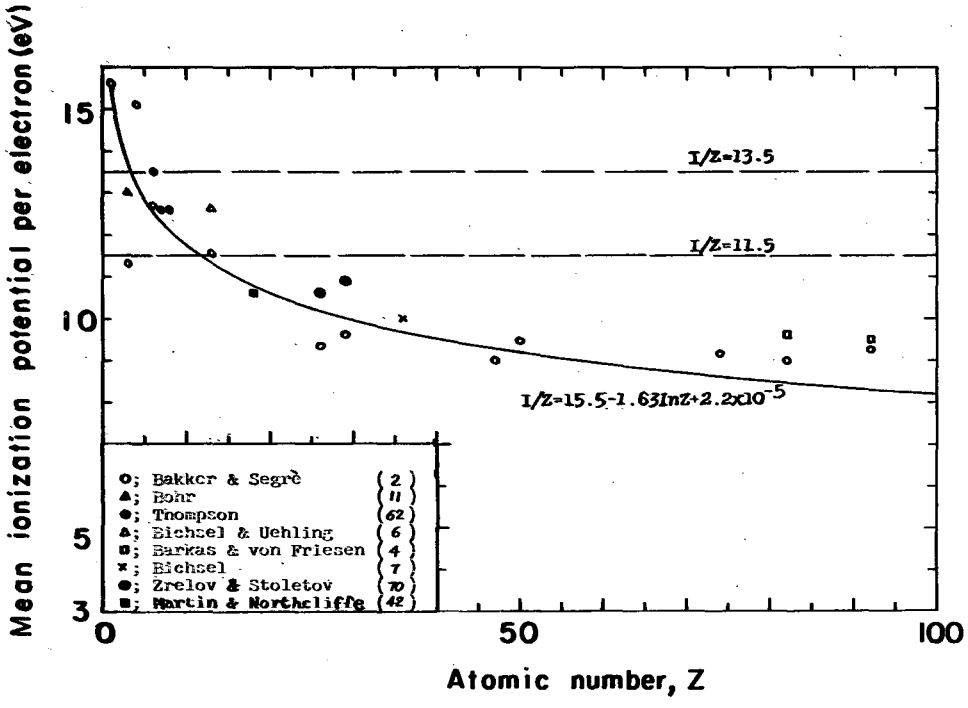

Fig. B.1. Mean ionization potential, I/Z, per electron as a function of atomic number.

where f_i is the sum of the oscillator strengths for all optical transitions of the i^{th} electron and $\bar{E}_i$ is the mean excitation energy for this electron. Evans[21] has suggested that f_i is close to unity and $\bar{E}_i$ can be replaced by the average ionization potential of the i^{th} electron, I_i, with sufficient accuracy. Using Eq. (B-3) in Eq. (B-2) yields

$$\frac{dE}{dx} = -\frac{4\pi e^4 z_m^2}{mV^2} N_o \sum_{i=1}^{Z} \left[\ln\frac{2mV^2}{I_i} - \ln(1-\beta^2) - \beta^2\right] . \qquad (B-4)$$

The mean charge on the energetic particle, z_m, is also dependent upon the particle velocity. At high particle energy the electrons of the incident particle are stripped off due to the large relative velocity between these electrons and the electrons of the stopping medium. As the energy decreases, the charged particle can capture atomic electrons from the stopping material with a resulting decrease in its mean charge. At very low energies ionization of the incident particle is improbable, and the scattering process is primarily of an atom-atom nature. In this energy region the stopping results primarily in the production of lattice defects as opposed to electron excitation.

As mentioned previously, the validity of the Born approximation determines the applicability of the Bethe stopping power equation. At low charged particle energy the factor $2z_m/137\beta$ becomes large compared to unity and the Born approximation is no longer valid. Fano[23] has suggested that, when the velocity of the incident particle is much less than the orbital electron velocity, the particle influence on the electron is much weaker than that of the nucleus and the Born approximation is once again valid. Mott[46] has also shown that the Born approximation gives the correct result independent of the condition that $2z_m/137\beta \ll 1$

provided $z_m \ll Z$ which is not rigorously satisfied for α-particle stopping in Si.

The factors $2z_m/137\beta$ and $Z/137\beta$ are shown in Fig. B.2 for the special case of α-particle stopping in Si where the velocity dependence of z_m presented in Fig. B.3 was used in the calculations. It can be seen that the condition $2z_m/137\beta \ll 1$ is never satisfied, and, therefore, use of the Born approximation is questionable. For energies such that $2z_m/137\beta \gg 1$, the stopping power can be calculated on the basis of classical coulomb scattering. Two stopping power equations obtained in this way will be discussed below. Figure B.2 shows that neither of the limits for $2z_m/137\beta$ is realized for α-particle stoping in Si, and over this energy interval (1KeV to 10MeV) Evans[21] has suggested that at a given energy the stopping power law yielding the least energy loss be used. It will be seen later that this corresponds to the Bethe equation for $2z_m/137\beta < 1$ and the classical equation for $2z_m/137\beta > 1$. Figure B.2 also shows that $Z/137\beta > 1$ over the energy range of interest. This means that K-shell ionization will become impossible in this energy range, and the same will be true for L- and M-shell electrons. For this reason it was necessary to use Eq. (B-4) rather than Eq.(B-1) when calculating the stopping power. At non-relativistic α-particle velocities Eq. (B-4) becomes

$$\frac{dE_\alpha}{dx}\,(\mathrm{KeV}/\mu) = -4.76 \times 10^{9}\,\left(\frac{z_m^{\,2}}{E_\alpha}\right) \sum_{i=1}^{Z} \ln\left[5.48 \times 10^{-3}\left(\frac{E_\alpha}{I_i}\right)\right] \qquad \text{(B-5)}$$

where E_α and I_i are in eV. The mean charge is dependent upon the particle type and stopping material. Experimental measurements of z_m for α particles in light elements such as air and mica have been summarized

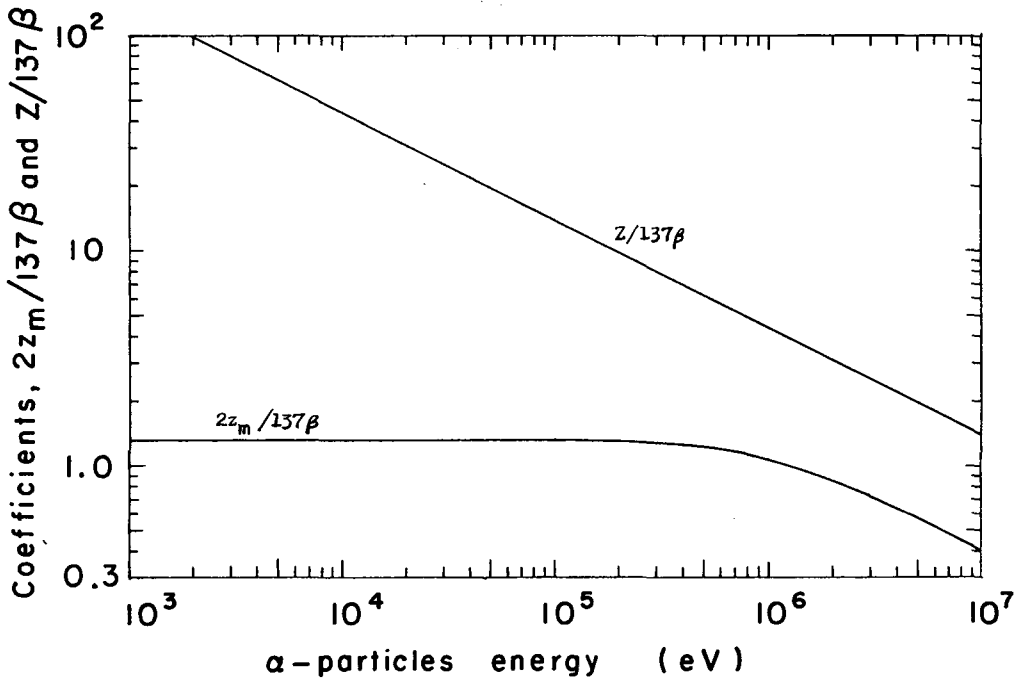

Fig. B.2. Coefficients which determine (a) the validity of the Born approximation and (b) the degree of excitation of the K electrons for α-particle stopping in Si.

by Evans,[21] and the curve drawn through the data is reproduced in Fig. B.3. The experimental results exist for α-particle energies above 300 KeV. Below this energy Evans extended the curve by assuming a linear velocity dependence for z_m. This is only an approximation, since the electron capture and ionization cross sections are not linear with velocity which suggests that the mean charge on the α particle should in reality go to zero in a more abrupt manner as its velocity decreases below the speed of its second orbital electron. The results of Fig. B.3 were nevertheless used for z_m in all the calculations of this report.

The average ionization potential to be used for the individual electrons is not easily obtained. This is due to the fact that it is to include the effect of excitation as well as ionization processes. Using Eq. (B-3) with $f_i = 1$ and the binding energies of the various atomic sub-shells obtained from spectroscopic data,[33] the mean ionization potential was found to be 85.5 eV. The individual binding energies are given in Table B.I. This result is much lower than the value obtained from the curve in Fig. B.1 which for Z = 14 yields

$$I = Z[15.5 - 1.63\ln Z + 2.22 \times 10^{-5} Z^2] = 157 \text{ eV}.$$

The excess energy must arise from the irreversible nature of the process whereby an α particle imparts energy to the other constituents of the atom during the time of interaction. If it is assumed that the average ionization potential for each electron can be related to the binding energy for that electron by a constant which is the same for all the atomic electrons, this constant can be obtained from

$$\ln C = \ln I - \frac{1}{Z} \sum_{i=1}^{Z} \ln E_{bi} \qquad \text{(B-6)}$$

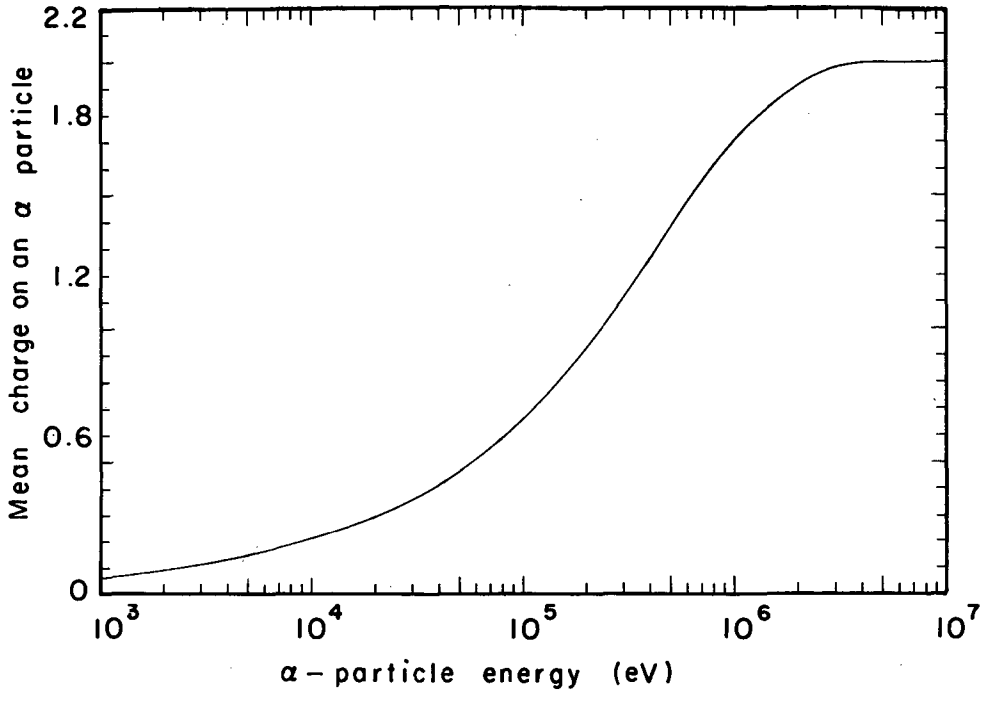

Fig. B.3 Mean charge on an α-particle as a function of energy (from Evans,[24] Chap. 22).

where the average ionization potential for each electron is then given by

$$I_i = \mathfrak{I} E_{bi} .$$

In the remainer of this appendix I_i is assumed to be identical for all the electrons in a given subshell (i.e. 1s, 2s, 2p, etc.). The results are summarized in Table B.I.

Figure B.4 depects the different stopping power curves obtained from the use of Eq. (B-1) with I = 157 eV and Eq. (B-4) with the set of I_i corresponding to I = 157 eV along with z_m as given in Fig. B.3. This figure clearly shows the ability of the outer electrons to take part in the stopping process even though the inner electrons can no longer contribute. The average electron approximation which is equivalent to considering only one mean excitation potential is seen to be a poor approximation below about 1 MeV. Also shown in this figure for comparison is the stopping power calculated from Eq. (B-4) assuming the α particle remains fully ionized ($z_m = 2$).

Bohr[9] has developed an expression for the stopping power which is based upon a classical treatment of the coulomb scattering between a heavy charged particle and the atomic electrons of the stopping material. The minimum inpact parameter is p=0, corresponding to a head-on collision, while the maximum impact parameter must remain finite in order to obtain a finite energy loss. Bohr assumed that only those collision times, $\tau \simeq p/V$, on the order of or less than the characteristic frequency of an atomic electron, were important in the energy transfer process. This characteristic frequency, ν , corresponds to the natural vibrational frequency of the electron produced by the atomic forces when the electron experiences the perturbation arising from the coulomb interaction with

Table B.I. Binding energy[(a)] and average ionization potentials of the atomic electrons in silicon.

Electron configuration: $1s^2 2s^2 2p^6 3s^2 3p^2$

Shell	Subshell	E_{bi}(ev)	I_i(ev)[(b)]	I_i(ev)[(c)]
		Binding energy	Average ionization energy	Average ionization energy
K	1s	1896	3508	3034
L	2s	149	275.7	238.4
	2p	98.9	183.0	158.2
M	3s	14.9	27.57	23.84
	3p	8	14.8	12.8
Mean ionization potential, I		85.5	158	137

(a) Binding energy data from Harnwell and Stephens (33).

(b) Calculated from Eq. (B-6) and $I_i = CE_{bi}$ for I=158.

(c) Calculated from Eq. (B-6) and $I_i = CE_{bi}$ for I=137.

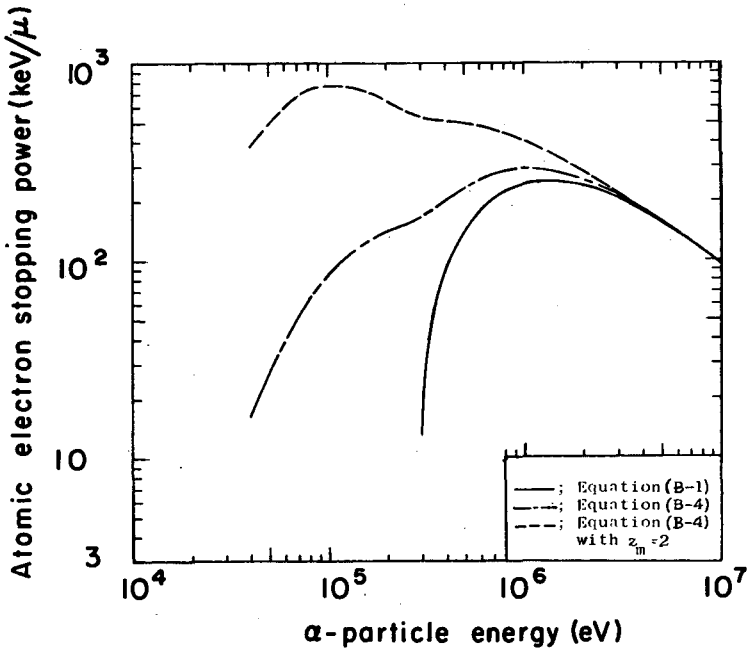

Fig. B.4. Atomic electron stopping power from Bethe's theoretical predictions for α-particle stopping in Si.

the passing α particle. The maximum impact parameter obtained by Bohr was

$$p_m = p_\nu = \tau_\nu V = \frac{1.123V}{2\pi\nu} \tag{B-7}$$

with a resulting stopping power of

$$\frac{dE}{dx} = -\frac{4\pi z_m^2 e^4}{mV^2} N_o \sum_{i=1}^{Z} \ln \frac{1.123mV^3M}{2\pi\nu_i z_m e^2(M+m)} \tag{B-8}$$

where ν_i is the characteristic frequency for the i^{th} atomic electron. The assumption was also made that the characteristic frequency and the average ionization potential for charged particle scattering are related by

$$I_i \simeq h\nu_i \ . \tag{B-9}$$

Bohr has defined the mean characteristic frequency as

$$Z\ln\bar{\nu} = \sum_{i=1}^{Z} \ln\nu_i . \tag{B-10}$$

Using Eq. (B-9) in Eq. (B-10) yields

$$Z\ln I = \sum_{i=1}^{Z} \ln I_i \tag{B-11}$$

which is similar to Eq. (B-3). For the previously mentioned case of α-particle stopping in Si, Eq. (B-8) becomes

$$\frac{dE_\alpha}{dx}\left(\frac{KeV}{\mu}\right) = -4.76 \times 10^9 \left(\frac{z_m^2}{E_\alpha}\right) \sum_{i=1}^{Z} \ln\left[9.76 \times 10^{-7}\left(\frac{E_\alpha^{3/2}}{z_m I_i}\right)\right] \tag{B-12}$$

where again E_α and I_i are in eV. In this classical analysis it was assumed that the electrons taking part in the interaction with the incident charge particle were initially at rest.

The effect of the orbital electron motion upon the classical coulomb scattering process has been considered by Gryzinski.[28] The stopping power equation obtained in this way is

$$\frac{dE}{dx} = -\frac{4\pi e^4 z_m^2}{mV^2} \int N(v_e) G[d(v_e), \lambda(v_e)] dv_e \qquad \text{(B-13)}$$

where v_e is the electron velocity, $\lambda = V/v_e$, $d = g^{1/2} v_e$, and $g = p_m m/z_m e^2$. p_m is the maximum impact parameter and the integral is carried out over the atomic electron velocity distribution of the stopping medium, $N(v_e)$. Gryzinski proposed that the maximum impact parameter can be determined from the minimum excitation energy of the first excited state of the atom, U_1.

For the large values of impact parameter corresponding to an energy transfer near the minimum excitation potential the maximum impact parameter is approximately equal to the distance of closest approach for the given trajectory, r_c.

The energy of interaction is then

$$U \simeq \frac{z_m e^2}{p_m} \simeq U_1$$

or

$$p_m \simeq \frac{z_m e^2}{U_1} \simeq \frac{2 z_m e^2}{U_j} \qquad \text{(B-14)}$$

where U_j is the ionization energy of the ground state for the outermost electron. Then since $U_j \simeq \frac{1}{2} m v_{ej}^2$, it is found that

$$g_j = \frac{p_m m}{z_m e^2} = \frac{2m}{U_j} = \frac{4}{v_{ej}^2}$$

and

$$d_j = g^{1/2} v_{ej} = 2.$$

The function $G[2;\lambda(v_e)]$ is plotted in Fig. B.5. In our application of Eq. (B-8) the atomic electrons are considered separately, and the form of distribution function is chosen to be

$$N(v_e) = \sum_{i=1}^{Z} N_o \delta(v_e - [\langle v_{ei}^2 \rangle \text{ avg}]^{1/2}) \tag{B-15}$$

where $m \langle v_{ei}^2 \rangle \text{ avg}/2 \simeq I_i$ is the energy an α particle must expend in a collision with the atomic system in order to ionize the i^{th} electron. Then the stopping power becomes

$$\frac{dE}{dx} = - \frac{4\pi e^4 z_m^2}{mV^2} N_o \sum_{i=1}^{Z} G[2,\lambda_i] \tag{B-16}$$

where $\lambda_i = V/[\langle v_{ei}^2 \rangle \text{ avg}]^{1/2} = (mE_\alpha/MI_i)^{1/2}$ and d has been assumed to be the same for all the electrons. We feel that this is not a bad approximation since the outermost electrons (for which $d \simeq 2$) make the dominant contribution to the stopping power. In the limit of $V \gg v_e$ (i.e., $\lambda \gg 1$)

$$G[2,\lambda] = \ln(4\lambda^2) \tag{B-17}$$

and the stopping power becomes

$$\frac{dE}{dx} = - \frac{4\pi e^4 z_m^2}{mV^2} N_o \sum_{i=1}^{Z} \ln\left(\frac{2mV^2}{I_i}\right) \tag{B-18}$$

which is just the Bethe stopping power equation. In the low energy limit where $V \ll v_e$ (i.e., $\lambda \ll 1$) Gryzinski has shown that Eq. (B-16) goes within a factor of 4 to the stopping power law of Fermi and Teller[24]

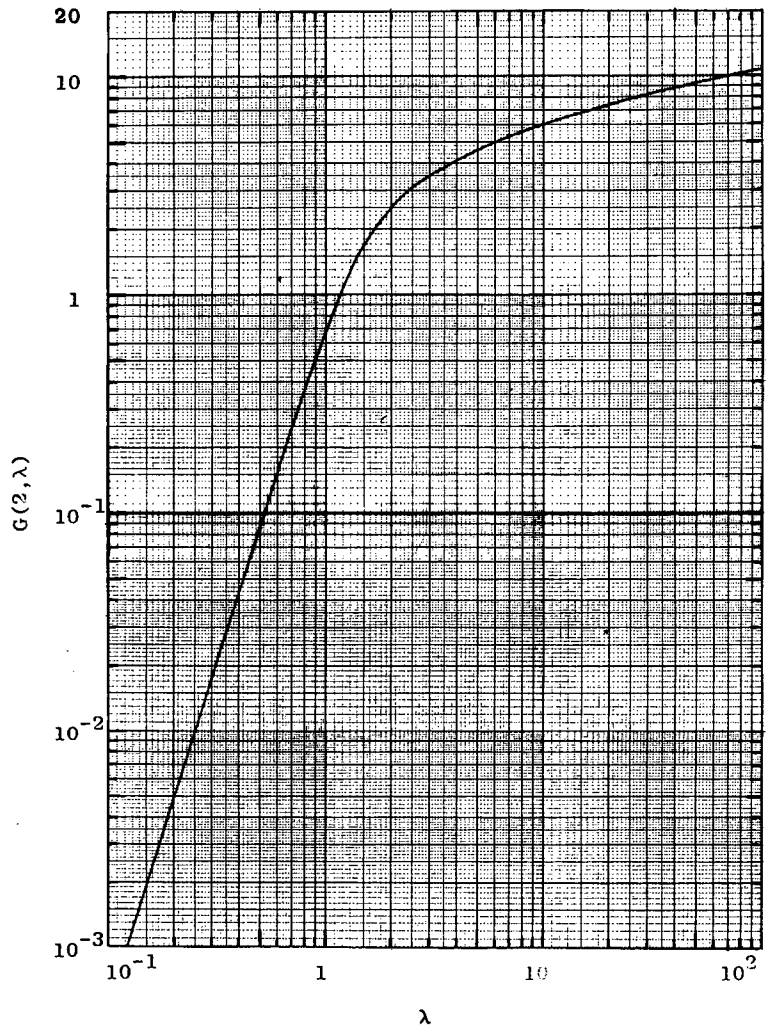

Fig. B.5. Plot of $G(2,\lambda)$ from Gryzinski's stopping-power equation.

which describes the energy lost be a charged particle to a completely degenerate electron gas. This is not the situation which exists for silicon as the stopping material since the conduction electron gas in normally doped material is non-degenerate. For this reason the Fermi and Teller stopping power equation will not be considered further. For the previously mentioned case of an α particle slowing down in Si Eq. (B-16) becomes

$$\frac{dE_\alpha}{dx}\left(\frac{KeV}{\mu}\right) = -4.76 \times 10^9 \left(\frac{z_m^2}{E}\right) \sum_{i=1}^{Z} G[2,\lambda_i] \qquad \text{(B-19)}$$

where $\lambda_i^2 = 1.37 \times 10^{-4}(E_\alpha/I_i)$ and as before E_α and I_i are in eV.

Bloch[8] carried out a quantum mechanical calculation of the stopping power for energetic charged particles valid for all values of $2z_m/137\beta$. His result goes to Bethe's and Bohr's results for the two limiting cases. In this development the stopping atoms were represented by the Thomas-Fermi model, in effect replacing the discrete atomic electrons by a continuous electron density distribution. The impact parameter was then specified as the distance from the nucleus to the path of the incident particle. The result obtained by Block is

$$\frac{dE}{dx} = -\frac{4\pi e^4 z_m^2}{mV^2} NZ\left[\log\frac{2mV^2}{I} + \psi(1) - R\psi\left(1+i\frac{z_m e^2}{hV}\right)\right] \qquad \text{(B-20)}$$

where ψ is the logarithmic derivative of the gamma-function and $R\psi$ denotes the real part of ψ. As we shall see shortly the decision was made to use the Gryzinski stopping power equation in the main body of the report and therefore Eq. (B-20) will not be considered further.

Calculations based upon the stopping power equations of Bethe (Eq. B-5) and Bohr (Eq. B-12) are compared with the experimental results of Gobeli for α-particle stopping in Si^{27} in Fig. B.6. It can be seen from the figure that for a given set of average ionization potentials for the atomic electrons (the curves labeled A are based upon the binding energies, and the curves labeled B are based upon the set of I_i which yield I = 158eV.) the two curves cross each other at an energy which corresponds to $2z_m/137\beta \approx 1$. This was discussed previously at which time it was pointed out that the resultant stopping power is best approximated by Bethe's equation for $2z_m/137\beta < 1$ and Bohr's equation for $2z_m/137\beta > 1$. The composite curve obtained in this manner from the curves A is not in good agreement with the experimental results of Gobeli, whereas the result obtained from curves B agrees fairly well with experiment. Two facts must be considered in judging the degree of agreement between theory and experiment as presented in this figure. They are (a) the neglect of the effect of atomic electron motion on the energy transfer process and (b) the fact that the analytical model of Bethe and Bohr do not properly account for the energy loss arising from the excitation of electrons from the valence band to the conduction band in a semiconductor for low α-particle energies. This latter process will be considered in detail in the following appendix. The effect of the electron motion can be accounted for by using Gryzinski's stopping power law. Curve A in Fig. B.7 is the stopping power obtained from Eq. (B-18) using the set of I_i corresponding to I = 158eV and z_m of Fig. B.3. The agreement with experiment is reasonably good, however, if a set of I_i is chosen which corresponds to a mean excitation potential of 137eV (see Table B.I), the curves labeled B are obtained using Bethe's

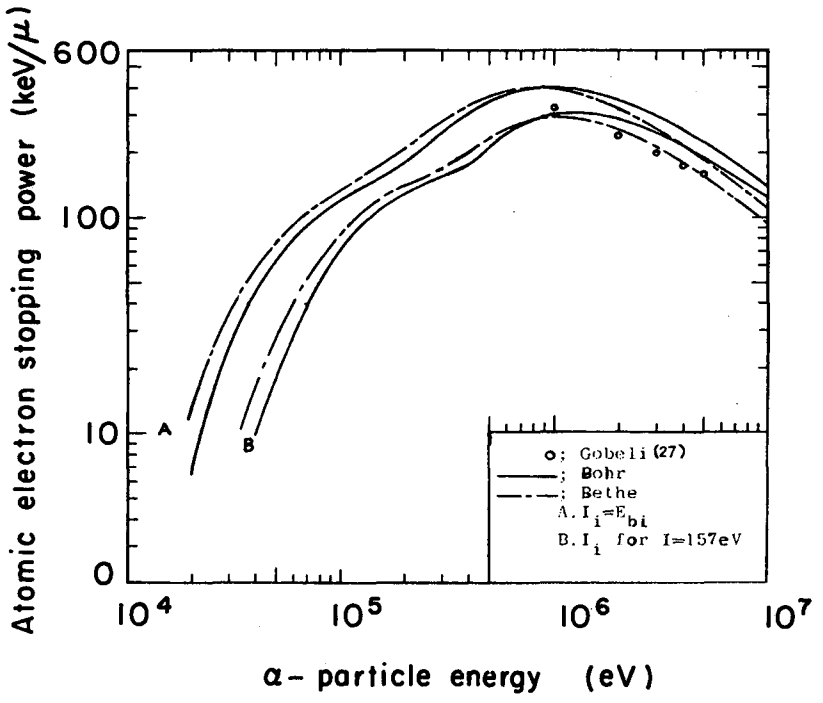

Fig. B.6. Comparison of the Bethe and Bohr atomic electron stopping-power equations with experiment for α-particle stopping in Si.

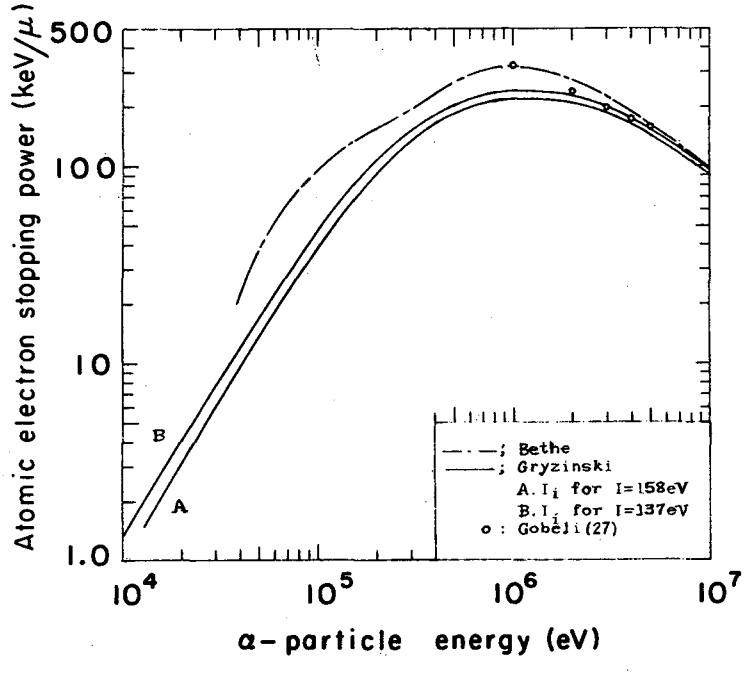

Fig. B.7. Comparison of the atomic electron stopping power of Bethe and Gryzinski with experiment for α-particle stopping in Si.

and Gryzinski's equations. The agreement with Gryzinski's stopping power law is quite good now, the calculated curve being slightly low. This is acceptable since a contribution to the stopping power from the valence band to conduction band transitions must be included. Figure B.9 shows that this contribution will not appreciably alter the agreement of the calculated stopping power with experiment. Therefore, the equation of Gryzinski was chosen to represent the atomic electron excitation and ionization contribution to the stopping power in the main body of this report. The stopping power considered in this appendix has been termed the atomic electron stopping power to contrast it with the interband stopping power to be considered next.

2. Valence Band to Conduction Band Electron Excitation. The excitation of an electron from the valence band to the conduction band in a semiconductor results for a perturbation of the electron potential produced by a heavy charged particle passing in the vicinity of the electron. The analysis of this process does not follow that for the conventional heavy charged particle energy loss laws described above since the electron is not ionized (a continuum of states is not available after the transition) but is instead excited into a band of energy states. This band of available states is narrow compared to the continuum encountered in the ionization process, and therefore only interactions over a limited range of impact parameter can make a strong contribution to the excitation process. A thorough analysis of this excitation process should include all possible transitions from the filled states in the valence band to the empty states in the conduction band. In the present analysis it will be assumed that the valence band is relatively thin so that all

the filled states are near the top of the valence band and that the available states which are the most important in the transition process lie near the bottom of the conduction band. This should be a reasonably good approximation for insulators with their large forbidden energy gaps. Semiconductors with their smaller forbidden energy gaps do not satisfy these approximate conditions well, but the approximation will nonetheless be made in order to facilitate the analysis of this section.

The perturbing potential, η, initially small, increases to a maximum at the distance of closest approach and then decreases as the charged particle travels away from the atom. The Hamiltonian for the system of valence and conduction electrons in question would then be

$$H = H^{o} + \eta(t) \tag{B-21}$$

where H^{o} is the unperturbed Hamiltonian with eigen functions

$$H^{o}\Phi_{n} = E_{n}\Phi_{n} \tag{B-22}$$

and Φ_{n} is the unperturbed wave function for the system of electrons in the valence and conduction bands. Using first order perturbation theory for a two level transition process the probability of the excited state being occupied at time t is found to be

$$P(t) = \frac{1}{\hbar^{2}} \left| \int_{-\infty}^{t} \eta_{21}(t) e^{\frac{1}{\hbar}(E_{2}-E_{1})t} \, dt \right|^{2} \tag{B-23}$$

and the excitation probability after the event is complete is

$$P = \frac{1}{\hbar^{2}} \left| \int \Phi_{2}^{*} \eta(t) \Phi_{1} e^{i\omega t} \, dv dt \right|^{2} \tag{B-24}$$

where the time integral extends from $-\infty$ to ∞ and

$$\omega = \frac{(E_{2}-E_{1})}{\hbar} \quad . \tag{B-25}$$

At this point the one electron approximation will be introduced. This assumes that all the electrons in a given band experience the same potential which arises from both the fixed atomic centers and an averaged out contribution from all the other electrons. Each electron is then treated separately. The wave functions Φ_1 and Φ_2 are those of an electron in the valence band at energy E_v and an electron in the conduction band at energy E_c respectively. The transition frequency becomes

$$\omega = \frac{(E_c - E_v)}{\hbar} = \frac{E_g}{\hbar} \qquad \text{(B-26)}$$

where E_g is the forbidden energy gap. The interaction potential for this limiting case is just the coulomb interaction between the incident charged particle and the electron under consideration,

$$\eta(t) = \frac{z_m e^2}{|r-R(t)|} \qquad \text{(B-27)}$$

where z_m, the mean charge on the energetic particle, is a function of its velocity, V, and $|r-R(t)|$ is the distance between the charged particle and the electron. For this term to be small compared to the unperturbed Hamiltonian, H^o, the smallest separation encountered during the interaction should be large compared to the distances separating the electron from both the nucleus and the other atomic electrons. This requires that the distance of closest approach for the alpha particle-electron interaction should be greater than a distance of the order of a_o, the radius of the first Bohr orbit.

For the case of repulsive coulomb scattering, this condition can be satisfied by imposing an upper limit on the energy considered. In this type of scattering the distance of closest approach $r_c(p)$ for a given impact parameter, p, is

$$r_c(p) = \frac{b}{2} + \sqrt{\left(\frac{b}{2}\right)^2 + p^2} \qquad \text{(B-28)}$$

which shows that the condition $r_c(p) \geq b$ is satisfied for the duration of the interaction. Therefore the perturbation method discussed above will be valid for an incident particle energy E_α which corresponds to $b > a_o$ where

$$b = \frac{|z_m e^2|}{E_\alpha} \left(\frac{M}{m}\right) \qquad \text{(B-29)}$$

is the classical distance of closest approach.

The situation is more complex for an attractive potential for which case $r_c(p)$ is

$$r_c(p) = -\frac{b}{2} + \sqrt{\left(\frac{b}{2}\right)^2 + p^2}, \qquad \text{(B-30)}$$

and the condition $r_c(p) \geq b$ is no longer satisfied during the time of collision. Then $r_c(p) > a_o$ is only satisfied when

$$p^2 > a_o^2 + ba_o \, . \qquad \text{(B-31)}$$

This sets a minimum limit on the impact parameter and in addition a maximum limit exists as a result of the finite extent of the interaction between the incident particle and the electron. The incident particle predominately interacts with an electron on another atom when the impact parameter exceeds the atomic radius, R. The contributions to the energy loss resulting from collisions which do not satisfy Eq. (B-31) are therefore neglected. This situation can be approximately compensated for by chosing a maximum impact parameter greater than the atomic radius with a resultant equal overestimate of the energy loss for collisions where $\eta(t) < H_o$. Seitz and Koehler,[55] when considering excitations of this type for a nearly neutral incident particle, assumed the interaction potential to be separable into spatial and time functions.

Making use of the same assumption, we obtain

$$\eta(t) = \eta(r_c)e^{-t^2/\tau^2} \tag{B-32}$$

where $\tau = r_c(p)/V$ and $\eta(r_c)$ is the coulomb interaction at the distance of closest approach. The time function is only approximate but does represent the actual character of the interaction. The form for the spatial term is a rougher approximation than that made by Seitz and Koehler who assumed the interaction matrix element to be given by

$$\int \phi_2^* \quad \eta\phi_1 dv = \eta_{21} e^{-t^2/\tau^2}. \tag{B-33}$$

In order to accurately evaluate η_{21}, it is necessary to know the initial and final wave functions for the electrons and to expand the interaction potential in multipoles and calculate the contribution to the matrix element for each term in the expansion. This is beyond the scope of the present analysis and therefore the approximation given by Eq. (B-32) was considered to be sufficient. Using this relation for the interaction potential in Eq. (B-24) yields

$$P(\tau) = \frac{\eta_{21}^2 \pi\tau^2}{\hbar^2} \exp\left\{ - \frac{\omega^2\tau^2}{2} \right\} \tag{B-34}$$

where we have assumed that $\eta_{21} = \int \phi_2^* \eta(r_c)\phi_1 dv \approx \eta(r_c)$. Equation (B-34) written in terms of the distance of closest approach is

$$P(r_c) = \frac{z_m e^2 \pi}{\hbar^2 V^2} \exp\left\{ - \frac{E_g^2 r_c^2}{2\hbar^2 V^2} \right\} \tag{B-35}$$

where we have also assumed that $\eta_{21} \approx \eta(r_c) = z_m e^2/r_c^2$. The differential scattering cross section for coulomb scattering is

$$d\sigma(E,p) = K(E,p)dp = - 2\pi p dp. \tag{B-36}$$

Assuming that the energy transfer per transition is approximately equal to E_g, (cf. Eq. (B-26)) the stopping power is given by

$$\frac{dE}{dx} = -E_g N_o \int_{p_{max}}^{p_{min}} d\sigma(E,p)P(p)dp \qquad (B-37)$$

or

$$\frac{dE}{dx} = -\frac{2\pi^2 z_m^2 e^4 N_o E_g}{\hbar^2 V^2} \int_{p_{min}}^{p_{max}} pdp \exp\left\{-\frac{E_g^2 r_c^2}{2\hbar^2 V^2}\right\} . \qquad (B-38)$$

The integration is most easily carried out over r_c so that making use of the equality $pdp = (r_c + b/2)dr_c$, Eq. (B-38) becomes

$$\frac{dE}{dx} = -\frac{\pi^2 z_m^2 e^4 N_o E_g}{\hbar^2 V^2} \int_{r_{c,min}}^{r_{c,max}} 2r_c dr_c \exp\left\{-\frac{E_g^2 r_c^2}{2\hbar^2 V^2}\right\} + b\int_{r_{c,min}}^{r_{c,max}} dr_c \exp\left\{\frac{E_g^2 r_c^2}{2\hbar^2 V^2}\right\} . \qquad (B-39)$$

The first term in the brackets can be integrated while the second must be evaluated numerically. Integrating the first term and considering α-particle stopping in Si yields

$$\frac{dE_\alpha}{dx}\left(\frac{KeV}{\mu}\right) = \delta\left(\frac{z_m^2}{E_\alpha}\right)\frac{1}{a}\left[e^{-ar_{c,min}^2} - e^{-ar_{c,max}^2}\right] + b\int_{r_{c,min}}^{r_{c,max}} dr_c e^{-ar_c^2} \qquad (B-40)$$

where $\delta = 5.39 \times 10^{24}$ eV/cm$^2\mu$, $a = 2.88 \times 10^{18}$ eV/cm^2, E_α is in eV, and r_c is in cm. The minimum limit on the distance of closest approach is taken to be $r_{c,min} \simeq 10^{-8}$cm; and as stated previously, the maximum should be greater than the atomic radius, $R \approx 1.7 \times 10^{-8}$ cm. In selecting a maximum value for r_c, the condition given by Eq. (B-51) was employed. This condition specifies the α-particle energy at which the electron excitation stopping power and atomic collision stopping power are comparable. At α-particle energies in excess of the cross over point

energy, electron excitation and/or ionization is the dominant mechanism for energy loss. The maximum was taken to be $r_{c,max} \simeq 3 \times 10^{-8}$ cm with a corresponding cross over energy of $E_\alpha \simeq 4$KeV (see Fig. B.18). This is in excess of the value obtained from Eq. (B-51) (that is, $E_i \simeq 1$KeV) which is consistent with the discussion which accompanies the introduction of this equation in the next section of this Appendix. The stopping power calculated using these limits is presented in Fig. B.8 where the relative contributions from the two integrals are indicated.

As the α-particle energy decreases, it captures electrons and approaches neutrality. This is just the situation considered by Seitz and Koehler as mentioned earlier. The neutral particle has neglibible probability of interaction unless its electron cloud penetrates the electron cloud of an atom of the stopping medium. Therefore, Seitz and Koehler assumed that the cross section for scattering will be zero for $r_c > R$ and $\sigma = \pi R^2$ if $r_c < R$. This assumes only minor penetration of the silicon atom electron cloud by the neutral helium atom which is reasonable at the low energies considered here. The characteristic interaction time in this case is $\tau \simeq R/V$. The interaction potential for this atom-atom scattering process is difficult to ascertain. For the present analysis we assumed that the scattering results in an interaction potential between the incident particle and a valence electron in the crystal of a coulomb nature where the net charge on the incident particle is z_m (i.e. that obtained from Evans). In the present case the orbital electron speed will be on the order of or greater than the incident particle speed so that their average separation will be approximately equal to the atomic radius inasmuch as the electron makes a number of orbits during the time of interaction. The condition $v_e > V$ is satisfied

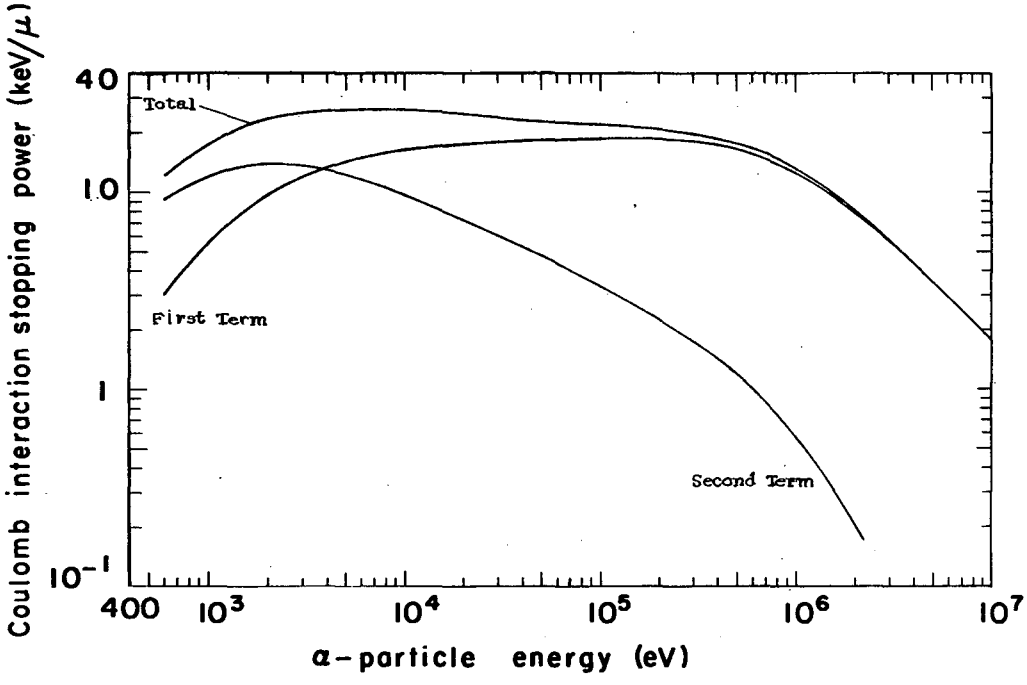

Fig. B.8. Coulomb interaction stopping power for valence band to conduction band transitions in Si.

so long as $E \lesssim 10KeV$ for α-particle stopping in Si. An impact parameter relative to the electron has no meaning due to the electron's orbital motion. As a result, the transition probability was assumed to be constant for any direction of travel of the incident particle taking it through a cross sectional area of πR^2 about the nucleus of a lattice atom. The interaction potential in this approximation is

$$\eta_{21} = \frac{z_m e^2}{R} \tag{B-41}$$

and the transition probability is

$$P(V) = \frac{\eta_{21}^2 \pi R^2}{\hbar^2 V^2} \exp\left(-\frac{\omega^2 R^2}{2V^2}\right) \tag{B-42}$$

or

$$P(V) = \frac{\pi z_m^2 e^4}{\hbar^2 V^2} \exp\left(-\frac{E_g^2 R^2}{2\hbar^2 V^2}\right) . \tag{B-43}$$

The stopping power for this neutral resonance excitation process is then given by

$$\frac{dE}{dx} = -E_g \sigma P(V) N_o \doteq -\frac{\pi^2 R^2 z_m^2 e^4 N_o E_g}{\hbar^2 V^2} \exp\left(-\frac{E_g^2 R^2}{2\hbar^2 V^2}\right) \tag{B-44}$$

and for the α-particle stopping in Si this becomes

$$\frac{dE_\alpha}{dx}\left(\frac{KeV}{\mu}\right) = -3.89 \times 10^9 \left(\frac{z_m^2}{E_\alpha}\right) \exp\left(-\frac{832}{E_\alpha}\right). \tag{B-45}$$

For incident particle energy less than 100 KeV which includes the energy range of interest for this energy loss mechanism the approximate linear dependence of mean charge on velocity yields

$$\frac{z_m^2}{E_\alpha} = 4.35 \times 10^{-6}\ eV^{-1}$$

and then the stopping power is

$$\frac{dE_\alpha}{dx}\left(\frac{KeV}{\mu}\right) = -16.9 \exp\left(-\frac{832}{E_\alpha}\right) \qquad (B\text{-}46)$$

where E_α is in eV. The stopping power calculated from Eq. (B-46) is presented as curve B in Fig. B.9. The composite curve for the stopping power is obtained from Eq. (B-46) for $E_\alpha \lesssim$ 10KeV, Eq. (B-40) for $E_\alpha \gtrsim$ 100KeV, with the two being connected in the energy interval 10 KeV $\lesssim E_\alpha \lesssim$ 100KeV.

The total electronic stopping power is equal to the sum of the atomic electron stopping power and the stopping power resulting from valence band to conduction band transitions. This is shown in Fig. B.10 where the individual contributions for each term are indicated by the dashed curves and the experimental results of Gobeli[27] are included for comparison. This is the stopping power relation which must be used in Eq. (B-83).

3. Atomic Collision Stopping Power and the Production of Lattice Displacements. As an energetic charged particle penetrates a stopping medium, energy is lost through atomic collisions with the lattice atoms as well as through electron excitation and ionization. Those atomic collisions for which the energy transfer exceeds that necessary to displace the atom from its lattice site lead to the production of radiation induced defect centers providing the effect of atom replacements is negligible. The interaction potential for the atomic collision is of the screened coulomb type,

$$V(r) = \frac{zZe^2}{r} \exp\left(-\frac{r}{a}\right), \qquad (B\text{-}47)$$

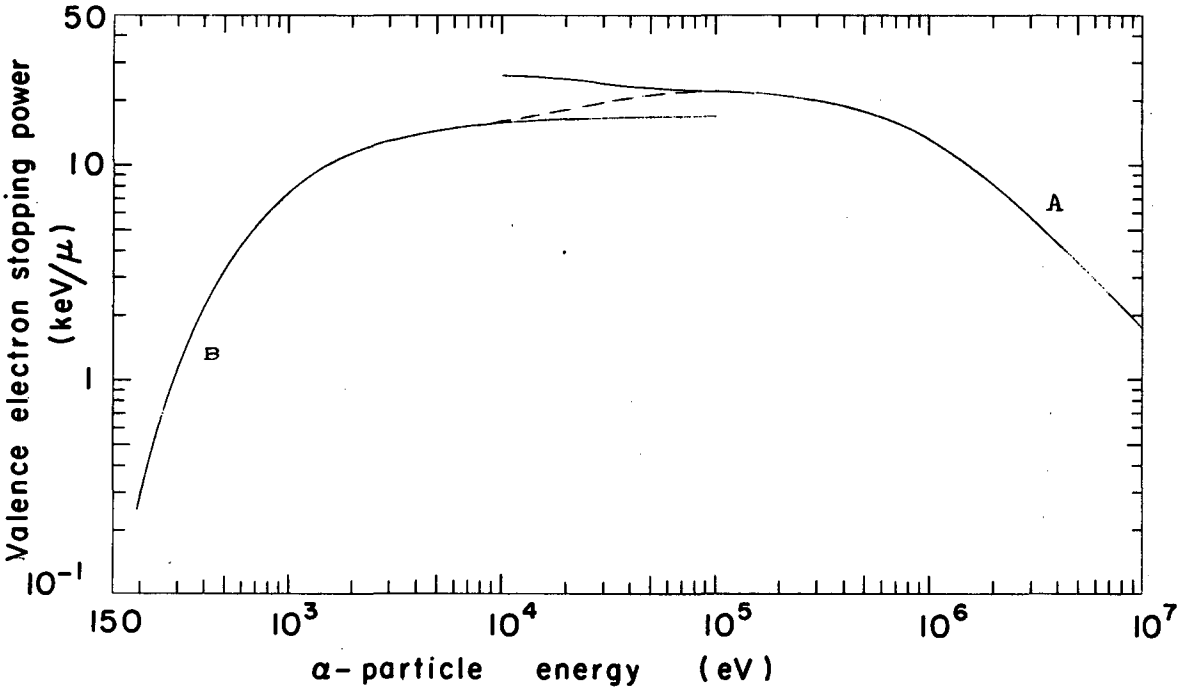

Fig. B.9. Stopping power for valence band to conduction band transitions in Si.

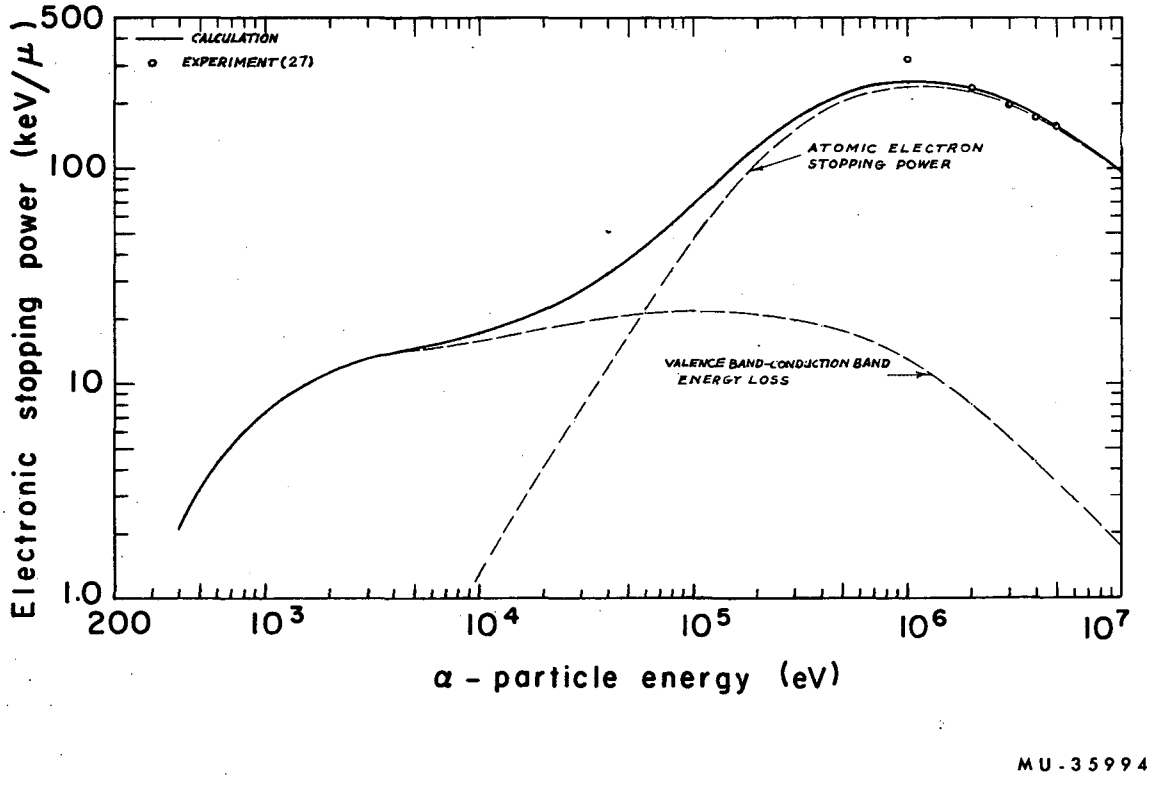

Fig. B.10. Total electronic stopping power for α-particle stopping in Si.

where Bohr[10] has suggested that

$$a = \frac{a_o}{(z^{2/3} + Z^{2/3})^{1/2}} , \qquad (B\text{-}48)$$

Z is the nuclear charge of the lattice atoms, and z is the nuclear charge of the incident particle. For high energyof the incident particle the screening is weak, and there is a direct coulomb interaction between the incident charged particle and the atomic nucleus. At low energy the screening is strong, and the particle undergoes hard sphere scattering with the lattice atoms.

Seitz and Koehler[55] have shown that the method of analyzing the scattering process depends upon the magnitude of the screening parameter, ζ , and the classicity parameter, κ, where

$$\kappa = 2zZ\left(\frac{R_h M_1}{Em}\right)^{1/2} \qquad (B\text{-}49)$$

and

$$\zeta = zZ \frac{2R_h}{E} \left(\frac{M_1 + M_2}{M_2}\right) \frac{a_o}{a} . \qquad (B\text{-}50)$$

Here R_h is the Rydberg energy for the hydrogen atom (13.54 eV), M_1 is the mass and E is the energy of the incident particle, and M_2 is the mass of the lattice atom. κ and ζ are presented in Fig. B.11 for α-particle scattering from silicon. It can be seen that $\zeta < 1$ is satisfied for $E_\alpha > 2.4$ keV, and $\zeta > 1$ for $E_\alpha < 2.4$keV. Seitz and Koehler state that when $\zeta \gg 1$ and $\kappa \gg 1$ (i.e. $E_\alpha < 240$eV) the α particle will suffer classical hard sphere scattering with the lattice atoms and, when $\zeta \ll 1$ and $\kappa \gg 1$ (i.e. for $E_\alpha > 24$keV up to several MeV), the scattering will be of the classical Rutherford type. In the energy interval, $240\text{eV} < E_\alpha < 24\text{keV}$, the scattering process undergoes a transition from classical hard sphere to classical Rutherford scattering.

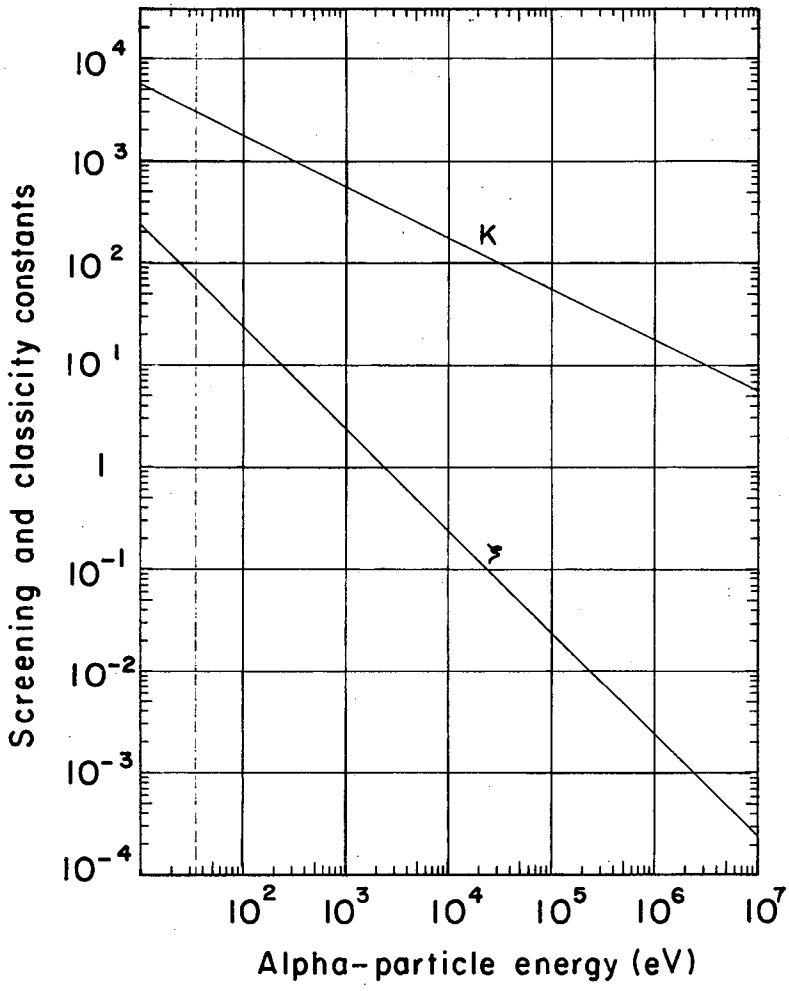

Fig. B.11. Screening and classicity constants for α-particle stopping in Si.

Seitz[54] has also suggested that the charged particle loses energy primarily through electron excitation above an energy

$$E_i = \frac{M}{m}\,\frac{\epsilon}{\delta} = \frac{ME_g}{m\delta}\,, \qquad \text{(B-51)}$$

where ϵ, the minimum excitation energy for electrons in the stopping material, has been set equal to the forbidden energy gap, E_g, for the special case of a semiconductor. If this transition process had been analyzed on the basis of hard sphere scattering, a minimum threshold energy of $ME_g/4m$ is predicted. The interaction is however quantum mechanical in nature and threfore exhibits a resonance behavior. A finite transition probability exists even through $E < E_{th}$. In light of this fact Seitz assumed that this electron excitation process becomes the dominant form of energy loss at $E_i \simeq E_{th}/2$ which led to Eq. (B-51). The resonance behavior of the interaction would lead to a decrease in the stopping power for $E > E_{th}$ if it were not for the coulomb nature of the interaction which enhances the stopping power for $E > E_{th}$ through those collisions corresponding to large impact parameters. The result of this is a stopping power curve which falls rapidly for $E < E_{th}$ and rises slowly for $E > E_{th}$. In light of these facts, we feel it more reasonable to assume that the two energy loss mechanisms (electron transitions and atomic collisions) are comparable at $E \gtrsim E_{th} = 2E_i$. Returning to Eq. (B-51) we find that, in Si, for displaced primaries

$$E_i(\text{Si}) \simeq 7\text{keV}$$

while for incident α particles

$$E_i(\alpha) \simeq 1\text{keV}.$$

For classical Rutherford scattering the cross section is

$$d\sigma_{DR}(E,T) = K_{DR}(E,T)dT = \frac{\pi b^2}{4} T_m \frac{dT}{T^2}, \qquad (B-52)$$

where T is the energy of the displaced atom after collision, the maximum energy transfer in a head on collision is

$$T_m = \frac{4M_1M_2}{(M_1+M_2)^2} E, \qquad (B-53)$$

and the classical distance of closest approach is

$$b = \frac{zZe^2}{E} \frac{(M_1+M_2)}{M_2} . \qquad (B-54)$$

The energy transfer, T, is limited to the values above the threshold for defect center production, E_D. The average energy of a primary displacement is then obtained from

$$\overline{E}_p(DR) = \overline{T} = \frac{\int_{E_D}^{T_m} T d\sigma_{DR}(E,T)}{\int_{E_D}^{T_m} d\sigma_{DR}(E,T)} . \qquad (B-55)$$

The cross section for classical hard sphere scattering is

$$d\sigma_{DHS}(E,T) = K_{DHS}(E,T)dT = \pi R_o^2 \frac{dT}{T_m} \qquad (B-56)$$

where R_o is the radius for hard sphere scattering. Again only those collisions for which $T \geq E_D$ are considered so that the average energy of a primary displacement resulting from classical hard sphere scattering is

$$\overline{E}_p(DHS) = \overline{T} = \frac{\int_{E_D}^{T_m} T d\sigma_{DHS}(E,T)}{\int_{E_D}^{T_m} d\sigma_{DHS}(E,T)} = \frac{1}{2}(T_m+E_D). \qquad (B-57)$$

In the rather broad energy interval over which the scattering undergoes the transition from classical hard sphere to classical Rutherford, Dienes and Vineyard[18] have suggested that the differential cross section for screened coulomb collisions can be represented by

$$d\sigma_{DSC}(E,T) \propto \frac{dT}{T^n} \tag{B-58}$$

where n is between 1 and 2. The average energy of a primary displaced atom in this case is

$$\bar{E}_p(DSC) = \frac{\int_{E_D}^{T_m} T d\sigma_{DSC}(E,T)}{\int_{E_D}^{T_m} dT_{DSC}(E,T)} = T_m \frac{(n-1)}{(n-2)} \frac{\left[\left(\frac{T_m}{E_D}\right)^{(n-2)} - 1\right]}{\left[\left(\frac{T_m}{E_D}\right)^{(n-1)} - 1\right]} . \tag{B-59}$$

Figure B.12 shows the average energy of a primary displaced atom for classical hard sphere scattering, for classical Rutherford scattering, and for a number of values of n in the scattering law applicable in the transition energy region.

The total cross section for the production of a primary displacement is given in Eqs. (B-55) and (B-57). For the case of classical Rutherford scattering

$$\sigma_{DR}(E) = \int_{E_D}^{T_m} d\sigma_{DR}(E,T)dT = \frac{\pi b^2}{4}\left(\frac{T_m}{E_D} - 1\right) \tag{B-60}$$

while for classical hard sphere scattering

$$\sigma_{DHS} = \int_{E_D}^{T_m} d\sigma_{DHS}(E,T)dT = \pi R_o^2\left(1 - \frac{E_D}{T_m}\right). \tag{B-61}$$

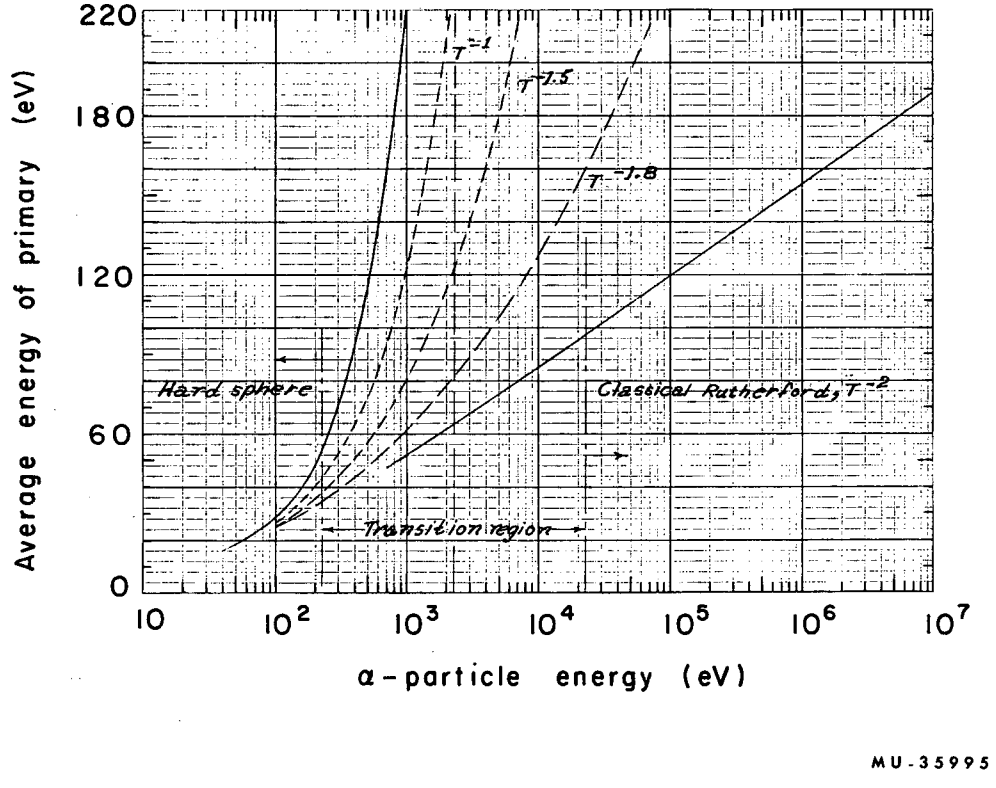

Fig. B.12. Average energy of primary displaced atom for α-particle stopping in Si using various scattering laws.

The radius for hard sphere scattering, R_o, is a function of energy in the keV energy region and slowly approaches the atomic radius as obtained from the atomic density when the incident particle energy is less than the threshold energy necessary for the production of a displacement. Seitz and Koehler state that the radius for hard sphere scattering is approximately equal to the distance of closest approach obtained by equating the kinetic energy of the two particle system to the screened coulomb interaction potential. Therefore

$$\frac{M_2 E}{(M_1+M_2)} = \frac{zZe^2}{R_o} \exp[-\frac{R_o}{a}] \qquad \text{(B-62)}$$

or

$$R_o = \frac{a_o}{[z^{2/3}+Z^{2/3}]^{1/2}} \ln[\frac{zZe^2}{ER_o}(\frac{M_2}{M_1+M_2})] . \qquad \text{(B-63)}$$

It is not possible to obtain the total cross section in the transition energy range from Eq. (B-58). The total displacement cross section obtained from Eqs. (B-60) and (B-61) for the interaction of an α particle with Si is presented in Fig. B.13, where the cross section is zero for $E_\alpha \leq 34.5$eV (this corresponds to the minimum threshold energy transfer of $E_D = 15$eV for Si).

The number of defects produced per unit track length by an incident particle of energy E in losing an increment of energy dE is

$$dn_D = n_D(E)dE = \int_{E_D}^{T_m} N_o K_D(E,T)\nu(T)dTdE \qquad \text{(B-64)}$$

where $\nu(T)$ is the number of displacements produced by a primary of energy T, N_o is the number of lattice atoms per unit volume, and $K_D(E,T)dT$ is the appropriate displacement cross section for the energy region under consideration.

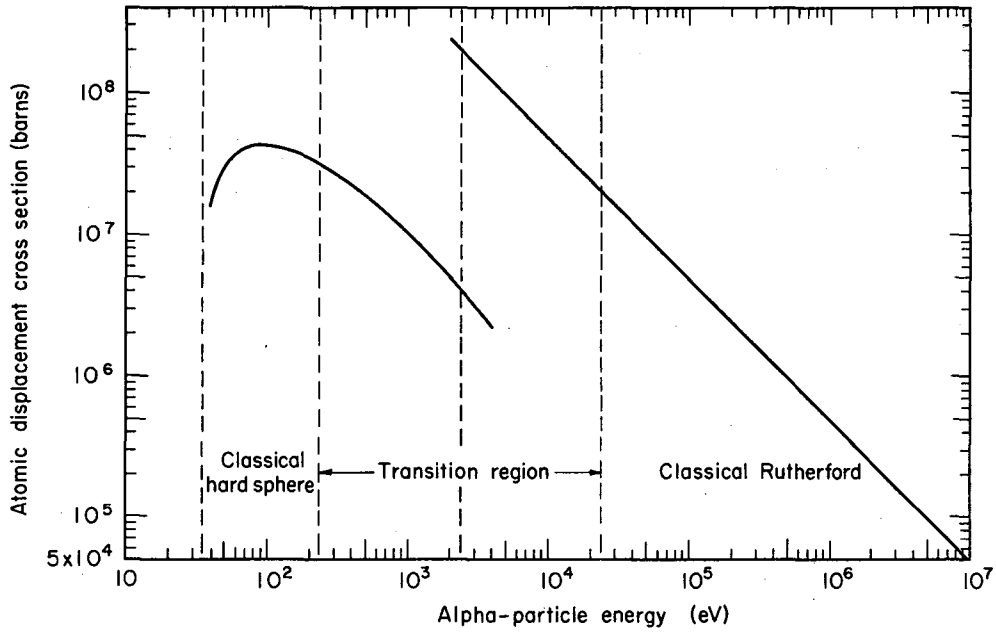

Fig. B.13. Atomic displacement cross section for α-particle stopping in Si.

The average number of displacements produced per primary by an incident particle of energy E is

$$\nu(E) = \frac{\int_{E_D}^{T_m} d\sigma_D(E,T)\nu(T)dT}{\int_{E_D}^{T_m} d\sigma_D(E,T)dT} \qquad \text{(B-65)}$$

where the relation of Kinchen and Pease[34] is to be used for $\nu(T)$. It is shown in Fig. B.14 and is given by

$$\nu(T) = \begin{cases} 0 & \text{for } T < E_D \\ 1 & \text{for } E_D \leq T \leq 2E_D \\ T/2E_D & \text{for } 2E_D \leq T \leq E_i \\ E_i/2E_D & \text{for } E_i \leq T \end{cases} \qquad \text{(B-66)}$$

The average number of lattice displacements produced per primary for classical coulomb scattering is then

$$\nu_R(E) = \frac{\int_{E_D}^{T_m} \frac{\nu(T)}{T^2}\, dT}{\int_{E_D}^{T_m} \frac{dT}{T^2}}$$

$$= \begin{cases} \frac{T_m}{2(T_m-E_D)}\left[1+\ln\left(\frac{E_i}{2E_D}\right)+\frac{(T_m-E_i)}{T_m}\right] & \text{for } T_m > E_i \\ \frac{T_m}{2(T_m-E_D)}\left[1+\ln\left(\frac{T_m}{2E_D}\right)\right] & \text{for } T_m \leq E_i \end{cases} \qquad \text{(B-67)}$$

while the number for classical hard sphere scattering is

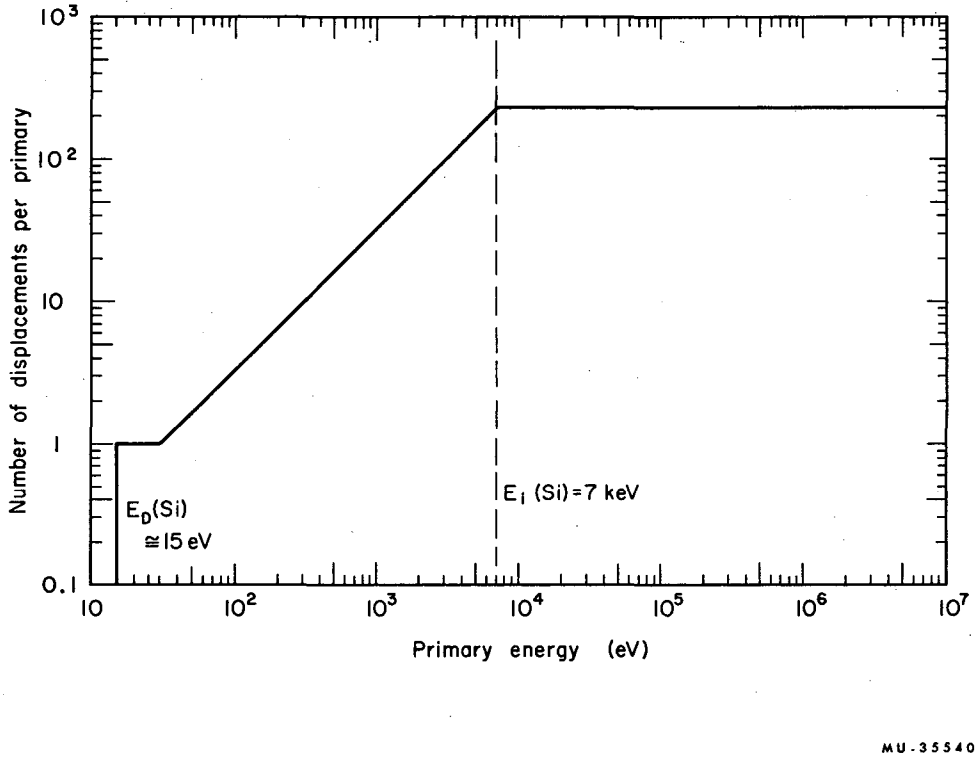

Fig. B.14. Number of displacements per primary displaced atom for Si.

$$\bar{\nu}_{HS}(E) = \frac{\int_{E_D}^{T_m} \nu(T)dT}{\int_{E_D}^{T_m} dT}$$

$$= \begin{cases} \dfrac{E_D}{(T_m-E_D)} + \dfrac{(E_i^2-4E_D^2)}{(T_m-E_D)4E_D} + \dfrac{E_i(T_m-E_i)}{2E_D(T_m-E_D)} & \text{for } T_m > E_i \\ \dfrac{E_D}{(T_m-E_D)} + \dfrac{T_m^2-4E_D^2}{(T_m-E_D)4E_D} & \text{for } T_m \leq E_i \end{cases} \qquad \text{(B-68)}$$

Equations (B-67) and (B-68) for the average number of displacements produced per primary in Si by an α particle of energy E_α are plotted in Fig. B.15).

The number of displacements produced per unit track length by an incident particle is then

$$dn_D = n_D(E)dE = \bar{\nu}(E)\sigma_D(E)dE \qquad \text{(B-69)}$$

and Eqs. (B-60), (B-61), (B-67), and (B-68) have been used to obtain curves A and B of Fig. B.16 for α-particle penetration of Si. A composite curve for the displacement production rate per α particle was obtained by connecting the two limiting curves with the assumed dotted line shown in the transition energy region.

The rate of energy loss through the atomic collisions under consideration here is given by

$$\frac{dE}{dx} = -N_o \int_{E_D}^{T_m} T d\sigma_D(E,T)dT. \qquad \text{(B-70)}$$

For the case of classical Rutherford scattering this becomes

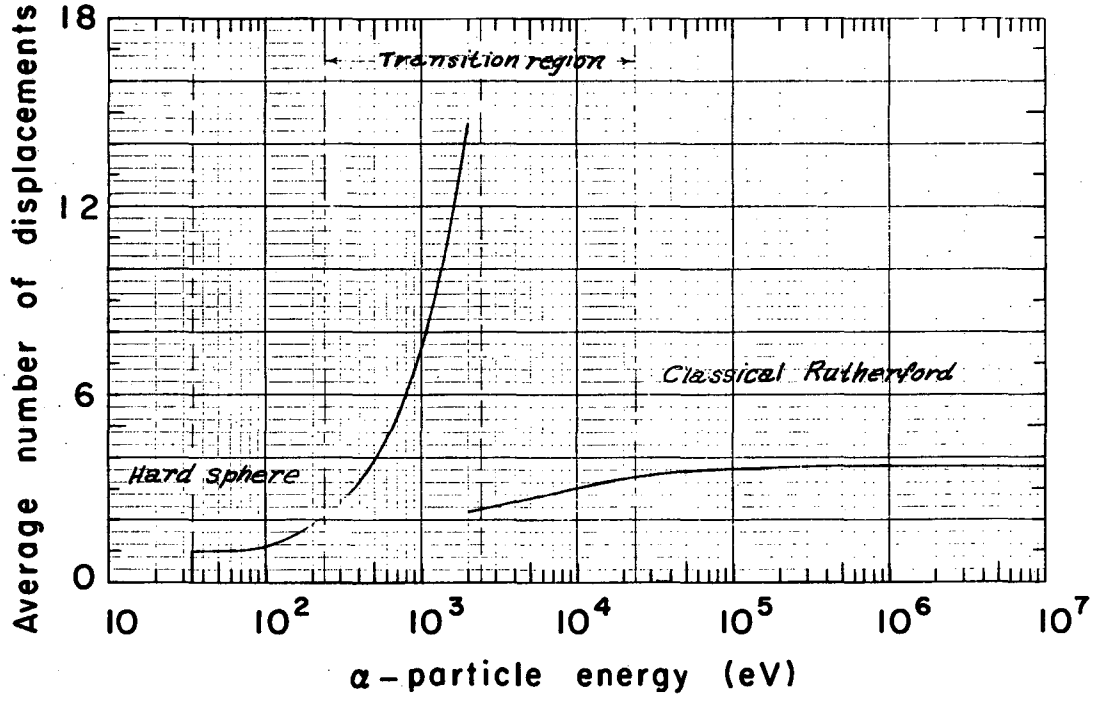

Fig. B.15. Average number of displacements per primary for α-particle hard sphere and Rutherford scattering in Si.

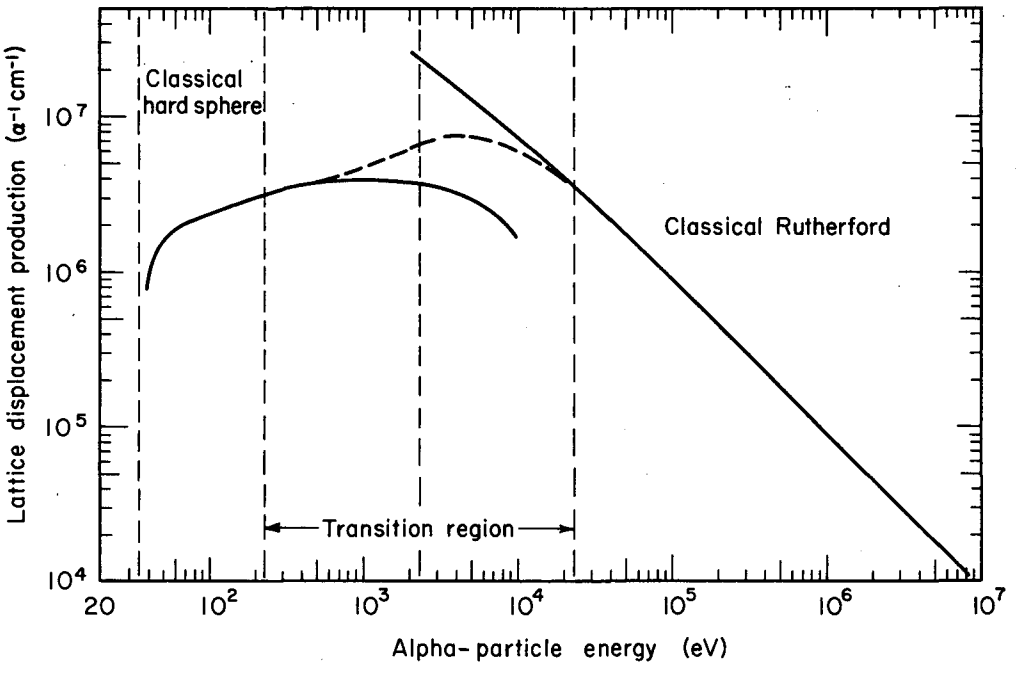

Fig. B.16. The number of lattice displacements produced per unit track length per α-particle for stopping in Si.

$$\frac{dE}{dx} = -\frac{\pi b^2}{4} T_m N_o \ln\left(\frac{T_m}{E_D}\right) \qquad \text{(B-71)}$$

where

$$\frac{\pi b^2}{4} T_m = \frac{\pi z^2 Z^2 e^4}{E} \left(\frac{M_1}{M_2}\right) , \qquad \text{(B-72)}$$

and for the case of classical hard sphere scattering

$$\frac{dE}{dx} = -\frac{\pi R_o^2}{2} T_m N_o \left[1-\left(\frac{E_D}{T_m}\right)^2\right] \qquad \text{(B-73)}$$

where T_m is given by Eq. (B-53). The atomic collision stopping power is presented in Fig. B.17 for α-particle stopping in Si. The classical hard sphere and classical Rutherford contributions are curves A and B respectively. Once again the composite curve is obtained by connecting the curves A and B by the assumed dotted line in the transition energy region. It must be noted that although there is no strict theoretical basis for the choice of the curve in the transition energy region the chosen shape appears reasonable.

The total stopping power which is composed of the electronic stopping power and the atomic collision stopping power is shown in Fig. B.18. This total stopping power relation was used to find $f(\overline{E}_{\alpha o}, x, E_\alpha)$; that is, the energy E_α that an α-particle of initial energy $\overline{E}_{\alpha o}$ has at position x is found through a numerical integration of the total stopping power. This numerical integration made it possible to determine the range of an α-particle with initial energy $\overline{E}_{\alpha o}$. These calculated ranges are compared with the experimental results of Gobeli[27] in Fig. B.19. In the comparison the calculated range is taken to be the position at which the α-particle energy has decreased to 200 keV which

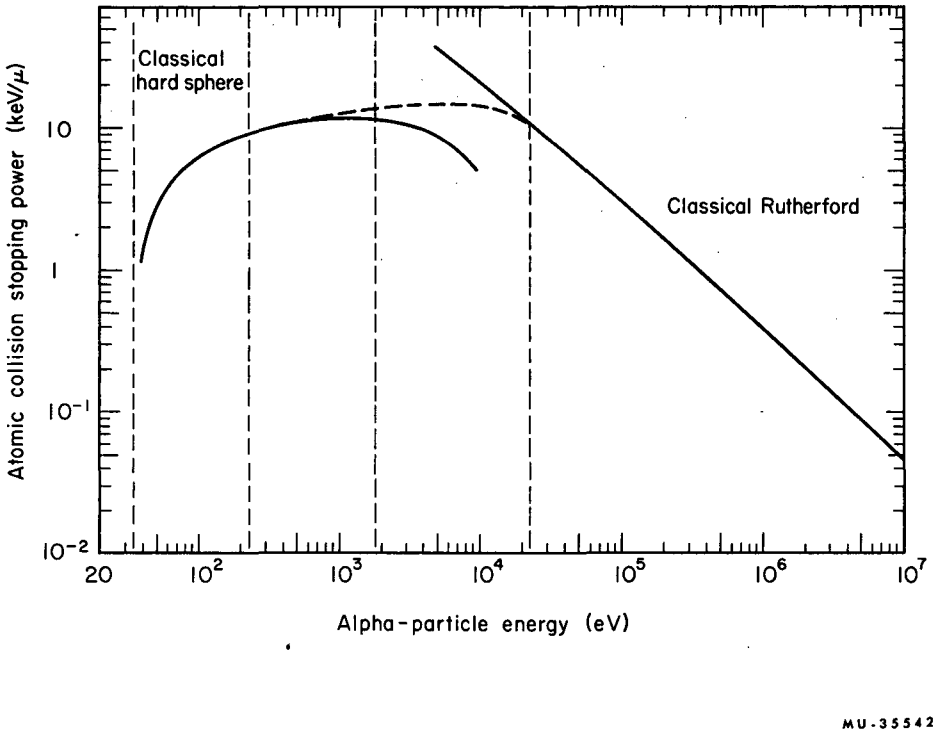

Fig. B.17. Atomic collision stopping power for α-particle stopping in Si.

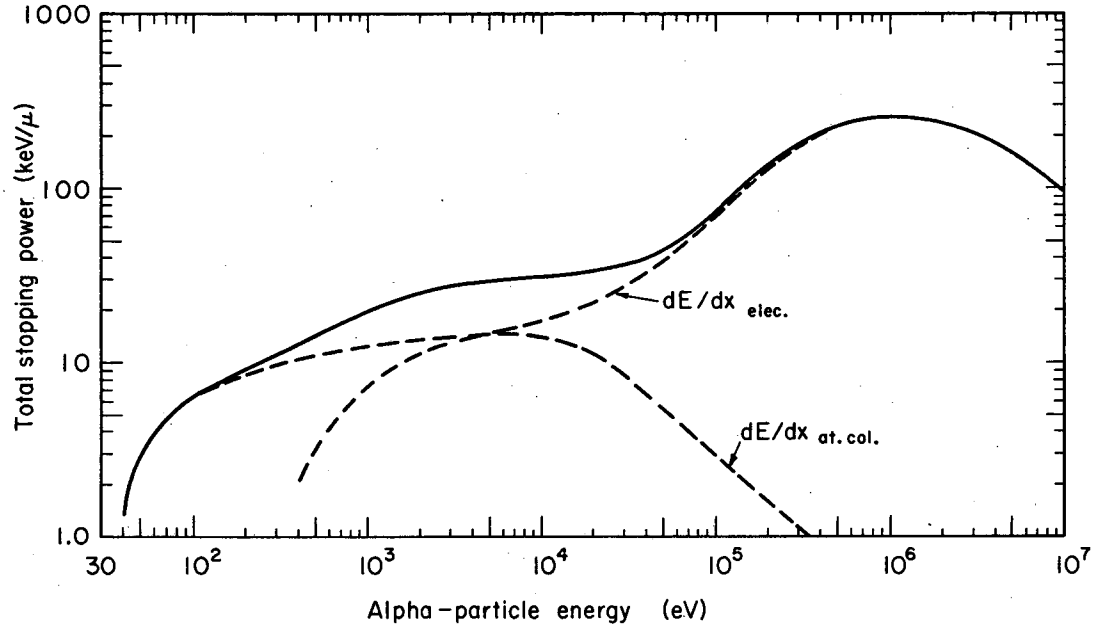

Fig. B.18. Total stopping power for α-particle stopping in Si.

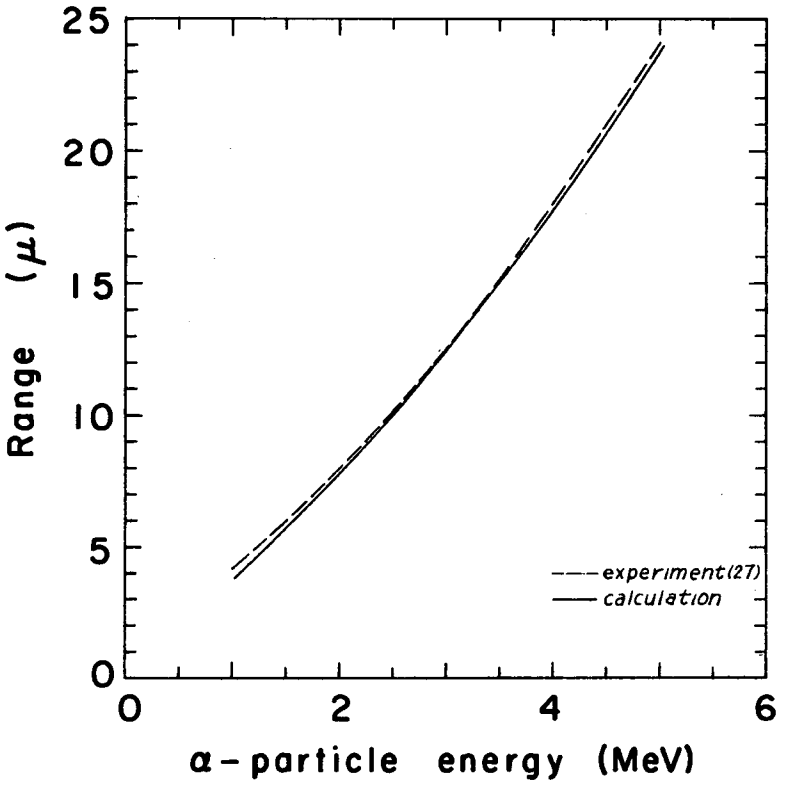

Fig. B.19. Range-energy curve for α-particle stopping in Si; comparison of theory and experiment.

is approximately 100 keV less than the noise level quoted for the apparatus used by Gobeli.

4. Spatial Variation of the Electronic Stopping Power and the Lattice Displacement Production Rate. We must now deal with the problem of determining the spatial variation of the electronic stopping power and the lattice displacement production rate. For the practical case of an α-voltaic device; namely, a semiconductor diode exposed to an alpha source but not in direct contact with it, the angular distribution and energy spectrum of the α-particles should be considered. In the development which follows the simplifying assumptions are made that the α-particles striking the diode are normal incident and monoenergetic.

The results of this appendix are employed in Sections III and V to determine the spatial variations of the electron-hole pair production rate and the lattice displacement production rate. The extent to which the simplifying assumptions influence the data analysis of Sections III and V is discussed in these sections as the need arises.

The incremental incident α-particle rate is, in general, given by

$$\dot{N}_{\alpha}(E_{\alpha o}, x, y, \underline{\Omega}) dE_{\alpha o} dx dy d\underline{\Omega}$$

where $\underline{\Omega}$ is the direction of travel of an α-particle and x and y the co-ordinates of a volume element dxdy on the diode surface. In the special case of a very large source and small diode the incident α-particle flux will be spatially uniform over the surface of the sample. In general the diode and alpha source will not be in contact so that the angular distribution of the incident α-particles will lie between the isotropic and normal incident situations. Assuming the source and diode to be discs located on a common central axis, the incremental incident α-particle rate becomes

$$\dot{N}_\alpha(E_{\alpha o}, x, y, \underline{\Omega})dxdyd\underline{\Omega} = \dot{N}_\alpha(E_{\alpha o}, r, \underline{\Omega})2\pi r dr d\underline{\Omega} \qquad \text{(B-74)}$$

If it is further assumed that angular distribution is independent of position on the diode surface, the incident α-particle rate in an increment of solid angle is

$$\dot{N}_\alpha(E_{\alpha o}, \underline{\Omega}) = \int_o^{R_c} \dot{N}_\alpha(E_{\alpha o}, r, \underline{\Omega})2\pi r dr = \dot{N}_\alpha(E_{\alpha o})Z(\underline{\Omega}) \ . \qquad \text{(B-75)}$$

The number of α particles of initial energy $E_{\alpha o}$ reaching position x below the surface and having energy E_α is then given by

$$\dot{N}_\alpha(E_{\alpha o}, x; E_\alpha) = \int \dot{N}_\alpha(E_{\alpha o})Z(\underline{\Omega})f(E_{\alpha o}, \underline{\Omega}, x; E_\alpha)d\underline{\Omega} \qquad \text{(B-76)}$$

where $f(E_{\alpha o}, \underline{\Omega}, x; E_\alpha)$ specifies the energy, E_α, of an α-particle at position x which was incident at angle $\underline{\Omega}$ with initial energy $E_{\alpha o}$. The energy loss at position x in interval Δx is then

$$\Delta E_T(x) = \iint [\frac{dE_\alpha(E_\alpha)}{dx}]\dot{N}_\alpha(E_{\alpha o})Z(\underline{\Omega})f(E_{\alpha o}, \underline{\Omega}, x; E_\alpha)d\underline{\Omega}dE_{\alpha o}\Delta x \ . \qquad \text{(B-77)}$$

At this point we shall make the simplfying assumption that the α-particles are incident normal to the diode surface in which case Eq. (B-76) becomes

$$\dot{N}_\alpha(E_{\alpha o}, x; E_\alpha)dx = \dot{N}_\alpha(E_{\alpha o})f(E_{\alpha o}, x; E_\alpha)dx \qquad \text{(B-78)}$$

where $\dot{N}_\alpha(E_{\alpha o})$ is the incident α-particle spectrum and $f(E_{\alpha o}, x; E_\alpha)$ gives the energy at position x for an α particle of initial energy $E_{\alpha o}$. The function $f(E_{\alpha o}, x; E_\alpha)$ is defined such that it has a magnitude of unity for $E_\alpha \geq 0$. The stopping power is a function of energy so that the energy lost by the α particles of initial energy $E_{\alpha o}$ in an interval δx is

$$\delta E_\alpha(x) = \frac{dE_\alpha(E_\alpha)}{dx} \dot{N}_\alpha(E_{\alpha o})f(E_{\alpha o}, x; E_\alpha)\delta x. \qquad \text{(B-79)}$$

Integrating over the incident α-particle spectrum yields the total energy lost in an interval Δx,

$$\Delta E_T(x) = \int_o^\infty \left[\frac{dE_\alpha(E_\alpha)}{dx}\right] \dot{N}_\alpha(E_{\alpha o}) f(E_{\alpha o}, x; E_\alpha) dE_{\alpha o} \; \Delta x \; . \tag{B-80}$$

Now, in the limit that the α-particle spectrum is very sharp, it is possible to make the approximation that

$$\dot{N}_\alpha(E_{\alpha o}) \simeq \dot{N}_\alpha \delta(E_{\alpha o} - \overline{E}_{\alpha o}), \tag{B-81}$$

and when this relation is used in Eq. (B-79), the total energy loss becomes

$$\Delta E(x) = \left[\frac{dE_\alpha(E_\alpha)}{dx}\right] \dot{N}_\alpha f(\overline{E}_{\alpha o}, x; E_\alpha) \; \Delta x \; . \tag{B-82}$$

The spectrum encountered for large α-particle sources is rather broad and the identity in Eq. (B-81) is only approximate. The energy expended to produce an electron-hole pair is assumed to be a constant over the entire α-particle range so that the total number of electron-hole pairs produced at position x in the interval Δx is

$$G_\alpha(x) \, \Delta x = \frac{\Delta E(x)}{\epsilon} = \frac{1}{\epsilon} \left[\frac{dE_\alpha(E_\alpha)}{dx}\right]_{el} \dot{N}_\alpha f(E_{\alpha o}, x; E_\alpha) \; \Delta x \tag{B-83}$$

and the total number of electron-hole pairs produced is

$$G = \frac{\dot{N}_\alpha}{\epsilon} \int_o^{R_\alpha} \left[\frac{dE_\alpha(E_\alpha)}{dx}\right]_{el} f(\overline{E}_{\alpha o}, x; E_\alpha) dx = \frac{\dot{N}_\alpha \overline{E}_{\alpha o}}{\epsilon} \tag{B-84}$$

where R_α is the α-particle range.

The function $f(\overline{E}_{\alpha o}, x; E_\alpha)$ was determined from a numerical integration of the total stopping power curve (see Fig. B.18) for a given $\overline{E}_{\alpha o}$, and the curves obtained in this way for the $\overline{E}_{\alpha o}$ = 4MeV and $\overline{E}_{\alpha o}$ = 5MeV are

presented in Fig. B.20 and Fig. B.21 respectively. These values of the initial energy are peculiar to the situations encountered in Sections III and V.

We now turn to the determination of the lattice displacement production rate. The number of displacements produced by an α-particle of initial energy $E_{\alpha o}$ at position x in an inverval δx is

$$\delta n_D(x) = n_D(x)\delta x = n_D(E_\alpha) f(E_{\alpha o}, x; E_\alpha)\delta x = \bar{\nu}(E_\alpha) N_o \sigma_D(E_\alpha) f(E_{\alpha o}, x; E_\alpha)\delta x \tag{B-85}$$

where $n_D(E_\alpha)$ is given in Fig.B.16. Therefore the displacement production rate obtained by integrating over the incident α-particle spectrum, $\dot{N}_\alpha(E_{\alpha o})$, is

$$\delta \dot{N}_D(x) = \int \dot{N}_\alpha(E_{\alpha o}) f(E_{\alpha o}, x, E_\alpha) n_D(E_\alpha) dE_{\alpha o}\delta x. \tag{B-86}$$

For the α-particle spectrum given by Eq. (B-81), the displacement production rate becomes

$$\delta \dot{N}_D(x) = \dot{N}_\alpha f(\bar{E}_{\alpha o}; x; E_\alpha) n_D(E_\alpha)\delta x = \dot{N}_\alpha n_D(x)\delta x \tag{B-87}$$

and using the results presented in Fig. B.16 for $n_D(E_\alpha)$ in conjunction with the interdependence of E_α and x presented in Figs. B.20 and B.21, $n_D(x)$ was determined and the results can be found in Sections III and V.

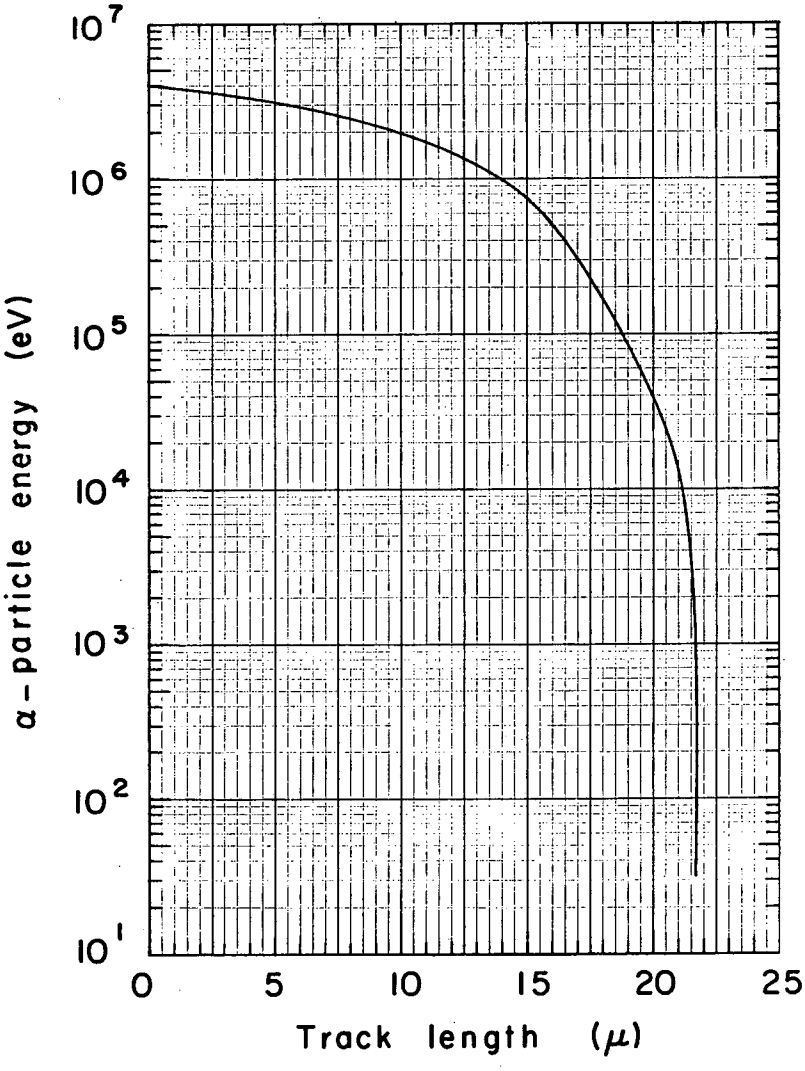

Fig. B.20. $f(\overline{E}_{\alpha o}, x; E_{\alpha})$ for 4-Mev α-particle stopping in Si.

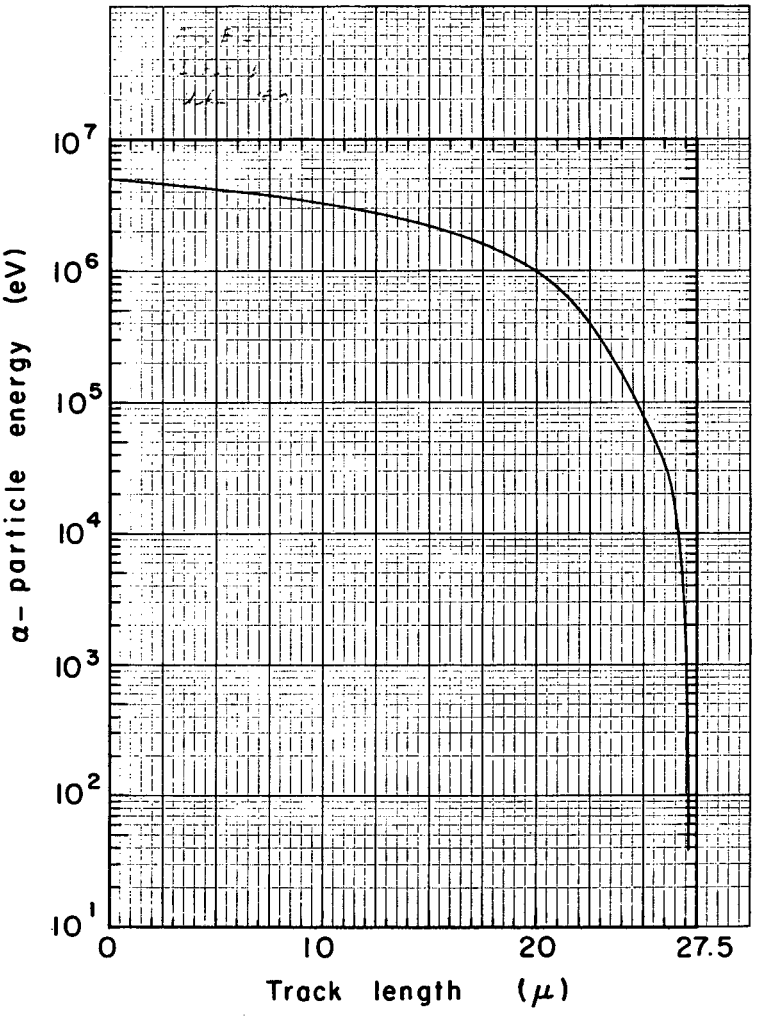

Fig. B.21. $f(\overline{E}_{\alpha o}, x; E_{\alpha})$ for 5-Mev α-particle stopping in Si.

C. Current-Voltage Characteristic of a Semiconductor Diode Under Charged Particle Bombardment.

There are two possible geometrical configurations for charged particle bombardment of a semiconductor diode. In the case of unidirectional bombardment, the energetic charged particles are incident upon only one surface of the diode, while in the case of bidirectional bombardment the two opposite faces of a broad area semiconductor diode are subject to particle bombardment. The diode geometry for unidirectional bombardment consists of a thin surface region and a relatively thick base region, while for bidirectional bombardment the thickness of both field free regions of the diode must be approximately equal to the charged particle range. Figure C.1 shows the diode geometry for the two bombardment schemes.

1. Unidirectional Bombardment. In the following analysis the surface region is taken to be p-type; and the base region, n-type. Also, it will be assumed that the spatial dependence of electron-hole pair production resulting from charged particle electron excitation can be adequately represented by

$$G(x) = a + bx + cx^2 + dx^3 + fx^4. \qquad (C\text{-}1)$$

In the p-type surface region the diffusion equation for the minority carrier electrons is solved for a plane source of strength $\frac{\dot{N}_\alpha}{A_x} g(x_o)dx_o$ located at x_o. The diffusion equation is

$$D_n \frac{d^2 \Delta n_p}{dx^2} - \frac{\Delta n_p}{\tau_n} = 0, \qquad (C\text{-}2)$$

where D_n is the electron diffusion coefficient, τ_n is the electron minority carrier lifetime, and $\Delta n_p = (n_p - n_{po})$ is the excess electron

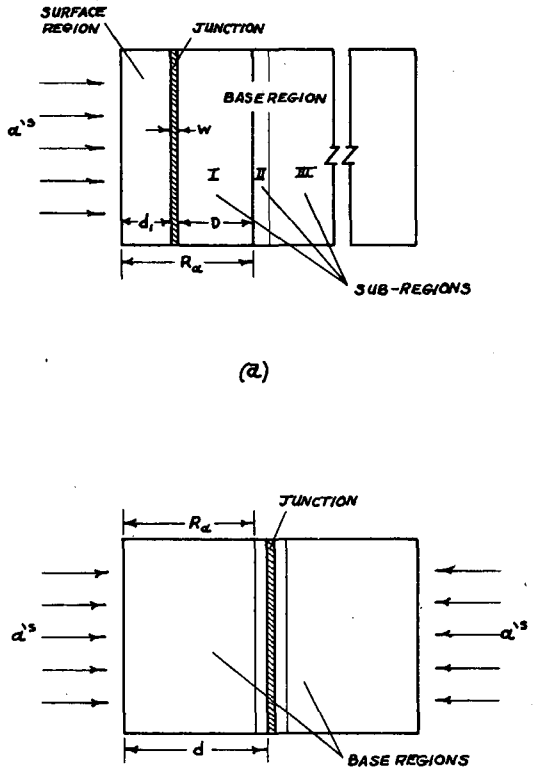

Fig. C.1. Device geometry for (a) unidirectional bombardment and (b) bidirectional bombardment.

concentration in the p-type surface region. The solution of Eq. (C-2) is

$$\Delta n_{p1} = A_1 e^{\frac{x}{L_n}} + B_1 e^{-\frac{x}{L_n}} \quad \text{for } x \leq x_o$$
$$\Delta n_{p2} = A_2 e^{\frac{x}{L_n}} + B_2 e^{-\frac{x}{L_n}} \quad \text{for } x \geq x_o, \tag{C-3}$$

where the electron diffusion length is $L_n^2 = D_n \tau_n$. It was necessary to consider independent solutions for $x \leq x_o$ and $x \geq x_o$. The boundary condition at the surface of the diode is obtained by equating the electron current to surface recombination rate,[56]

$$-D_n \left.\frac{\Delta n_{p1}}{dx}\right|_{x=0} = -S_n \Delta n_{p1}(0) . \tag{C-4}$$

At the junction the electron concentration is greater than the equilibrium value due to carrier injection, and the boundary condition is[56]

$$\Delta n_{p2}(d_1) = n_{po}(e^{\lambda V} - 1). \tag{C-5}$$

The remaining boundary conditions at the source position are the equality of electron concentration

$$\Delta n_{p1}(x_o) = \Delta n_{p2}(x_o) \tag{C-6}$$

and the continuity of electron current

$$D_n \left.\frac{d\Delta n_{p1}}{dx}\right|_{x=x_o} - D_n \left.\frac{d\Delta n_{p2}}{dx}\right|_{x=x_o} = \frac{\dot{N}_\alpha}{A_x} g(x_o) dx_o . \tag{C-7}$$

Using these boundary conditions, the excess electron concentration is found to be

$$\Delta n_{p2}(x) = \frac{n_{po}(e^{\lambda V}-1)}{\sinh\left(\frac{x_o-d_1}{L_n}\right)} \left\{ \frac{\left[\gamma_n \cosh\left(\frac{x_o}{L_n}\right)+\sinh\left(\frac{x_o}{L_n}\right)\right]}{\left[\gamma_n \cosh\left(\frac{d_1}{L_n}\right)+\sinh\left(\frac{d_1}{L_n}\right)\right]} \right.$$

$$\left. + \left[\cosh\left(\frac{x-d_1}{L_n}\right)\sin\left(\frac{x_o-d_1}{L_n}\right) - \cosh\left(\frac{x_o-d_1}{L_n}\right)\sinh\left(\frac{x-d_1}{L_n}\right)\right] \right\}$$

$$- \frac{\dot{N}_\alpha}{A_x} g(x_o)dx_o\left(\frac{L_n}{D_n}\right) \frac{\left[\gamma_n \cosh\left(\frac{x_o}{L_n}\right)+\sinh\left(\frac{x_o}{L_n}\right)\right]}{\left[\gamma_n \cosh\left(\frac{d_1}{L_n}\right)+\sinh\left(\frac{d_1}{L_n}\right)\right]} \sinh\left(\frac{x-d_1}{L_n}\right) \qquad \text{(C-8)}$$

and from this the electron current at the junction is found to be

$$I_e(V) = qA_x D_n \left.\frac{d\,\Delta n_{p2}}{dx}\right|_{x=d_1}$$

$$= qA_x\left(\frac{D_n}{L_n}\right)n_{po}(e^{\lambda V}-1) \frac{\left[\gamma_n \sinh\left(\frac{d_1}{L_n}\right)+\cosh\left(\frac{d_1}{L_n}\right)\right]}{\left[\gamma_n \cosh\left(\frac{d_1}{L_n}\right)+\sinh\left(\frac{d_1}{L_n}\right)\right]}$$

$$- q\dot{N}_\alpha g(x_o)dx_o \frac{\left[\gamma_n \cosh\left(\frac{x_o}{L_n}\right)+\sinh\left(\frac{x_o}{L_n}\right)\right]}{\left[\gamma_n \cosh\left(\frac{d_1}{L_n}\right)+\sinh\left(\frac{d_1}{L_n}\right)\right]}\,, \qquad \text{(C-9)}$$

where q is the magnitude of the electron charge, $\lambda = q/kT$, and $\gamma_n = D_n/L_n s_n$. Making use of the source term given by Eq. (C-1), the electron current for V = 0 becomes

$$I_e(0) = -\dot{q}N_\alpha \int_o^t g(x) \frac{\left[\gamma_n \cosh\left(\frac{x}{L_n}\right)+\sinh\left(\frac{x}{L_n}\right)\right]}{\left[\gamma_n \cosh\left(\frac{d_1}{L_n}\right)+\sinh\left(\frac{d_1}{L_n}\right)\right]} dx$$

$$= -q\dot{N}_\alpha L_n \left[\frac{X_n(d_1)M_n(d_1)-X_n(0)}{K_n(d_1)}\right] + q\dot{N}_\alpha L_n^2 \left[\frac{X_n'(d_1)K_n(d_1)-\gamma_n X_n'(0)}{K_n(d_1)}\right], \quad \text{(C-10)}$$

where

$$M_n(x) = \gamma_n \sinh\left(\frac{x}{L_n}\right) + \cosh\left(\frac{x}{L_n}\right), \quad \text{(C-11)}$$

$$K_n(x) = \gamma_n \cosh\left(\frac{x}{L_n}\right) + \sinh\left(\frac{x}{L_n}\right), \quad \text{(C-12)}$$

$$X_n(x) = a+bx+c(x^2+2L_n^2)+d(x^3+6xL_n^2)+f(x^4+12L_n^2x^2+24L_n^4), \quad \text{(C-13)}$$

and

$$X_n'(x) = b+2cx+d(3x^2+6L_n^2)+f(4x^3+24xL_n^2). \quad \text{(C-14)}$$

Therefore the electron current is

$$I_e(V) = qA_x\left(\frac{D_n}{L_n}\right)n_{po}(e^{\lambda V}-1)\frac{M_n(t)}{K_n(t)} - q\dot{N}_\alpha L_n\left[\frac{X_n(d_1)M_n(d_1)-X_n(0)}{K_n(d_1)}\right]$$

$$+ q\dot{N}_\alpha L_n^2\left[\frac{X_n'(d_1)K_n(d_1)-\gamma_n X_n'(0)}{K_n(d_1)}\right], \quad \text{(C-15)}$$

which in the limit of b=c=d=f=0 (i.e., a spatially constant electron-hole pair production rate) becomes

$$I_e(V) = qA_x\left(\frac{D_n}{L_n}\right)n_{po}(e^{\lambda V}-1)\frac{M_n(d_1)}{K_n(d_1)} - qL_n\dot{N}_\alpha g_o \frac{[M_n(d_1)-1]}{K_n(d_1)}, \quad \text{(C-16)}$$

where g_o is the pair production rate.

In the base region the diffusion equation for holes,

$$D_p \frac{d^2 \Delta p_n}{dx^2} - \frac{\Delta p_n}{\tau_n} = 0, \qquad \text{(C-17)}$$

must be solved for a plane source of strength $\frac{\dot{N}_\alpha}{A_x} g(x_o)dx_o$ at position x_o for the three sub-regions indicated in Fig. C.1(a). The reasons for this division of the base region are discussed in Sections III and V. The three regions are characterized by different hole diffusion lengths. The solutions are

$$\begin{aligned}
\Delta p_{n1} &= A_1 e^{\frac{x}{L_{pI}}} + B_1 e^{-\frac{x}{L_{pI}}} \quad \text{for } d_2 \le x \le x_o \\
\Delta p_{n2} &= A_2 e^{\frac{x}{L_{pI}}} + B_2 e^{-\frac{x}{L_{pI}}} \quad \text{for } x_o \le x \le d_3 \\
\Delta p_{n3} &= A_3 e^{\frac{x}{L_{pI}}} + B_3 e^{-\frac{x}{L_{pI}}} \quad \text{for } d_3 \le x \le d_4 \\
\Delta p_{n4} &= B_4 e^{-\frac{x}{L_{po}}} \quad \text{for } d_4 \le x.
\end{aligned} \qquad \text{(C-18)}$$

The boundary conditions to be employed in the base region are obtained from the injected excess hole concentration,

$$\Delta p_{n1}(d_2) = p_{no}(e^{\lambda V} - 1) , \qquad \text{(C-19)}$$

and the equality of hole concentration and continuity of hole current at the boundaries between the three regions

$$\Delta p_{n3}(d_4) = \Delta p_{n4}(d_4) , \qquad \text{(C-20)}$$

$$D_p \left.\frac{d\,\Delta p_{n3}}{dx}\right|_{x=d_4} = D_p \left.\frac{d\Delta p_{n4}}{dx}\right|_{x=d_4} , \qquad \text{(C-21)}$$

$$\Delta p_{n2}(d_3) = \Delta p_{n3}(d_3) , \tag{C-22}$$

$$D_p \left.\frac{d\Delta p_{n2}}{dx}\right|_{x=d_3} = D_p \left.\frac{d\Delta p_{n3}}{dx}\right|_{x=d_3} , \tag{C-23}$$

$$\Delta n_{p1}(x_o) = \Delta n_{p2}(x_o), \tag{C-24}$$

and

$$D_p \left.\frac{d\Delta p_{n1}}{dx}\right|_{x=x_o} - D_p \left.\frac{d\Delta p_{n2}}{dx}\right|_{x=x_o} = \frac{\dot{N}_\alpha}{A_x} g(x_o)dx_o . \tag{C-25}$$

The excess hole concentration is then found to be

$$\Delta p_{n1}(x) = \left(\frac{D_p}{L_p}\right)\frac{\dot{N}_\alpha}{A_x} g(x_o)dx_o \sinh\left(\frac{x-d_2}{L_{pI}}\right)\frac{\left[\Delta_1 \cosh\left(\frac{d_3-x_o}{L_{pI}}\right)+\Delta_2 \sinh\left(\frac{d_3-x_o}{L_{pI}}\right)\right]}{\left[\Delta_1 \cosh\left(\frac{D}{L_{pI}}\right)+\Delta_2 \sinh\left(\frac{D}{L_{pI}}\right)\right]}$$

$$+ \frac{p_{no}(e^{\lambda V}-1)}{\sinh\left(\frac{x_o-d_2}{L_{pI}}\right)} \left\{ \left[\cosh\left(\frac{x-d_2}{L_{pI}}\right)\sinh\left(\frac{x_o-d_2}{L_{pI}}\right) - \cosh\left(\frac{x_o-d_2}{L_{pI}}\right)\sinh\left(\frac{x-d_2}{L_{pI}}\right)\right] \right.$$

$$\left. + \sinh\left(\frac{x-d_2}{L_{pI}}\right)\frac{\left[\Delta_1 \cosh\left(\frac{d_3-x_c}{L_{pI}}\right)+\Delta_2 \sinh\left(\frac{d_3-x_o}{L_{pI}}\right)\right]}{\left[\Delta_1 \cosh\left(\frac{D}{L_{pI}}\right)+\Delta_2 \sinh\left(\frac{D}{L_{pI}}\right)\right]} \right\}, \tag{C-26}$$

where $D = d_3 - d_2$.

The hole current obtained from Eq. (C-26) is

$$I_h(V) = -qA_x D_p \left.\frac{d\Delta p_{n1}}{dx}\right|_{x=d_2}$$

$$= -q\dot{N}_\alpha g(x_o)dx_o \frac{[\Delta_1 \cosh(\frac{d_3 - x_o}{L_{pI}}) + \Delta_2 \sinh(\frac{d_3 - x_o}{L_{pI}})]}{[\Delta_1 \cosh(\frac{D}{L_{pI}}) + \Delta_2 \sinh(\frac{D}{L_{pI}})]}$$

$$+ qA_x(\frac{D_p}{L_{pI}})p_{no}(e^{\lambda V}-1) \frac{[\Delta_1 \sinh(\frac{D}{L_{pI}}) + \Delta_2 \cosh(\frac{D}{L_{pI}})]}{[\Delta_1 \cosh(\frac{D}{L_{pI}}) + \Delta_2 \sinh(\frac{D}{L_{pI}})]} \qquad \text{(C-27)}$$

where $\Delta_1 = \cosh(\frac{t}{L_{pII}}) + (\frac{L_{pII}}{L_{po}})\sinh(\frac{t}{L_{pII}})$, (C-28)

$$\Delta_2 = (\frac{L_{pI}}{L_{po}})\cosh(\frac{t}{L_{pII}}) + (\frac{L_{pI}}{L_{pII}})\sinh(\frac{t}{L_{pII}}) \ , \qquad \text{(C-29)}$$

and $t = d_4 - d_3$. Using the source term given by Eq. (C-1), the electron current at V = 0 becomes

$$I_h(0) = -q\dot{N}_\alpha \left[\int_{d_2}^{d_3} g(x) \frac{[\Delta_1 \cosh(\frac{d_3 - x}{L_{pI}}) + \Delta_2 \sinh(\frac{d_3 - x}{L_{pI}})]}{[\Delta_1 \cosh(\frac{D}{L_{pI}}) + \Delta_2 \sinh(\frac{D}{L_{pI}})]} dx + \int_{d_3}^{R_\alpha} g(x)f(x)dx \right]$$

$$= -q\dot{N}_\alpha L_{pI} \left[[X_p(d_2)\frac{R_p(D)}{P_p(D)} + L_{pI}X'_p(d_2)] - [X_p(d_3) + L_{pI}X'_p(d_3)]\frac{R_p(0)}{P_p(D)} \right] \ , \qquad \text{(C-30)}$$

where R_α is the position at which $g(R_\alpha) = 0$,

$$P_p(x) = \Delta_1 \cosh(\frac{x}{L_{pI}}) + \Delta_2 \sinh(\frac{x}{L_{pI}}) \ , \qquad \text{(C-31)}$$

$$R_p(x) = \Delta_1 \sinh(\frac{x}{L_{pI}}) + \Delta_2 \cosh(\frac{x}{L_{pI}}), \qquad \text{(C-32)}$$

where $X_p(x)$ is given by Eq. (C-13) with n replaced by p. The integral term from d_3 to R_α has been neglected which leads to less than a 4% error in $I_h(0)$ for the applications of this equation in Sections III and V. Therefore, the hole current-voltage characteristic is

$$I_h(V) = qA_x\left(\frac{D_p}{L_{pI}}\right)p_{no}(e^{\lambda V}-1)\frac{R_p(D)}{P_p(D)} - q\dot{N}_\alpha L_{pI}\left[\left[X_p(d_2)\frac{R_p(D)}{P_p(D)}+L_{pI}X'_p(d_2)\right]\right.$$

$$\left. - \left[X_p(d_3)+L_{pI}X_p(d_3)\right]\frac{R_p(0)}{P_p(D)}\right], \qquad (C\text{-}33)$$

which for a spatially constant electron-hole pair production rate becomes

$$I_h(V) = qA_x\left(\frac{D_p}{L_{pI}}\right)p_{no}(e^{\lambda V}-1)\frac{R_p(D)}{P_p(D)} - q\dot{N}_\alpha L_{pI}g_o\,\frac{[R_p(D)-R_p(0)]}{P_p(D)}. \qquad (C\text{-}34)$$

For $L_{pI} = L_{pII} = L_{po}$ and d_3 approaches infinity (i.e. the situation prevailing prior to appreciable damage), Eq. (C-33) becomes

$$I_h(V) = qA_x\left(\frac{D_p}{L_{po}}\right)p_{no}(e^{\lambda V}-1) - q\dot{N}_\alpha L_{po}\left[U_p(d_2)-U_p(R_\alpha)\exp\left(-\frac{(R_\alpha-d_2)}{L_{po}}\right)\right] \qquad (C\text{-}35)$$

where $U_p(x) = X_p(x) + L_{po}X'_p(x)$.

The current resulting from electron-hole pair production in the junction is suitably approximated by

$$I_j = -q\dot{N}_\alpha\int_{d_1}^{d_2} G(x)\,dx, \qquad (C\text{-}36)$$

where it has been tacitly assumed that the electric field existing in the junction is sufficiently large to sweep out all the charge carriers with negligible recombination.

The resultant current-voltage characteristic is

$$I(V) = I_e + I_h + I_j = I_o(e^{\lambda V}-1) - I_G \,, \tag{C-37}$$

where

$$I_o/qA_x = [\,(\frac{D_n}{L_n})n_{po}\frac{M_n(d_1)}{K_n(d_1)} + (\frac{D_p}{L_{po}})p_{no}\frac{R_p(D)}{P_p(D)}\,], \tag{C-38}$$

$$I_G/q\dot{N}_\alpha = \left\{ L_n[\frac{X_n(d_1)M_n(d_1)-X_n(0)}{K_n(d_1)}] - L_n^2[\frac{X_n'(d_1)K_n(d_1)-\gamma_n X_n'(0)}{K_n(d_1)}] \right\}$$

$$+[H(d_2)-H(d_1)]+L_{pI}\left\{ [X_p(d_2)\frac{R_p(D)}{P_p(D)} + L_{pI}X_p'(d_2)] \right.$$

$$\left. -[X_p(d_3)+L_{pI}X_p'(d_3)]\,\frac{R_p(0)}{P_p(D)} \right\}, \tag{C-39}$$

and $H(x) = ax + \frac{bx^2}{2} + \frac{cx^3}{3} + \frac{dx^4}{4} + \frac{fx^5}{5}$.

For a spatially constant pair production rate, g_o, Eq. (C-38) remains unchanged, and Eq. (C-39) becomes

$$I_G/q\dot{N}_\alpha = g_o \quad L_n\frac{[M_n(d_1)-1]}{K_n(d_1)} + W + L_{pI}\frac{[R_p(D)-R_p(0)]}{P_p(D)} \tag{C-40}$$

2. Bidirectional Bombardment. In the case of bidirectional bombardment (see Fig. C.1(b)), the solution for the minority carrier concentration is of identical form for either of the two field free regions of the diode. Therefore, one such region need only be considered in detail. Let us choose the p-type region of thickness d. Then the minority carrier diffusion equation is given by Eq. (C-2). The solution proceeds in an identical manner to that taken in the derivation of Eq. (C-8) for the excess carrier concentration for zero exposure level.

The electron current arising from a source of strength $\frac{\dot{N}_\alpha}{A_x} g(x_o)dx_o$ at position x_o is therefore given by Eq. (C-9), which for the source described by Eq. (C-1) becomes

$$I_e(V) = qA_x\left(\frac{D_n}{L_n}\right)n_{po}(e^{\lambda V}-1)\frac{M_n(d)}{K_n(d)} - q\dot{N}_\alpha L_n\left[\frac{X_n(R)M_n(d)-X_n(0)}{K_n(d)}\right]$$

$$+ q\dot{N}_\alpha L_n^2\left[\frac{X_n'(R)K_n(d)-\gamma_n X_n'(0)}{K_n(d)}\right] . \qquad (C-41)$$

In a similar manner the solution for the hole current is found to be

$$I_h(V) = qA_x\left(\frac{D_p}{L_p}\right)p_{no}(e^{\lambda V}-1)\frac{M_p(d)}{K_p(d)} - q\dot{N}_\alpha L_p\left[\frac{X_p(R)M_p(d)-X_p(0)}{K_p(d)}\right]$$

$$+q\dot{N}_\alpha L_p^2\left[\frac{X_p'(R)K_p(d)-\gamma_p X_p'(0)}{K_p(d)}\right] , \qquad (C-42)$$

and the current-voltage characteristic is given by

$$I = I_o(e^{\lambda V}-1) - I_G, \qquad (C-43)$$

where

$$I_o/qA_x = \left(\frac{D_n}{L_n}\right)n_{po}\frac{M_n(d)}{K_n(d)} + \left(\frac{D_p}{L_p}\right)p_{no}\frac{M_p(d)}{K_p(d)} \qquad (C-44)$$

and

$$I_G/q\dot{N}_\alpha = L_n\left[\frac{X_n(R)M_n(d)-X_n(0)}{K_n(d)}\right] - L_n^2\left[\frac{X_n'(R)K_n(d)-\gamma_n X_n'(0)}{K_n(d)}\right]$$

$$+ L_p\left[\frac{X_p(R)M_p(d)-X_p(0)}{K_p(d)}\right] - L_p^2\left[\frac{X_p'(R)K_p(d)-\gamma_p X_p'(0)}{K_p(d)}\right] . \qquad (C-45)$$

In this development the condition $R \lesssim d$ was assumed to be satisfied and this explains the absence of a current contribution from the junction inasmuch as there is negligible electron-hole pair production in the junction region.

D. Performance of a Particle-Voltaic Device.

The equivalent circuit for a particle-voltaic device under steady state exposure is shown in Fig. D.1. An additional capacitance in parallel with the junction would be included when considering transient behavior. The current-voltage characteristic of the device is given by

$$I = \frac{(V-IR_s)}{R_{SH}} + I_j(V-IR_s) - I_G, \qquad (D\text{-}1)$$

where $V_j = V-IR_s$ is the voltage drop across the junction and the junction I-V characteristic, $I_j(V-IR_s)$, is in general composed of one or more of the current contributions discussed in Appendix A. The power is

$$P = -IV \qquad (D\text{-}2)$$

where the current and voltage can be written in terms of the voltage drop across the junction,

$$V = V_j+IR_s = V_j(1+\frac{R_s}{R_{SH}})+R_sI_j(V_j)-R_sI_G \qquad (D\text{-}3)$$

$$\text{and } I = \frac{V_j}{R_{SH}} + I_j(V_j) - I_G. \qquad (D\text{-}4)$$

Then the power can be written

$$P = -[\frac{V_j}{R_{SH}} +I_j(V_j)-I_G][(1+\frac{R_s}{R_{SH}})V_j+R_sI_j(V_j) - R_sI_G]. \qquad (D\text{-}5)$$

The condition used to determine the voltage at maximum power is

$$\frac{\partial P}{\partial V_j} = 0 = [\frac{V_{jmp}}{R_{SH}} +I_j(V_{jmp})-I_G][(1+\frac{R_s}{R_{SH}})+ R_sI_j'(V_{jmp})]$$

$$+ [\frac{1}{R_{SH}} +I_j'(V_{jmp})][(1+\frac{R_s}{R_{SH}})V_{jmp}+R_sI_j(V_{jmp})-R_sI_G] \qquad (D\text{-}6)$$

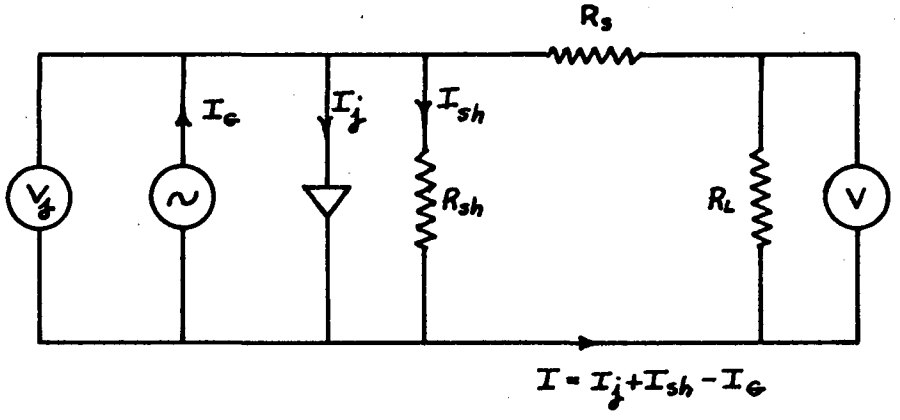

MU-35593

Fig. D.1. Equivalent circuit for a semiconductor diode under energetic particle bombardment.

or

$$2\frac{V_{jmp}}{R_{SH}}\left(1+\frac{R_s}{R_{SH}}\right)+\left(1+2\frac{R_s}{R_{SH}}\right)\left[I_j(V_{jmp})-I_G\right]+2R_s I_j(V_{jmp})I_j'(V_{jmp})$$

$$-2I_G R_s I_j'(V_{jmp})+\left(1+2\frac{R_s}{R_{SH}}\right)V_{jmp}I_j'(V_{jmp}) = 0 \ . \qquad \text{(D-7)}$$

The current at maximum power is then obtained for Eq. (D-4)

$$I_{mp} = \frac{V_{jmp}}{R_{SH}} + I_j(V_{jmp}) - I_G \qquad \text{(D-8)}$$

and therefore

$$P_{max} = -I_{mp}V_{mp} = \left[I_G - \frac{V_{jmp}}{R_{SH}} - I_j(V_{jmp})\right]\left[V_{jmp}+I_{mp}R_s\right] \ . \qquad \text{(D-9)}$$

The junction I-V characteristic can be written as a sum of ideal and non-ideal current contributions so that

$$I_j(V_{jmp}) = I_{j,NI}(V_{jmp}) + I_o(e^{\lambda V_{jmp}}-1), \qquad \text{(D-10)}$$

where $I_{j,NI}(V_{jmp})$ results from one or more of the non-ideal current contributions discussed in Appendix A. In the low voltage region where $I_d = I_o(e^{\lambda V_j}-1) < I_{j,NI}(V_j)$, the series resistance may be neglected with the result that

$$I_j(V_{jmp}) = I_{j,NI}(V_{jmp}) \qquad \text{(D-11)}$$

and Eq. (D-7) becomes

$$2\frac{V_{jmp}}{R_{SH}} + I_{j,NI}(V_{jmp}) + V_{jmp}I_{j,NI}(V_{jmp}) = I_G. \qquad \text{(D-12)}$$

At this point let us consider two specific forms for the non-ideal current contribution.

where I_{ol} is the effective reverse saturation current and the exponential factor has been modified through the introduction of the non-ideality factor, A. Substitution of Eq. (D-17) into Eq. (D-12) yields

$$\frac{2V_{jmp}}{I_{ol}R_{SH}} + (1+\frac{\lambda V_{jmp}}{A})e^{\frac{\lambda V_{jmp}}{A}} = (\frac{I_G}{I_{ol}} + 1) \qquad \text{(D-18)}$$

as the determining relationship for V_{jmp}. The maximum power for this form of the non-ideal junction current is

$$P_{max} = \frac{V_{jmp}^2}{R_{SH}} + I_{ol}(\frac{\lambda V_{jmp}^2}{A})e^{\frac{\lambda V_{jmp}}{A}} . \qquad \text{(D-19)}$$

The maximum power is also given by

$$P_{max} = \frac{V_{mp}^2}{R_{Lmp}} = [\frac{1}{R_{SH}} + I_{ol}(\frac{\lambda}{A})\exp(\frac{\lambda V_{jmp}}{A})]V_{jmp}^2 \qquad \text{(D-20)}$$

where R_{Lmp} is the load resistance at maximum power. The junction resistance at maximum power is found from Eq. (D-17) to be

$$\frac{1}{R_{jmp}} = \frac{\partial I(V_{jmp})}{\partial V_j} = I_{ol}(\frac{\lambda}{A})\exp(\frac{\lambda V_{jmp}}{A}) \qquad \text{(D-21)}$$

so that the load resistance for maximum power satisfies the condition that

$$\frac{1}{R_{Lmp}} = \frac{1}{R_{SH}} + \frac{1}{R_{jmp}} . \qquad \text{(D-22)}$$

Let us consider two situations in the high voltage region. A condition common to both is that of a negligible shunt conductance current, but the series resistance must be included in both cases.

Generation-Recombination Current. Providing that the non-ideal current contribution results from the generation or recombination of electron-hole pairs in the junction, the junction current is given by

$$I_j(V_j) = I_{rg}(V_j) = \frac{qn_i AW}{\sqrt{\tau_{no}\tau_{po}}} \frac{2\sinh(\frac{\lambda V_j}{2})}{\lambda(\psi_D - V_j)} f(b) \qquad \text{(D-13)}$$

which is Eq. (A-33) of Appendix A. In the low voltage forward bias region ($V_j < \psi_D$), $f(b) \approx \pi/2$ so that

$$I_j(V_j) \approx \frac{\pi q n_i A_x W}{2\sqrt{\tau_{no}\tau_{po}\psi_D}} \sinh(\frac{\lambda V_j}{2}) \equiv I_{o,rg}\sinh(\frac{\lambda V_j}{2}), \qquad \text{(D-14)}$$

where the junction width, W, is approximately constant for small applied bias. The maximum power as obtained from Eq. (D-9) for this case is

$$P_{max} = \frac{V_{jmp}^2}{R_{SH}} + I_{o,rg}(\frac{\lambda V_{jmp}^2}{2}) \cosh(\frac{\lambda V_{jmp}}{2}), \qquad \text{(D-15)}$$

where V_{jmp} is found from

$$\frac{2V_{jmp}}{I_{o,rg}R_{SH}} + [\sinh(\frac{\lambda V_{jmp}}{2}) + (\frac{\lambda V_{jmp}}{2})\cosh(\frac{\lambda V_{jmp}}{2})] = \frac{I_G}{I_{o,rg}} . \qquad \text{(D-16)}$$

Equation (D-16) was obtained from Eq. (D-12).

Modified Exponential Current-Low Voltage. It has been experimentally observed that over any limited voltage range it is possible to express the junction I-V characteristic of a semiconductor diode using an exponential form similar to that for the ideal diffusion current, so that

$$I_j(V_j) = I_{o1}[\exp(\frac{\lambda V_j}{A}) - 1] , \qquad \text{(D-17)}$$

Ideal Diffusion Current. It is possible for the condition $I_d > I_{j,NI}$ to be satisfied in the high voltage region in which case the junction current is given by the ideal diffusion term,

$$I_j(V_j) = I_o(e^{\lambda V_j} - 1) , \qquad (D\text{-}23)$$

so that the total current becomes

$$I = I_o(e^{\lambda V_j} - 1) - I_G . \qquad (D\text{-}24)$$

This can be placed in the form

$$V_j = \frac{1}{\lambda} \ln\left(\frac{I+I_G+I_o}{I_o}\right)$$

or

$$V = R_s I + \frac{1}{\lambda} \ln\left(\frac{I+I_G+I_o}{I_o}\right) . \qquad (D\text{-}25)$$

Making use of Eqs. (D-24) and (D-25) and the fact that $R_{SH} \longrightarrow \infty$, we find from Eq. (D-7)

$$2R_s I_{mp} + \frac{1}{\lambda} \ln\left(\frac{I_{mp}+I_G+I_o}{I_o}\right) + \frac{1}{\lambda} \frac{I_{mp}}{(I_{mp}+I_G+I_o)} = 0 \qquad (D\text{-}26)$$

for the condition from which the current at maximum power is to be determined. The maximum power is obtained upon substitution of Eqs. (D-25) and (D-26) into Eq. (D-9) with the result that

$$P_{max} = R_s I_{mp}^2 + \frac{1}{\lambda}\left(\frac{I_{mp}^2}{I_{mp}+I_G+I_o}\right) . \qquad (D\text{-}27)$$

Modified Exponential Current - High Voltage. In practice it is seldom possible to use Eq. (D-23) for the junction current but rather the modified form given by Eq. (D-17) is a more suitable approximation.

The maximum power for this form of the junction current (including the effect of the series resistance) is given by

$$P_{max} = R_s I_{mp}^2 + \frac{A}{\lambda}\left(\frac{I_{mp}^2}{I_{mp}+I_G+I_{ol}}\right), \tag{D-28}$$

where the current at maximum power is obtained from

$$2R_s I_{mp} + \frac{A}{\lambda}\ln\left(\frac{I_{mp}+I_G+I_{ol}}{I_{ol}}\right) + \frac{A}{\lambda}\left(\frac{I_{mp}}{I_{mp}+I_G+I_{ol}}\right) = 0. \tag{D-29}$$

The maximum power corresponds to a load resistance of

$$R_{Lmp} = -\frac{V_{jmp}}{I_{mp}} = -R_s - \frac{A}{\lambda}\left(\frac{1}{I_{mp}}\right)\ln\left(\frac{I_{mp}+I_G+I_o}{I_o}\right) \tag{D-30}$$

where Eq. (D-25) has been used with I_o and λ replaced by I_{ol} and λ/A respectively. Substituting Eq. (D-29) into Eq. (D-30) yields

$$R_{Lmp} = R_s + \frac{A}{\lambda}\frac{1}{(I_{mp}+I_G+I_o)} \quad . \tag{D-31}$$

The resistance of the junction is given by

$$R_j = \frac{dV_j}{dI} \tag{D-32}$$

where $$V_j = V - IR_s = \frac{A}{\lambda}\ln\left(\frac{I+I_G+I_o}{I_o}\right) \quad . \tag{D-33}$$

Then $$R_j = \frac{A}{\lambda}\frac{1}{(I+I_G+I_o)} \tag{D-34}$$

and $$R_{jmp} = \frac{A}{\lambda}\frac{1}{(I_{mp}+I_G+I_o)} \quad . \tag{D-35}$$

Therefore it can be seen that

$$R_{Lmp} = R_s + R_{jmp} \quad . \tag{D-36}$$

In the intermediate voltage region the junction current must be expressed in detail using the appropriate non-ideal current contributions with the result that the solution becomes very complex. An alternate technique is to approximate the junction current by the modified form given in Eq. (D-17) over limited voltage intervals (including both series and shunt resistance effects). In any given voltage interval it is then possible to use either Eqs. (D-19) or (D-28) depending upon the specific values of R_s and R_{SH}.

E. Error Analysis Technique.

The propagation of errors was treated in the following conventional manner. Consider the case of a quantity W which is calculated from the measured quantities x_1, x_2, x_3 . . . . . and is given by

$$W = f(x_1, x_2, x_3 \ldots). \tag{E-1}$$

The variance in W resulting from the variances associated with the x_i's is given by

$$(\sigma_w)^2 = \sum_i (\frac{\partial w}{\partial x_i})^2 (\sigma_{x_i})^2 \tag{E-2}$$

where the variances are those of the mean and not of the individual observations. In some cases only one measurement was made for a given x_i in which case the variance of the measured value had to be estimated. The pessimistic assumption was made that the variance was approximately equal to the random uncertainty associated with the measurements. Such random undertainties have been estimated for each measuring device used and are listed in each of the Sections dealing with the experimental work.

The other technique used extensively in analyzing the experimental results was the method of least squares as applied to a linear dependence between interdependent measurables such as

$$y = mx + b . \tag{E-3}$$

In the application of this technique in Section V, $y = I_{sc}(\theta)$ and $x = \theta^{-1/2}$ and the constants determined from the fitting technique are $m = K_1$ and $b = I_c$. For a set of measured points (x_i, y_i) the most probable values of m and b are given by

$$m = \frac{1}{\Delta}\left[N(\Sigma x_i y_i) - (\Sigma x_i)(\Sigma y_i)\right] \tag{E-4}$$

and

$$b = \frac{1}{\Delta}\left[N(\Sigma y_i)(\Sigma x_i^2) - (\Sigma x_i y_i)(\Sigma x_i)\right] \tag{E-5}$$

and providing that there are no errors present in the measured x_i's, the variances in m and b are given by

$$\sigma_m^2 = \frac{N\sigma^2}{\Delta} \tag{E-6}$$

and

$$\sigma_b^2 = \frac{\sigma^2 \Sigma x_i^2}{\Delta} \tag{E-7}$$

where $\Delta = N(\Sigma x_i^2) - (\Sigma x_i)^2$. The variance of the parent distribution for the y_i's, σ, is estimated from

$$\sigma^2 = \frac{1}{N}\Sigma d_i^2 = \frac{1}{N}\Sigma (m x_i + b - y_i)^2 . \tag{E-8}$$

In effect this method of analysis lumps all the uncertainties in the measurements into the y_i. It is therefore reasonable to use this technique providing the resulting σ^2 is found to be less than σ_y^2 as estimated from the random uncertainties inherent in the measurements. In certain cases (i.e. $x_i = \theta_i$) the variance in x_i, σ_x, is known. The total variances in m and b were then obtained from

$$\sigma_m^2 = \left(\frac{\partial m}{\partial y_i}\right)^2 \sigma^2 + \left(\frac{\partial m}{\partial x}\right)^2 \sigma_x^2 = \frac{N\sigma^2}{\Delta} + m^2\left(\frac{\sigma_x}{x}\right)^2 \tag{E-9}$$

and

$$\sigma_b^2 = \left(\frac{\partial b}{\partial y_i}\right)^2 \sigma^2 + \left(\frac{\partial b}{\partial x}\right)^2 \sigma_x^2 = \frac{\sigma^2 \Sigma x_i^2}{\Delta} + m^2 \sigma_x^2 . \tag{E-10}$$

The use of these equations will yield conservative estimates for the errors in m and b. In the event that each point y_i had a different

variance, $\sigma_i^2 \neq \sigma^2$, the above equations would have to be modified. A number of specific examples whose results are used in the main body of this report are now considered.

i) In Section V the incident α-particle rate is used to determine θ and K_1. The source was calibrated and found to have a strength $S = (10.2 \pm 0.2)X10^7\ \alpha/sec.$[56] In this reference a machine code was used to calculate I(Z), the fraction of emitted α-particles which strike an equivalent solar cell (the solar cell being replaced by a disc of equal area). Then $\dot{N}_\alpha(Z) = SI(Z)$ where Z is the normalized source-solar cell separation and the variance in $\dot{N}_\alpha(Z)$ is given by

$$\left(\frac{\sigma_{\dot{N}_\alpha}}{\dot{N}_\alpha}\right)^2 = \left(\frac{\sigma_{I(Z)}}{I(Z)}\right)^2 + \left(\frac{\sigma_S}{S}\right)^2 . \qquad \text{(E-11)}$$

The variance in I(Z) is dependent upon the variances in source radius, R_s, equivalent solar cell radius, R_d, and source-solar cell separation, z, so that

$$\left(\frac{\sigma_{I(Z)}}{I(Z)}\right)^2 = \left(\frac{z}{I}\frac{\partial I(Z)}{\partial z}\right)^2 + \left(\frac{R_s}{I}\frac{\partial I(Z)}{\partial R_s}\right)^2\left(\frac{\sigma_{R_s}}{R_s}\right)^2$$

$$+ \left(\frac{R_c \partial I(Z)}{I \partial R_c}\right)^2\left(\frac{\sigma_{R_c}}{R_c}\right)^2 = 15.4X10^{-4} \qquad \text{(E-12)}$$

where $\sigma_z/z \simeq \pm 2.3\%$, $\sigma_{R_c}/R_c = \pm 0.29\%$, and $\sigma_{R_s}/R_s \simeq \pm 5\%$. Therefore

$$\left(\frac{\sigma_{\dot{N}_\alpha}}{\dot{N}_\alpha}\right) = \left[15.4 + 3.8\right]^{1/2} X10^{-2} = \pm 4.4\%. \qquad \text{(E-13)}$$

ii) In Section IV a least squares fit is used to find Λ from a set of measurements for (I_i, V_i) where $I = \Lambda V$. In this limiting situation (b=0) the constant of proportionality is found to be

$$\Lambda = \frac{\Sigma I_i V_i}{V_i^2} , \tag{E-14}$$

and the variance in Λ is

$$\sigma_\Lambda^2 = \frac{(\Sigma V_i)^2}{(\Sigma V_i^2)^2} \sigma^2 \tag{E-15}$$

where

$$\sigma^2 = \frac{1}{N} \Sigma (\Lambda V_i - I_i)^2 . \tag{E-16}$$

iii) In Section IV the method of least squares is used to determine $\ell n I_o$ and λ_m from a set of measured points $(\ell n\, I_i', V_i)$ using Eqs. (E-4) and (E-5). The current I_i' is the difference of the measured value and the non-ideal current term at V_i,

$$I_i'(V_i) = I_i(V_i) - I_{ol}(e^{\delta V_i} - 1) - \frac{V_i}{R_{SH}} , \tag{E-17}$$

so that

$$\left(\sigma_{\ell n I_i'}\right)^2 = \left(\frac{I_i}{I_i'}\right)^2 \left(\frac{\sigma_{I_i}}{I_i}\right)^2 + \left(\frac{I_{ol} e^{\delta V_i}}{I_i'}\right)^2 \left[\left(\frac{\sigma_{I_{ol}}}{I_{ol}}\right)^2 + (\delta V_i)^2 \left(\frac{\sigma_\delta}{\delta}\right)^2 \right] , \tag{E-18}$$

where the contribution from the variance in R_{SH} is small and has been neglected. The variance for each point of the set is therefore different and must be weighted by $(\omega_i = 1/\sigma_i^2)$ when determining the variances in

$\ell n I_o$ and λ_m. Then Eqs. (E-9) and (E-10) are used to estimate these variances with the result that

$$\sigma_{\lambda_m}^2 = \frac{N}{\Delta}\sigma^2 + \lambda_m^2\left(\frac{\sigma_{V_i}}{V_i}\right)^2 \qquad \text{(E-19)}$$

and

$$\sigma_{\ell n I_o}^2 = \frac{\Sigma V_i^2}{\Delta}\sigma^2 + \lambda_m^2(\sigma_{V_i})^2 \qquad \text{(E-20)}$$

where $\sigma^2 = \sigma_{LS}^2 + \overline{\sigma^2}$. σ_{LS}^2 is defined by Eq. (E-8) and arises from the least squares fit of the set of data points $(\ln I_i', V_i)$. $\overline{\sigma^2}$ arises from the propagation of the variances in I_{ol} and δ as given by the second term in Eq. (E-18) and is estimated from

$$\overline{\sigma^2} = \frac{\Sigma\omega_i\sigma_i^2}{\Sigma\omega_i} = \frac{N}{\Sigma\omega_i}. \qquad \text{(E-21)}$$

These last three equations were applied to the data of Section IV and the results for typical cells can be found in Table IV.IV.

REFERENCES

1. J. A. Baicker and B. W. Faughnan, Radiation-Induced Changes in Silicon Photovoltaic Cells, J. Appl. Phys. 33, 3271 (1962).

2. C. J. Bakker and E. Segre, Stopping Power and Energy Loss for Ion Pair Production for 340-Mev Protons, Phys. Rev. 81, 489 (1951).

3. E. Baldinger, W. Czaja, and J. Gutmann, An Exact Determination of the Work per Electron-Hole Pair in Si Diode Counters, Helv. Phys. Acta. 35, 559 (1962).

4. W. H. Barkas and S. von Friesen, High-Velocity Range and Energy-Loss Measurements in Al, Cu, Pb, U and Emulsion, Nuovo Cimento, Suppl., 19, 41 (1961).

5. H. A. Bethe, Zur Theorie des Durchgaugs Sneller Korpuskularstrahlen durch Materie, Ann. Physik 5, 325 (1930).

6. H. Bichsel and E. A. Uehling, Multiple Scattering Correction for Proton Ranges and the Evaluation of the L-Shell Correction and I Value for Aluminum, Phys. Rev. 119, 1670 (1960).

7. H. Bichsel, Passage of Charged Particles Through Matter, Univ. of So. Calif. Rept. No. 2 (Contract AT(04-3)-136, 1961); Higher Shell Corrections in Stopping Power, Univ. So. Calif. Rept. No. 3 (Contract AT(04-3)-136, 1961).

8. F. Bloch, Zur Bremsung Rasch Bewegter Teilchen beim Durchgang durch Materie, Ann. Physik 16, 285 (1933); Bremsvermögen von Atomen mit Mehreren Elektronen, Z. Physik 81, 363 (1933).

9. N. Bohr, On the Theory of the Decrease of Velocity of Moving Electrified Particles on Passing Through Matter, Phil. Mag. 25, 10 (1913); On the Decrease of Velocity of Swiftly Moving Electrified Particles in Passing Through Matter, Phil. Mag. 30, 581 (1915).

10. N. Bohr, The Penetration of Atomic Particles Through Matter, Kgl. Danske Videnskab. Selskab. Biol. Medd. 18, No. 8 (1948).

11. A. Bohr, Atomic Interaction in Penetration Phenomena, Kgl. Danske Videnskab. Selskab, Mat.-Fys. Medd. 24, No. 19 (1948).

12. H. Christensen, Surface Conduction Channel Phenomena in Germanium, Proc. Inst. Radio Engrs. 42, 1371 (1954).

13. A. G. Chynoweth, W. L. Feldmann, and R. A. Logan, Excess Tunnel Current in Silicon Esaki Junctions, Phys. Rev. 121, 684 (1961).

14. R. L. Cummerow, Photovoltaic Effect in p-n Junctions, Phys. Rev. 95, 16 (1954).

15. M. Cutler and H. M. Bath, Surface Leakage Current in Silicon Fused Junction Diodes, Proc. Inst. Radio Engrs. 45, 39 (1957).

16. B. Dale and F. P. Smith, Spectral Response of Solar Cells, J. Appl. Phys. 32, 1377 (1961).

17. J. M. Denney, R. G. Downing and A. Grenall, High Energy Proton Radiation Damage, in Progress in Astronautics and Rocketry Vol. 3, Academic Press, Inc. New York, N. Y. (1961).

18. G. T. Dienes and G. H. Vineyard, Radiation Effects in Solids (Interscience Publishers Ltd., London, 1957), Chap. 2.

19. W. T. Eriksen, H. Statz, and G. A. deMars, Excess Surface Currents on Germanium and Silicon Diodes, J. Appl. Phys. 28, 133 (1957).

20. L. Esaki and Y. Miyahara, A New Device Using the Tunneling Process in Narrow p-n Junctions, Solid-State Electron. 1, 13 (1960).

21. R. D. Evans, The Atomic Nucleus, (McGraw-Hill Book Co., Inc., New York, 1955), Chap. 18.

22. G. Fabri, E. Gatti, and V. Svelto, Energy for Electron-Hole Pair Generation in Silicon by α-Particles, Phys. Rev. 131, 134 (1963).

23. U. Fano, Penetration of Protons, Alpha Particles, and Mesons, Ann. Rev. of Nucl. Sci. 13, 1 (1963).

24. E. Fermi and E. Teller, The Capture of Negative Mesotrons in Matter, Phys. Rev. 72, 399 (1947).

25. H. Flicker, J. J. Loferski, and J. Scott-Monck, Radiation Defect Introduction Rates in n- and p-type Silicon in the Vicinity of the Radiation Damage Threshold, Phys. Rev. 128, 2557 (1962).

26. H. Flicker and J. J. Loferski, Distribution of Electron-Bombardment-Induced Radiation Defects with Depth in Silicon, J. Appl. Phys. 34, 2146 (1963).

27. G. W. Gobeli, Range Energy Relation for Low-Energy Alpha Particles in Si, Ge, and InSb, Phys. Rev. 103, 275 (1956).

28. M. Gryzinski, Stopping Power of a Medium for Heavy, Charged Particles, Phys. Rev. 107, 1471 (1957).

29. Iu. K. Guskov, A. V. Zvonarev, and V. P. Klichkova, An Investigation of the E.M.F. Developed When a System of Semiconductors Containing Uranium is Irradiated in a Reactor, J. of Nucl. Energy 8, 231(L) (1961).

30. G. P. Harnwell and W. E. Stephens, Atomic Physics, (McGraw-Hill Book Co., Inc., New York, 1955), Chap. 4.

31. C. L. Hemenway, R. W. Henry, and M. Caulton, Physical Electronics, (John Wiley and Sons, New York, 1962).

32. C. Hilsum and A. C. Rose-Innes, Semiconducting III-V Compounds, (Pergamon Press, New York, 1961).

33. R. Hofstadter, Crystal Counters-I, Nucleonics 4, No. 4, 2 (1949); Proc. Inst. Radio Engrs. 38, 726 (1950).

34. G. H. Kinchen and R. S. Pease, The Displacement of Atoms in Solids by Radiation, Rept. Progr. Phys. 18, 1 (1955).

35. M. F. Lamorte, Internal Power Dissipation in Gallium Arsenide Solar Cells, Advan. Energy Conversion J.3, 551 (1963).

36. J. J. Loferski, Theoretical Considerations Governing the Choice of the Optimum Semiconductor for Photovoltaic Solar Energy Conversion, J. Appl. Phys. 27, 777 (1956).

37. J. J. Loferski and J. J. Wysocki, Spectral Response of Photovoltaic Cells, RCA Rev. 22, 38 (1961).

38. J. J. Loferski and P. Rappaport, The Effect of Radiation on Silicon Solar Energy Converters, RCA Rev. 19, 536 (1958).

39. J. J. Loferski and P. Rappaport, Radiation Damage in Ge and Si Detected by Carrier Lifetime Changes: Damage Thresholds, Phys. Rev. 111, 432 (1958).

40. J. J. Loferski, Recent Research on Photovoltaic Solar Energy Converters, Proc. Inst. Elec. Electron. Engrs. 51, 667 (1963).

41. G. G. Macfarland, T. P. McLean, J. E. Quarrington, and V. Roberts, Fine Structure in the Absorption-Edge Spectrum of Si, Phys. Rev. 111, 1245 (1958).

42. F. W. Martin and L. C. Northcliffe, Energy Loss and Effective Charge of He, C. and Ar Ions Below 10 Mev/amu in Gases, Phys. Rev. 128, 1166 (1962).

43. K. G. McKay, Electron-Hole Production in Germanium by Alpha Particles, Phys. Rev. 84, 829 (1951).

44. A. L. McWhorter and R. H. Kingston, Channels and Excess Reverse Current in Grown Germanium p-n Junction Diodes, Proc. Inst. Radio Engrs. 42, 1376 (1954).

45. B. Ya. Moizhes, On the Theory of Photocells with a p-n Junction, Soviet Phys.-Solid State 2, 202 (1960).

46. N. F. Mott, On the Theory of Excitation by Collision with Heavy Particles, Proc. Cambridge Phil. Soc. 27, 553 (1931).

47. W. G. Pfann and W. van Roosbroeck, Radioactive and Photoelectric p-n Junction Power Sources, J. Appl. Phys. 25, 1422 (1954).

48. J. G. Poksheva, Alpha-Voltaic Study of Radiation Damage Imparted by 4-Mev Alpha Particles to Silicon Solar Cells, UCRL-16061, June 1965.

49. H. J. Queisser, Forward Characteristics and Efficiencies of Silicon Solar Cells, Solid-State Electron. 5, 1 (1962).

50. P. Rappaport, J. J. Loferski, and E. G. Linder, The Electron-Voltaic Effect in Germanium and Silicon p-n Junctions, RCA Rev. 17, 100 (1956).

51. P. Rappaport, The Photovoltaic Effect and Its Utilization, RCA Rev. 21, 373 (1959).

52. W. Rosenzweig, H. K. Gummel, and F. M. Smits, Solar Cell Degradation Under 1-Mev Electron Bombardment, Bell System Tech. J. 42, 399 (1963).

53. C. Sah, R. N. Noyce, and W. Shockley, Carrier Generation and Recombination in p-n Junctions and p-n Junction Characteristics, Proc. Inst. Radio Engrs. 45, 1228 (1957).

54. F. Seitz, On the Disordering of Solids by Action of Fast Massive Particles, Discussions Faraday Soc. 5, 271 (1949).

55. F. Seitz and J. S. Koehler, Displacement of Atoms During Irradiation Solid State Phys. 2, 305 (1956).

56. W. Shockley, The Theory of p-n Junctions in Semiconductors and p-n Junction Transistors, Bell System Tech. J. 28, 435 (1949).

57. W. Shockley and W. T. Read, Jr., Statistics of the Recombinations of Holes and Electrons, Phys. Rev. 87, 835 (1952).

58. W. Shockley, Electrons and Holes in Semiconductors, (D. Van Nostrand Co., Inc., New York, 1950), Chap. 4.

59. W. Shockley and H. J. Queisser, Detailed Balance Limit of Efficiency of p-n Junction Solar Cells, J. Appl. Phys. 32, 510 (1961).

60. H. Statz, G. A. deMars, L. Davis, Jr., and A. Adams, Jr., Surface States on Silicon and Germanium Surfaces, Phys. Rev. 101, 1272 (1956).

61. V. K. Subashiev, Distribution of Losses and the Efficiency of Different Processes in Photoelectric Converters of Solar Energy, Soviet Phys.-Solid State 2, 181 (1960).

62. T. J. Thompson, Effect of Chemical Structure on Stopping Power for High-Energy Protons, UCRL-1910 (1952).

63. H. S. Veloric and M. B. Prince, High Voltage Conductivity-Modulated Silicon Rectifier, Bell System Tech. J. 36, 975 (1957).

64. G. D. Watkins and J. W. Corbett, Defects in Irradiated Silicon, I. Electron Spin Resonance of the Si-A Center, Phys. Rev. 121, 1001 (1961).

65. G. K. Wertheim, Energy Levels in Electron-Bombarded Silicon, Phys. Rev. 105, 1730 (1957); Electron-Bombardment Damage in Silicon, Phys. Rev. 110, 1272 (1958).

66. M. Wolf and H. Rauschenbach, Series Resistance Effects on Solar Cell Measurements, Advan. Energy Conversion 3, 455 (1963).

67. J. J. Wysocki and P. Rappaport, Effect of Temperature on Photovoltaic Solar Energy Conversion, J. Appl. Phys. 31, 571 (1960).

68. J. J. Wysocki, The Effect of Series Resistance on Photovoltaic Solar Energy Conversion, RCA Rev. 22, 57 (1961).

69. See for example, J. M. Ziman, Electrons and Phonons, (Oxford Univ. Press, London, 1960)., Chap. 5.

70. V. P. Zrelov and G. D. Stoletov, Range-Energy Relations for 660-Mev Protons, Soviet Phys. JETP 9, 461 (1959).